Entwicklung neuer Anodenmaterialien auf Basis von Kupfer, Eisen und Schwefel

Kumulative Dissertation

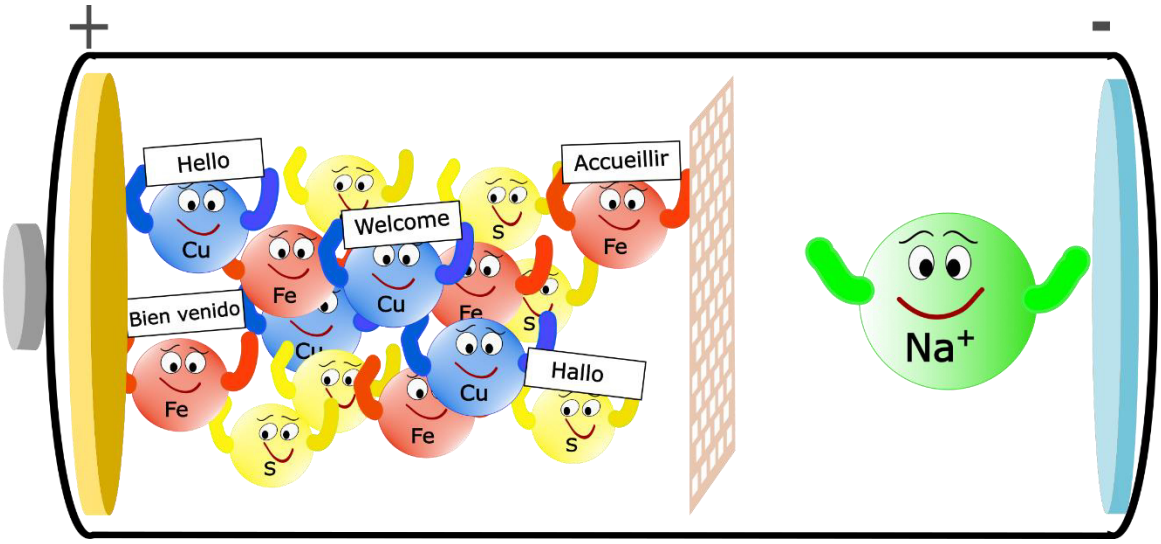

Zur Erlangung des Doktorgrades an der Mathematisch Naturwissenschaftlichen Fakultät der Christian-Albrechts-Universität zu Kiel

Bearbeitet und vorgelegt von

Svenja Senkale

Kiel 2024

Erster Gutachter: Prof. Dr. Wolfgang Bensch

Zweiter Gutachter: Prof. Dr. Norbert Stock

Tag der mündlichen Prüfung:

29.04.2024

Die vorliegende Dissertation wurde unter Anleitung von

Prof. Dr. Wolfgang Bensch

in der Zeit von

2012 bis 2024

am Institut für Anorganische Chemie

der Christian-Albrechts-Universität zu Kiel

angefertigt.

Eidesstattliche Erklärung

Ich erkläre, dass ich meine vorliegende Dissertation mit dem Thema: „Entwicklung neuer Anodenmaterialien auf Basis von Kupfer, Eisen und Schwefel“ selbstständig und ohne Benutzung anderer als der angegebenen Hilfsmittel angefertigt habe und dass ich alle Stellen, die ich wörtlich oder sinngemäß aus Veröffentlichungen entnommen habe, als solche kenntlich gemacht habe. Die Arbeit hat bisher in gleicher oder ähnlicher Form oder auszugsweise noch keiner Prüfungsbehörde vorgelegen und wurde unter Einhaltung der Regeln guter wissenschaftlicher Praxis der Deutschen Forschungsgemeinschaft angefertigt. Ich bestätige, dass mir kein akademischer Grad entzogen wurde.

Kiel, 12.02.2024 Svenja Senkale

Kurzzusammenfassung

Das Hauptaugenmerk dieser Dissertation liegt auf der Untersuchung ternärer Kupfer-Eisen-Sulfide als potentielle Anodenmaterialien in Natrium-Ionen-Batterien (NIB). Die drei Verbindungen $CuFeS_2$, $CuFe_2S_3$ und Cu_5FeS_4 wurden mittels Hochtemperatursynthese als Volumenmaterial synthetisiert und ohne zusätzliche Behandlung als Anodenmaterial für NIB getestet. Um die elektrochemische Leistungsfähigkeit zu erfassen, wurden galvanostatische und potentiostatische Messungen durchgeführt. Die Ergebnisse zeigen unter anderem eine gute Langzeitstabilität als auch eine hervorragende Ratenstabilität für alle drei Materialien.

Um ein besseres Verständnis über Reaktionsmechanismen dieser Materialklasse in NIB zu erhalten, wurde bei unterschiedlichen Natriumaufnahme- und Abgabestufen die Entladung bzw. Ladung abgebrochen, das Anodenmaterial isoliert und mit unterschiedlichen Methoden untersucht. Neben Standardmethoden wie Röntgendiffraktotmetrie wurden auch spezielle Techniken wie Röntgenabsorptionsspektroskopie, Mößbauer- oder Festkörper-Kernspinresonanz-Spektroskopie eingesetzt. Mit dieser Kombination an Methoden konnten die elektronischen und strukturellen Zustände der einzelnen Abbruchstufen umfassend charakterisiert werden.

Bei den Untersuchungen hat sich herausgestellt, dass jede Verbindung einen eigenen Reaktionsmechanismus aufweist. Jedoch gibt es eine Gemeinsamkeit: Es tritt stets ein Chvilevaite verwandtes Intermediat auf, $NaCu_xFe_yS_2$. Zusätzlich weisen die Anodenmaterialien bei Abbrüchen nach mehreren hundert Zyklen immer noch nanokristalline Strukturen auf, was bei Konversionsmaterialien äußerst selten ist, da meist schon nach wenigen Zyklen nur noch amorphe Materialien vorliegen. Der Erhalt kristalliner Strukturen könnte einer der Faktoren sein, warum diese guten Langzeitstabilitäten erreicht werden können. Dabei scheint bei den ternären Verbindungen ein Synergieeffekt vorzuliegen, da die binären Randphasen die im Rahmen dieser Arbeit nachgewiesenen elektrochemischen Eigenschaften bei weitem nicht erreichen.

Solche Synergieeffekte sollten auch bei Multielementverbindungen zu beobachten sein. Das war die Motivation, um in dieser Dissertation ein weiteres innovatives Material zu synthetisieren und zu charakterisieren: einen entropie-stabilisierten Spinell mit der Zusammensetzung $Mn_{0.2}Co_{0.2}Ni_{0.2}Cu_{0.2}Zn_{0.2}Fe_2O_4$. Bei der Charakterisierung dieses Materials

wurde ersichtlich, dass ein TEM-Mapping und ein Röntgenpulverdiffraktogramm nicht ausreichen, um solch ein komplexes Material als einphasig und/oder entropiestabilisiert einzuordnen.

Abstract

The main focus of this thesis is to investigate ternary copper-iron sulfides as potential anode materials in sodium-ion batteries (SIBs). The three sulfides, $CuFeS_2$, $CuFe_2S_3$, and Cu_5FeS_4, were synthesized as bulk materials by high-temperature synthesis and they were tested as anode materials without any additional treatment. Galvanostatic and potentiostatic measurements were performed to investigate the electrochemical performance. Among others, a good long-term stability as well as an excellent rate stability could be evidenced for all three materials.

In order to gain a deeper understanding of the reaction mechanism of this class of materials, the discharge and charge reactions were stopped at different sodium uptake and release levels, the anode material was isolated and investigated by different analytical methods. These included standard methods such as X-ray powder, as well as special techniques such as X-ray absorption spectroscopy, Mößbauer or solid-state nuclear magnetic resonance spectroscopy. Thus, the electronic and structural states of the different charge and discharge levels could be characterized comprehensively.

It has been observed that each reaction mechanism proceeds differently. However, there is a common observation: a Chvilevaite related intermediate, $NaCu_xFe_yS_2$, always occurs. In addition, the anode materials still show some nanocrystalline structures after several hundred cycles, which is extremely rare for conversion materials, since usually only amorphous structures are present after a few cycles. The preservation of crystalline structures could be one of the main factors why such good long-term stabilities can be achieved. It seems that the ternary sulfides exhibit a synergistic effect because the binary bulk phases do not reach the high electrochemical performance observed here.

Such synergistic effects can be expected for other multi-element compounds. This was a motivation to synthesize and characterize an entropy-stabilized spinel with composition $Mn_{0.2}Co_{0.2}Ni_{0.2}Cu_{0.2}Zn_{0.2}Fe_2O_4$. The characterization of this material demonstrates that it takes more than a TEM mapping and an X-ray powder diffraction pattern to call such a complex material single-phase or entropy-stabilized.

Abkürzungsverzeichnis

Abkürzung	Bedeutung
OECD	Organization for Economic Co-Operation and Development
WEC	World Energy Council
SSES	Stationäre Energiespeichersysteme
LIB	Lithium-Ionen-Batterien
NIB	Natrium-Ionen-Batterien
LCO	Lithium-Kobaltoxid
LMO	Lithium-Manganoxid
LFP	Lithium-Eisenphospat
NCA	Lithium-Nickel-Kobalt-Aluminiumoxid
NMC	Lithium-Nickel-Mangan-Kobaltoxid
SEI	Solid Electrolyte Interphase
XRD	Röntgendiffraktometrie
PDF	Paarverteilungsfunktion
XAS	Röntgenabsorptionsspektroskopie
Na-NMR	Natrium-Resonanzspektroskopie
rGO	Reduziertes Graphenoxid
CNTs	Kohlenstoffnanoröhren
TEM	Transmissionselektronenmikroskopie
EFG	Elektrischer Feldgradient

Inhaltsverzeichnis

1. Einleitung

1.1 Motivation

Die wachsende Population im Zusammenspiel mit der fortschreitenden Industrialisierung lassen den weltweiten Energiebedarf drastisch ansteigen. In den vergangenen Jahren von 1970 bis 2019 ist der Energiebedarf von 66378 zu 173340 TWh um das Zweieinhalbfache gestiegen[1], während die Population sich in dieser Zeit auf 7.3 Milliarden verdoppelt hat. Die Prognosen zeigen zudem, dass der Energiebedarf zukünftig noch steigen wird. Dabei wird insbesondere der Energiebedarf der Nicht-OECD Länder (OECD = Organization for Economic Co-Operation and Development) stark ansteigen im Vergleich zu den OECD Ländern aufgrund des starken Wirtschafts- und Bevölkerungswachstums (Abbildung 1).[2]

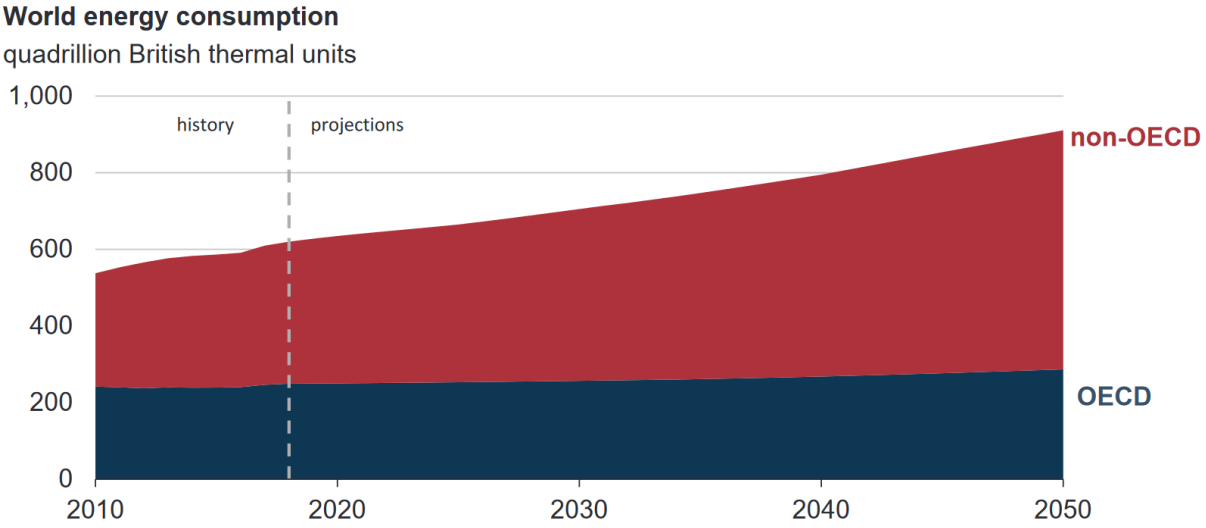

Abbildung 1: Prognose für den weltweiten Energieverbrauch. [2]

Abbildung 6 zeigt die Zusammensetzung der unterschiedlichen Quellen für die Energieproduktion. Es ist ersichtlich, dass der Hauptanteil aus fossilen Brennstoffen wie Erdgas, Erdöl und Kohle gewonnen wird. Nur ein sehr geringer Teil wird aus erneuerbaren Energien generiert. Würde der steigende Energiebedarf mit eben einer solchen Zusammensetzung produziert werden, würde dies zu einer enormen Steigerung des CO_2-Ausstoßes führen, der mit 79% den Hauptanteil aller Treibhausgase ausmacht. Von diesem Anteil werden wiederum 72% auf die Energiegewinnung zurückgeführt.[3,4]

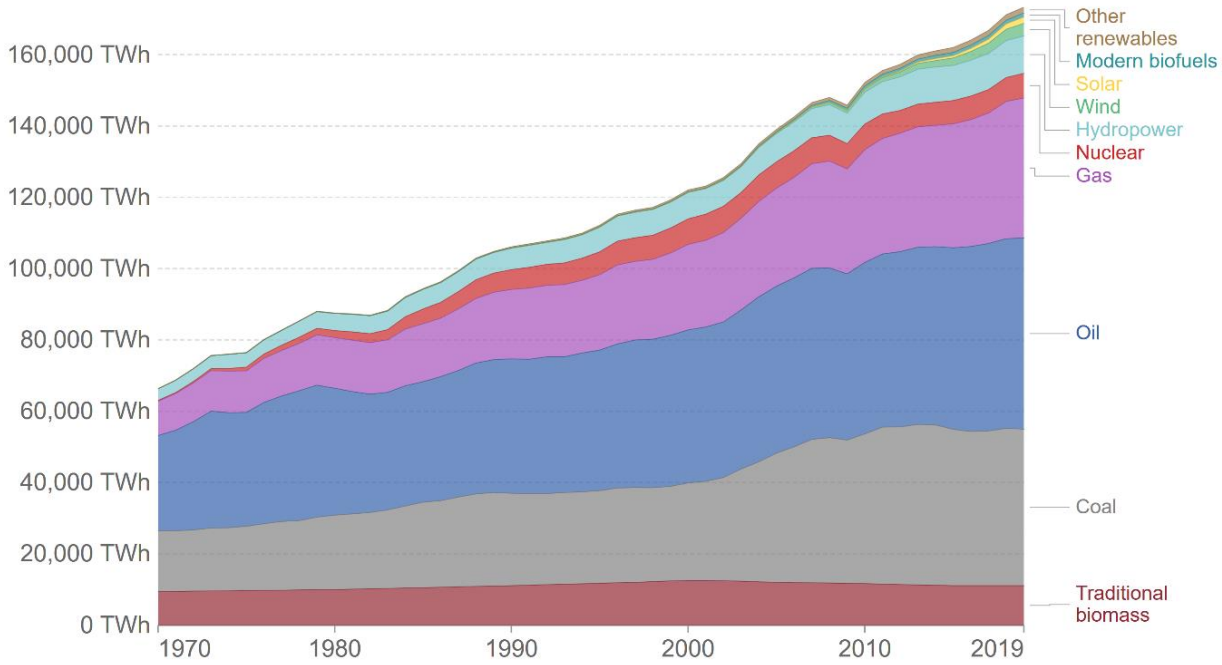

Abbildung 2: Quellen des weltweiten Energieverbrauchs.[5]

Aufgrund der langen Verweildauer von CO_2 in der Atmosphäre ist der Emissionsort unerheblich, da die CO_2-Moleküle während dieser Zeit die Erde mehrfach umrunden. Auch die Quelle, aus der das CO_2 stammt, spielt keine Rolle; einzig allein die absolute Emissionsmenge ist ausschlaggebend. Um der Klimaerwärmung Einhalt zu gebieten ist es somit zwingend erforderlich den absoluten CO_2-Ausstoß zu reduzieren. Da ein Großteil des gesamten CO_2 aus dem Elektrizitäts-/Wärme- und Transportsektor stammt (Abbildung 3)[6], sind dies die vielversprechendsten Angriffspunkte zur Reduzierung der CO_2-Emissionen. Im Transportbereich liegt der Fokus ganz klar auf dem Ausbau der Elektromobilität, da Alternativen wie Brennstoffzellen noch nicht so weit implementiert sind bzw. die dafür benötigte Infrastruktur nur eingeschränkt vorhanden ist.[7] Der direkte CO_2-Ausstoß bei Elektroautos ist gleich null, jedoch zeigen diverse Studien, dass der indirekte CO_2-Ausstoß, bedingt durch die Stromproduktion, durchaus zu negativen ökologischen Auswirkungen führen kann. Daher ist diese Vorgehensweise nur sinnvoll, wenn der genutzte Strom aus CO_2-neutralen erneuerbaren Quellen wie Wind-, Wasser- oder Solarenergie stammt. [8–10]

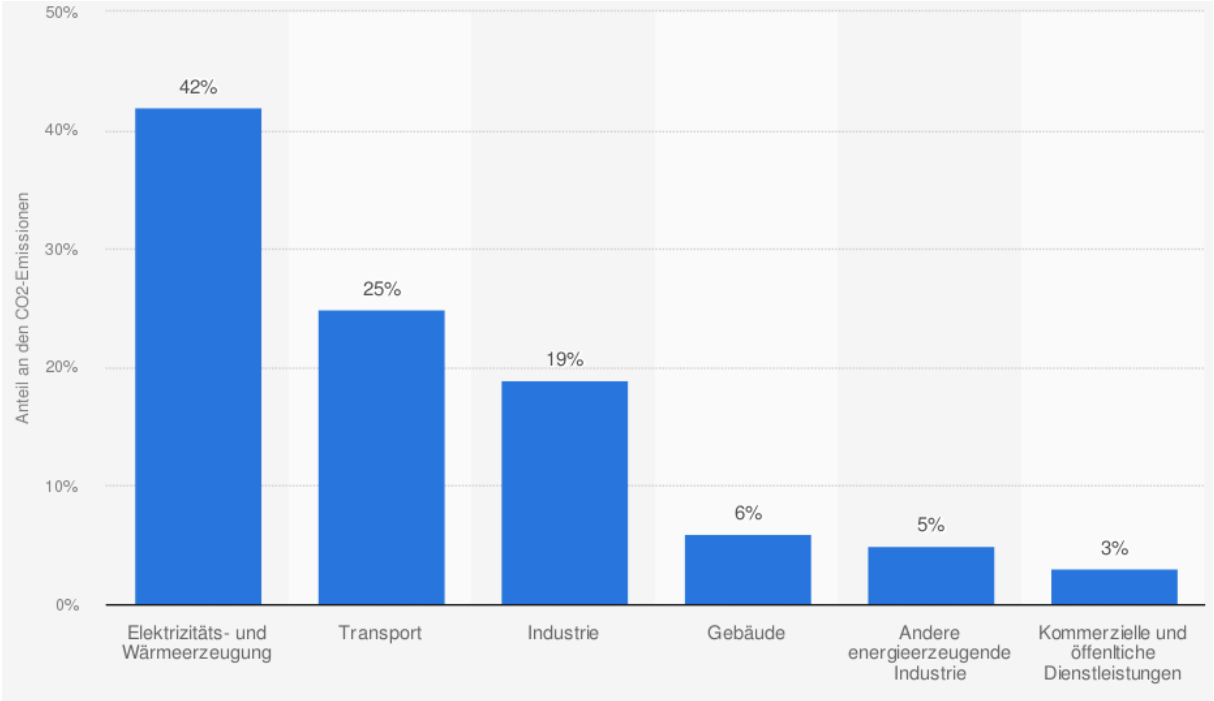

Abbildung 3: Verteilung der energiebedingten CO_2-Emissioenn weltweit nach Sektor im Jahr 2018.[6]

Im Jahr 2016 wurde vom Weltenergierat WEC (engl.: World Energy Council) eine Expertengruppe zusammengerufen, welche zum World Energy Congress in 2019 drei unterschiedliche Szenarien für eine Transformation der Energieversorgung entwickelten. Dabei ist der *Modern Jazz* ein marktgeriebener Ansatz, *Unfinished Symphony* verfolgt einen regierungsgesteuerten Ansatz und im *Hard Rock* stehen die nationalen Interessen der Länder im Vordergrund.[11] Allen drei Szenarien gemein ist ein Anstieg der erneuerbaren Energien auf bis zu 60% der Gesamtenergieproduktion (Abbildung 4).

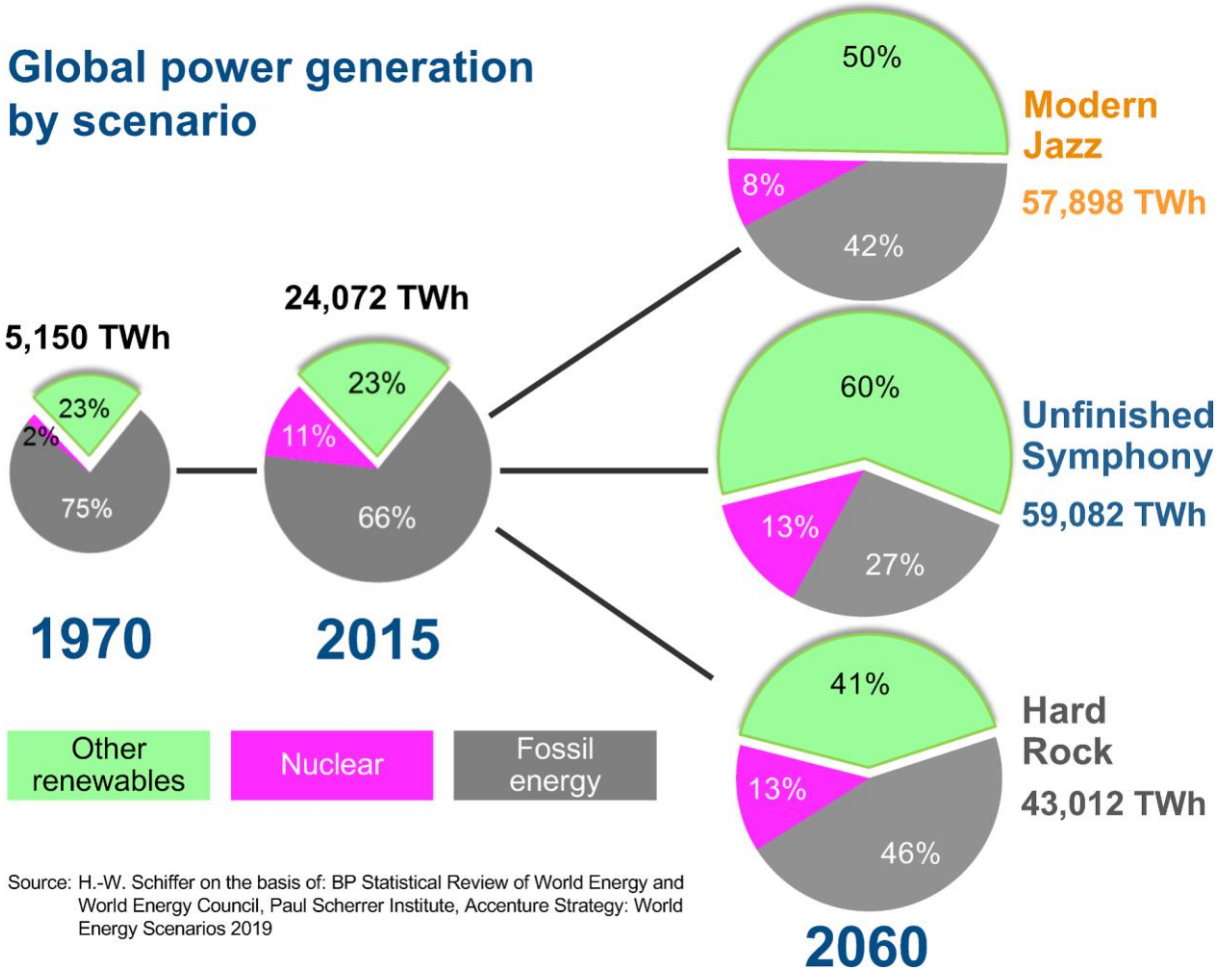

Abbildung 4: Zusammensetzung der globalen Stromerzeugung abhängig vom jeweiligen Szenario.[1]

Erneuerbare Energien können die Kohlekraftwerke jedoch nicht einfach ersetzen, da grüner Strom einer hohen Volatilität unterliegt. Aufgrund dieser Tatsache werden die konventionellen Anlagen als Substitute benötigt und dürfen somit nicht vom Netz genommen werden.[12] Das Stromnetz benötigt eine konstante Frequenz, so dass die Kohle- und Gaskraftwerke während einer Flaute hochgefahren bzw. gedrosselt werden, wenn viel Strom aus Sonnen und Windkraftwerken eingespeist wird. Mit steigendem Anteil an regenerativen Energien, können auftretende Stromspitzen jedoch nicht mehr durch die Drosselung konventioneller Kraftwerke abgefangen werden. Dieser Anteil liegt in Deutschland bei ca. 30 %, also nur knapp über dem jetzigen Stand von 25.2%.[13] Sollte eine Abpufferung der überschüssigen Energie unmöglich sein und sie soll nicht verfallen, d.h. die Wind- oder Solarkraftwerke werden abgeschaltet, müssen Wege genutzt werden diese zusätzliche Energie zu speichern oder in Gegenden abzutransportieren, in denen zu der Zeit ein größerer Energiebedarf besteht. Dies setzt allerdings eine gute und über weite Strecken verfügbare Energieinfrastruktur voraus. In

Ländern mit einer hohen Populationsdichte ist dies durchaus machbar und auch schon zum Teil mit dem europäischen Stromverbund in kleinem Maße umgesetzt. In Gegenden wie z.B. Nordafrika mit ausgesprochen guten Voraussetzungen für Solarenergie ist es jedoch aufgrund der geringen Bevölkerungsdichte (die Küstenregionen ausgenommen) schwer vorstellbar und mit sehr großen Kosten verbunden die gesamte Bevölkerung mit einem Stromnetz zu versorgen. Hier wären lokale stationäre Energiespeichersysteme (SESS) eine Alternative. Während es bei einer guten Energieinfrastruktur durchaus attraktiv ist die Energie in Pumpspeicherwerke zu leiten (trotz teilweise hohen Wirkungsgradverlusten), sind ohne diese Möglichkeit Alternativen gefragt. Möglichkeiten dafür sind die chemische Speicherung als Wasserstoff oder auch die Speicherung in Batterien. Während ersteres auch eine spezifische Infrastruktur für den Transport des Gases benötigt, kann die Speicherung in Batterien durchaus direkt vor Ort in großen stationären Energiespeichersystemen erfolgen. Siemens Gamesa startete just ein Pilotprojekt, bei dem eine Kopplung aus Windenergie, Batteriespeichersystem und Elektrolyse grünen Wasserstoff effizient produzieren soll. Dabei hat diese Kombination das Potential bestehende Windkraftprojekte zu übertreffen, da die vorgeschaltete Batterie es erlaubt, den Elektrolyseur länger konstant laufen und somit effizienter grünen Wasserstoff produzieren zu lassen. Bei starker Stromproduktion können die Batterien überschüssigen Strom ins Netz einspeisen, so dass maximale Flexibilität gewährleistet ist.[14] SESS werden demnach in der Zukunft eine immer bedeutendere Rolle einnehmen insbesondere im Hinblick auf den steigenden Primärenergieverbrauch gerade in Gebieten mit einer stark eingeschränkten Infrastruktur (Abbildung 5).

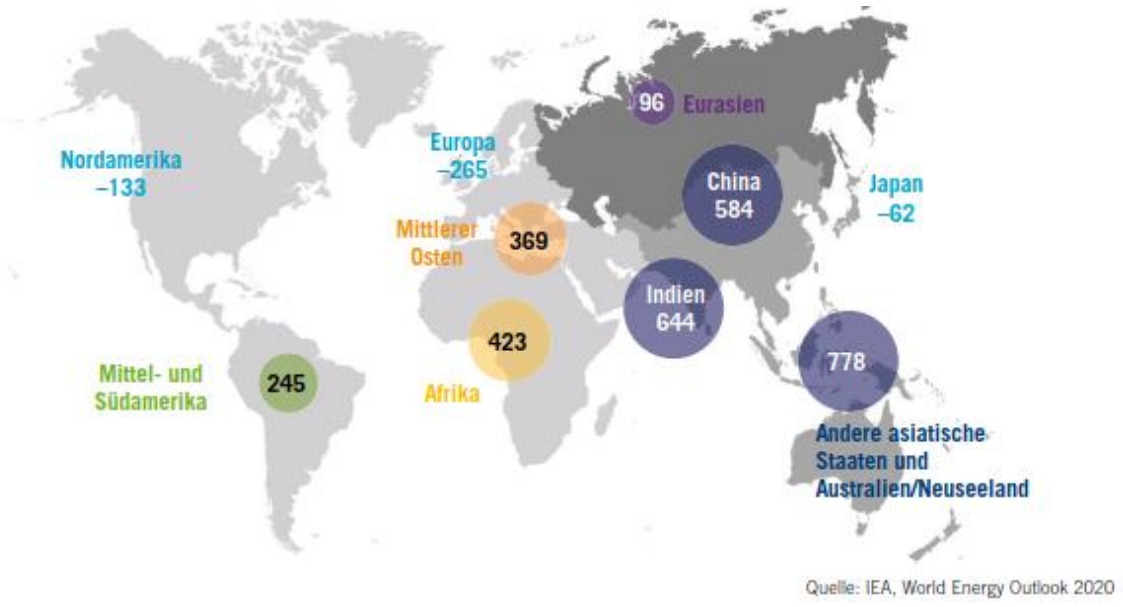

Abbildung 5: Prognostizierter Zuwachs im Primärenergieverbrauch nach Weltregionen 2019 bis 2040.[15]

Da der Bedarf an Energiespeichersystemen stark ansteigt, insbesondere im Bereich der Elektromobilität[16], nehmen die weltweiten im Moment zur Verfügung stehenden Lithiumressourcen stark ab, der Weltmarktpreis für Li_2CO_3 hat sich in den letzten 2 Jahren fast versiebenfacht und die Vorkommen befinden sich zusätzlich in sensiblen geopolitischen Regionen wie Chile, China und Argentinien.[17] Die Forschung Lithium aus weiteren Quellen, z.B. Meerwasser, zu extrahieren, macht große Fortschritte, wurde aber aufgrund des hohen Aufwands und der Energiekosten noch nicht im industriellen Maßstab eingesetzt.[18,19] Oben erwähnte Bedenken machen die Erforschung von Alternativen notwendig. Dabei ist Natrium im Hinblick auf wirtschaftliche und ökologische Nachhaltigkeit und aufgrund der ähnlichen elektrochemischen Eigenschaften sehr vielversprechend. Aufgrund der großen Abundanz kommt es zu deutlich niedrigeren Materialkosten, Na_2CO_3 ist etwa 50-mal günstiger als Li_2CO_3. Natrium ist allerdings ca. dreimal so schwer und 1,3-mal so groß wie Lithium und das elektrochemische Potential ist um 0.3 V geringer. Diese Nachteile sind für SESS jedoch überwiegend irrelevant, da Gewicht und Menge bei stationären Systemen nur eine geringe Rolle spielen. Daher gilt Natrium als vielversprechendste Alternative für SESS und die verfügbaren Lithiumressourcen stünden ohne Einschränkungen für die mobilen Anwendungen zur Verfügung.

1.2 Ziele dieser Arbeit

Ein simpler Austausch des Lithiums gegen Natrium in die etablierten Interkalationssysteme ist aufgrund der physikalischen Eigenschaften des Natriums nicht so trivial. Während die Forschung gute Ergebnisse bei der Übertragung auf die Kathodenmaterialien erzielt[20–22], gestaltet sich dies bei den Anodenmaterialien komplizierter. Während das meist verwendete Material Graphit mit Lithium, lithiumreiche Interkalationsverbindungen (LiC_6) bildet, ist das mit Natrium nicht möglich, ohne dass spezielle Strategien zum Einsatz kommen.[23,24] Daher hängt der Erfolg, kommerzielle sekundäre Batterien auf Natriumbasis zu produzieren, im Wesentlichen vom Erfolg der Identifizierung geeigneter Anodenmaterialien ab. Optimalerweise sollten diese hohe spezifische Kapazitäten, hohe Energiedichten und eine gute Langzeitstabilität aufweisen und zudem aus gut verfügbaren, nachhaltigen und preiswerten Materialien bestehen. Konversionsmaterialien scheinen vielversprechend zu sein, da sie aufgrund ihres Multi-Elektronen-Reaktionsmechanismus diesen Anforderungen entsprechen. Konversionsmaterialien basieren auf der elektrochemischen Materialumwandlung, bei denen

in den meisten Fällen die Metallionen in der Anode bis zu ihrem metallischen Zustand reduziert werden, so dass eine hohe spezifische Kapazität erreicht werden kann.

Jedoch bringen diese Art von Anodenmaterialien auch Nachteile mit sich. Eine große Volumenarbeit führt oft zu einer geringen Langzeitstabilität, während eine ausgeprägte Spannungshysterese die Energieeffizienz und Ausgangsspannung der Zelle verringern können. Um erfolgreich Konversionsmaterialien einsetzen zu können, muss daher noch ein tieferes Verständnis für Konversionsreaktionen geschaffen werden. Deswegen wurden in dieser Arbeit auf Sulfid basierende Aktivmaterialien für Anoden synthetisiert und untersucht, wobei ein Schwerpunt auf der Identifizierung des zugrundeliegenden Mechanismus lag.

Sulfide haben sich als vorteilhaft für Konversionsmaterialien herausgestellt, da das dabei entstehende Na_2S eine größere Leitfähigkeit im Vergleich zu Na_2O hat und die schwächeren Metall-Sulfid-Bindungen kinetisch vorteilhaft sind.

Viele binäre Metallsulfide wurden schon untersucht, wobei Eisensulfide sehr attraktiv in Anbetracht des günstigen Preises, der guten Verfügbarkeit und der Umweltverträglichkeit sind. Oftmals weisen sie jedoch eine schlechte Zyklenstabilität auf, weswegen Additive (CNTs, Graphen, rGO etc.) zugegeben oder aufwendige morphologische Modifizierungen durchgeführt werden müssen, um eine befriedigende Zyklenstabilität zu erreichen (siehe Kapitel 2.4).

Ternäre Sulfide sind seltener untersucht worden, insbesondere wurde der Aufklärung der Reaktionsmechanismen wenig Aufmerksamkeit gewidmet, obwohl sich diese Verbindungen aufgrund von Synergieeffekten und Mehrphasenbildung häufig von Vorteil erweisen. Z.B. zeigten verschiedene ternäre Kupferverbindungen außerordentlich gute elektrochemische Eigenschaften im Vergleich zu ihren bivalenten Pendants.[25,26]

Diese Beobachtung stellt das Leitmotiv dieser Arbeit dar: Elektrochemische Eigenschaften der vielversprechenden Eisensulfide als Anodenmaterial durch Integration von Kupfer zu optimieren und zu stabilisieren. Dabei liegt der Fokus auf der Entschlüsselung der Reaktionsmechanismen, so dass zukünftig zielgerichteter neue Anodenmaterialien designt werden können. Um die genauen Reaktionsschritte identifizieren zu können, wurden Methoden wie Röntgendiffraktometrie (XRD), Paarverteilungsfunktion (PDF), Röntgenabsorptionsspektroskopie (XAS) und Mößbauer-Spektroskopie verwendet. Diese Kombination analytischer Methoden war notwendig, da sich oft nanoskopische oder sogar amorphe Zwischenprodukte bilden, welche nicht mit Standardmethoden charakterisiert werden können.

2. Theoretischer Hintergrund

2.1 Alkalimetall-Ionen-Batterien

Alkalimetall-Ionen-Batterien wandeln chemische Energie in elektrische Energie um. Dabei besteht eine Batterie aus einer oder mehreren Zellen, die parallel oder in Serie verbunden sind, abhängig von der gewünschten Ausgangsspannung und Kapazität. Eine solche Zelle besteht aus einer positiven Elektrode (Kathode), einer negativen Elektrode (Anode), einem Separator und dem Elektrolyten. Während die Elektronen beim Betrieb durch einen elektrischen Leiter wandern, bewegen sich die Ionen durch den Elektrolyten, um die Ladungsneutralität zu gewährleisten. In Alkalimetall-Ionen-Batterien ist überwiegend Li^+ vorhanden, während Na^+ selten und K^+ noch nicht industriell eingesetzt werden. Basierend auf der Reversibilität der chemischen Reaktion können die Batterien in primäre und sekundäre Batterien unterteilt werden. Primäre Batterien werden nur einmalig genutzt und können hohe Kapazitäten und Spannungen erreichen. Bei sekundären, also wieder-aufladbaren Batterien hingegen, können durch das Anlegen einer elektrischen Spannung die bei der Entladung ablaufenden Reaktionen umgekehrt werden. Dabei gelang mit den Lithium-Ionen-Batterien (LIB) der Durchbruch in der elektrochemischen Energiespeicherung.

2.2 Lithium-Ionen-Batterien

LIB sind neben den Blei-Säure-Akkus die meistverkauften sekundären Batterien. Der Durchbruch gelang mit der Entwicklung der Graphit-Anode, welche eines der Hauptprobleme der LIB löste, die Lithium-Dendritenbildung.[27–29] Diese führte oftmals zu elektrischen Kurzschlüssen mit spontanen Entzündungen oder Explosionen. Die daraus von Whittingham, Goodenough und Yoshino entwickelte ‚rocking chair battery' wurde 1991 von Sony kommerzialisiert und ist bis heute das basierende Prinzip der LIB.[30–33] Ständige und bis heute andauernde Forschungen führten und führen zu stetigen Verbesserungen in Hinblick auf Energiedichte, Langzeitstabilität und Ökologie.[34–37]

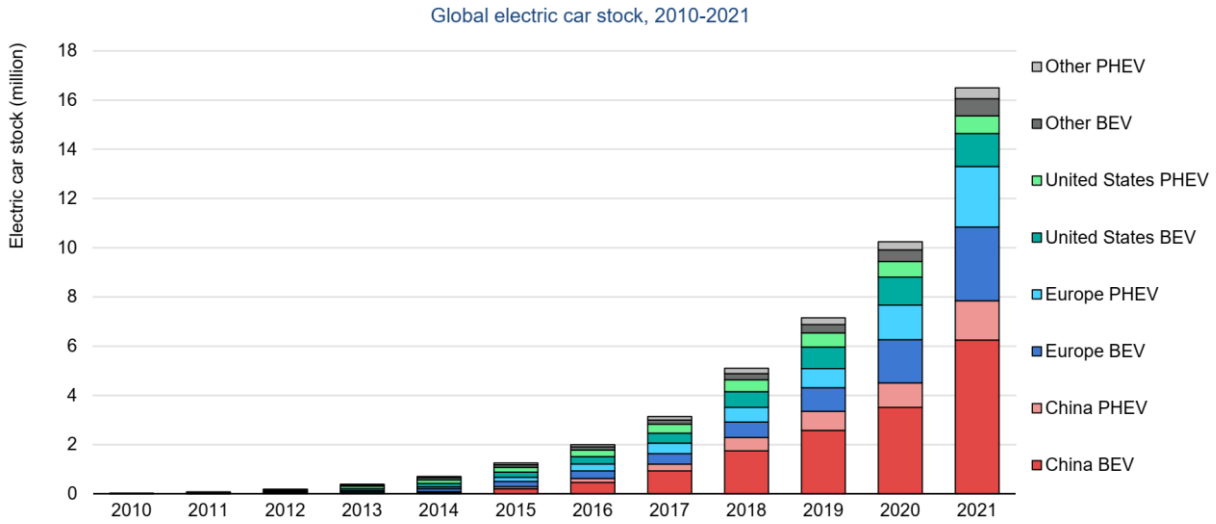

Abbildung 6: Der weltweite Bestand an wieder aufladbaren Elektrofahrzeugen, 2010-2021.[38]

LIB gewinnen rasant an Nachfrage insbesondere aufgrund der stetig wachsenden Elektromobilität. (Abbildung 6). LIB dominieren aufgrund ihrer Eigenschaften den Markt für portable Anwendungen. Sie sind leicht, kompakt, langlebig und bieten eine sehr gute Leistungs- und Energiedichte. Dabei werden die LIB nach ihrem Lithium-Ionen-Donator in der Kathode benannt, wie z.B. Lithium-Kobaltoxid (LCO), Lithium-Manganoxid (LMO), Lithium-Eisenphosphat (LFP), Lithium-Nickel-Kobalt-Aluminiumoxid (NCA) oder Lithium-Nickel-Mangan-Kobaltoxid (NMC).[39] Je nach Materialwahl weisen die Batterien unterschiedliche Eigenschaften bezüglich der Kapazität, der Entladungsspannung und natürlich des Preises auf.[40] Als Anodenmaterial wird überwiegend Graphit verwendet, aber auch $Li_4Ti_5O_{12}$ entwickelte sich in den letzten Jahren zu einem vielversprechenden Anodenmaterial und wird als beste Alternative zu Graphit angesehen.[41]

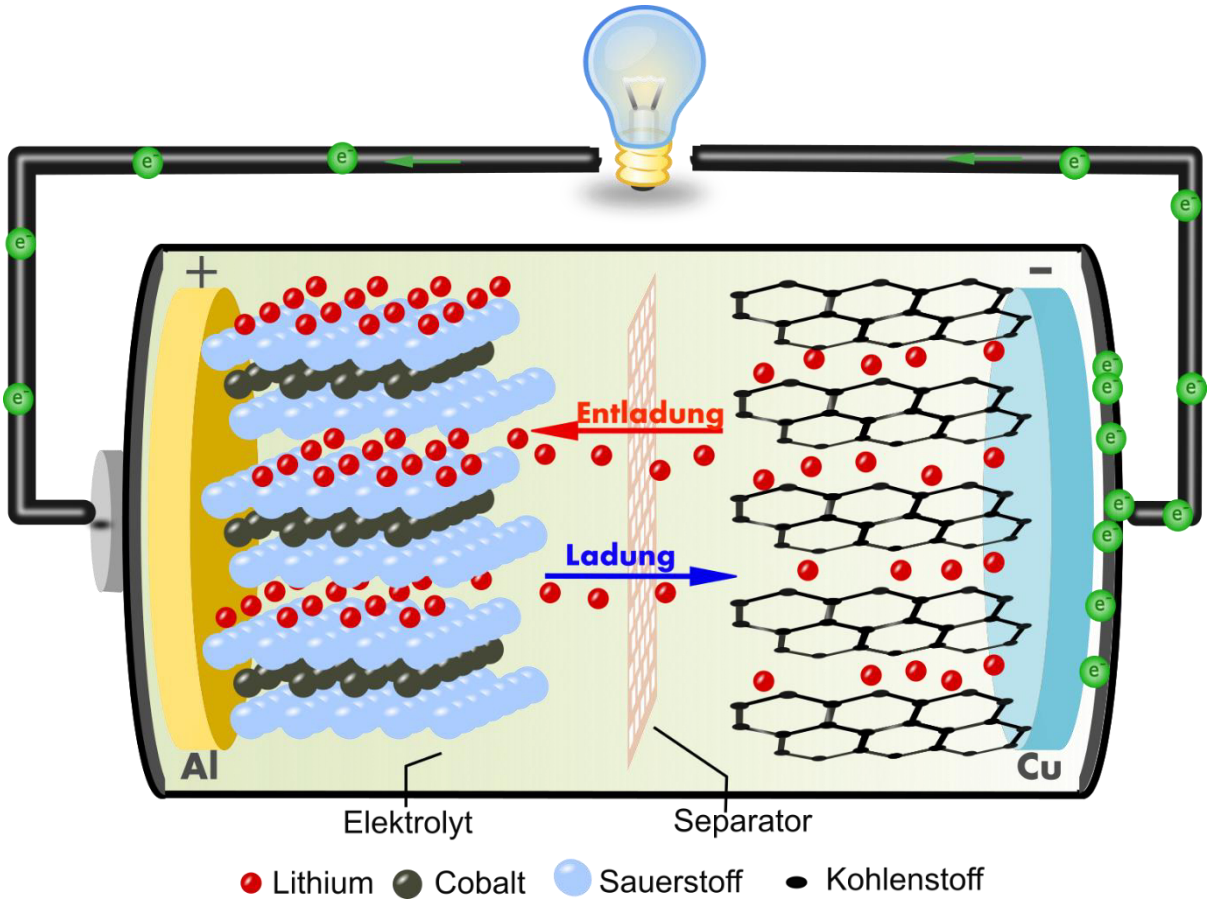

Abbildung 7: Grundsätzlicher Aufbau einer LIB (gezeichnet mit *Inkscape 1.3*).

Das Funktionsprinzip bei all diesen Materialien basiert auf der reversiblen Interkalation von Lithium-Ionen. Die Ionen werden während des Entladens aus der negativen Anode deinterkaliert und in den Elektrolyten abgegeben. Der Elektrolyt transportiert die positiv geladenen Lithium-Ionen von der Anode durch den Separator (meist eine Polymermembran) zur Kathode, wo sie reversibel eingelagert werden. Zur Aufrechterhaltung des Ladungsausgleichs wird diese dabei reduziert. Der Separator ist nur permeabel für Ionen, nicht jedoch für Elektrolytmoleküle, und trennt Anode und Kathode räumlich voneinander, um einem Kurzschluss vorzubeugen. Bei der Deinterkalation von Li aus der Anode (Oxidationsprozess) werden in der Anode Elektronen freigesetzt, welche über den äußeren Stromkreis durch einen Verbraucher der Kathode zugeführt werden. (Abbildung 7). Der Grund für diesen Elektronen- und Ionenfluss ist in der Potentialdifferenz zwischen Anode und Kathode begründet. Dabei hat jedes Material sein spezifisches Oxidations-/Reduktionspotential.[42] Während die Eigenschaften der Elektroden die elektrochemische Leistung der Batterie direkt beeinflussen und damit eine elementare Rolle spielen, darf die Wahl des Elektrolyten nicht unterschätzt werden. Neben der Ermöglichung des Transports der Lithium-Ionen hat der Elektrolyt durch die sogenannte SEI-Bildung (solid electrolyte

interphase) einen großen Einfluss auf Lebenszeit, Sicherheit und Ratenkapazität. Die SEI entsteht durch Zersetzung einer kleinen Menge Elektrolyts während der ersten Entlade- und Lade-Zyklen. Das durch Reduktion des Elektrolyten gebildete Intermediat reagiert mit Lithium-Ionen aus dem Lithiumvorrat der Kathode zur endgültigen SEI-Schicht.[43] Rund 10 % der ursprünglichen Kapazität des ersten vollständigen Zyklus wird durch die SEI-Bildung verbraucht.[44] Wann und bei welchem Potential dies passiert, hängt von vielen Faktoren wie z.B. der Elektrolytzusammensetzung oder der Stromrate ab.[45] Die SEI-Schicht ist ein Lithium-Ionen-Leiter aber ein Isolator für den Elektronenfluss und gewährleistet die Fortsetzung der elektrochemischen Reaktionen und verbessert somit die Zykluslebensdauer der LIB.

LIB erreichen heutzutage bis zu 770 Wh l^{-1} bzw. 260 Wh kg^{-1}, was fast dem physikalisch-chemischen Limit entspricht.[46] LIB wurden sukzessive dem wachsenden Bedarf der mobilen Anwendungen angepasst. Aber mit zunehmendem Anteil an erneuerbaren Energien und zukunftsorientierter Grid-Technologie werden die Mengen an Energiespeichermaterialien drastisch ansteigen, so dass auf kostengünstige und besser verfügbare Materialien ausgewichen werden muss. Natrium ist als Lithiumersatz die naheliegende Wahl, da es weltweit nahezu unbegrenzt verfügbar ist, im Vergleich deutlich billiger ist (Na_2CO_3: 252.96 USD/mt; Li_2CO_3: 10495 USD/mt)[47] und ähnliche Eigenschaften wie Li aufweist. Dies sind die Gründe, warum die Forschungen auf natriumbasierten Speichermaterialien in den letzten Jahren so stark angestiegen sind (siehe Abbildung 8).

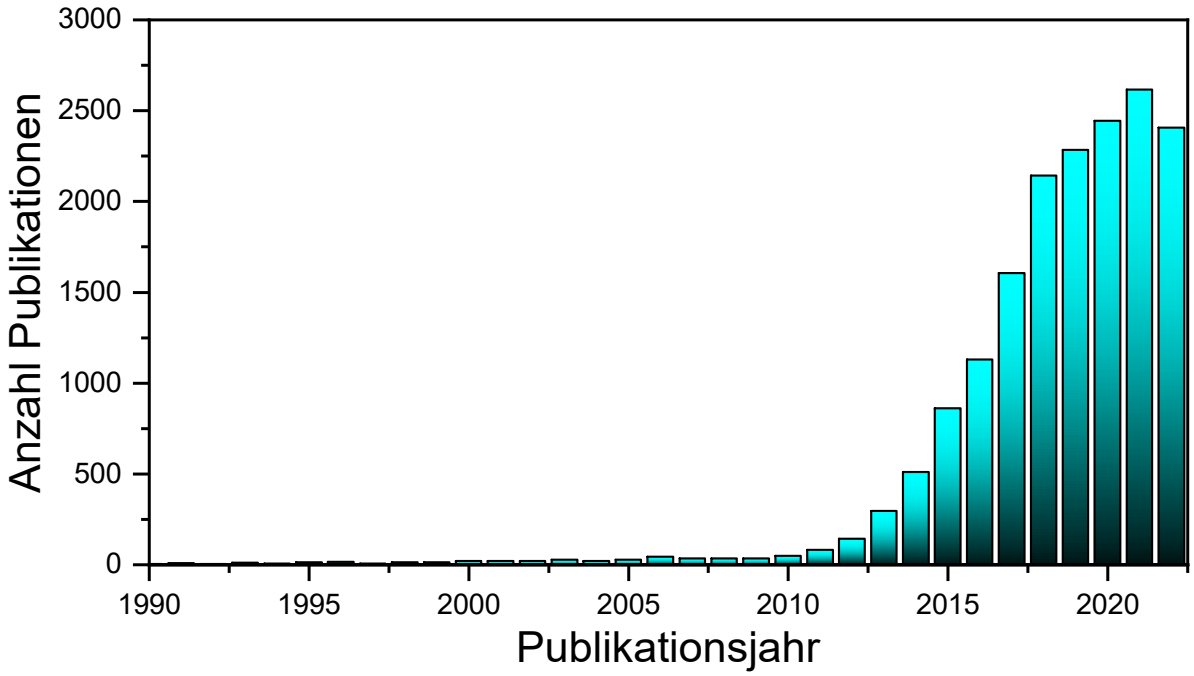

Abbildung 8: Anzahl der Publikationen mit dem Schlagwort 'Sodium ion batteries' (Datenquelle: web of science 01.12.2022).

2.3 Natrium-Ionen-Batterien als Alternative zu LIB

Die Forschung an Natrium-Ionen-Batterien (NIB) begann schon parallel zu LIB in den 70er und 80er Jahren. Die Forschungsaktivitäten gingen jedoch drastisch zurück, als die LIB ihren Durchbruch als kommerzielle Batterie hatte. Jedoch wurden auch einige Natrium-Batterien kommerzialisiert, wie die Natrium-Schwefel-Batterie oder die ZEBRA-Batterie (Zero-Emission Battery Research Activities). Beide sind sogenannte Salzschmelze- oder Thermal-Batterien, bei denen flüssiges Natrium als Anode dient. Daher benötigen diese Batterien Anwendungstemperaturen von 270-350 °C für einen ordnungsgemäßen Betrieb. Aufgrund der hohen Temperaturen sind die Sicherheitsaspekte dieser Batterien nicht vollständig erfüllt. Folglich liegt der Hauptfokus aktuell in der Entwicklung von Elektrolyten und Natriumeinlagerungsmaterialien, die bei Raumtemperatur nutzbar sind, ähnlich zu den LIB.[48] Wie schon in der Motivation erwähnt ist ein Austausch von Lithium gegen Natrium in das vorhandene System jedoch nicht problemlos umsetzbar. Die Unterschiede zwischen diesen Ionen sind in erster Linie der Ionenradius (Li^+: 76 pm; Na^+: 102 pm) und das Atomgewicht, da Natrium nahezu dreimal schwerer ist als Lithium.[49] Das Reduktionspotential ist im Vergleich zur Standardwasserstoffelektrode mit -2,714 V etwas geringer als bei Lithium mit -3,045 V. Obwohl diese Unterschiede nur minimal sind, haben sie einen signifikanten Einfluss auf die Chemie in den Batterien, sowohl in positiver als auch negativer Hinsicht. Natrium bildet mit

Aluminium keine Legierung, so dass dieses anstelle von Kupfer als Kollektor in der Batterie genutzt werden kann. Das würde die Batterie erheblich kostengünstiger machen. Die Vorteile Aluminium an der Anode zu verwenden wären eine geringere Masse, weniger Probleme mit Überentladung, minimierte Kosten und ein sicherer Transport.[50]
Der größere Radius und das höhere Gewicht des Natrium-Ions führen zu einer langsameren Diffusion in feste Elektroden und zu einer größeren Volumenausdehnung im Vergleich zu LIB. Ein weiterer Nachteil sind die geringeren Zellspannungen.[51,52] Diese resultieren jedoch nicht nur aus dem höheren Reduktionspotential, da sich die eigentliche Zellspannung aus der Summe der Potentiale von Anode und Kathode ergibt. Meist jedoch weist Natrium eine niedrigere Zellspannung auf, da die Verschiebung der Redoxpotentiale zu niedrigeren Werten bei positiven Elektroden größer ist als bei den meisten negativen Elektroden.[53] Die daraus resultierenden geringeren Energiedichten sind jedoch für Anwendungen in SESS weniger bedeutend, da hier ein größerer Fokus auf Preis und Nachhaltigkeit gelegt wird.

Die größte Herausforderung ist die Entwicklung von passenden Anodenmaterialien, da für Graphit, welches in fast allen kommerziellen LIB eingesetzt wird, keine natriumreichen Interkalationsverbindungen bekannt sind. Während Lithium eine Interkalationsverbindung LiC_6[54,55] mit einer resultierenden Speicherkapazität von 372 mA h g^{-1} bildet, zeigt Natrium lediglich eine maximale Konzentration von NaC_{168}[56] oder NaC_{64}[57] (12 oder 35 mA h g^{-1}), was Graphit für die Verwendung in Natrium-Ionen-Batterien inakzeptabel macht. Aufgrund der vielen Vorteile von Graphit (günstig, gute Verfügbarkeit, umweltfreundlich und große Vielseitigkeit) wurden die Forschungen, Graphit doch in irgendeiner Weise als Anode nutzen zu können, nicht aufgegeben. Während Jache *et al.* und Kim *et al*. unabhängig voneinander von einem erfolgreichen Kointerkalationsmechanismus berichteten, bei dem solvatisierte Natrium-Ionen in Graphit interkaliert werden, der es ermöglichte stabile Kapazitäten von rund 100 mA h g^{-1} zu erreichen,[58,59] gab und gibt es viele weitere Versuche Graphit zu modifizieren, um es für die Natriuminterkalation zugänglich zu machen. Dazu gehören u.a. die harten Kohlenstoffe[60,61], reduziertes Graphen-/Graphitoxid[62,63], expandierendes Graphit[64,65] oder auch unterschiedliche Kompositmaterialien.[66,67] Diese sind zum Teil sehr aufwendig herzustellen oder es ist kompliziert die Herstellung auf einen großen Maßstab zu übertragen.

Aus diesem Grund wurde die Forschung auch auf anorganischen Interkalationsverbindungen vorangetrieben, insbesondere auf Titanat-basierenden Materialien.[68,69] Allen gemein sind jedoch die träge Reaktionskinetik, die geringe Energiedichte und der anfänglich geringe Coulomb-Wirkungsgrad[70]. Daher wird nach alternativen Materialien mit hohen spezifischen

Kapazitäten, guter Zyklen- und guter Langzeitstabilität gesucht, die zudem auch bei hohen Stromraten betrieben werden können. Dabei sollten weiterhin die Nachhaltigkeit, die Kosten und die ökologischen Aspekte nicht aus den Augen gelassen werden. In Anbetracht der geringen Energiedichte von Interkalationselektroden sind Materialien auf der Basis von Konversionsreaktionen sicherlich von großer Bedeutung.

2.4 Konversionsmaterialien als Anode in NIB

Der größte Vorteil von Konversionsmaterialien im Vergleich zu Interkalationsmaterialien ist deren hohe theoretische spezifische Kapazität. Bei der Konversion wird während des Entladevorgangs eine redoxaktive Metallverbindung M_yX_z, (X oft Chalkogenid oder Halogenid) durch Natrium-Ionen vollständig zum elementaren, häufig nanoskopischen oder amorphem Metall M^0 reduziert. Simultan wird Na_nX gebildet, welche das elementare Metall als Matrix umschließt (Gleichung 1). Idealerweise ist dieser Vorgang beim Aufladen reversibel. So kann eine Übertragung von mehreren Elektronen pro Formeleinheit erreicht werden, was zu deutlich höheren spezifischen Kapazitäten führt im Vergleich zu den Interkalationsmaterialien.

$$M_yX_z + (nz)Na^+ + (nz)e^- \rightarrow yM + zNa_nX \quad (1)$$

Allerdings hat dieser Mechanismus mit den attraktiven hohen spezifischen Kapazitäten auch einige gravierende Nachteile, aufgrund derer eine Kommerzialisierung bisher unmöglich war. So führt die Bildung von komplett neuen Phasen zu drastischen Volumenänderungen, die bis zu 200% ausmachen.[71] Diese können zu mechanischer Degradation, Rissbildung bis hin zum Kontaktverlust führen. Zudem wird die empfindliche SEI Schicht modifiziert, da diese auf dem neu entstehenden Material weiterwächst, was die Leitfähigkeit des Elektrodenmaterials und die Kinetik negativ beeinflussen.[72] Konversionsmaterialien weisen überwiegend eine große Spannungshysterese auf, bedingt durch die unterschiedliche Ionendiffusionsfähigkeit der entstehenden Spezies bei der Konversion. Während Natrium-Ionen bei der Entladung in das M_yX_z diffundieren und die Na_nX Matrix gebildet wird, diffundieren bei der Ladung Metallionen aus der Na_nX Matrix und bilden M_yX_z Nanopartikel. Die Mobilität von Na^+ ist deutlich höher als die von Übergangsmetallkationen, so dass diese Reaktionspfade gegensätzliche Eigenschaften aufweisen, welche eine Spannungshysterese induzieren.[73] Ebenso fördern große Polarisationseffekte und Überspannungen die Ausbildung der Spannungshysterese, welche mit der Ionisierung der M-X-Bindung steigt.[71,74]

Zudem führt die träge Reaktionskinetik oftmals dazu, dass die Ausgangsoxidationsstufe von M^{n+} beim Laden nicht wieder erreicht wird, was zu einem Kapazitätsverlust führt. Desgleichen können die in jedem Zyklus wieder neu gebildete SEI oder inerte Metallnanopartikel zu einer reduzierten Kapazität führen.[75]

Um diese Hürden zu überwinden, wurden viele Strategien entwickelt, wie das Designen von unterschiedlichen nanoskopischen Morphologien wie Blumen[76,77], Stäbchen/Drähte[78–80] oder Kugeln[81,82], oder das Entwickeln von Kompositmaterialien mit leitenden Additiven wie reduziertem Graphenoxid (rGO)[83–85], Kohlenstoffnanoröhrchen (CNTs)[86] oder MoS_2[87,88], um die strukturelle Stabilität der Elektroden zu verbessern. Dabei werden rGO, Graphen, CNTs zusätzlich zugesetzt, um den Kontakt zwischen den Nanoteilchen zu verbessern, was eine bessere Leitfähigkeit ermöglicht. Trotz der damit erreichten Erfolge haben diese Ansätze alle gemein, dass ein intensiver synthetischer Aufwand nötig ist und damit hohe Kosten einhergehen. Weitere damit auftretende Schwierigkeiten sind die Aufskalierung, Reproduzierbarkeit und der irreversible Verlust von Chemikalien.
Vorteilhaft für die Konversionsmaterialien auf Natriumbasis haben sich Sulfide erwiesen, da das Entladungsprodukt Na_2S im Vergleich zu den Oxiden eine bessere Leitfähigkeit aufweist und aufgrund der schwächeren M-S-Bindung kinetische Vorteile aufweist. Zudem zeigen Sulfide eine geringere Volumenarbeit als Oxide.[71] Denkt man an die Nachhaltigkeit, den Preis, die Verfügbarkeit und ökologische Aspekte sind Mangan, Kupfer, Eisen und Zink sehr interessante Kandidaten. Allerdings leiden die binären Verbindungen dieser Elemente ebenso an den oben genannten Problemen und weisen meistens nur mit Hilfe von Additiven oder speziellen Designs eine adäquate Zyklenstabilität auf.[53,89,90] Interessanterweise zeigen einige ternäre kupferhaltige Verbindungen wie CuV_2S_4 oder $CuCrS_2$ eine durchaus attraktive Zyklenstabilität ohne Zusatz von Additiven.[25,26] In den Publikationen wurde der positive Einfluss des Kupfers auf die Performance als Anodenmaterial herausgearbeitet. Daher ist es durchaus naheliegend, ökologisch und preislich attraktivere ternäre Kupferverbindungen zu untersuchen. Ein besonders attraktives Element ist Eisen, welches aufgrund seiner Redoxaktivität, des günstigen Preises, der sehr guten Verfügbarkeit und der hervorragenden Umweltverträglichkeit ein aussichtsreicher Kandidat ist. Es ist auch anzumerken, dass schon verschiedene Eisensulfide als vielversprechende Elektrodenmaterialien untersucht wurden.[91–94] Aufgrund dieser Beobachtungen und Befunde wurden in dieser Arbeit Kupfer-Eisen-Sulfide auf ihre Nutzbarkeit als Anodenmaterial in NIB untersucht. Ein Schwerpunkt liegt dabei auf der Entschlüsselung der zugrundeliegenden Reaktionsmechanismen, da ein besseres

Verständnis der Mechanismen die Grundlage darstellt, um die unterschiedlichen strukturellen, elektronischen und elektrochemischen Herausforderungen zu meistern und in Zukunft geeignete Materialien designen zu können. In absehbarer Zukunft wird der Energiemarkt kostengünstige stationäre Energiespeichersysteme brauchen ohne auf die Lithiumressourcen zurückgreifen zu müssen.

2.5 Kupfer-Eisen-Sulfide (CFS)

Es gibt eine große chemische Variation an ternären Kupfer-Eisen-Sulfiden wie z.B. Cu_5FeS_4, $CuFeS_2$ $CuFe_2S_3$, $Cu_9Fe_8S_{16}$ oder $Cu_2Fe_4S_7$.

In dieser Arbeit wird die Eignung solcher Kupfer-Eisen-Sulfide als Anodenmaterial in NIB untersucht. Da von einem positiven synergistischen Effekt des Kupfers in der FeS_x-Matrix ausgegangen wird, wurde der Fokus auf drei unterschiedliche Kupfer-Eisen-Sulfide gelegt: das eisenreiche $CuFe_2S_3$, das stöchiometrische $CuFeS_2$ und das kupferreiche Cu_5FeS_4, um möglichst viele Informationen über den Einfluss des Verhältnisses von Kupfer zu Eisen herauszuarbeiten.

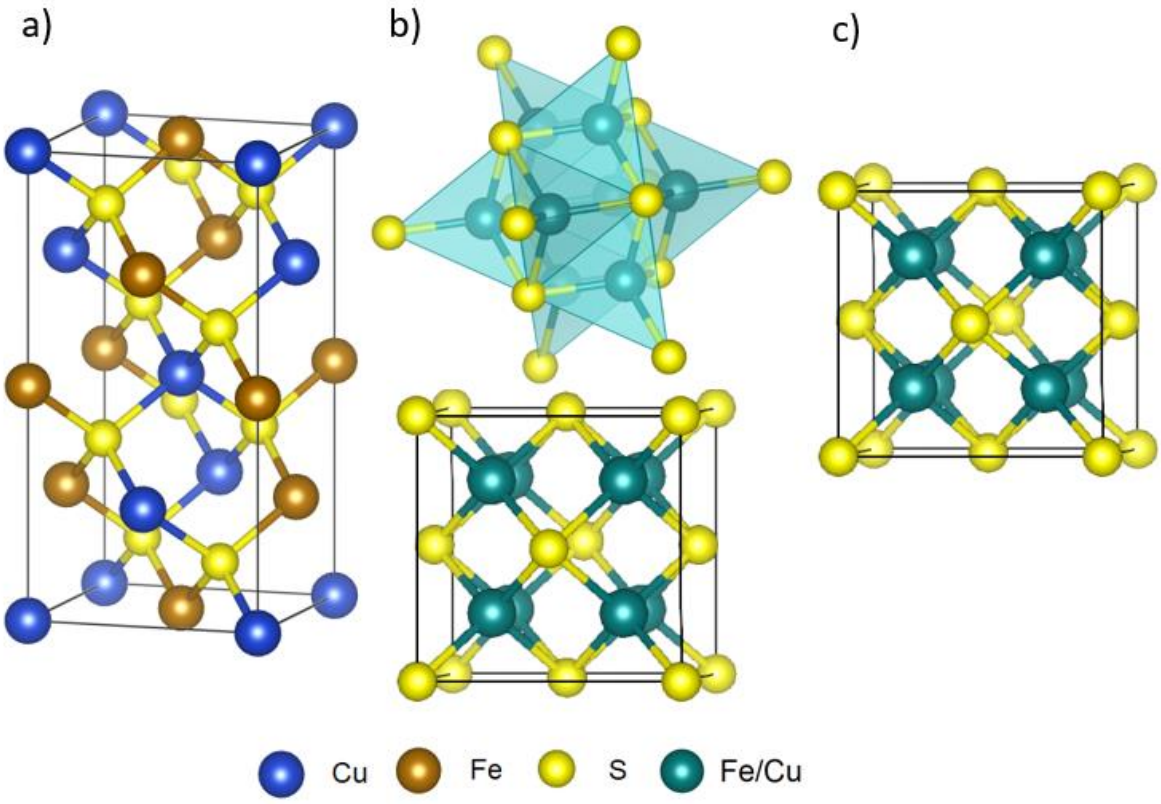

Abbildung 9: Strukturbilder der drei Kupfer-Eisensulfide: a) $CuFeS_2$, b) $CuFe_2S_3$ und c) Cu_5FeS_4, wobei letzteres in der kubischen Hochtemperatur-Phase $Fm\bar{3}m$ dargestellt ist. (VESTA 3.5.8)

$CuFeS_2$ (Abbildung 9a) auch Chalkopyrit genannt, ist eines der häufigsten vorkommenden Kupfer-Eisen-Sulfide in der Natur und liegt oft phasenrein als goldglänzendes Mineral vor, aber auch in Paragenese mit Bornit und Pyrit. Daher ist diese Verbindung gut untersucht und sowohl als Bulkmaterial als auch im nanoskopischen Maßstab synthetisiert worden.[95,96]

Bornit weist die chemische Zusammensetzung Cu_5FeS_4 auf (Abbildung 9c). Während des Abkühlungsprozesses von den hohen Synthesetemperaturen durchläuft Bornit mehrere Strukturumwandlungen. Während es zunächst in der kubischen Raumgruppe $Fm\bar{3}m$ kristallisiert, wandelt es sich bei etwa 270 °C in eine metastabile kubische Phase um, bis es sich bei etwa 205 °C in die stabile orthorhombische Phase mit der Raumgruppe $Pbca$ umwandelt. Letztere kommt in der Natur meistens als buntglänzendes Mineral vor, welches häufig in Paragenese mit anderen Sulfiden in Kupfererzen auftritt.[97,98]

Isocubanit ist mit der chemischen Summenformel $CuFe_2S_3$ (Abbildung 9b) die eisenreichste der hier untersuchten Verbindungen. Es ist die kubische Hochtemperatur-Modifikation von Cubanit, welches in der orthorhombischen Raumgruppe $Pcmn$ kristalliert, während Isocubanit in der Raumgruppe $F\bar{4}3m$ kristallisiert. Es ist im Verhältnis zu $CuFeS_2$ und Cu_5FeS_4 ein eher selten vorkommendes Mineral und wird nur in enger Paragenese vor allem mit Chalkopyrit und Pyrrhotit gefunden. Auch die synthetische Herstellung ist nicht trivial, da es eigentlich immer zu Verunreinigungen durch die letztgenannten Sulfide kommt, so dass mittels Hochtemperatursynthese noch kein phasenreines Isocubanit hergestellt werden konnte.[99,100]

In der vorliegenden Arbeit wurden bewusst Bulk-Materialien eingesetzt, um aufwendige und teure Synthesestrategien für die Generierung nanoskopischer Morphologien zu vermeiden. Die drei Verbindungen wurden mittels Hochtemperatursynthesen in Quarzglasampullen mit unterschiedlichen zusätzlichen Schritten oder Behandlungen hergestellt. Dabei wurden alle Materialien phasenrein erhalten, was besonders für das Isocubanit ein enormer Erfolg ist.

3. Methoden

Wie in Kapitel 2 erwähnt liegt ein Hauptaugenmerk auf der Aufklärung der zugrundeliegenden Reaktionsmechanismen während der Natriumaufnahme und -abgabe. Aufgrund der enormen Komplexität der ablaufenden Reaktionen ist es unumgänglich auf eine Kombination von Charakterisierungsmethoden zurückzugreifen. Dazu gehören auch einige Methoden, die nicht zu den klassischen Standardmethoden zählen. Daher werden die Grundlagen der hier angewendeten Methoden (Röntgenabsorptionsspektroskopie (XAS), Paarverteilungsfunktion (PDF), Natrium-Resonanzspektroskopie (Na-NMR) und Mößbauer-Spektroskopie) kurz diskutiert.

Weitere Informationen zu dem Aufbau der Messzellen, der genutzten Programme und experimentellen Details befinden sich in Kapitel 4.

3.1 Röntgenabsorptionsspektroskopie

Die Röntgenabsorptionsspektroskopie ist eine Technik zur Untersuchung der elektronischen und lokalen geometrischen Struktur eines Materials. Der am häufigsten genutzte Aufbau ist die Transmissionsgeometrie, d.h. die Intensität der eingestrahlten Röntgenphotonen vor (I_0) und nach der Probe (I_1) mit einer Schichtdicke d in Abhängigkeit der Photonenenergie E wird gemessen und folgt dem Lambert-Beer'schen Gesetz (2). Die erforderlichen duchstimmbaren monochromatischen Röntgenstrahlen werden überwiegend durch Synchrotronquellen bereitgestellt. Ein großer Vorteil dieser Methode im Vergleich zu anderen Methoden, z.B. der Röntgenspektroskopie, ist, dass eine langreichweitige Ordnung nicht erforderlich ist und somit auch amorphe Proben untersucht werden können.

$$I_1(E) = I_0(E) \times e^{-\mu(E)d} \tag{2}$$

I_1 = Intensität nach Absorption, I_0 = Intensität vor Absorption, d = Schichtdicke, μ = linearer Absorptionskoeffizient

Während einer Messung wird die Energie der Röntgenphotonen kontinuierlich erhöht, wobei der Röntgenabsorptionskoeffizient als Funktion der Energie stetig abnimmt. Weisen die Röntgenphotonen jedoch eine Energie auf, die der Bindungsenergie eines kernnahen Elektrons entspricht, kommt es zu einem sprunghaften Anstieg des Absorptionskoeffizienten, welcher als Absorptionskante bezeichnet wird. Dabei wird das Röntgenphoton durch ein Elektron absorbiert, wodurch es aus seinem elektronischen Niveau zunächst in einen unbesetzten

Zustand angeregt wird. Dieses Elektron wird als Photoelektron bezeichnet und kann als Welle aufgefasst werden. Die zu der Welle gehörende de Broglie-Wellenlänge liegt im Bereich interatomarer Abstände.

Je nachdem aus welchem Niveau das Photoelektron stammt, wird von der K-Kante (1s-Niveau), der L-Kante (die sich gemäß dem Bahndrehimpuls und dem Gesamtdrehimpuls in L_I – L_{III} unterteilt) etc. gesprochen. Dabei lässt sich grob abschätzen, dass die Energie der Absorptionskante in etwa quadratisch von der Ordnungszahl *Z* des Elements abhängt. Die XAS-Spektroskopie ist demnach, aufgrund der bestimmbaren Photonenenergie und einhergehend auch des absorbierenden Elements, elementspezifisch.

Der Bereich nahe der Absorptionskante (± 50 EV) wird als XANES-Bereich (X-ray absorption near-edge structure spectroscopy) bezeichnet und kann mit Hilfe von Referenzmaterialien Auskunft über die formale Valenz und die direkte Koordination des Absorberatoms geben. Da die vom Absorberatom ausgehende Photoelektronenwelle an den Elektronen vorhandener Nachbaratomen rückgestreut werden kann, können diese zurückgestreuten Wellen mit den ausgehenden Photoelektronenwellen interferieren und daher die Absorptionswahrscheinlichkeit beeinflussen. Je nach Phasenbeziehung zwischen den Wellen kommt es zu konstruktiven oder destruktiven Interferenzen, wodurch sich ein Interferenzmuster, der sogenannte EXAFS-Bereich (extended X-ray absorption fine structure), ausbildet. Durch die Analyse der Muster ist es möglich, die lokalen Strukturinformationen wie Koordinationszahl, Bindungslänge und interatomare Abstände im Material zu bestimmen. In günstigen Fällen ist es auch möglich den Rückstreuer, also den nächsten Nachbarn, zu identifizieren.

Der beim Absorptionsprozess freigewordene Platz im kernnahen Orbital wird durch ein Elektron aus einer höherenergetischen Schale aufgefüllt. Dabei entsteht Röntgenfluoreszenzstrahlung mit einer elementspezifischen Energie, welcher der Energiedifferenz der beiden Orbitale entspricht und dementsprechend ebenfalls Informationen über das Absorberatom enthält. Der Konkurrenzeffekt ist der Auger-Effekt. Dies ist ein strahlungsfreier Prozess, bei dem das entstandene Elektronenloch ebenfalls mit einem Elektron eines höheren Orbitals aufgefüllt wird, jedoch wird gleichzeitig ein sogenanntes Auger-Elektron (oft derselben Schale) ins Kontinuum emittiert, welches eine für das Absorberatom spezifische kinetische Energie aufweist (Abbildung 10).

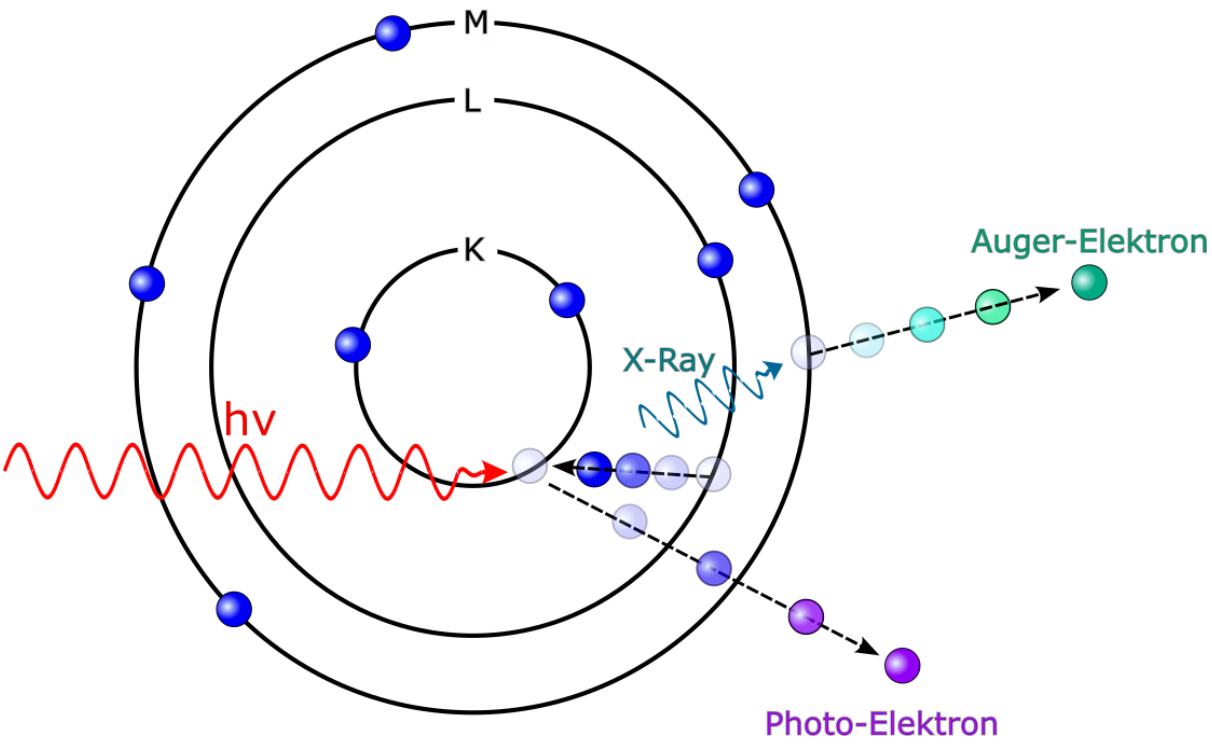

Abbildung 10: Schematische Darstellung des Elektronen-Emissionsprozesses. Ein hochenergetisches Photon regt das Zielatom zur Emission von Elektronen aus einem elektronischen Niveau an (lila). Ein Elektron fällt von einem höheren Energieniveau in das Elektronenloch, indem es Röntgenstrahlung aussendet oder ein Auger-Elektron emittiert wird (türkis) (gezeichnet mit *Inkscape 1.3*).

Für die Extraktion der enthaltenden Informationen aus den Rohdaten sind einige datenverarbeitende Schritte notwendig. Anhand eines Referenzmaterials wird die Energieachse kalibriert, da diese um einige eV verschoben ist. Anschließend wird die monoton abfallende Kurve des Absorptionskoeffizienten abgezogen und es erfolgt eine Normierung des Kantensprungs auf 1, um Einflüsse wie Probendicke oder Probenmatrix auf den Kantensprung zu eliminieren. Mit dem erhaltenen Spektrum kann nun zunächst die Auswertung des XANES-Bereichs beginnen.

Für die EXAFS-Auswertung folgt zusätzlich zuerst die Umwandlung in den *k*-Raum, wobei die Energieachse des Spektrums durch die entsprechende Achse des Wellenvektors *k* ersetzt wird (3).[101]

$$k = \sqrt{\frac{(2\pi m_e)(E-E_0)}{h^2}} \qquad (3)$$

mit m_e = Elektronenmasse, E = Energie, E_0 = Energie der Absorptionskante in eV und h = Planck‘sches Wirkungsquantum.

Anschließend werden die EXAFS-Oszillationen isoliert, indem von dem Spektrum der Teil subtrahiert wird, der auf das Absorberatom zurückzuführen ist. Dafür wird eine langsam oszillierende Funktion verwendet, die durch eine Spline-Funktion angenähert werden kann.

Mit einer entsprechenden Gewichtung durch Multiplikation mit k, k^2 oder k^3 wird versucht die Abnahme der Oszillation mit steigendem k-Wert auszugleichen. Im letzten Schritt werden die Daten vom k-Raum durch Fourier-Transformation in den R-Raum (R=Radialabstand) überführt. Der experimentelle Radialabstand muss mit Hilfe eines Referenzmaterials korrigiert werden, da bei der Interferenz der Wellen eine Phasenverschiebung stattfindet. Aus den Radialabstandsverteilungen lassen sich Informationen über die lokale Struktur wie Koordinationszahl und Bindungslängen extrahieren.

3.2 Paar-Verteilungsfunktion

Bei kristallinen anorganischen Materialien ist die Röntgenpulverbeugung (XRPD = X-ray Powder Diffraction) eine leistungsfähige Standard-Charakterisierungsmethode, die eine qualitative und quantitative Phasenanalyse ermöglicht, sowie einer Verfeinerung der Struktur mittels Rietveldmethode erlaubt.[102,103] Liegt die Kristallitgröße des zu untersuchenden Materials im Nanometerbreich oder liegt es amorph vor, versagt diese Methode, da entweder nur sehr breite oder keine Bragg-Reflexe vorhanden sind. Um trotzdem strukturelle Informationen dieser Proben zu gewinnen, wird der Vorteil der Totalstreuungsmethoden wie es die Paarverteilungsfunktion (PDF, aus dem Englischen: Pair Distribution Function) ist, genutzt. Der Begriff Totalstreuung umfasst alle Formen von Streuung, einschließlich diffuser, elastischer, inelastischer und Bragg-Streuung. Die diffuse Streuung gibt Auskunft über die Anordnung der Atome auf lokaler Ebene und ist daher für die Untersuchung von nanokristallinen und amorphen Materialien von enormer Bedeutung.[104,105]

Um Informationen aus den Totalstreuungsexperimenten zu extrahieren, müssen die gemessenen Totalstreudaten in die PDF umgewandelt werden, wobei die Strukturinformationen aus dem reziproken Q-Raum in ein reales Histogramm der Bindungslängen zwischen Atomen überführt wird. Die PDF gibt dabei die Wahrscheinlichkeit an, zwei Atome in einem Abstand r vorzufinden und ist wie folgt definiert:[106]

$$G(r) = 4\pi r[\rho(r) - \rho_0\gamma_0(r)] \quad \text{.....(4)}$$

Mit $\rho(r)$ als Teilchendichte für den beobachteten Abstand (r), ρ_0 die gemittelte Teilchendichte und γ_0 die charakteristische Autokorrelationsfunktion der Partikelformfunktion. Für die Umwandlung in die PDF müssen zunächst zusätzliche Beiträge zur diffusen Streuung, die aus der Umgebung stammen (Probenhalter, Luftstreuung usw.) von

den eigentlichen Messdaten subtrahiert werden, indem eine Leermessung mit identischem experimentellem Aufbau ohne Probe gemessen wird. Die korrigierten Daten werden mit dem Programm PDFgetX3, welches in der xPDFsuite enthalten ist, weiteren Korrekturen (Polarisation, Absorption, sowie inelastische- und Mehrfachstreuung) unterzogen. Durch eine anschließende Datennormierung wird erreicht, dass der Mittelwert über den vollständigen *Q*-Bereich gleich 1 ist, so dass die Strukturfunktion *S(Q)* erhalten wird. Letztendlich erhält man die Paarverteilungsfunktion $G(r)$ durch Fourier-Transformation von $S(Q)$ vom Reziproken in den Realraum.

Aus der PDF lassen sich nun verschiedene Strukturinformationen extrahieren. So gibt die Signalposition den Abstand zweier Atome an, während das Integral proportional zur relativen Häufigkeit (Multiplizität) dieser Abstände sowie der lokalen Elektronendichte der Streupartner ist. Die Signalbreite enthält die Informationen über die dynamische und statische Fehlordnung eines Atompaares. Durch die Dämpfung der Signale mit zunehmendem Abstand kann die Domänengröße bestimmt werden. Hierbei ist jedoch darauf zu achten, dass ein zusätzlicher Beitrag durch die begrenzte Auflösung im *Q*-Raum berücksichtigt werden muss.[106]

3.3 ^{23}Na-MAS NMR

MAS NMR steht für Magic Angle Spinning Nuclear Magnetic Resonance und ist eine fortgeschrittene Technik zur Untersuchung der strukturellen Eigenschaften von Festkörpern mittels kernmagnetischer Resonanz, wobei hier das ^{23}Na Isotop die Sonde darstellt.

Natriumkerne haben einen Spin $I = 3/2$ und sind daher in der Lage, vier mögliche Orientierungen im Magnetfeld anzunehmen. Wenn ein äußeres Magnetfeld auf den Kern wirkt, spalten sich diese Energiezustände gemäß dem Zeeman-Effekt auf. Die Energiedifferenz zwischen den Zeeman-Niveaus ist proportional zum äußeren Magnetfeld und führt zu unterschiedlichen Resonanzfrequenzen für die Natriumkerne. Die Aufspaltung in die Zeeman-Zustände und die Frequenzen, die für die Resonanz nötig sind, werden oft als chemische Verschiebung bezeichnet. Die chemische Verschiebung δ ist ein Maß für die lokale magnetische Umgebung des Kerns und wird als Bruchteil der Differenz zwischen der Frequenz eines bestimmten Kerns und einer Standardverbindung angegeben und in ppm angegeben. Ein Kern, mit höherer Elektronendichte, wird eine positive chemische Verschiebung aufweisen,

während ein Kern mit niedrigerer Elektronendichte eine negative chemische Verschiebung aufweist. [107]

Aufgrund anisotroper Wechselwirkungen im Kristallgitter zeigen Festkörper-NMR-Spektren eine ausgeprägte Linienverbreiterung im Vergleich zu flüssigen Proben.[108] Durch Drehen des Probenhalters mit hohen Geschwindigkeiten um die sogenannte magische Achse (54.74 ° zum Magnetfeld) können anisotrope Wechselwirkungen unterdrückt bzw. signifikant reduziert werden.[109,110]

Insgesamt ist das MAS-NMR eine leistungsfähige Technik zur Untersuchung der Struktur und Dynamik von Ionen. Es liefert interessante Strukturinformationen, da die chemische Verschiebung und die Spin-Spin-Kopplung in Abhängigkeit von der Kristallstruktur bzw. der chemischen Umgebung variieren und findet in vielen Bereichen wie Materialwissenschaft und Pharmazie Anwendung.[111–113]

3.4 Mößbauer-Spektroskopie

Die rückstoßfreie Kernresonanzabsorption von Gammastrahlen wurde 1958 von Rudolf L. Mößbauer im Rahmen seiner Doktorarbeit entdeckt. Für diesen nach ihm benannten Mößbauer-Effekt erhielt er 1961 den Nobelpreis.[114] Die Entdeckung dieses Effekts ermöglichte die Entwicklung der Mößbauer-Spektroskopie. Bei der Mößbauer-Spektroskopie werden von einer radioaktiven Quelle (hier z.B. $^{57}Co \rightarrow {}^{57}Fe + h\cdot\nu$), durch den Übergang von einem angeregten Zustand in den Grundzustand (hier als Beispiel $^{57}Co \rightarrow {}^{57}Fe + h\cdot\nu$), Gammastrahlen emittiert. Ein identisches Absorberatom kann dieses Gammaquant absorbieren, wobei das Energieniveau des Kerns in einen angeregten Zustand gehoben wird. Nach einer endlichen Lebensdauer fällt der Kern wieder in seinen Grundzustand zurück und das Quant wird wieder als Gammastrahlung emittiert.[115]

Ist die lokale Umgebung des emittierenden und absorbierenden Kerns exakt gleich sind die Übergangsenergien der Kerne identisch. Chemische Unterschiede in der lokalen Umgebung des absorbierenden Kerns führen zu winzigen Energieverschiebungen. Die Energie der Emission wird nun bei der Detektion so moduliert, dass wieder Resonanz zwischen den Übergangsenergien auftritt. Diese minimalen Modulationen werden durch den Dopplereffekt über eine Schwingung/Bewegung der Strahlungsquelle realisiert. Durch die ermittelte Energiemodulation kann so die Verschiebung des Energieniveaus gemessen und Rückschlüsse

auf die chemische und elektronische Umgebung des Atomkerns des Absorbers gezogen werden.

Bei der Mößbauer-Spektroskopie steht nicht der eigentliche Effekt im Mittelpunkt, sondern die Auswirkungen der substanzeigenen inneren elektrischen und magnetischen Felder, welche die energetische Lage der Kernniveaus beeinflussen. Dabei werden drei unterschiedliche Wechselwirkungen beobachtet. Die Isomerieverschiebung reagiert empfindlich auf Veränderungen in der elektronischen Umgebung des Kerns, wie z. B. Veränderungen der Oxidationsstufe oder der Koordinationsgeometrie, und kann Informationen über die chemische Bindung und die lokale Struktur des Festkörpers liefern. Die Isomerieverschiebung wird durch die unterschiedlichen s-Elektronendichten in emittierenden und absorbierenden Atomen induziert.

Die Quadrupolaufspaltung enthält Informationen über die lokale Symmetrie und die elektronische Struktur eines Festkörpers. Sie ergibt sich aus der Wechselwirkung zwischen dem elektrischen Feldgradienten (EFG) am Kern und dem Kernquadrupolmoment. Der Gradient des elektrischen Feldes ist ein Maß für die Geschwindigkeit, mit der sich das elektrische Feld mit der Entfernung vom Kern ändert. Er entsteht durch das Vorhandensein von geladenen Teilchen in der Nähe des Kerns, wie z. B. Elektronen in den umgebenden Atomen oder Ionen. In einem Festkörper ist der Gradient des elektrischen Feldes nicht unbedingt isotrop, d. h. das EFG kann in verschiedenen Richtungen unterschiedliche Werte haben. Das Kernquadrupolmoment hingegen ist eine Eigenschaft einiger Atomkerne, die eine nicht-sphärische Ladungsverteilung aufweisen, wie Kerne mit einer Drehimpulsquantenzahl von $l > ½$. Die Wechselwirkung zwischen dem Kernquadrupolmoment und dem EFG führt zu einer Aufspaltung der Kernenergieniveaus. Die Größe der Aufspaltung ist proportional zur Stärke des EFG und zur Größe des Kernquadrupolmoments. Besitzt ein Absorber eine kubische Valenzelektronenverteilung und kubische Molekülsymmetrie wie z.B. $[Fe(CN)_6]^{4-}$ ist der EFG isotrop und die Quadrupolaufspaltung gleich Null. Weist dieser jedoch keine kubische Molekülsymmetrie und keine kubische Valenzelektronenverteilung auf wie in $[Fe^{2+}(CN)_5X^{n-}]^{(3+n)-}$ (X^{n-} ungleich CN^-) so ist der EFG nicht isotrop und die Quadrupolaufspaltung ist ungleich Null. Die Größe und das Vorzeichen der Quadrupolaufspaltung hängen auch von der chemischen Umgebung des Absorberkerns ab, z. B. von der Oxidationsstufe oder der Koordinationsgeometrie der umgebenden Atome oder Ionen. Daher kann die Quadrupolaufspaltung zur Untersuchung der lokalen elektronischen Struktur und der chemischen Bindung in Festkörpern verwendet werden.[115,116]

Das magnetische Hyperfeinfeld ist ein weiterer wichtiger Parameter der Mößbauer-Spektroskopie, der Informationen über die magnetischen Eigenschaften eines Festkörpers liefert. Befindet sich der Kern nicht nur in einem inhomogenen elektrischen Feld, sondern auch in einem externen oder internen magnetischen Feld, so spalten die Niveaus des angeregten- und des Grundzustandes aufgrund des Zeemann-Effektes weiter auf, wenn der Absorber ein magnetisches Dipolmoment μ besitzt (Abbildung 11). Der Energieunterschied zwischen den Subniveaus ist proportional zur Stärke des magnetischen Hyperfeinfelds.[117]

Dabei sind folgende Auswahlregeln zu beachten[118]:

- $\Delta I = \pm 1$ ΔI: Änderung der Spinquantenzahl
- $\Delta m = 0$ oder ± 1 Δm: Änderung der magnetischen Quantenzahl

Das magnetische Hyperfeinfeld kann wertvolle Informationen über die magnetischen Eigenschaften eines Festkörpers liefern.

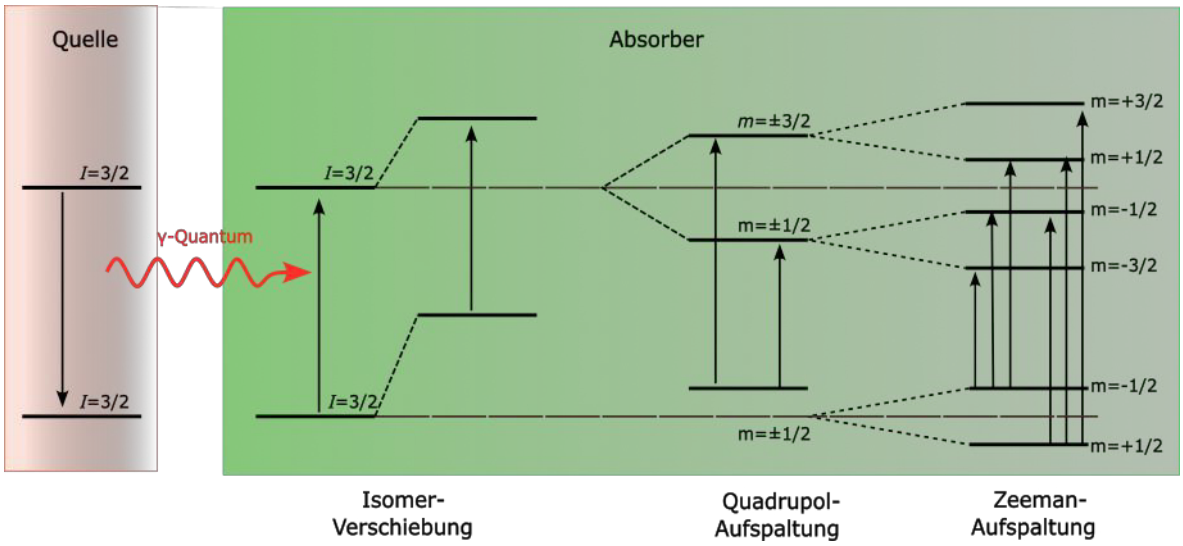

Abbildung 11: Isomer-Verschiebung, Quadrupol-Aufspaltung und Zeeman-Aufspaltung der Kernniveaus beim Mößbauer-Übergang in ^{57}Fe-Kernen (gezeichnet mit *Inkscape 1.3*).

4. Publikationen

4.1 $CuFeS_2$ as a Very Stable High-Capacity Anode Material for Sodium-Ion Batteries: A Multimethod Approach for Elucidation of the Complex Reaction Mechanisms during Discharge and Charge Processes

Die erste im Rahmen dieser Arbeit veröffentlichte Studie befasst sich mit der Anwendung von $CuFeS_2$ als Anodenmaterial in NIB und der Untersuchung des ablaufenden Reaktionsmechanismus während der Na-Aufnahme und -Abgabe. $CuFeS_2$ oder auch Chalkopyrit genannt, ist das bekannteste der Kupfer-Eisen-Sulfide und ist in der Natur häufig auch in seiner Reinform zu finden. Obwohl Sulfide als vielversprechende Kandidaten für den Einsatz als Anoden in NIB gelten, wurde Chalkopyrit bisher nur in LIB getestet. Für die Charakterisierungen wurde bewusst das phasenreine Volumenmaterial eingesetzt, um aufwendige Syntheserouten zu vermeiden, welche für nanoskopische oder Kompositmaterialien oft notwendig sind. Allerdings haben Volumenmaterialien oft den Nachteil, dass aufgrund der ausgeprägten Volumenarbeit bereits nach wenigen Zyklen ein Kontaktverlust eintritt und die Batterie nicht mehr zyklisiert werden kann. Überraschenderweise wies $CuFeS_2$ bei den Untersuchungen eine erstaunliche Zyklenstabilität auf, so dass nach 550 Zyklen immer noch eine konstante Kapazität von 444 mAh g^{-1} erreicht wurde. Bei der Zyklisierung gegen Na durchlief die Kapazitätskurve ein Maximum, was auf eine Änderung des Reaktionsmechanismus hindeutet. Um ein tieferes Verständnis zu erlangen, wurde der erste Zyklus gezielt mittels XRPD, PDF, ^{23}Na NMR und Mößbauer-Spektroskopie untersucht. Zunächst wird $NaCuFeS_2$ gebildet gefolgt von der Reduktion von Cu^+ zu Cu^0. Weitere Na-Aufnahme reduziert Fe^{2+} zu Fe^0 und parallel wird Na_2S gebildet. Beim Ladevorgang wird überwiegend nanokristallines $NaCuFeS_2$ erhalten. XRPD Untersuchungen während der Änderung des Reaktionsmechanismus (Zyklus 150) zeigen die Bildung von Cu_xS und bei Zyklus 250 konnten Cu_2S, NaF und $Cu_{7.2}S_4$ im entladenen Zustand nachgewiesen werden. Im geladenen Zustand wurden bei diesen Zyklen NaF und Cu_5FeS_4 identifiziert. Ein wesentlicher Rückschluss ist, dass der Erhalt der guten Kristallinität eine Schlüsselrolle für die gute Zyklenstabilität bei hohen spezifischen Kapazitäten spielt. Die Mobilität von Cu/Cu^+ spielt vermutlich eine entscheidende Rolle und die Ergebnisse belegen, dass das Cu-Fe-S-System eine gute Materialklasse darstellt.

Veröffentlicht in: *ACS Appl. Mater. Interfaces*, **2021**, 13, 26034-26045.

DOI: https://doi.org/10.1021/acsami.1c04946

© 2021 American Chemical Society

ACS APPLIED MATERIALS & INTERFACES

www.acsami.org Research Article

$CuFeS_2$ as a Very Stable High-Capacity Anode Material for Sodium-Ion Batteries: A Multimethod Approach for Elucidation of the Complex Reaction Mechanisms during Discharge and Charge Processes

Svenja Senkale, Sylvio Indris, Martin Etter, and Wolfgang Bensch*

Cite This: *ACS Appl. Mater. Interfaces* 2021, 13, 26034−26045 Read Online

ACCESS | Metrics & More | Article Recommendations | Supporting Information

ABSTRACT: Highly crystalline $CuFeS_2$ containing earth-abundant and environmentally friendly elements prepared via a high-temperature synthesis exhibits an excellent electrochemical performance as an anode material in sodium-ion batteries. The initial specific capacity of 460 mAh g^{-1} increases to 512 mAh g^{-1} in the 150th cycle and then decreases to a still very high value of 444 mAh g^{-1} at 0.5 A g^{-1} in the remaining 550 cycles. Even for a large current density, a pronounced cycling stability is observed. Here, we demonstrate that combining the results of X-ray powder diffraction experiments, pair distribution function analysis, and ^{23}Na NMR and Mössbauer spectroscopy investigations performed at different stages of discharging and charging processes allows elucidation of very complex reaction mechanisms. In the first step after uptake of 1 $Na/CuFeS_2$, nanocrystalline $NaCuFeS_2$ is formed as an intermediate phase, which surprisingly could be recovered during charging. On increasing the Na content, Cu^+ is reduced to nanocrystalline Cu, while nanocrystalline Na_2S and nanosized elemental Fe are formed in the discharged state. After charging, the main crystalline phase is $NaCuFeS_2$. At the 150th cycle, the mechanisms clearly changed, and in the charged state, nanocrystalline Cu_xS phases are observed. At later stages of cycling, the mechanisms are altered again: NaF, Cu_2S, and $Cu_{7.2}S_4$ appeared in the discharged state, while NaF and Cu_5FeS_4 are observed in the charged state. In contrast to a typical conversion reaction, nanocrystalline phases play the dominant role, which are responsible for the high reversible capacity and long-term stability.

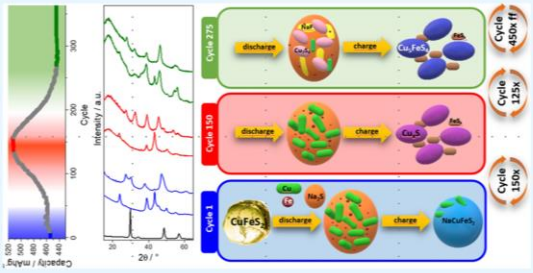

KEYWORDS: *sodium-ion batteries, anode material, ternary sulfides, $CuFeS_2$, X-ray scattering, pair distribution function, Mössbauer spectroscopy, MAS NMR*

1. INTRODUCTION

Lithium-ion batteries (LIBs) were successfully improved over the past decades for energy storage systems like portable electronic devices or electric vehicles, and daily life would be unthinkable without these batteries. Nevertheless, with the increasing demand for renewable energies, the desire for cost-effective large-scale stationary energy storage systems (ESS) is also increasing. Consequently, a very large amount of Li is necessary to meet these requirements in future. To prevent resource problems in terms of abundance and geographical distribution and to make stationary storage systems affordable, the focus is shifting toward the research of new electrode materials for sodium-ion batteries (SIBs) due to the higher availability, lower cost, and wider distribution of Na compared to Li.[1−3]

To compete with the established Li-ion technology, new electrode materials should have high specific capacities and stable cyclability. These prerequisites can be achieved using conversion instead of intercalation reactions, since during the former reaction the metal ions are often completely reduced to the metallic state and more alkali metal cations can be converted.[4] Metal oxides often show good electrochemical performances for LIBs,[5,6] but for SIBs, metal sulfides are in many cases advantageous because the discharge product Na_2S formed after full discharge enables better conductivity than that of Na_2O if metal oxides are discharged. In addition, application of sulfides may be kinetically favorable for conversion reactions because the M−S bonds are weaker compared to M−O bonds.[7]

Many binary transition metal sulfides have already been investigated for application in SIBs such as TiS_2,[8,9] MnS,[10,11]

Received: March 17, 2021
Accepted: May 19, 2021
Published: May 31, 2021

ACS Publications © 2021 American Chemical Society

https://doi.org/10.1021/acsami.1c04946
ACS Appl. Mater. Interfaces 2021, 13, 26034−26045

VS_2,[12,13] or MoS_2,[14,15] and in most cases nanoscaled or specially modified materials like reduced graphene oxide (RGO)-composite materials were used to reach a satisfying rate and cycle stability. Ternary sulfides, on the other hand, have been studied less intensively as electrode materials in SIBs, although the use of such compounds could be beneficial. Synergistic effects as well as the formation of more phases during the discharge process may improve the contact of the products, which in turn is beneficial for the diffusion paths.[16−18] Pure copper sulfides, for example, show poor rate and cycle stability, unless they are elaborately synthesized or combined with different carbon-containing species like RGO or single-walled carbon nanotubes.[19−22] In addition, copper is not the cheapest transition metal and is an essential ingredient in many technologically important devices. Due to its price, abundancy, environmental compatibility, and electrochemical properties, iron is an attractive transition metal in combination with copper in sulfidic compounds. Many binary iron sulfides have already been investigated as anode materials. However, like for binary Cu sulfides often a poor cycle stability is observed, which is mainly traced back to contact loss between nanosized particles. Hence, to prevent this contact loss Fe sulfides were morphologically modified by, e.g., preparing ultrafine nanoparticles, carbon-coated nanospheres, or combining FeS_x species with RGO.[23−27] But one should keep in mind that the synthesis of RGO by the Hummer method is not scalable to an industrial scale and the role during cycling of conversion electrodes is not clear.

In recent years, ternary Cu sulfides like $CuCrS_2$[18] and CuV_2S_4[17] were investigated concerning their suitability as anode materials in SIBs. Interestingly, these samples showed outstanding electrochemical performances like e.g., long-term stability, high-rate capability, and high specific capacity. For example, $CuCrS_2$ exhibits excellent capacity retention of about 420 mAh g^{-1}. CuV_2S_4 also showed very good electrochemical properties like capacity retention from 410 to 580 mAh g^{-1} at 0.7 A g^{-1} for over 300 cycles. Evidence is presented that elementary copper, which is formed during the discharge process, plays a crucial role preventing contact loss between the nanosized particles.[18,28]

Another ternary compound is chalcopyrite $CuFeS_2$ that may also have promising electrochemical properties, even without using any additive like RGO or CNTs or applying nanoparticles. Assuming a full conversion of the material with reduction of Cu^+ and Fe^{3+} to their elemental state, as shown in eq 1, the theoretical specific capacity is 584 mAh g^{-1}

$$4Na^+ + CuFeS_2 + 4e^- \rightarrow Cu + Fe + 2Na_2S \quad (1)$$

We note that $CuFeS_2$ has been investigated as an anode material for LIBs,[29−33] but until now, to the best of our knowledge there are no reports for the application as the anode material in SIBs.

To gain more understanding of this type of material, the electrochemical properties as well as the underlying mechanism have been investigated in detail in this study using ex situ X-ray diffraction (XRD), pair distribution function (PDF) analysis, Mössbauer spectroscopy, and ^{23}Na magic-angle spinning (MAS) nuclear magnetic resonance (NMR) spectroscopy. The results show an exceptionally good cycle stability at a high specific capacity.

2. EXPERIMENTAL SECTION

2.1. Synthesis of $CuFeS_2$. $CuFeS_2$ was synthesized via a high-temperature solid-state reaction. Stoichiometric amounts of copper (Alfa Aesar, 99.9%), iron (Alfa Aesar, 99.99%), and sulfur (Alfa Aesar, 99.999%) were mixed and ground in a mortar. The mixture was placed in a quartz tube, which was sealed under vacuum ($<10^{-4}$ mbar). The mixture was heated to 800 °C with a heating rate of 25 °C/h and was maintained at that temperature for 2 days and was then allowed to cool to room temperature over a period of 18 h. The annealed samples were removed from the quartz tube and ground in an agate mortar in an argon-filled glovebox. The material was again sealed in an evacuated silica tube and heated at 800 °C for an additional 4 days. The heating rate and cooling time were similar to the first step. Finally, the sample was washed with hydrochloric acid and distilled water to remove tiny amounts of undesirable FeS_2.

2.2. Electrochemical Tests. Electrodes were prepared with 70 wt % $CuFeS_2$, 20 wt % SUPER C65 carbon (Timcal, Switzerland), and 10 wt % poly(vinylidene difluoride) (PVDF, Solvay, Germany) suspended in *N*-methyl-2-pyrrolidone (NMP). The mixtures were spread on a Cu or Al foil using the doctor-blade casting method. Drying of the electrode foils was carried out in a vacuum oven at 60 °C for 24 h. Afterward, 10 mm discs with about 1.1−1.7 mg of the active material were punched out. Assembly of the Swagelok type cells was carried out in an argon-filled glovebox (water and oxygen contents below 1 ppm) using Na metal as the anode, glass fiber filter disks (Whatman, United Kingdom), a Celgard membrane as the separator, and a solution of 1 M sodium trifluoromethanesulfonate $NaCF_3SO_3$ (Sigma-Aldrich, 98%) in bis(2-methoxyethyl)ether (diglyme, Acros, 99+%, anhydrous) as the electrolyte. Galvanostatic measurements were performed on a BST8-WA (MTI Corporation) and BTS 3000 (Neware) battery analyzer. For ex situ measurements, approximately 20 mg of a mixture containing 70 wt % $CuFeS_2$ and 30 wt % Super C65 carbon were pressed into pellets at 5 t/50 mm^2, prepared in Swagelok type cells, as described above, and discharged/charged against Na in Swagelok cells with a C/20 rate (MTI BST8-WA). After a defined Na uptake/release, the electrochemical reaction was interrupted and the cells were disassembled in an argon-filled glovebox. The pellets were recovered and washed with anhydrous bis(2-methoxyethyl)ether (diglyme) and dried for 24 h.

Cyclic voltammetric measurements were done with a Zahner XPot at a scan rate of 0.1 mV s^{-1} between 0.01 and 3.00 V.

2.3. Material Characterization. SEM images and EDX data were obtained with a Philips ESEM XL 30 equipped with an EDAX New XL-30 detector. An acceleration voltage of 20 kV was used to detect the K-lines of the elements. Elemental analysis (EA) was performed with an Euro Vector Instruments Euro EA equipped with a HEKAtech CHNS analyzer.

Powder X-ray diffraction (XRD) investigations were carried out in transmission geometry on a PANalytical Empyrean with Cu Kα radiation, a focusing mirror, and PIXcel1D detector.

For ex situ synchrotron XRD and pair distribution function analysis measurements, the powders were placed in borosilicate capillaries with a diameter of 0.7 mm. The X-ray experiments were performed in Debye−Scherrer geometry using high-energy synchrotron radiation (60 keV, λ = 0.20703 Å) at beamline P02.1 at Petra III (DESY, Hamburg). The patterns were collected with an XRD 1621 Perkin Elmer amorphous silicon image plate detector with a sample to detector distance (SDD) of 1000 mm for XRD experiments and 300 mm for total scattering experiments. The 2D data was processed using DAWN Science.[34] The total scattering patterns were transformed into atomic pair distribution functions, $G(r)$, using xPDFsuite[35] with an optimal Q_{max} of 21.2 Å. To account for instrumental contributions to XRD and PDF, LaB_6 (NIST 660b) was measured as the standard material. To compensate for the contribution of the glass capillary, an empty capillary was measured under identical conditions.

^{57}Fe Mössbauer spectroscopy was performed at room temperature in transmission mode with a constant acceleration spectrometer and a $^{57}Co(Rh)$ source. All isomer shifts are given relative to that of α-Fe at

https://doi.org/10.1021/acsami.1c04946
ACS Appl. Mater. Interfaces 2021, 13, 26034−26045

room temperature. Powder samples were sealed in polyethylene/aluminum bags in an argon atmosphere.

^{23}Na MAS NMR spectroscopy was performed at a magnetic field of 4.7 T, corresponding to a resonance frequency of 52.9 MHz. Samples were packed in 1.3 mm rotors in an argon atmosphere and the spinning speed was 50−60 kHz. Spectra were acquired with a rotor-synchronized Hahn echo pulse sequence with a $\pi/2$ pulse length of 1.5 μs and a recycle delay of 1 s. The ^{23}Na NMR shifts are referenced to an aqueous 1 M NaCl solution at 0 ppm. Signal intensities were normalized with respect to the number of scans and the sample mass.

3. RESULTS AND DISCUSSION

3.1. Characterization of Pristine $CuFeS_2$. The compound $CuFeS_2$ crystallizes in the tetragonal space group $I\bar{4}2d$ with lattice parameters a = 5.29 Å and c = 10.42 Å.[36] Fe^{3+} and Cu^{+} cations occupy positions 4a and 4b, and are in a tetrahedral environment of S^{2-} anions. We note that two ionic states were discussed with chemical formulas $Cu^{1+}Fe^{3+}(S^{2-})_2$ and $Cu^{2+}Fe^{2+}(S^{2-})_2$. But results of recent investigations suggest that the former assignment is correct,[37,38] as also confirmed by our Mössbauer investigations described below. Figure 1

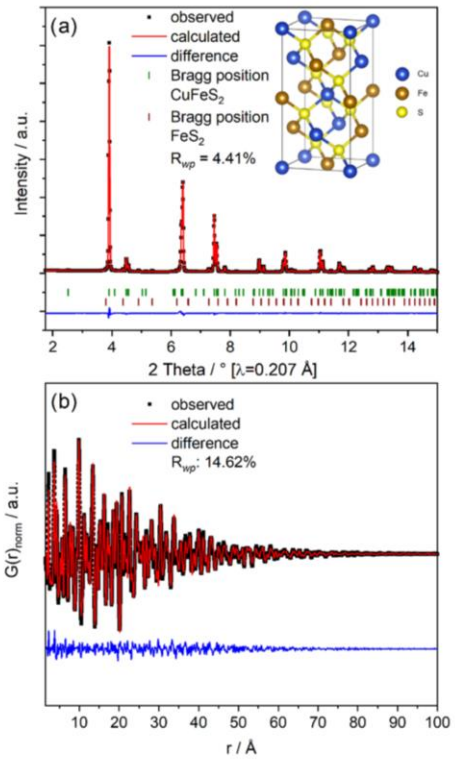

Figure 1. (a) Rietveld refinement results against the XRD pattern of $CuFeS_2$. Observed (black markers), calculated (red line), and difference (blue line) profiles. The inset shows the crystal structure. (b) PDF analysis. Observed (black markers), calculated (red line), and difference (blue line) profiles.

displays the XRD pattern of the pristine material together with the results of the Rietveld refinement, demonstrating phase purity of the material. The Rietveld refinement of the XRD pattern yields lattice parameters of a = 5.28830(9) and c = 10.4181(2) Å, very similar to those reported in the literature. Modeling the corresponding PDF (Figure 1, bottom) with a real space model of tetragonal $CuFeS_2$ in a Rietveld-like least-squares approach leads to a good reliability factor R_{wp} = 14.6%. The derived lattice parameters a = 5.2851(2) and c = 10.4028(7) Å are in very good agreement with the values obtained from the Rietveld refinement. Detailed refinement parameters are listed in Table S1.

The EDX measurement (Table S2) yields a stoichiometric ratio of Cu and Fe close to 1:1 while the S content is slightly too small. This can be explained by the low energy of the S-K_α emission line, which is easily absorbed by the matrix. Therefore, an additional elemental analysis is performed (Table S3), and taking the results of both analyses into account the composition of the sample is $Cu_{1.01}Fe_{0.96}S_{2.02}$.

3.2. Electrochemical Characterization. In several publications, it was demonstrated that ether-based electrolytes show an improved cycle life,[17,39−41] and therefore $NaCF_3SO_3$ in diglyme was chosen for the present electrochemical investigations.

The cycling performance of Na/$CuFeS_2$ at 0.5 A g^{-1} is shown in Figure 2a. To improve the cycling stability, different cutoff potentials were applied at this current density. Cycling in the voltage range of 3−0.1 V, the specific capacity is initially stable at 560 mAh g^{-1} and passes a maximum after 86 cycles reaching 638 mAh g^{-1}. After this maximum, the capacity drops to 580 mAh g^{-1} followed by a small increase to 585 mAh g^{-1} at the 150th cycle. A pronounced drop of the specific capacity to only 45 mAh g^{-1} occurs between the 160th and 200th cycles and during further cycling a value of 25 mAh g^{-1} at the 700th cycle is observed. When the cutoff voltage is limited to 0.3 V, a constant specific capacity at 460 mAh g^{-1} is observed and a steady increase occurs between the 70th and 150th cycles reaching 512 mAh g^{-1}. Beyond the 200th cycle, a decrease is observed reaching an excellent capacity retention of about 444 mAh g^{-1} until the 700th cycle corresponding to 3.04 Na/$CuFeS_2$. The Coulombic efficiencies are constantly higher than 99.9% for over 700 cycles. An explanation why the limitation of the potential window has such a pronounced positive effect on cycling stability is presented below by the detailed analysis ex situ XRD powder pattern.

Figure 2b displays the galvanostatic charge/discharge profiles of Na/$CuFeS_2$. The first discharge is accompanied by a fast decrease of the voltage at the early stage of Na uptake followed by a first short plateau at 1.15 V until 0.25 Na/f.u. is inserted. When the amount of inserted Na is increased, a long pseudo-plateau occurs in the region from 0.7 to 0.5 V. After insertion of 4 Na/f.u. the voltage steadily decreases until the cutoff of 0.3 V is reached with a specific capacity of 619 mAh g^{-1}. This value is larger than the theoretically expected value of 584 mAh g^{-1} despite the cutoff potential being limited, and the excess capacity is caused by the formation of the solid electrolyte interphase (SEI). During the charge process, no significant well-resolved plateaus can be identified and only a pseudo-plateau is visible, which can be assigned to the broad anodic signal between 1.1 and 1.7 V in the CV curve (Figure S1). After charging to 3 V, an uptake of 3.1 Na/f.u. is achieved, which corresponds to an irreversible capacity loss of 166 mAh g^{-1} with a Coulombic efficiency of 73.1%. In the following cycle a Coulombic efficiency of 97.1 is obtained, and after the 2nd cycle the Coulombic efficiency is >99%. The profiles of the subsequent cycles show a slowly evolving but a significant difference compared to the first cycle. In the discharge profile, two new pseudo-plateaus are developed at approx. 1.6 and 0.75 V, and the potential decreases steadily until the cell is fully

https://doi.org/10.1021/acsami.1c04946
ACS Appl. Mater. Interfaces 2021, 13, 26034−26045

ACS Applied Materials & Interfaces www.acsami.org Research Article

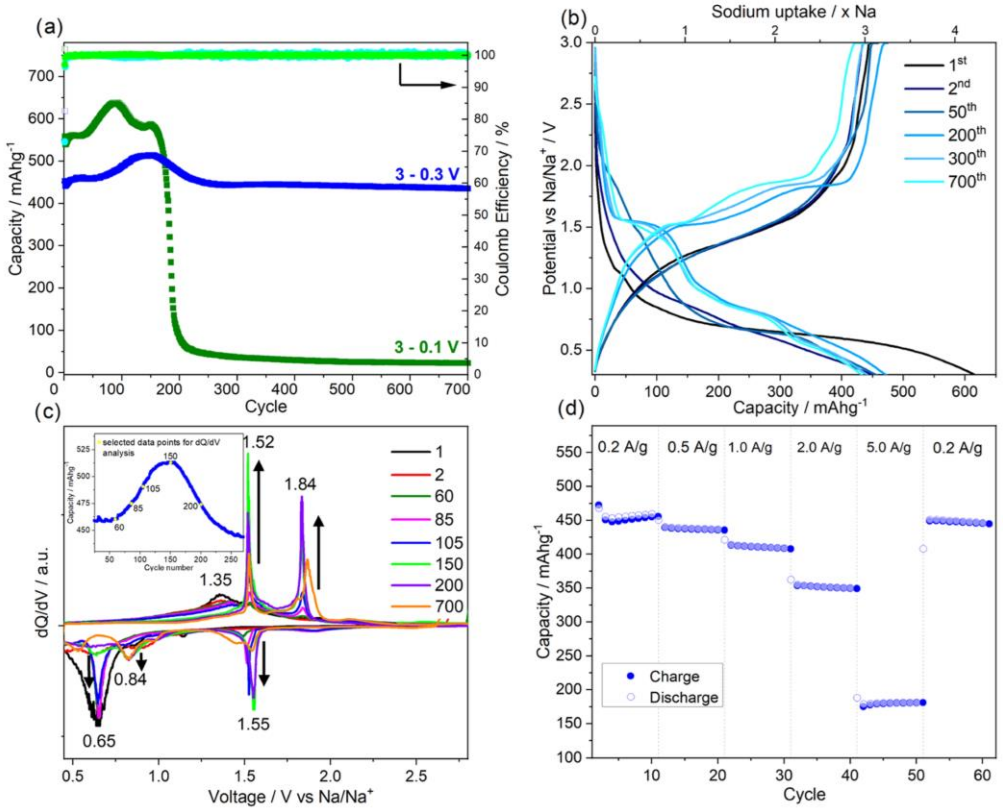

Figure 2. (a) Electrochemical cycling performance and charge efficiency of $Na/CuFeS_2$ test cells. A current rate of 0.5 A g^{-1} was applied in the potential windows of 3.0−0.1 V (green) and of 3.0−0.3 V (blue). (b) Discharge and charge profiles at a current rate of 0.2 A g^{-1} of the 1st, 2nd, 50th, 200th, 300th, and 700th cycles of $Na/CuFeS_2$. (c) dQ/dV analysis of selected cycles; the arrows indicate the development of signals during cycling, and the inset shows the region where the specific capacity passes a maximum. (d) Rate capability at several current rates from 0.2 to 5 A g^{-1} for $CuFeS_2$.

discharged. While the alteration in the discharge profile is already clearly visible from cycle 100, the change in the charge profile is only detectable from cycle 200 onwards. Like observed before, two pseudo-plateaus are formed at about 1.5 and 1.75 V.

The successive alterations of the chemical reactions and their beginning can be seen more clearly in the derivative curve dQ/dV (Figure 2c). In the first cycle, a broad reduction signal is located at about 0.6 V, which disappears already in the 2nd cycle. Instead, a new peak develops at 0.65 V reaching the highest intensity in the 85th cycle, and the intensity drops during further cycling and is not visible in the 150th cycle, which corresponds to the maximum in the specific capacity curve (Figure 2a and the inset in Figure 2c). A second reduction peak at 1.5 V appears at the 60th cycle, which gains intensity up to cycle 150 and simultaneously shifts to 1.55 eV (see Figure 2a,c). The intensity of this signal slowly decreases but does not disappear completely in the following cycles. Another reduction peak develops at 0.84 V after passing the maximum of the specific capacity and the intensity of this event remains quite constant up to the 700th cycle.

In the first cycle, the oxidation reaction is accompanied by a broad peak at 1.35 V, a small shoulder is located at 1.55 V, and two very weak signals at 1.94 and 2.15 V can be identified. These events successively disappear, while a new peak develops at 1.52 V with increasing intensity up to the 150th cycle (see Figure 2c and inset), followed by a successive decrease of the intensity up to cycle 700. Simultaneously, a second oxidation signal at 1.84 V starts to develop having the highest intensity in the 200th cycle. This peak gradually loses intensity in the following cycles, becomes broader and shifts to 1.87 V (Figure 2c).

Summarizing, the dQ/dV results highly suggest that during cycling several changes occur in the reaction mechanism before an apparently constant and stable mechanism occurs. For gaining more insight into the reaction mechanisms, ex situ XRD experiments are performed and discussed in detail in Section 3.3.

The rate performance of the $Na/CuFeS_2$ electrode is displayed in Figure 2d. The cell delivered reversible specific capacities of 456, 437, 412, 352, and 180 mAh g^{-1} for current densities of 0.2, 0.5, 1, 2, and 5 A g^{-1}, respectively. When the current density is reset to 0.2 A g^{-1}, a specific capacity of 483 mAh g^{-1} could be recovered, which is an outstanding performance for conversion materials. Neither pure iron sulfide (FeS_2) (640 mAh g^{-1} at 0.02 A g^{-1} to 290 mAh g^{-1} at 0.2 A g^{-1})[40] nor pure copper sulfide (CuS) (~330 mAh g^{-1} at 0.1 A g^{-1} to less than 50 mAh g^{-1} at 3 A g^{-1})[20] achieved such high rate stability. Not even the ternary compound $CuCrS_2$ (450 mAh g^{-1} at 0.4 A g^{-1} to 158 mAh g^{-1} at 2 A

https://doi.org/10.1021/acsami.1c04946
ACS Appl. Mater. Interfaces 2021, 13, 26034−26045

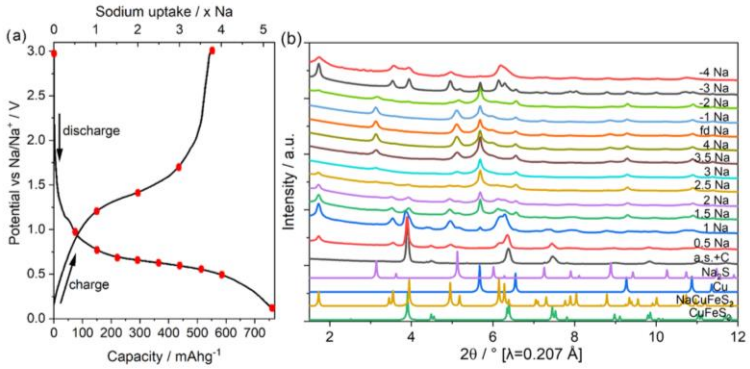

Figure 3. (a) Discharge/charge profile of the first cycle of the Na/$CuFeS_2$ powder electrode. (b) Ex situ X-ray diffraction patterns of the Na/$CuFeS_2$ electrode collected at several states of discharge/charge compared to simulated patterns of Na_2S, $CuFeS_2$, $NaCuFeS_2$, and Cu.

g^{-1})[18] showed such exceptional rate stability. Hence, an outstanding rate performance is observed keeping in mind that no additives like GO or RGO were used and that a bulk material is applied.

3.3. Ex Situ X-ray Diffraction and PDF Investigations. After the uptake and release of defined amounts of Na/f.u., the electrochemical reaction was interrupted and XRD as well as PDF investigations were performed. The XRD patterns recorded with an increasing/decreasing content of Na/f.u. together with the discharge/charge profiles are displayed in Figure 3. The first changes in the XRD pattern occur after insertion of 0.5 Na/f.u. and the new reflections can be assigned to $NaCuFeS_2$ coexisting with the pristine material. The intensities of the reflections of the new phase increased for the sample with 1 Na/f.u., while the intensities of the reflections of the pristine material decreased (Figure 4a). These observations allow the formulation of a chemical reaction in the first step, in which Fe^{3+} is reduced to Fe^{2+} according eq 2

$$CuFeS_2 + Na + e^- \rightarrow NaCuFeS_2 \quad (2)$$

After the uptake of 1.5 Na/f.u., the reduction of Cu^+ to metallic Cu is evidenced by the appearance of the (111) and (200) reflections of Cu in the XRD pattern (Figure 4c). The ratio of the intensities of these reflections deviates significantly from the theoretical value of ≈1.5 assuming crystallites with random orientation. However, the present value of ≈5 is estimated, demonstrating a preferential growth in the direction of the {111} faces (Table S4). The reflections are relatively broad indicating coherently scattering domains in the nano-regime. A further increase of the Na content leads to an increase of the Cu content, while the $NaCuFeS_2$ fraction decreases. After insertion of 3 Na/f.u., an additional weak and broad reflection located at 3.1° 2θ can be assigned to nanocrystalline Na_2S (size: ≈8 nm, Table S5), which gains intensity during further Na uptake. Since only 3.1 Na is cycled in the restricted potential window, the complete crystallization of Na_2S can be suppressed, which may contribute to the improved cycle stability. At the fully discharged state, only reflections of Cu and Na_2S are visible. We note that no reflections of elemental Fe can be identified in the XRD data suggesting that the particles are too small to be detected due to the lack of a long-range order. But for the electrode with >1.5 Na/f.u., the background of the XRD patterns becomes more modulated and the reflections are broadened leading to a partial overlap of reflections, thus masking reflections of Fe. These observations may also indicate that another nanosized phase is formed, but introducing elemental Fe in the Rietveld refinement resulted in a better fit with an improved R_{wp} (Table S6). Because the reflections related to Fe are extremely broadened, estimated sizes of coherently scattering domains are between 1 and 2 nm (Table S5).

The evaluation of the PDF data confirms the results obtained by the analysis of the XRD data. The peaks in the PDF at 2.27, 3.74, 6.47, 9.89, and 13.42 Å associated with $CuFeS_2$ disappear completely for a Na uptake of up to 1.5 Na/f.u., while new signals related to the intermediate compound $NaCuFeS_2$ appear (blue arrows in Figure 4b). The domain sizes of $NaCuFeS_2$ at different stages of Na insertion are extracted from the damping of the PDF data, since the values estimated from the refinement of XRD patterns are not unambiguous due to the existing strain and absence of well-shaped reflection profiles. The values for the crystallite sizes are 6.5 nm (0.5 Na/f.u.) and 8.1 nm (1 Na/f.u.) (Table S7). As observed in the XRD patterns, the formation of elemental Cu is also clearly visible in the PDF data (green arrows in Figure 4d), and a domain radius of ≈3 nm was determined, which remains relatively constant for further Na uptake. An improved R_{wp} value for the data after an uptake of 1.5 Na/f.u. is achieved considering nanosized Fe in the fitting procedure of the data. Introducing nanosized Fe particles in the modeling of the PDF data, only a moderate improvement of the R_{wp} value was obtained for samples up to 2 Na/f.u., but a significant drop of the R_{wp} up to 12.65% is observed with further Na insertion (Table S6). The difference curve of the experimental and modeled PDF including Fe particles with a 10 nm diameter in the model (blue line, Figure 5a) evidences an amazingly good agreement. This is also obvious from the remarkable good agreement of the major features of the simulated Fe PDF with the signals of the experimental PDF for the fully discharged sample (green dotted line in Figure 5a). Consequently, these features in the PDF can be attributed to Fe−Fe bonds, including iron in the fitting model results in a significantly improved fit (Figure 5b). It is not surprising that high atomic displacement parameters were observed using the above-mentioned model caused by the small particle sizes and a pronounced disorder of the nanoparticles.[42]

It is a common observation that for Cu^+ containing ternary conversion materials, nanocrystalline Cu is formed during discharge while other transition metals convert to an X-ray

https://doi.org/10.1021/acsami.1c04946
ACS Appl. Mater. Interfaces 2021, 13, 26034−26045

ACS Applied Materials & Interfaces www.acsami.org Research Article

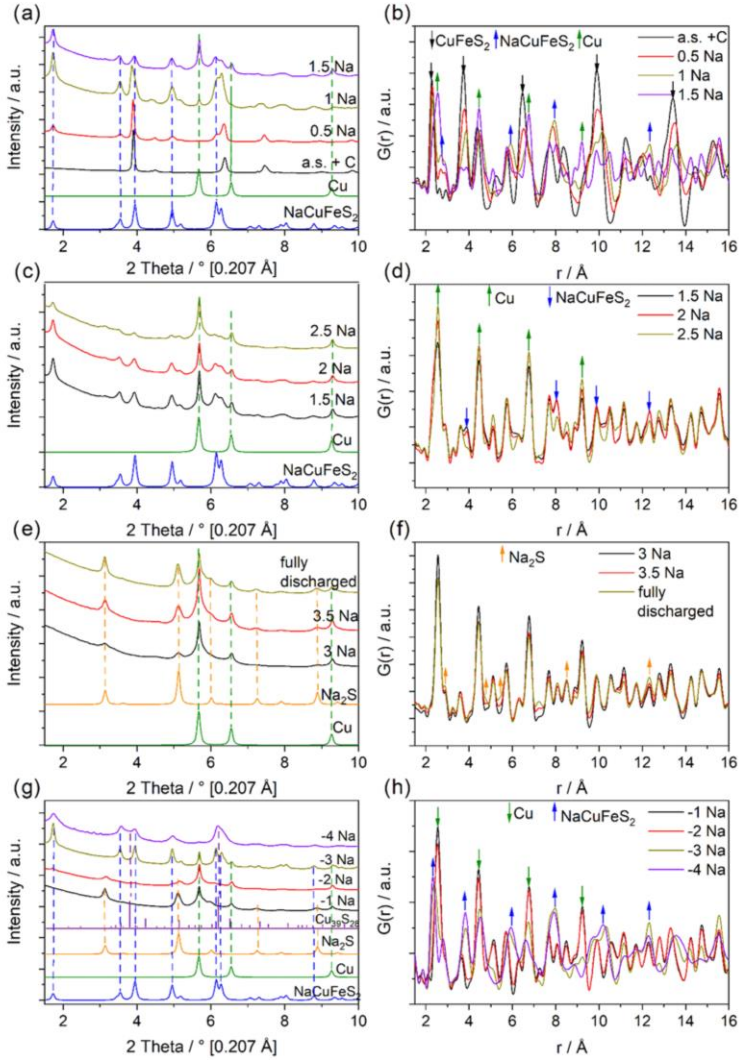

Figure 4. (a) Ex situ XRD patterns of Na/$CuFeS_2$/C65 powder cells with 0−1.5 Na/f.u. compared to simulated data of $NaCuFeS_2$ and Cu. (b) Ex situ pair distribution function between 1.5 and 16 Å showing the uptake of 0−1.5 Na/f.u. (colored arrows show the alteration during the Na uptake). (c) Ex situ XRD patterns for cells with 1.5−2.5 Na/f.u. (d) Ex situ pair distribution function for 1.5−2.5 Na/f.u. (e) Ex situ XRD patterns from 4Na—full discharge compared to simulated patterns of Na_2S and Cu. (f) Ex situ pair distribution function for 3 Na/f.u., i.e., full discharge. (g) Ex situ XRD patterns of Na/$CuFeS_2$/C65 powder cells during charge (−1 Na−4 Na/f.u.) compared to the simulated data of $NaCuFeS_2$, Na_2S, and $Cu_{39}S_{28}$. (h) Ex situ pair distribution function between 1.5 and 16 Å showing the release of Na.

amorphous state.[18,39,43] This could be related to the higher diffusivity of the Cu atoms leading to the formation of larger Cu particles, while the slow diffusion of Fe produces many small nuclei, resulting in smaller and finely dispersed particles.[44]

During the charge process, the intensity of the reflections of Na_2S decreases in the XRD patterns (Figure 4g), while the reflections of Cu do not show significant changes up to the release of 2 Na/f.u. This observation suggests that at this stage Fe is oxidized and probably amorphous FeS_x phases are generated. In the PDF, a real space model based on nanocrystalline Na_2S, Cu, and FeS_2 leads to an improved R_{wp} value of 26.6% compared to a model considering only Na_2S and Cu (R_{wp} = 32.9%), which supports the assumption of the presence of FeS_x phases. After the release of 3 Na/f.u., a reduction of the intensity of the reflections of Cu occurs and reflections of the $NaCuFeS_2$ intermediate appear. This is an astonishing observation because the formation of a crystalline phase was not observed in the overwhelming cases of conversion materials, which were in the fully charged state. In the last step of the charging process, the remaining Cu is oxidized, visible by the disappearance of the Cu reflections. Since formally only 0.7 Na is released in the last step, the structure of $NaCuFeS_2$ is not completely destroyed, but a pronounced broadening of the reflections in the XRD pattern suggests a significant reduction of the sizes of the coherently scattering domains. In addition, the intensities deviate significantly from the $NaCuFeS_2$ intermediate, which may be due to the fact that an additional CuS_x phase is formed during the oxidation of Cu (Figure 4g). The disappearance of signals

https://doi.org/10.1021/acsami.1c04946
ACS Appl. Mater. Interfaces 2021, 13, 26034−26045

ACS Applied Materials & Interfaces www.acsami.org Research Article

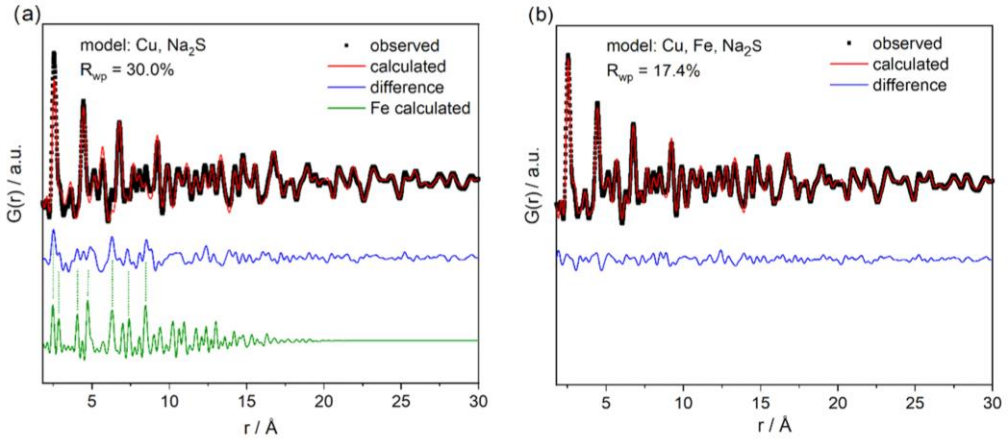

Figure 5. (a) Fitting of the atomic pair distribution function of $CuFeS_2$ after the uptake of 4 Na with a model including only Cu and Na_2S. The difference curve is compared to a model for Fe (D_m = 10 nm), as indicated by the green dashed lines. (b) Atomic pair distribution function analysis of $CuFeS_2$ after full discharge with a model including Fe, Cu, and Na_2S.

of Cu in the PDF in the fully charged sample and the occurrence of peaks of the $NaCuFeS_2$ intermediate is clearly visible in the PDF data. However, modeling the PDF with only $NaCuFeS_2$ leads to significant deviations, which may be regarded as a further indication that another phase has been formed during the oxidation of Cu.

We note that complete oxidation of Cu during the charge process is not always observed, and for other conversion materials an extrusion mechanism has even been postulated in which a part of the elemental Cu survived in the fully charged state.[18]

3.4. Ex Situ ^{57}Fe Mössbauer Investigations. Detailed analyses of the XRD and PDF data give hints about the nature of Fe during Na uptake and release, and further support is obtained about the change in the oxidation state of Fe from selected ex situ samples using ^{57}Fe Mössbauer spectroscopy.

Figure 6 shows the room temperature ^{57}Fe Mössbauer spectra of $CuFeS_2$ at different discharge/charge states. For the pristine material, the dominating contribution stems from a sextet with hyperfine splitting B_{hf} = 35.6 T, isomer shift IS = 0.25 mm/s, quadrupole splitting QS = −0.01 mm/s, and line width Γ = 0.32 mm/s (Table 1). These values are in good agreement with values reported earlier for $CuFeS_2$[38,45,46] and represent Fe^{3+} in the high-spin state. A second contribution to the spectrum can be modeled as a doublet with IS = 0.24 mm/s and QS = 0.32 mm/s, representing high-spin Fe^{3+} located in smaller particles, which leads to a lowering of the Neel temperature.[45] After insertion of 1 Na/f.u., the sextet is still visible but its area fraction is reduced to 16.4%. The spectrum is now dominated by a doublet with IS = 0.53 mm/s and QS = 1.07 mm/s (Table 1), revealing that the majority of the Fe^{3+} cations have been reduced to Fe^{2+}. This result confirms the intermediate formation of $NaCuFeS_2$ derived from the XRD data. After increasing the inserted amount of Na (2Na, 4Na), the doublet of the Fe^{2+} species disappears and new components with IS close to 0 mm/s develop with increasing intensity. These results clearly demonstrate that in the second step Fe^{2+} cations are reduced to metallic Fe^0 and support the assumption that small Fe^0 particles exist in an X-ray amorphous state. During charging, the components at IS = 0 mm/s disappear and the doublet at IS = 0.5 mm/s successively appears. For the charging step of 2 Na/f.u., 77.2% of Fe is

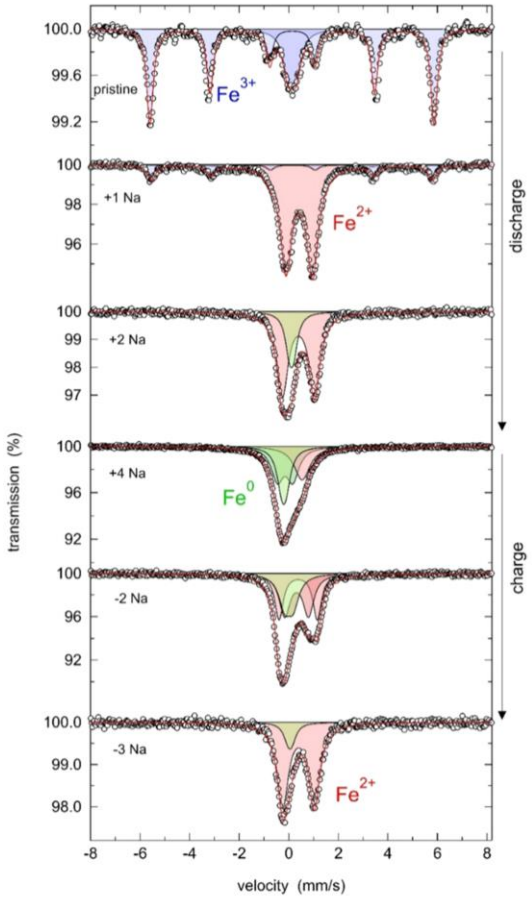

Figure 6. ^{57}Fe Mössbauer spectra of $CuFeS_2$ at different charge states. Experimental data points are shown as white spheres, the overall fit as the red line, and the subspectra are shown as blue, red, and green doublets/sextets.

https://doi.org/10.1021/acsami.1c04946
ACS Appl. Mater. Interfaces 2021, 13, 26034−26045

Table 1. Fit Parameters Derived from the Mössbauer Spectra of $CuFeS_2$ at Different Charge States: Isomer Shift (IS), Quadrupole Splitting (QS), Hyperfine Field (B_{hf}), Line Width (Γ), and Area Fraction[a]

sample		IS	QS	B_{hf}	Γ	area frac. (%)
$CuFeS_2$	Fe^{3+}	0.246 ± 0.003	−0.012 ± 0.006	35.6 ± 0.1	0.321 ± 0.009	75.4
	Fe^{3+}	0.239 ± 0.011	0.318 ± 0.024		0.494 ± 0.039	24.6
+1 Na	Fe^{2+}	0.530 ± 0.001	1.067 ± 0.002		0.582 ± 0.002	83.6
	Fe^{3+}	0.256 ± 0.005	−0.031 ± 0.010	35.2 ± 0.1	0.387 ± 0.017	16.4
+2 Na	Fe^{2+}	0.504 ± 0.002	1.290 ± 0.003		0.542 ± 0.003	76.9
	Fe^{0}	0.113 ± 0.003	0.172 ± 0.015		0.401 ± 0.020	23.1
+4 Na	Fe^{0}	−0.068 ± 0.027	0.597 ± 0.035		0.588 ± 0.026	34.9
	Fe^{0}	−0.108 ± 0.014	0.167 ± 0.014		0.468 ± 0.074	33.5
	Fe^{2+}	0.603 ± 0.038	0.225 ± 0.067		0.726 ± 0.023	31.6
−2 Na	Fe^{2+}	0.422 ± 0.102	0.958 ± 0.202		0.532 ± 0.032	38.0
	Fe^{2+}	0.486 ± 0.004	1.538 ± 0.009		0.419 ± 0.011	33.2
	Fe^{0}	0.113 ± 0.150	0.345 ± 0.309		0.564 ± 0.053	28.9
−3 Na	Fe^{2+}	0.504 ± 0.003	1.270 ± 0.005		0.543 ± 0.009	87.4
	Fe^{0}	0.158 ± 0.011	0.144 ± 0.083		0.483 ± 0.091	12.6

[a]IS, QS, and Γ are given in mm/s. B_{hf} is given in T.

present as Fe^{2+}. After extraction of 3 Na/f.u., 87.4% of the iron is present as Fe^{2+}, demonstrating the reversibility of the reaction mechanism.

3.5. Ex Situ ^{23}Na MAS NMR Spectroscopy. The ^{23}Na MAS NMR spectra of $CuFeS_2$ are shown in Figure 7 for different Na contents. In all NMR spectra, except for the pristine material, a narrow peak is visible at about −16.2 ppm, which can be assigned to residues of the Na salt of the electrolyte used in the electrochemical cells (Na triflate).[17] After the uptake of 1 Na/f.u., an additional broader signal is visible at −15 ppm. This signal decreases during further Na uptake (2 Na) until it disappears completely, while at this stage a further component emerges at 48.4 ppm. The latter signal can be assigned to the formation of Na_2S during discharging. This signal is broadened for the sample containing 4 Na, due to the increased formation of metallic iron, as confirmed by the Mössbauer measurements. During charging, the intensity of the signal at 48.4 ppm increases indicating that Fe is oxidized. After the release of 3 Na/f.u., this signal disappeared due to the consumption of Na_2S in the chemical reaction with Fe. Interestingly, the signal at −15 ppm is formed again, which can be regarded as an indication that this signal can be assigned to the $NaCuFeS_2$ intermediate. Unfortunately, there is no further literature data available for comparison. A broad signal is observed at +4500 ppm (Figure S4). This is a ^{63}Cu resonance that mostly belongs to the NMR radiofrequency coil located around the sample. For some of the sodiated/desodiated samples, this signal reveals some spinning sidebands (marked with an asterisk in Figure 7), revealing that at least part of this signal belongs to metallic Cu inside these samples, in good agreement with the XRD results described above.

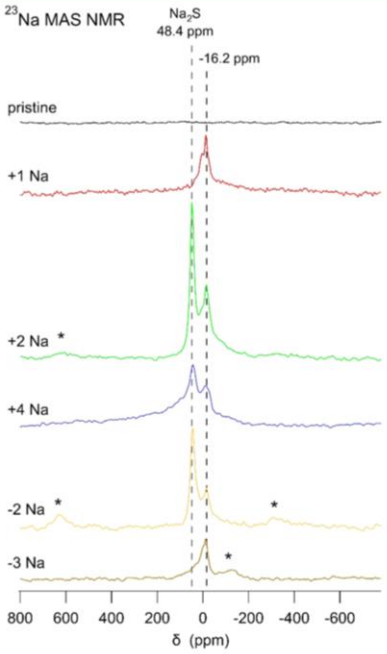

Figure 7. ^{23}Na MAS NMR spectra of $CuFeS_2$ for different Na contents obtained during discharging and charging against the Na metal. The signals marked with an asterisk are spinning sidebands belonging to a ^{63}Cu resonance at 4500 ppm, which stems from metallic Cu.

3.6. Investigation of the Change in the Reaction Mechanisms at Later Cycling Stages. The dQ/dV curves presented in Figure 2c clearly show that a change in the reaction mechanisms occurs during extended cycling. To gain more insight into the mechanisms, the test cells were stopped at the maximum of the specific capacity curve (150th cycle) and in the constant capacity region (250th cycle) both in the discharged and charged states and the products were examined by XRD (Figure 8). The first surprise is that the samples recovered are still crystalline after such a large number of cycles exhibiting a long-range order as evidenced by Bragg reflections, which are indeed broad but well developed (Figure 8).

At the maximum of the cycling curves (150th cycle, discharged state), the XRD pattern is characterized by broad reflections, which can be assigned to nanosized elemental Cu and Na_2S (Figure 8b). XRD investigation of the material in the charged state at this cycle exhibits a totally different pattern (Figure 8c). The reflections of Cu and Na_2S disappeared and new broad reflections developed, which are assignable to Cu_2S and $Cu_{1.8}S$ (Figure 8c). In different publications it was demonstrated that Cu sulfides mainly react with Na according to eqs 3 and 4[47,48]

https://doi.org/10.1021/acsami.1c04946
ACS Appl. Mater. Interfaces 2021, 13, 26034−26045

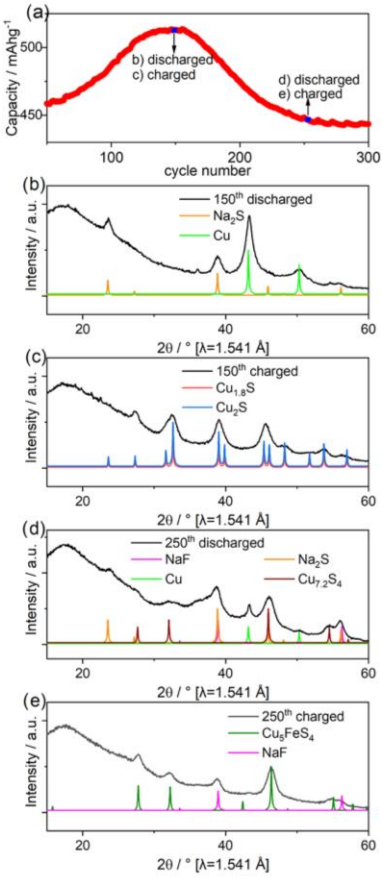

Figure 8. (a) Electrochemical cycling performance and charge efficiency of $CuFeS_2$ with blue points indicating the points of measurement. (b–e) XRD patterns of the electrode at cycle 150 (maximum in the capacity curve) and cycle 275 (region of constant capacity) in the discharged and charged states, compared with the calculated patterns of the proposed phases.

$$Cu_2S + xNa^+ + xe^- \rightarrow Na_xCu_xS \quad (3)$$

$$Na_xCu_xS + (2 - x)Na^+ + (2 - x)e^- \rightarrow 2Cu + Na_2S \quad (4)$$

On the basis of the present data no conclusive explanation can be given about the role of Fe that is still present in the electrode. A reasonable assumption is that iron sulfide is formed, and Fe^{n+} is reduced to the elemental state during discharge, thus contributing to the missing capacity. If Cu reacts as formally described in eqs 3 and 4, a contribution to the capacity of 146 mAh g^{-1} is estimated. For achieving the maximum capacity of 512 mAh g^{-1}, the calculation suggests that the remaining Fe at the maximum of the specific capacity curve (cycle 150) is in a mixed valent oxidation state of +2/+3 in a ratio of 1 to 1.

After the maximum of the specific capacity is passed and the capacity remains almost constant from the 250th cycle on, further changes are discernible in the XRD patterns of the material recovered in the discharged state at cycle 250 (Figure 8d). The clearly recognizable (111) reflection of Cu and a broad hump at the position of the (220) reflection indicate that Cu is only partially reduced. Furthermore, the intensity ratios of the reflections of Na_2S changed, which may be explained by the occurrence of reflections of NaF, which has been formed by a side reaction with the electrolyte, overlapping with reflections of Na_2S. Some broad features and shoulders in the XRD pattern reveal the presence of another phase and using the reflection positions of $Cu_{7.2}S_4$ (space group: $Fm\bar{3}m$) a reasonable good match of reflection positions is obtained. Accordingly, a significant amount of Cu remains as Cu^+. Analyzing the XRD pattern of the sample in the charged state at this cycle, pronounced differences are obvious to both the pattern recorded for the charged sample at the 150th cycle and the discharged state at the present cycle (Figure 8e). The reflections of NaF are still present and the remaining reflections can be assigned to Cu_5FeS_4 (space group $Fm\bar{3}m$). Hence, it can be postulated that about one-fifth of the iron is incorporated into the structure of $Cu_{7.2}S_4$ during Na release, yielding a specific capacity of 88 mAh g^{-1}. From the XRD patterns, no conclusions can be drawn concerning the nature and role of the remaining Fe. Based on the specific capacity of 444 mAh g^{-1} observed in the constant capacity range, the remaining Fe^{3+} has to be reduced during discharge providing the difference in capacity, i.e., about 350 mAh g^{-1}. From this amount of fully reduced iron, only the stoichiometric amount of completely reduced Cu^+ would have to be subtracted, since this part also contributes a specific amount to the capacity.

Concerning the assignment of the different phases in the XRD patterns, the strong broadening of the reflections caused by the nanosized nature of the particles may prevent identification of a certain amount of Cu_5FeS_4 already contained in the electrode at the 150th cycle.

Summarizing the results, the electrochemical reaction starts from Na and $CuFeS_2$ and proceeds via formation of a Cu_xS/FeS_x mixture most probably up to the 150th cycle. Further cycling generates a mixture of Cu_5FeS_4 and most likely FeS_x which are the active materials during the remaining cycles. To get a more precise insight into the mechanisms, further ex situ measurements are required at the distinct plateaus to determine possible intermediates.

4. CONCLUSIONS

Polycrystalline $CuFeS_2$ was synthesized by a traditional high-temperature synthesis. We demonstrated that this material is an excellent anode material for sodium-ion storage. A high and stable capacity of 444 mAh g^{-1} is achieved at 0.5 A g^{-1} for 700 cycles.

Considering the results of the structural investigations, we assume the following reactions for the first discharge. The first step is the formation of the intermediate $NaCuFeS_2$ (eq 5) accompanied by the reduction from Fe^{3+} to Fe^{2+}, followed by the reversible full conversion of the intermediate phase to Cu, Fe, and Na_2S (eq 6). The formation of Na_2S and metallic Cu is clearly demonstrated by ex situ XRD and NMR measurements, while PDF analysis and especially Mössbauer measurements unveiled the presence of nanoscaled, most probably highly disordered metallic Fe in the discharged state.

$$CuFeS_2 + Na^+ + e^- \rightarrow NaCuFeS_2 \quad (5)$$

$$NaCuFeS_2 + 3Na^+ + 3e^- \rightarrow Cu + Fe + 2Na_2S \quad (6)$$

Crystalline Na_2S is formed by the uptake of 3 Na, so it is reasonable to assume that this crystallization may have some

https://doi.org/10.1021/acsami.1c04946
ACS Appl. Mater. Interfaces 2021, 13, 26034–26045

relation to the improved cycling in a smaller potential window, due to the poor conductivity and volume expansion of crystalline Na_2S formed in the larger voltage window. The limited potential window inhibits complete crystallization of Na_2S.

During charging, most probably Fe sulfide phases are formed first. The results of the Mössbauer investigations confirm that an amorphous intermediate state must be present. This is most likely an FeS_x or $NaFeS_x$ phase, as discussed in Section 3.3 (eq 7). Another assumption would be that $NaCuFeS_2$ is amorphous before it crystallizes, but the constantly present reflections of elemental Cu contradict this assumption. The intensity of the reflections of Cu decreases after the release of 3 Na/f.u. during the charging process accompanied by the simultaneous appearance of the reflections of $NaCuFeS_2$ (eq 8). After this stage of charging, a partial development of the $NaCuFeS_2$ intermediate during further Na release is observed, with simultaneous oxidation of Cu. However, parts of Cu remain in the elemental state, until it seems to react to form Cu_xS in the last reaction step (eq 9).

$$\mathrm{Cu} + \mathrm{Fe} + 2\mathrm{Na_2S} \rightarrow \mathrm{Cu} + x\mathrm{FeS_x} + (2-x)\mathrm{Na_2S} + x\mathrm{Na^+} + 2x\mathrm{e^-} + 2 - x\mathrm{Fe} \quad (7)$$

$$x\mathrm{Cu} + x\mathrm{FeS_x} + x/2\mathrm{Na_2S} \rightarrow x\mathrm{NaCuFeS_2} + x\mathrm{Na^+} + x\mathrm{e^-} + (2-x)\mathrm{Cu} + (2-x)\mathrm{FeS_x} \quad (8)$$

$$x\mathrm{Cu} + \mathrm{Na_2S} \rightarrow \mathrm{Cu_xS} + 2\mathrm{Na^+} + 2\mathrm{e^-} \quad (9)$$

We also clearly demonstrated a unique phenomenon of a change of the charge/discharge profiles occurring at later stages of cycling. A comprehensive XRD investigation was performed and the patterns could be interpreted due to the remarkable crystallinity at these large cycle numbers with amazing and surprising novel results. In addition, the results obtained during the present studies imply that retaining good crystallinity of discharged and charged electrodes plays a key role in achieving outstanding stable cyclization and simultaneously maintaining high specific capacities. Based on theoretical calculations (Tables S8 and S9), the occurrence of crystalline phases during cycling should reduce the volume change compared to amorphization observed by full conversion of electrode materials, where large volume expansions limit cyclization stability. This may be one of the factors for the very good long-term stability, as a smaller volume change keeps the electrochemical active material in better contact with the collector. Furthermore, the good electrical conductivity of several phases identified here in combination with the limitation of the potential window lead to exceptionally good stability.

■ ASSOCIATED CONTENT

Supporting Information

The Supporting Information is available free of charge at https://pubs.acs.org/doi/10.1021/acsami.1c04946.

Tables of refinement parameters of all Rietveld and PDF refinements; R_{wp} improvement, determined copper reflection intensities, and results of EDX measurements; cyclic voltammograms of the first five cycles of $CuFeS_2$; figures from Rietveld and PDF fits; and the full view of the ^{23}Na MAS NMR spectra of $CuFeS_2$ for different discharge/charge states (PDF)

■ AUTHOR INFORMATION

Corresponding Author

Wolfgang Bensch − *Institute of Inorganic Chemistry, Kiel University, 24118 Kiel, Germany;* orcid.org/0000-0002-3111-580X; Phone: +49 431 880-2091; Email: wbensch@ac.uni-kiel.de; Fax: +49 431 880-1520

Authors

Svenja Senkale − *Institute of Inorganic Chemistry, Kiel University, 24118 Kiel, Germany*

Sylvio Indris − *Institute for Applied Materials, Karlsruhe Institute of Technology, 76021 Karlsruhe, Germany;* orcid.org/0000-0002-5100-113X

Martin Etter − *Deutsches Elektronen-Synchrotron (DESY), 22607 Hamburg, Germany*

Complete contact information is available at: https://pubs.acs.org/10.1021/acsami.1c04946

Notes

The authors declare no competing financial interest.

■ ACKNOWLEDGMENTS

Financial support by the State of Schleswig-Holstein is gratefully acknowledged. The authors thank the German Electron Synchrotron (DESY). Parts of this research were carried out at PETRA III. The authors kindly thank Huayna Terraschke for beamtime allocation.

■ REFERENCES

(1) Panwar, N. L.; Kaushik, S. C.; Kothari, S. Role of Renewable Energy Sources in Environmental Protection: A Review. *Renewable Sustainable Energy Rev.* **2011**, *15*, 1513−1524.

(2) Larcher, D.; Tarascon, J.-M. Towards Greener and More Sustainable Batteries for Electrical Energy Storage. *Nat. Chem.* **2015**, *7*, 19−29.

(3) Hwang, J.-Y.; Myung, S.-T.; Sun, Y.-K. Sodium-Ion Batteries: Present and Future. *Chem. Soc. Rev.* **2017**, *46*, 3529−3614.

(4) Permien, S.; Neumann, T.; Indris, S.; Neubüser, G.; Kienle, L.; Fiedler, A.; Hansen, A.-L.; Gianolio, D.; Bredow, T.; Bensch, W. Transition Metal Cations on the Move: Simultaneous Operando X-Ray Absorption Spectroscopy and X-Ray Diffraction Investigations during Li Uptake and Release of a $NiFe_2O_4$/CNT Composite. *Phys. Chem. Chem. Phys.* **2018**, *20*, 19129−19141.

(5) Fang, S.; Bresser, D.; Passerini, S. Transition Metal Oxide Anodes for Electrochemical Energy Storage in Lithium- and Sodium-Ion Batteries. *Adv. Energy Mater.* **2020**, *10*, No. 1902485.

(6) Cao, K.; Jin, T.; Yang, L.; Jiao, L. Recent Progress in Conversion Reaction Metal Oxide Anodes for Li-Ion Batteries. *Mater. Chem. Front.* **2017**, *1*, 2213−2242.

(7) Klein, F.; Jache, B.; Bhide, A.; Adelhelm, P. Conversion Reactions for Sodium-Ion Batteries. *Phys. Chem. Chem. Phys.* **2013**, *15*, 15876−15887.

(8) Tang, J.; Huang, X.; Lin, T.; Qiu, T.; Huang, H.; Zhu, X.; Gu, Q.; Luo, B.; Wang, L. MXene Derived TiS_2 Nanosheets for High-Rate and Long-Life Sodium-Ion Capacitors. *Energy Storage Mater.* **2020**, *26*, 550−559.

(9) Tao, H.; Zhou, M.; Wang, R.; Wang, K.; Cheng, S.; Jiang, K. TiS_2 as an Advanced Conversion Electrode for Sodium-Ion Batteries with Ultra-High Capacity and Long-Cycle Life. *Adv. Sci.* **2018**, *5*, No. 1801021.

(10) Pham, D. T.; Sambandam, B.; Kim, S.; Jo, J.; Kim, S.; Park, S.; Mathew, V.; Sun, Y.-K.; Kim, K.; Kim, J. Dandelion-Shaped Manganese Sulfide in Ether-Based Electrolyte for Enhanced Performance Sodium-Ion Batteries. *Commun. Chem.*. **2018**, *1*, No. 83.
(11) Gao, X.; Zhang, X.; Jiang, J.; Chen, J. Rod-like Carbon-Coated MnS Derived from Metal-Organic Frameworks as High-Performance Anode Material for Sodium-Ion Batteries. *Mater. Lett.* **2018**, *228*, 42−45.
(12) Sun, R.; Wei, Q.; Li, Q.; Luo, W.; An, Q.; Sheng, J.; Wang, D.; Chen, W.; Mai, L. Vanadium Sulfide on Reduced Graphene Oxide Layer as a Promising Anode for Sodium Ion Battery. *ACS Appl. Mater. Interfaces* **2015**, *7*, 20902−20908.
(13) Qi, H.; Wang, L.; Zuo, T.; Deng, S.; Li, Q.; Liu, Z.; Hu, P.; He, X. Hollow Structure VS_2@Reduced Graphene Oxide (RGO) Architecture for Enhanced Sodium-Ion Battery Performance. *ChemElectroChem* **2020**, *7*, 78−85.
(14) David, L.; Bhandavat, R.; Singh, G. MoS_2/Graphene Composite Paper for Sodium-Ion Battery Electrodes. *ACS Nano* **2014**, *8*, 1759−1770.
(15) Hu, Z.; Wang, L.; Zhang, K.; Wang, J.; Cheng, F.; Tao, Z.; Chen, J. MoS_2 Nanoflowers with Expanded Interlayers as High-Performance Anodes for Sodium-Ion Batteries. *Angew. Chem., Int. Ed.* **2014**, *53*, 12794−12798.
(16) Yu, X. Y.; David Lou, X. W. Mixed Metal Sulfides for Electrochemical Energy Storage and Conversion. *Adv. Energy Mater.* **2018**, *8*, No. 1701592.
(17) Krengel, M.; Hansen, A.-L.; Kaus, M.; Indris, S.; Wolff, N.; Kienle, L.; Westfal, D.; Bensch, W. CuV_2S_4: A High Rate Capacity and Stable Anode Material for Sodium Ion Batteries. *ACS Appl. Mater. Interfaces* **2017**, *9*, 21283−21291.
(18) Krengel, M.; Hansen, A.-L.; Hartmann, F.; van Dinter, J.; Bensch, W. Elucidation of the Sodium − Copper Extrusion Mechanism in $CuCrS_2$: A High Capacity, Long-Life Anode Material for Sodium-Ion Batteries. *Batteries Supercaps* **2018**, *1*, 176−183.
(19) Shi, B.; Liu, W.; Zhu, K.; Xie, J. Synthesis of Flower-like Copper Sulfides Microspheres as Electrode Materials for Sodium Secondary Batteries. *Chem. Phys. Lett.* **2017**, *677*, 70−74.
(20) Kim, N. R.; Choi, J.; Yoon, H. J.; Lee, M. E.; Son, S. U.; Jin, H.-J.; Yun, Y. S. Conversion Reaction of Copper Sulfide Based Nanohybrids for Sodium-Ion Batteries. *ACS Sustainable Chem. Eng.* **2017**, *5*, 9802−9808.
(21) Li, H.; Wang, K.; Cheng, S.; Jiang, K. Controllable Electrochemical Synthesis of Copper Sulfides as Sodium-Ion Battery Anodes with Superior Rate Capability and Ultralong Cycle Life. *ACS Appl. Mater. Interfaces* **2018**, *10*, 8016−8025.
(22) Feng, C.; Zhang, L.; Yang, M.; Song, X.; Zhao, H.; Jia, Z.; Sun, K.; Liu, G. One-Pot Synthesis of Copper Sulfide Nanowires/Reduced Graphene Oxide Nanocomposites with Excellent Lithium-Storage Properties as Anode Materials for Lithium-Ion Batteries. *ACS Appl. Mater. Interfaces* **2015**, *7*, 15726−15734.
(23) Wang, Y.-X.; Yang, J.; Chou, S.-L.; Liu, H. K.; Zhang, W.; Zhao, D.; Dou, S. X. Uniform Yolk-Shell Iron Sulfide−Carbon Nanospheres for Superior Sodium−Iron Sulfide Batteries. *Nat. Commun.* **2015**, *6*, No. 8689.
(24) Douglas, A.; Carter, R.; Oakes, L.; Share, K.; Cohn, A. P.; Pint, C. L. Ultrafine Iron Pyrite (FeS_2) Nanocrystals Improve Sodium−Sulfur and Lithium−Sulfur Conversion Reactions for Efficient Batteries. *ACS Nano* **2015**, *9*, 11156−11165.
(25) Tan, Y.; Wong, K.-W.; Zhang, Z.; Ng, K. M. In Situ Synthesis of Iron Sulfide Embedded Porous Carbon Hollow Spheres for Sodium Ion Batteries. *Nanoscale* **2017**, *9*, 19408−19414.
(26) Wang, Q.; Guo, C.; Zhu, Y.; He, J.; Wang, H. Reduced Graphene Oxide-Wrapped FeS_2 Composite as Anode for High-Performance Sodium-Ion Batteries. *Nano-Micro Lett.* **2018**, *10*, No. 30.
(27) Xiang, J.; Liu, Z.; Song, T. Hierarchical Iron Sulfide-Graphene Nanocubes Consisting of Multiple Nanoparticles with Superior Sodium Ion Storage Properties. *Electrochim. Acta* **2018**, *283*, 683−690.
(28) Bodenez, V.; Dupont, L.; Laffont, L.; R Armstrong, A.; M Shaju, K.; G Bruce, P.; Tarascon, J.-M. The Reaction of Lithium with $CuCr_2S_4$—Lithium Intercalation and Copper Displacement/Extrusion. *J. Mater. Chem.* **2007**, *17*, 3238−3247.
(29) Zhou, J.; Jiang, F.; Li, S.; Xu, Z.; Sun, W.; Ji, X.; Yang, Y. $CuFeS_2$ as an Anode Material with an Enhanced Electrochemical Performance for Lithium-Ion Batteries Fabricated from Natural Ore Chalcopyrite. *J. Solid State Electrochem.* **2019**, *23*, 1991−2000.
(30) Guo, P.; Song, H.; Liu, Y.; Wang, C. $CuFeS_2$ Quantum Dots Anchored in Carbon Frame: Superior Lithium Storage Performance and the Study of Electrochemical Mechanism. *ACS Appl. Mater. Interfaces* **2017**, *9*, 31752−31762.
(31) Ding, W.; Wang, X.; Peng, H.; Hu, L. Electrochemical Performance of the Chalcopyrite $CuFeS_2$ as Cathode for Lithium Ion Battery. *Mater. Chem. Phys.* **2013**, *137*, 872−876.
(32) Wu, X.; Zhao, Y.; Yang, C.; He, G. PVP-Assisted Synthesis of Shape-Controlled $CuFeS_2$ Nanocrystals for Li-Ion Batteries. *J. Mater. Sci.* **2015**, *50*, 4250−4257.
(33) Zhang, Y.; Zhao, G.; Lv, X.; Tian, Y.; Yang, L.; Zou, G.; Hou, H.; Zhao, H.; Ji, X. Exploration and Size Engineering from Natural Chalcopyrite to High-Performance Electrode Materials for Lithium-Ion Batteries. *ACS Appl. Mater. Interfaces* **2019**, *11*, 6154−6165.
(34) Filik, J.; Ashton, A. W.; Chang, P. C. Y.; Chater, P. A.; Day, S. J.; Drakopoulos, M.; Gerring, M. W.; Hart, M. L.; Magdysyuk, O. V.; Michalik, S.; Smith, A.; Tang, C. C.; Terrill, N. J.; Wharmby, M. T.; Wilhelm, H. Processing Two-Dimensional X-Ray Diffraction and Small-Angle Scattering Data in DAWN 2. *J. Appl. Crystallogr.* **2017**, *50*, 959−966.
(35) Yang, X.; Juhas, P.; Farrow, C. L.; Billinge, S. J. L. XPDFsuite: An End-to-End Software Solution for High Throughput Pair Distribution Function Transformation, Visualization and Analysis. 2015, arXiv:1402.3163. arXiv.org e-Print archive. https://arxiv.org/abs/1402.3163 (accessed Feb 23, 2015).
(36) Hall, S. R.; Stewart, J. M. The Crystal Structure Refinement of Chalcopyrite, $CuFeS_2$. *Acta Crystallogr., Sect. B* **1973**, *29*, 579−585.
(37) Pearce, C. I.; Pattrick, R. A. D.; Vaughan, D. J.; Henderson, C. M. B.; van der Laan, G. Copper Oxidation State in Chalcopyrite: Mixed Cu D9 and D10 Characteristics. *Geochim. Cosmochim. Acta* **2006**, *70*, 4635−4642.
(38) Boekema, C.; Krupski, A. M.; Varasteh, M.; Parvin, K.; van Til, F.; van der Woude, F.; Sawatzky, G. A. Cu and Fe Valence States in $CuFeS_2$. *J. Magn. Magn. Mater.* **2004**, *272*−*276*, 559−561.
(39) Li, H.; Wang, Y.; Jiang, J.; Zhang, Y.; Peng, Y.; Zhao, J. CuS Microspheres as High-Performance Anode Material for Na-Ion Batteries. *Electrochim. Acta* **2017**, *247*, 851−859.
(40) Zhu, Y.; Suo, L.; Gao, T.; Fan, X.; Han, F.; Wang, C. Ether-Based Electrolyte Enabled Na/FeS_2 Rechargeable Batteries. *Electrochem. Commun.* **2015**, *54*, 18−22.
(41) Hu, Z.; Zhu, Z.; Cheng, F.; Zhang, K.; Wang, J.; Chen, C.; Chen, J. Pyrite FeS_2 for High-Rate and Long-Life Rechargeable Sodium Batteries. *Energy Environ. Sci.* **2015**, *8*, 1309−1316.
(42) Masadeh, A. S.; Božin, E. S.; Farrow, C. L.; Paglia, G.; Juhas, P.; Billinge, S. J. L.; Karkamkar, A.; Kanatzidis, M. G. Quantitative Size-Dependent Structure and Strain Determination of CdSe Nanoparticles Using Atomic Pair Distribution Function Analysis. *Phys. Rev. B* **2007**, *76*, No. 115413.
(43) Walter, M.; Zünd, T.; V Kovalenko, M. Pyrite (FeS_2) Nanocrystals as Inexpensive High-Performance Lithium-Ion Cathode and Sodium-Ion Anode Materials. *Nanoscale* **2015**, *7*, 9158−9163.
(44) Wang, F.; Robert, R.; Chernova, N. A.; Pereira, N.; Omenya, F.; Badway, F.; Hua, X.; Ruotolo, M.; Zhang, R.; Wu, L.; Volkov, V.; Su, D.; Key, B.; Whittingham, M. S.; Grey, C. P.; Amatucci, G. G.; Zhu, Y.; Graetz, J. Conversion Reaction Mechanisms in Lithium Ion Batteries: Study of the Binary Metal Fluoride Electrodes. *J. Am. Chem. Soc.* **2011**, *133*, 18828−18836.
(45) DiGiuseppe, M.; Steger, J.; Wold, A.; Kostiner, E. Preparation and Characterization of the System Copper Gallium Iron Sulfide ($CuGa_{1-X}Fe_xS_2$). *Inorg. Chem.* **1974**, *13*, 1828−1831.

https://doi.org/10.1021/acsami.1c04946
ACS Appl. Mater. Interfaces 2021, 13, 26034−26045

(46) Ok, H. N.; Baek, K. S.; Choi, E. J. Mössbauer Study of Antiferromagnetic $CuFeS_2$. *Phys. Rev. B* **1994**, *50*, 10327−10330.
(47) Wang, J.; Okabe, J.; Urita, K.; Moriguchi, I.; Wei, M. Cu_2S Hollow Spheres as an Anode for High-Rate Sodium Storage Performance. *J. Electroanal. Chem.* **2020**, *874*, No. 114523.
(48) Yang, Z.; Chen, T.; Wu, C.; Qu, J.; Wu, Z.; Guo, X.; Zhong, B.; Liu, H.; Dou, S. Interpreting Abnormal Charge−Discharge Plateau Migration in Cu_xS during Long-Term Cycling. *ACS Appl. Mater. Interfaces* **2019**, *11*, 3961−3970.

https://doi.org/10.1021/acsami.1c04946
ACS Appl. Mater. Interfaces 2021, 13, 26034−26045

4.2 Synthetically Produced Isocubanite as an Anode Material for Sodium-Ion Batteries: Understanding the Reaction Mechanism during Sodium Uptake and Release

Nach erfolgreicher Synthese und Charakterisierung von $CuFeS_2$ wurden weitere Kupfer-Eisen-Sulfide untersucht, um die Auswirkungen der Stöchiometrie und der Struktur auf die elektrochemischen Eigenschaften und den Reaktionsmechanismus zu erfassen. Isocubanit ($CuFe_2S_3$) ist eine eisenreichere Variante und ist im Hinblick auf die Materialkosten sehr attraktiv. Im Vergleich zu $CuFeS_2$ ist Isocubanit ein eher selten zu findendes Mineral und kommt nur in enger Paragenese vor allem mit Chalkopyrit und Pyrrhotit vor, was die Synthese deutlich erschwert. Aber durch mehrstufige Hochtemperatursynthese mit geringsten Zugaben von zusätzlichem Eisen konnte das Material phasenrein hergestellt werden.

Beim Einsatz als Anodenmaterial zeigte $CuFe_2S_3$ eine exzellente elektrochemische Performanz. Nach 1000 Zyklen wurde bei einer Stromrate von 0.5 A g^{-1} eine Kapazität von 422 mA h g^{-1} erreicht. Um Einblicke in den Reaktionsmechanismus zu gewinnen, wurden einzelne Lade- und Entladestufen des ersten und zweiten Zyklus mittels XRPD untersucht sowie im ersten Zyklus XAS-Messungen durchgeführt. Interessanterweise bilden sich im ersten Entladezyklus zunächst simultan $CuFeS_2$ und $NaFe_{1,5}S_2$. Bei weiterer Na-Aufnahme wird zuerst Cu^+ zu Cu^0 reduziert, gefolgt von der Reduktion von Fe^{2+} zu amorphen Fe^0, was durch XAS- und Magnetmessungen bestätigt werden konnte. Besonders hervorzuheben ist, dass sich während des Ladens nicht $CuFe_2S_3$ zurückbildet, sondern ein Gemisch aus $NaFe_{1.5}S_2$ und einer nicht identifizierbaren neuen Phase. Diese Phase scheint eine essentielle Rolle zu spielen, da im zweiten Zyklus ausgehend von dieser Phase elementares Kupfer gebildet wird, einhergehend mit der Bildung des $NaFe_{1.5}S_2$ Intermediats und der anschließenden Reduzierung des Eisens. Bei der nächsten Ladung verläuft der Mechanismus rückwärts bis wieder die unbekannte Phase erscheint.

Ähnlich zu $CuFeS_2$ ist auch ab Zyklus 135 eine Änderung des Reaktionsmechanismus zu erkennen. Hier bilden sich ebenfalls nanokristalline Intermediate, die einen Einblick in die Änderungen geben können. Dies bestätigt unsere Annahme, dass die Aufrechterhaltung einer gewissen Kristallinität zu einer optimierten Zyklenstabilität führt.

Veröffentlicht in: *ACS Appl. Mater. Interfaces*, **2021**, 13, 58552-58565.
DOI: https://doi.org/10.1021/acsami.1c16814
© 2021 American Chemical Society

ACS APPLIED MATERIALS & INTERFACES

www.acsami.org Research Article

Synthetically Produced Isocubanite as an Anode Material for Sodium-Ion Batteries: Understanding the Reaction Mechanism During Sodium Uptake and Release

Svenja Senkale, Giannantonio Cibin, Alan V. Chadwick, and Wolfgang Bensch*

Cite This: ACS Appl. Mater. Interfaces 2021, 13, 58552−58565 Read Online

ACCESS | Metrics & More | Article Recommendations | Supporting Information

ABSTRACT: Bulk isocubanite ($CuFe_2S_3$) was synthesized via a multistep high-temperature synthesis and was investigated as an anode material for sodium-ion batteries. $CuFe_2S_3$ exhibits an excellent electrochemical performance with a capacity retention of 422 mA h g^{-1} for more than 1000 cycles at a current rate of 0.5 A g^{-1} (0.85 C). The complex reaction mechanism of the first cycle was investigated via PXRD and X-ray absorption spectroscopy. At the early stages of Na uptake, $CuFe_2S_3$ is converted to form crystalline $CuFeS_2$ and nanocrystalline $NaFe_{1.5}S_2$ simultaneously. By increasing the Na content, Cu^+ is reduced to nanocrystalline Cu, followed by the reduction of Fe^{2+} to amorphous Fe^0 while reflections of nanocrystalline Na_2S appear. During charging up to −5 Na/f.u., the intermediate $NaFe_{1.5}S_2$ appears again, which transforms in the last step of charging to a new unknown phase. This unknown phase together with $NaFe_{1.5}S_2$ plays a key role in the mechanism for the following cycles, evidenced by the PXRD investigation of the second cycle. Even after 400 cycles, the occurrence of nanocrystalline phases made it possible to gain insights into the alteration of the mechanism, which shows that Cu_xS phases play an important role in the region of constant specific capacity.

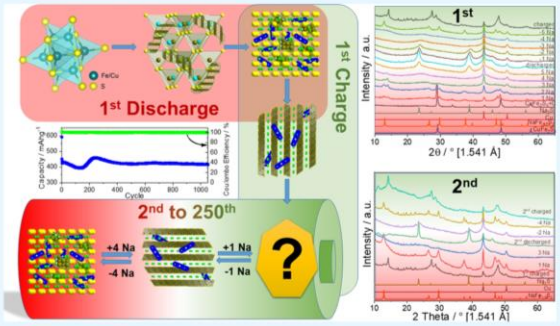

KEYWORDS: *sodium-ion battery, anode material, isocubanite, X-ray diffraction, X-ray absorption spectroscopy, ternary sulfides*

1. INTRODUCTION

To meet the ever-growing demand for power for portable devices and electric vehicles, lithium-ion batteries (LIBs) have been greatly optimized, and they are the state-of-the-art technologies.[1,2] The increasing demand for renewable energy requires effective large scale energy storage devices, and due to the high price and limited availability of Li, alternatives to LIBs in the foreseeable future are needed.[3] One obvious alternative to lithium is sodium, which is one of the most abundant elements and is cheap and environmentally friendly.[4−6] Graphite is the standard anode for commercial LIBs, but it is not suitable for sodium ions without extensive chemical modifications due to slow electrochemical reaction and limited diffusion kinetics.[6,7] Hard carbons have been in the focus of research due to their high initial Coulombic efficiency and stable cycling capacity.[8] In the meantime, energy densities of sodium-ion battery (SIB) full cells of 200 W h kg^{-1} have been achieved, which could compete with commercial LIBs on a graphite/$LiFePO_4$ basis.[9] Hard carbons are promising candidates for anodes in commercial SIBs, but their lower carbon yield, greater irreversible capacity (especially when carbonized at low temperatures), and higher cost compared to the soft carbons used in LIBs still limit further commercialization.[10] Hence, intense research activities are underway to identify the most suitable anode material for SIBs, and until an applicable material for intercalation/deintercalation processes is identified, the main focus is on conversion reactions due to the advantage of higher achievable specific capacity. The metal cations are completely reduced to the metallic state, and more alkali metal cations are converted.[11,12] A drawback of this type of reaction is the limited long-term stability and large voltage hysteresis, which can reduce the energy efficiency and the voltage output.[13] If these hurdles are overcome, this type of battery should be able to compete with the established LIBs. Besides other compounds, transition metal sulfides are in the focus of research (MS_x, M = Fe, Co, Ni, Sn, Mo, Cu, etc.)[14−22] due to the weaker metal sulfur bond compared to the metal oxide bond, leading to improved kinetics. Furthermore, the discharge product Na_2S shows better conductivity[11] compared to Na_2O. Among the metal sulfides, iron sulfides are promising

Received: September 1, 2021
Accepted: November 16, 2021
Published: November 30, 2021

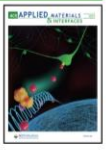

ACS Publications © 2021 American Chemical Society

https://doi.org/10.1021/acsami.1c16814
ACS Appl. Mater. Interfaces 2021, 13, 58552−58565

ACS Applied Materials & Interfaces www.acsami.org Research Article

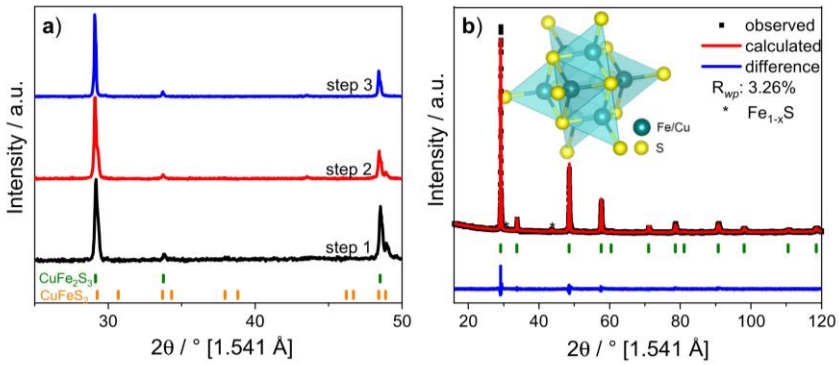

Figure 1. (a) PXRD pattern of the different synthesis steps of $CuFe_2S_3$. (b) Rietveld refinement results against the PXRD pattern of $CuFe_2S_3$. Observed (black markers), calculated (red line), and difference (blue line) profiles are shown. The inset shows the crystal structure.

candidates due to their high natural abundance, low price, nontoxicity, and high theoretical capacity, for example, pyrite (FeS_2)[17,23,24] 894 mA h g^{-1} or greigite (Fe_3S_4)[25,26] 725 mA h g^{-1}. However, pure iron sulfides show a rapid capacity decay caused by the dramatic volume change from 100 up to 200% during the conversion, which leads to contact loss from the collector.[5] A further issue contributing to the capacity decay is the shuttling effect leading to a loss of active material.[27] To overcome these drawbacks, several strategies have been developed, such as designing nanoscopic structures (like flowers[28,29] or spheres[30,31]) due to the better accommodation of large volume change by pulverization or developing composite materials with conductive additives like reduced graphene oxide[32,33] or carbon nanotubes[16,34] to suppress the shuttling effect.[27] In most cases, however, such complex methods are not suitable for large-scale applications or are associated with very high costs.

Analogous to the Fe sulfides, pure Cu sulfides show similar limited stability during cycling accompanied by significant capacity decay.[35−37] Compared to binary sulfides, which have been widely studied, ternary sulfides have not been in focus to a comparable degree, although the ternary element can often exhibit an unexpected positive synergistic effect. For example, $CuCrS_2$[38] or CuV_2S_4[39] showed improved cycling stability without any additives in contrast to Cu_xS where the abovementioned modifications were necessary.[40] Based on these results, we recently investigated $CuFeS_2$ and achieved similar outstanding electrochemical performance as observed for the two ternaries mentioned above.[41] In comparison to the overwhelming number of cases, in which only amorphous products are formed after the first cycle, $CuFeS_2$ showed crystalline phases with coherently scattering domains in the nanoregime after 250 cycles, responsible for the exceptional long-term stability. The promising and outstanding results obtained with $CuFeS_2$ encouraged us to investigate the related compound $CuFe_2S_3$. The questions in focus for the present studies are as follows: (i) Can similar reaction mechanisms be observed during cycling? (ii) How do the different Cu/Fe/S ratios influence the electrochemical behavior? (iii) Are crystalline products generated during discharge and charge? Finally, the costs are reduced by the higher iron content, making $CuFe_2S_3$ interesting as anodes in SIBs.

$CuFe_2S_3$ was investigated as anode material for LIBs,[42] but until now, no report was available for its application as anode material in SIBs. The electrochemical properties as well as the underlying mechanisms have been investigated in a detailed study using ex situ PXRD and X-ray absorption spectroscopy (XAS). The results provide evidence of exceptionally good cycle stability at a high specific capacity.

2. EXPERIMENTAL SECTION

2.1. Synthesis of $CuFe_2S_3$. $CuFe_2S_3$ was synthesized via high-temperature solid-state reaction. Stoichiometric amounts of Cu (Alfa Aesar, 99.9%), Fe (Alfa Aesar, 99.99%), and S (Alfa Aesar, 99.999%) with a total mass of 2 g were mixed and ground in a mortar. The mixture was placed in a quartz tube, which was sealed under vacuum ($<10^{-4}$ mbar). The mixture was heated to 550 °C with a heating rate of 25 °C/h, maintained at that temperature for 1 day, and then heated to 950 °C with a similar heating rate and held for 4 days. The tube was cooled to 800 °C over a period of 8 h and quenched in an ice bath. The samples were removed and ground in an agate mortar in an argon-filled glovebox. Due to $CuFeS_2$ impurities, small amounts of iron (~200 mg) were added and the mixtures were treated under the abovementioned conditions. This step was repeated until a near phase-pure sample of $CuFe_2S_3$ was obtained (Figure 1a).

2.2. Material Characterization. EDX data were obtained with Philips ESEM XL 30 equipped with an EDAX New XL-30 detector (acceleration voltage: 20 kV). Elemental analysis (EA) was performed with EURO VECTOR Instruments EURO EA equipped with a HEKAtech CHNS analyzer.

The PXRD investigations were carried out in transmission and reflection geometry on PANalytical Empyrean with Cu Kα radiation, a focusing mirror, and a PIXcel1D detector.

XAS spectra were collected at the Fe K-edge and the Cu K-edge at the B18 beamline, Diamond Light Source (UK), with a collection time of 3 min at each edge. Each sample was measured three times, and these spectra were averaged. Energy calibration of the raw data was performed using spectra from a Fe or Cu foil.

Analysis of the magnetic properties was performed with Quantum Design PPMS (Physical Property Measurement System) model 600 in the ACMS setup. The investigation was done with magnetic field strengths between 1 and 9 T. The samples were prepared from finely ground powder that was encapsulated into a gelatin capsule.

2.3. Electrochemical Tests. Electrodes were prepared with 70 wt % $CuFe_2S_3$, 20 wt % SUPER C65 Carbon (Timcal, Switzerland), and 10 wt % polyvinylidene difluoride (PVdF, Solvay, Germany) suspended in *N*-methyl-2-pyrrolidone. The mixtures were spread on Cu foils using the doctor-blade casting method. Drying of the electrode foils was carried out in a vacuum oven at 60 °C for 24 h. Afterward, 10 mm discs with about 1.0−0.1.4 mg active material were punched out. Assembly of the Swagelok type cells was carried out in an argon-filled glovebox (water and oxygen contents below 1 ppm) using Na metal as the counter electrode, glass fiber filter disks (Whatman, United Kingdom) and Celgard membranes as the separator, and a solution of 1 M sodium trifluoromethanesulfonate

https://doi.org/10.1021/acsami.1c16814
ACS Appl. Mater. Interfaces 2021, 13, 58552−58565

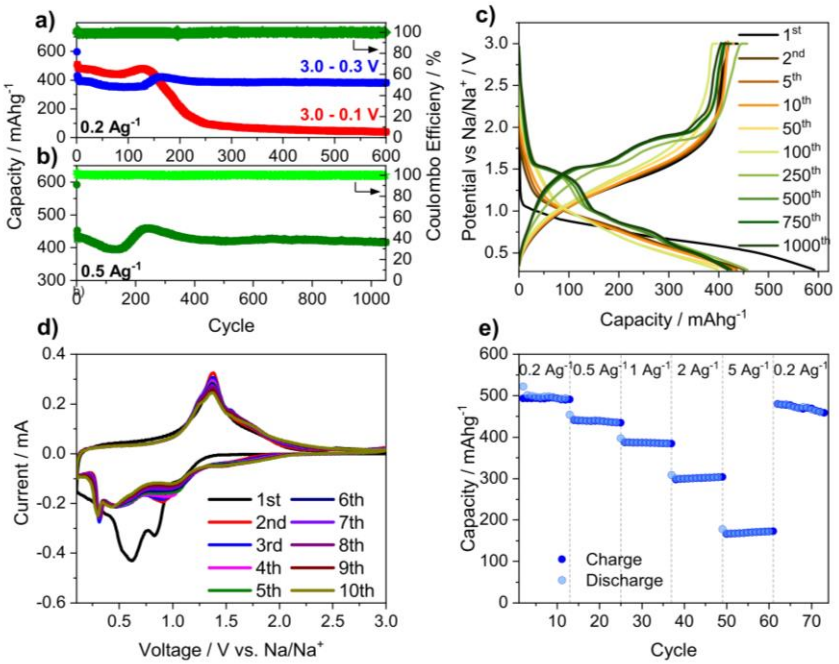

Figure 2. (a) Electrochemical cycling performance and charge efficiency of Na/$CuFe_2S_3$ test cells. A current rate of 0.2 A g^{-1} was applied in the potential windows of 3.0−0.1 V (red) and 3.0−0.3 V (blue). (b) Electrochemical cycling performance and charge efficiency at a current rate of 0.5 A g^{-1} in the potential window of 3.0−0.3 V. (c) Discharge and charge profiles at a current rate of 0.5 A g^{-1} of various cycles. (d) CV analysis in the potential window 3.0−0.1 V for cycles 1 to 10 collected for Na/$CuFe_2S_3$. (e) Rate capability at several current rates from 0.2 to 5 A g^{-1} for $CuFe_2S_3$.

$NaCF_3SO_3$ (Sigma-Aldrich, 98%) in bis(2-methoxyethyl) ether (diglyme, Acros, 99+%, anhydrous) as the electrolyte. Galvanostatic measurements were performed on BST8-WA (MTI Corporation) and BTS 3000 (Neware) battery analyzers. For ex situ measurements, approximately 27 mg of a mixture containing 70 wt % $CuFe_2S_3$ and 30 wt % Super C65 Carbon was pressed into pellets at 5 t/50 mm^2, prepared in Swagelok type cells as described above, and discharged/charged against Na in Swagelok cells with a C/20 rate (MTI BST8-WA). Due to the fact that these powder cells cannot go through more than the first cycle, the second cycle was carried out with the abovementioned film cells. After the distinct Na uptake/release, the electrochemical reaction was interrupted and the cells were disassembled in an argon-filled glovebox. The pellets were recovered and washed with anhydrous bis(2-methoxyethyl)ether (diglyme) and dried for 24 h. For the investigation of the alteration of the reaction mechanism, the active material was transferred from the 10 mm disc by using self-adhesive Kapton foil and measured in transmission, which leads to a very high background, especially at small angles.

For the galvanostatic intermittent titration technique (GITT) experiment, a current pulse duration of 10 min with a current of 0.11 A corresponding to C/10 was applied. After each pulse, a relaxation time of 120 min was used to reach quasi-equilibrium potentials. This procedure was conducted in the potential range of 0.1−3.0 V.

Cyclovoltammetric measurements were done with Zahner XPot at a scan rate of 0.1 mV s^{-1} between 0.01 and 3.00 V.

3. RESULTS AND DISCUSSION

3.1. Characterization of Pristine $CuFe_2S_3$ (Isocubanite). Isocubanite is the high-temperature cubic polymorph of the orthorhombic $CuFe_2S_3$ (cubanite). It crystallizes in the cubic space group $F\bar{4}3m$. The structure can be described as cubic close-packed S^{2-} anions with metal cations occupying randomly half of the two structurally equivalent tetrahedral sites 4c (1/4, 1/4, and 1/4) and 4d (3/4, 3/4, and 3/4). In nature, both polymorphs are usually found intimately intergrown with other sulfides, preferably chalcopyrite ($CuFeS_2$) and pyrrhotite.[43−45] This could possibly be the reason why it has not yet been possible to synthesize phase-pure isocubanite via high-temperature synthesis.[46,47] The PXRD patterns of the individual steps during the synthesis (Figure 1a) demonstrate that the (204) reflection at 49.0° of $CuFeS_2$ decreases with each annealing step until it is no longer visible, resulting in almost phase-pure isocubanite. The Rietveld refinement of the PXRD pattern of the sample of the last heat treatment exhibits a very good fit (R_{wp} = 3.26%) and only a very low impurity of $Fe_{1-x}S$ of 3.3% is observed (Figure 1b). The lattice parameter a = 5.3045(9) Å is in good agreement with recently published data.[44] Detailed refinement parameters are listed in Table S1.

The EDX measurement (Table S2) yields a stoichiometric Cu/Fe ratio close to 1:2 while the S content is slightly too small, which is caused by the low energy of the S Kα emission line. An additional EA was performed (Table S3), and by taking the results of both analyses into account, the composition is $Cu_1Fe_{1.93}S_{2.96}$.

3.2. Electrochemical Characterization. Long-term galvanostatic cycling performed within a potential window 3−0.1 V by applying a current rate of 0.2 A g^{-1} (=0.34 C) (Figure 2a, red curve) resulted in a discharge capacity of 748 mA h g^{-1} in the first cycle, which is slightly higher than the theoretical capacity of 592 mA h g^{-1}; the excess capacity is presumed to arise from solid electrolyte interphase (SEI) formation as shown in related systems.[48] After the 1st cycle, there is a slight decrease from 480 mA h g^{-1} (~4.9 Na/f.u.) to 440 mA h g^{-1}

https://doi.org/10.1021/acsami.1c16814
ACS Appl. Mater. Interfaces 2021, 13, 58552−58565

ACS Applied Materials & Interfaces www.acsami.org Research Article

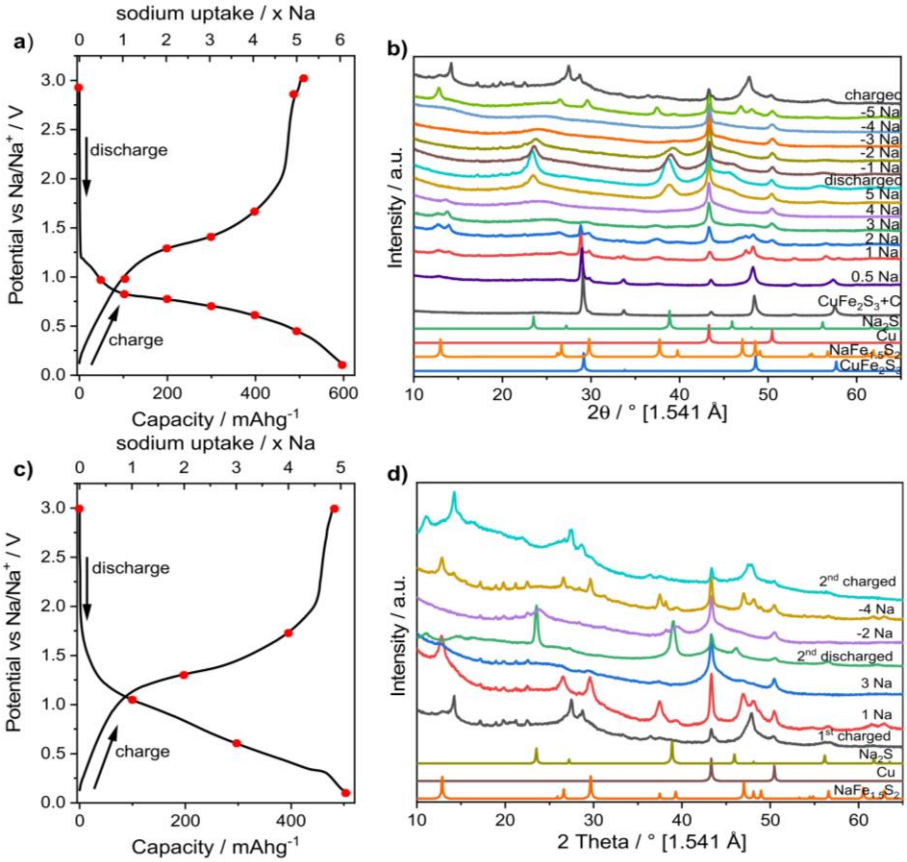

Figure 3. (a) Discharge/charge profile of the first cycle of the Na/$CuFe_2S_3$ powder electrode. (b) Ex situ PXRD patterns of the Na/$CuFe_2S_3$ electrode collected at several states of discharge/charge compared to simulated patterns for Na_2S, $CuFe_2S_3$, $NaFe_{1.5}S_2$, and Cu. (c) Discharge/charge profile of the second cycle of the Na/$CuFe_2S_3$ powder electrode. (d) Ex situ PXRD patterns of the Na/$CuFe_2S_3$ electrode collected at several states of discharge/charge from the second cycle compared to simulated patterns for Na_2S, $NaFe_{1.5}S_2$, and Cu. The red dots in (a,c) present the cycling points for X-ray data collection.

(~4.5 Na/f.u.) until cycle 90 before the curve passes through a maximum at cycle 130 with 478 mA h g^{-1} (~4.8 Na/f.u.). From cycle 150 onward, continuous capacity fading occurred. For this reason and based on previous experience, the potential window has been limited to 3−0.3 V (Figure 2a, blue curve).[41] A similar behavior is observed but with a slightly lower capacity of 352 mA h g^{-1} (~3.6 Na/f.u.). From cycle 130 onward, a maximum is reached before a constant capacity of 389 mA h g^{-1} (~3.94 Na/f.u.) is observed from cycle 225 to over 600 cycles. Even at a rate of 0.5 A g^{-1}, high cycle stability of more than 1000 cycles is achieved with a capacity of 422 mA h g^{-1} (~4.27 Na/f.u.) (Figure 2b). After the first cycle, the Coulombic efficiency reached nearly 100% in all curves.

Selected galvanostatic discharge−charge profiles are shown in Figure 2c for the small potential window at 0.5 A g^{-1} (Figure S1 for the large potential window). In the first discharge curve, no well-resolved plateau can be observed and just a pseudo plateau developed from 1.05 to 0.5 V, followed by a slightly faster decrease until a limiting voltage of 0.3 V is reached. The subsequent cycles are very similar to each other until cycle 10. These observations are confirmed by the cyclovoltammograms (CVs) (Figure 2d). The first discharge curve shows a broad and intensive signal from 1.08 to 0.37 V, which is composed of four different signals at 1.08, 0.83, 0.61, and 0.37 V. The subsequent cycles are similar to each other and show three different signals, at 0.90 V (shifting to 1.02 V during cycling), a broad peak at 0.43, and a sharp signal at 0.30 V. The profiles of the charging curves 1−10 are very similar, with the potential showing a constant increase from 0.5 to 1.7 V, which is reflected in a broad peak in the CV. However, it can be seen in the CV that two shoulders develop at 1.25 and 1.54 V after the first cycle. After cycle 100, a clear change in the galvanostatic curves can be seen, which corresponds with the beginning increase in the cycling curve. Two pseudo-plateaus form in the discharge curve at approximately 1.5 and 0.9 V. There are also two plateaus in the charging curve at 1.5 and 1.8 V that are visible. These alterations indicate a change in the reaction mechanism, which will be discussed in detail in chapter 3.4. After ≈400 cycles, the curve remains unchanged, which indicates a constant and stable mechanism.

The rate performance test delivered reversible capacities of 497, 439, 387, 301, and 170 mA h g^{-1} for current densities of 0.2, 0.5, 1, 2, and 5 A g^{-1}, respectively (Figure 2e). When the current density is reset to 0.2 A g^{-1}, a capacity of 470 mA h g^{-1} could be recovered, which is an outstanding performance for conversion materials especially compared to the corresponding binary compounds.

https://doi.org/10.1021/acsami.1c16814
ACS Appl. Mater. Interfaces 2021, 13, 58552−58565

ACS Applied Materials & Interfaces www.acsami.org Research Article

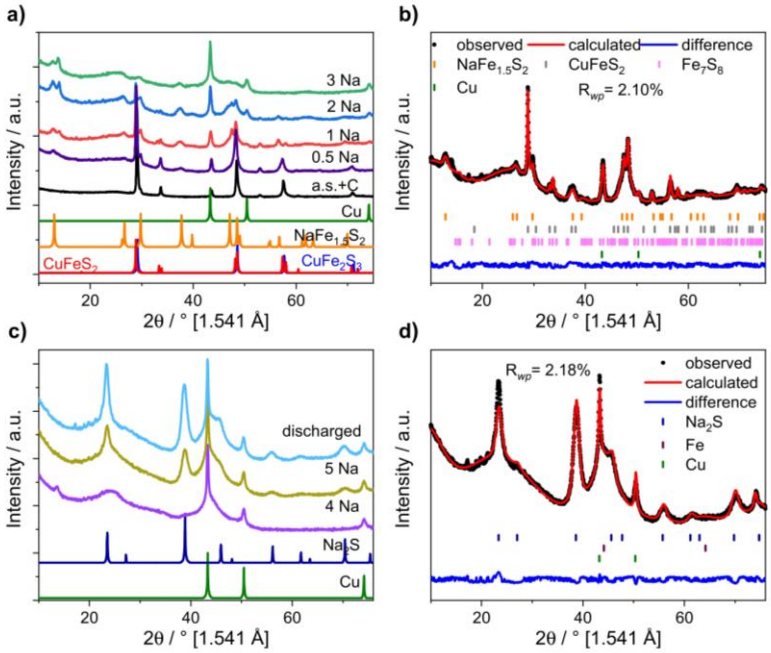

Figure 4. (a) Ex situ PXRD patterns of $Na/CuFe_2S_3/C65$ powder cells with 0−3 Na/f.u. compared to simulated data of $CuFe_2S_3$, $NaCuFeS_2$, and Cu. (b) Rietveld refinements of the PXRD pattern of $CuFe_2S_3$ at sodium uptake of 1 Na/f.u. Observed (black line), calculated (red line), and difference (blue line) profiles. Vertical bars indicate the positions of Bragg reflections. (c) Ex situ PXRD patterns of $Na/CuFe_2S_3/C65$ powder cells with 4 Na/f.u. fully discharged compared to simulated data of Na_2S and Cu. (d) Rietveld refinements of the PXRD pattern of $CuFe_2S_3$ in the discharged state.

3.3. Ex Situ PXRD Investigation of the Sodium Storage Mechanism. The PXRD patterns were collected after charging and discharging processes of the first and second cycles interrupted at defined points of Na uptake and release (Figure 3). For the first cycle, pressed powder cells were used, and the second cycle was carried out with film electrodes. The electrochemical profiles of powder and film cells are very similar, evidencing identical reaction mechanisms (Figure S2), and only the initial discharge capacity is larger in the film cells. Due to the different mass loadings of the electrodes (powder electrodes:~37.6 mg vs foil electrodes: ~1.42 mg), we assume that the difference in the discharge capacity results in a mixture of Na^+ transport limitations as well as in a varying degree of SEI formation. The PXRD pattern of the $CuFe_2S_3/C65$ slurry homogenized in a ball mill shows additional reflections of Fe_7S_8, which is formed by the energy input of the milling process. However, this impurity disappears after the first discharge.

During uptake of 0.5 Na/f.u., reflections of $CuFe_2S_3$ increase, while reflections of a new crystalline phase emerge, which closely resembles the structure of $CuFeS_2$ with space group $I\bar{4}2d$ until after the uptake of 1 Na/f.u., just reflections of $CuFeS_2$ remains. However, Rietveld refinements yield larger lattice parameters a = 5.415(1) Å and c = 10.499(3) Å [V = 307.9(1) Å^3] compared to a = 5.289(1) Å and c = 10.423(1) Å (V = 291.6 Å^3) (Figure 4b).[49] A possible explanation is that during Na uptake, $CuFe_2S_3$ may convert from $F\bar{4}3m$ to $I\bar{4}2d$. This would explain the still high crystallinity compared to the additional appearing phase of $NaFe_{1.5}S_2$, showing no relation to the pristine structure (Figure 4a). This phase increases up to 2 Na/f.u. until it disappears completely after 4 Na/f.u. The amount of $CuFeS_2$ decreases steadily, and reflections are absent after 3 Na/f.u. Simultaneously, Cu^+ is reduced to metallic Cu as evidenced by the (111) and (200) reflections located at 43.3° and 50.4° (Figure 4a).

A single reflex at 13.6° is conspicuous, which cannot be assigned to any compound. This only occurs in connection with the $NaFe_{1.5}S_2$ structure. Due to the layered structure (Figure S3) in which sodium occupies the octahedral sites in the "van der Waals gap," it is possible that this is an additional layer reflex caused by differently filled domains within the structure.

For 5 Na/f.u., broad reflections located at 23.4° and 38.7° appear, which can be assigned to nanocrystalline Na_2S. The intensity of the reflections increases until complete discharge (Figure 4c). The PXRD pattern of the completely discharged electrode shows only reflections of Na_2S and Cu with estimated particle sizes of ≈6 and 16 nm (Figure 4d and Table S4). The intensity ratio of the (111) and (200) reflections of Cu (3.6) deviates significantly from the theoretical value of 1.6.[50] This larger ratio can be explained by preferential growth in the direction of the {111} faces or as a preferred orientation arising from the anisotropic particle shape (Table S5).

As observed for FeS_2, the chemical state of Fe during the discharge stage cannot be unambiguously explained.[51] Notably, by increasing the Na content, the background of the PXRD pattern becomes more and more modulated. Even though no reflections of elemental Fe can be seen, including nanosized Fe (estimated size: 1−2 nm) in the Rietveld refinement clearly improved R_{wp} (Figure S4). Chemically, $Fe^{2+/3+}$ must be reduced to explain the achieved specific capacity. This is the reason why we assume the formation of highly nanoscopic iron particles and integrate it into the refinements of the fully

https://doi.org/10.1021/acsami.1c16814
ACS Appl. Mater. Interfaces 2021, 13, 58552−58565

ACS Applied Materials & Interfaces www.acsami.org Research Article

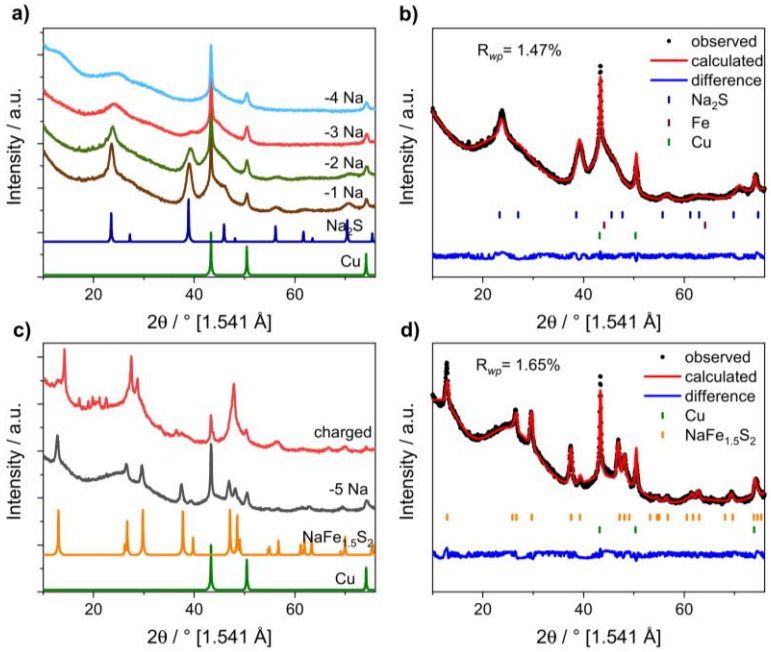

Figure 5. (a) Ex situ PXRD patterns of $Na/CuFe_2S_3/C65$ powder cells during charge from −1 to −4 Na/f.u. compared to simulated data of Na_2S and Cu. (b) Rietveld refinements of the PXRD pattern of $CuFe_2S_3$ at sodium release of 2 Na/f.u. Observed (black line), calculated (red line), and difference (blue line) profiles are shown. The vertical bars indicate the positions of Bragg reflections. (c) Ex situ PXRD patterns of $Na/CuFe_2S_3/C65$ powder cells during charge from −5 Na/f.u. to full charge compared to simulated data of $NaFe_{1.5}S_2$ and Cu. (d) Rietveld refinements of the PXRD pattern of $CuFe_2S_3$ at sodium release of 5 Na/f.u.

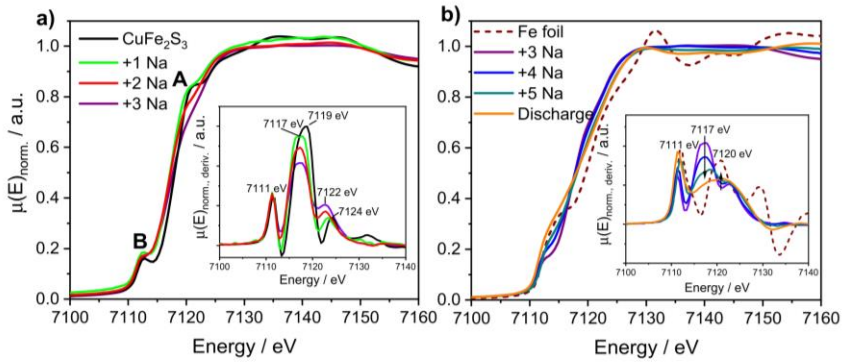

Figure 6. (a) Ex situ XANES spectra at the Fe K-edge with the corresponding first derivatives (inset) of discharge until −3 Na/f.u. and (b) up to the complete discharge.

discharged state and at the release of 2 Na/f.u. This is not unusual, as iron produces many nuclei due to its slow diffusion, which leads to smaller and more finely distributed particles, whereas copper can form larger particles due to its higher diffusivity.[52] To confirm the formation of the elemental Fe, a magnetic hysteresis curve was measured at 5 K from the fully discharged sample. The sample shows ferromagnetic-type curves demonstrated by the presence of the hysteresis loop (Figure S5). The value for the saturation magnetization M_s was found to be 52.9 emu g^{-1}. This large value is just explainable with the presence of elemental iron due to the fact that neither iron sulfides[53−55] nor copper iron sulfides[53,56] or Cu[57] exhibit such large M_s values. The magnetic moment (n_B) in Bohr magneton (μ_B), can be calculated by using the relation[58]

$$n_B = (M_W \times M_S)/5585 \quad (1)$$

From the calculated value of 2.4 μ_B per Fe atom (Table S6), it can be concluded that almost all Fe must have been reduced to elemental Fe. A higher value compared to an expected value of 2.2 for bulk Fe was also observed in Fe clusters with a size of 1−5 nm.[59] In addition, the contribution of Cu^0 was neglected due to the low value.

During charging, the reflections of Na_2S decrease continuously until they disappear completely at 4 Na/f.u. Meanwhile, the intensity of the reflections of Cu remains constant, that is, Fe must be oxidized to Fe^{2+} (Figure 5a). At 2 Na/f.u., Rietveld refinements with just Cu, Fe, and Na_2S resulted in a good fit with R_{wp} = 1.47% (Figure 5b). For release >5 Na/f.u., a crystalline phase appears with a pattern corresponding to

https://doi.org/10.1021/acsami.1c16814
ACS Appl. Mater. Interfaces 2021, 13, 58552−58565

ACS Applied Materials & Interfaces www.acsami.org Research Article

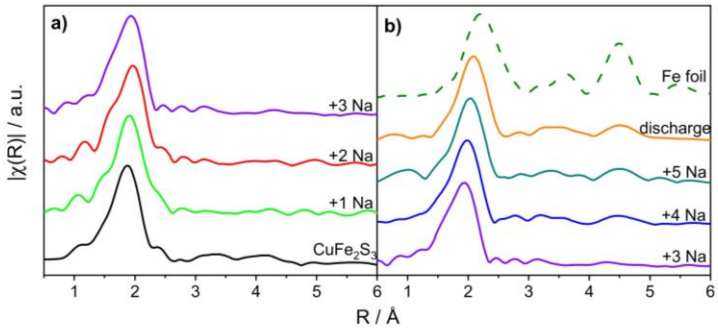

Figure 7. EXAFS R-space plots for Fe absorber atoms of (a) discharge states up to 3Na/f.u. and (b) up to the complete discharge.

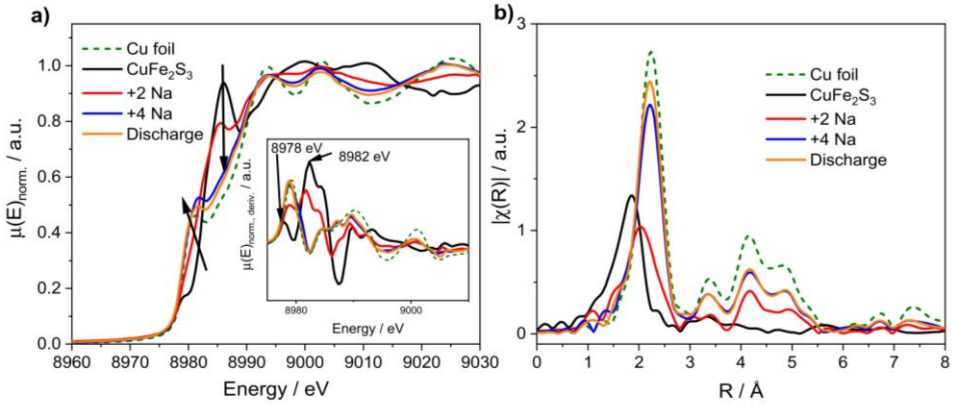

Figure 8. (a) Ex situ XANES spectra at the Cu K-edge with the corresponding first derivatives (inset) and (b) EXAFS R-space plots for Cu absorber atoms of the pristine $CuFe_2S_3$ and various states of discharge.

$NaFe_{1.5}S_2$ (Figure 5c), and reflections of Cu are also present. The Rietveld refinements resulted in a consistent fit with estimated particle sizes of 14 nm for $NaFe_{1.5}S_2$ and 19 nm for Cu (Figure 5d). Only in the last step of charging, Cu is partially oxidized, resulting in the formation of an unknown structure (Figure 5c). Due to the nanocrystalline nature and the overlapping reflections of several phases, it is not possible to identify the unknown phase.

However, this unknown phase seems to play an important role in the mechanism, as indicated by analyzing the reaction mechanism of the second cycle (Figure 3d). The mechanism after the first cycle thus seems to proceed as follows: starting with the unknown phase, Cu is reduced first with simultaneous formation of the $NaFe_{1.5}S_2$ intermediate. Further Na insertion leads to reduction of Fe cations to the elemental state and disappearance of $NaFe_{1.5}S_2$ at ≈5 Na/f.u., and nanocrystalline Na_2S is formed. The amount of Na_2S decreases during charging and no reflections can be detected at the release of 3 Na/f.u., and for >4 Na/f.u., $NaFe_{1.5}S_2$ is formed again, which is accompanied by the oxidation of Fe^0 to Fe^{2+} (Figure 3d). In the last step, Cu is almost completely oxidized to Cu^+ and the reflections of the unknown phase appear again in the PXRD pattern (Figure 3d). These findings imply a sodium shuttle of 5 Na/f.u., resulting in a capacity of 493 mAh g^{-1}, agreeing very well with the experimental results of the first cycles (480 mA h g^{-1}).

3.4. Ex Situ XAS Investigation of the Sodium Storage Mechanism. The Fe K-edge of the pristine $CuFe_2S_3$ is located at 7118 eV, a characteristic pre-edge feature at 7112 eV **B** together with a shoulder **A** (Figure 6a). The pre-edge structure **B** arises in tetrahedrally coordinated iron sulfides from the Fe 3d−S 4p mixing. Similarly, shoulder **A** at 7121 eV corresponds to transitions to hybridized Fe 4s−S 3p states as shown in band-structure calculations in tetrahedrally coordinated Fe-(II)−S systems[60,61] After uptake of 1 Na/f.u., the Fe−K edge is shifted to a lower energy of 7117 eV, indicating a reduction of Fe^{3+}. The pre-edge feature is still observable, suggesting that Fe still occupies a tetrahedral and/or noncentrosymmetric site like in $CuFeS_2$ or $NaFe_{1.5}S_2$. While the intensity of the pre-edge decreases at 2 Na/f.u., further Na uptake results in slow disappearance of both the pre-edge feature and the signal **A**. Simultaneously, the intensity of the Fe-K edge at 7112 eV increases, indicating a reduction of Fe^{2+} to Fe^0 (Figure 6b). The XANES spectrum continuously changes up to the complete discharge explainable by the slow reduction of remaining Fe^{2+} cations. Compared to the reference Fe foil, the Fe K-edge of the discharged sample shows almost no oscillatory structures post-edge. This is not surprising due to the fact that the reference foil is highly crystalline body-centered cubic (bcc)-Fe, while the Fe formed during the discharge process is amorphous and disordered. Similar observations were made for amorphous iron and amorphous alloys.[62,63]

The first peak in the extended X-ray absorption fine structure (EXAFS) real (R)-space plot (Figure 7) of pristine $CuFe_2S_3$ located at 1.87 Å is assigned to the Fe−S bond, the small shoulder at 2.36 Å may be attributed to the Fe-(Cu/Fe) distance, and the two broadened signals at 3.28 and 4.11 Å

https://doi.org/10.1021/acsami.1c16814
ACS Appl. Mater. Interfaces 2021, 13, 58552−58565

ACS Applied Materials & Interfaces www.acsami.org Research Article

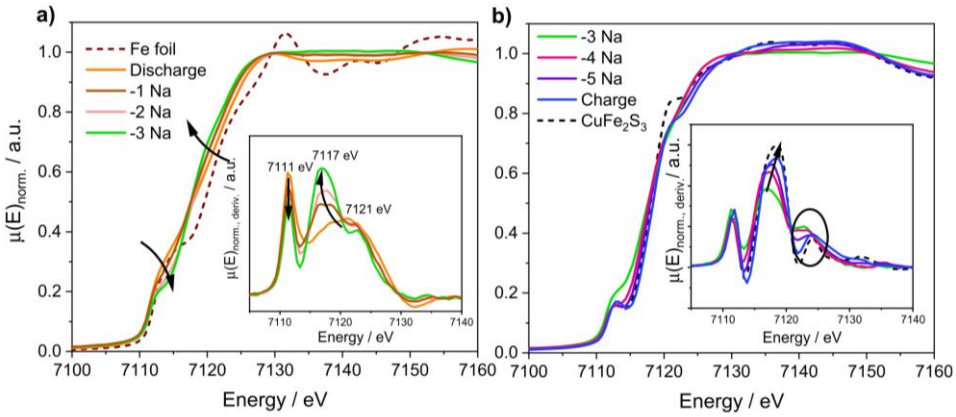

Figure 9. (a) Ex situ XANES spectra at the Fe K-edge with the corresponding first derivatives (inset) of discharge until −3 Na/f.u. and (b) up to the complete charge.

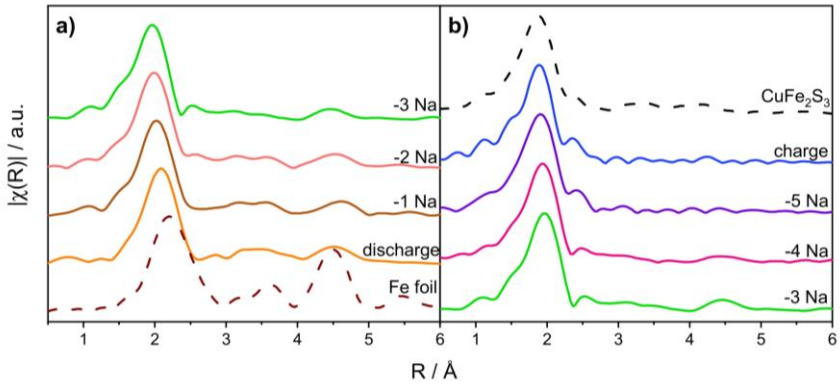

Figure 10. EXAFS R-space plots for Fe absorber atoms of (a) charge states up to −3 Na/f.u. and (b) up to the complete charge.

correspond to the Fe−Fe/Cu and Fe−S bonds of further coordination shells (Figure 7a), respectively. During discharge, the first signal shifts to 2.08 Å, which is close to the first peak shown for the reference Fe foil at 2.20 Å. Continuing with the discharge process, structures at 3.62 and 4.49 Å increase in intensity, corresponding with the higher coordination shell signals displayed by the reference metallic foil Fe (Figure 7b), supporting the interpretation of the formation of a disordered/nanocrystalline Fe^0 phase.

The evolution of the Cu K-edge during the discharge process is displayed in Figure 8. The main edge feature of pristine $CuFe_2S_3$ is located at 8982 eV, which agrees with the value reported for Cu^+ and is assigned to the Cu 1s → 4p electric dipole that allowed the transition to a maximum of the p-projected density of states.[64,65] A pre-edge feature at 8978 eV is discussed in the literature as a signal associated with the presence of holes in the Cu 3d orbitals, that is, the Cu cations have some $3d^9$ character,[66,67] which may also be the case for $CuFe_2S_3$. The observation of this pre-edge was made for $CuFeS_2$ as well.[68]

At 2 Na/f.u., features of both Cu^+ in a non-centrosymmetric environment and Cu^0 can be recognized. During further discharge, the white line of $CuFe_2S_3$ disappears and the Cu K-edge at 8979 eV increases, indicating the reduction to elemental Cu. For >4 Na/f.u., the spectrum is quite similar to that of elemental Cu and there is no significant alteration until full discharge. The results demonstrate that between 3 and 4 Na/f.u., Cu^+ was completely reduced to Cu^0, which confirms the interpretation of the XRD data (Figure 8a).

The Cu-K edge EXAFS R-space plots of $CuFe_2S_3$ shows one clear first shell signal at 1.87 Å (Figure 8b). At 2 Na/f.u., the EXAFS structure evolves approaching elemental Cu. The signal of the first coordination shell is now observed at longer distances, indicating that contributions related to the first coordination shell of face-centered cubic (fcc) Cu and remaining Cu−S bonds overlap. The evolution of the series proceeds until at 4 Na/f.u. and at full discharge all signals agree very well with those of metallic Cu. Cu is then completely reduced and exhibits a remarkable degree of crystallinity compared to Fe (Figure 8b). This observation is in line with the PXRD data discussed above.

During the charging process, the Fe K-edge feature at 7111 eV decreases, indicating oxidation of Fe^0. Additionally, the position of the absorption edge shifts to 7117 eV, which is a typical value for Fe^{2+} (see above) (Figure 9a). For Na removal at ≥4 Na/f.u., the pre-edge signal at 7112 eV forms again, indicating the formation of a tetrahedral environment for the Fe cations. In the last steps, we observe a further shift to higher energy, suggesting partial oxidation of Fe^{2+} to Fe^{3+} and recovery of an overall spectral structure closely resembling the pristine $CuFe_2S_3$ (Figure 9b), with the exception of lower intensity for the shoulder previously mentioned at 7121 eV.

https://doi.org/10.1021/acsami.1c16814
ACS Appl. Mater. Interfaces 2021, 13, 58552−58565

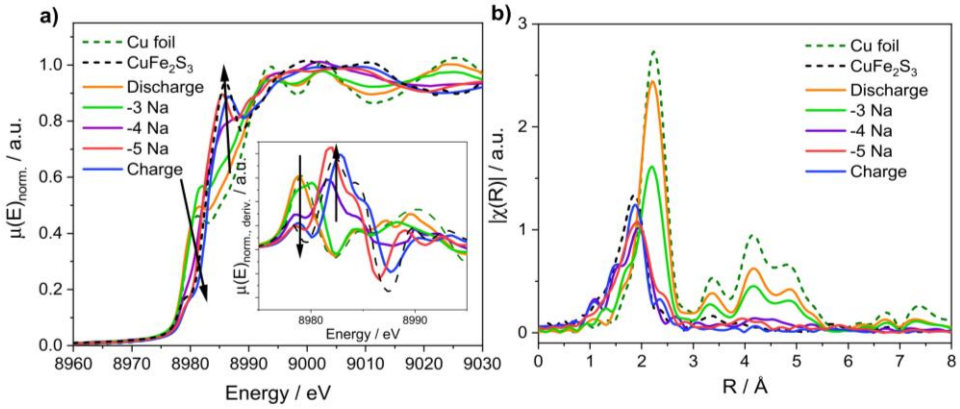

Figure 11. (a) Ex situ XANES spectra at the Cu K-edge with the corresponding first derivatives (inset) and (b) EXAFS R-space plots for Cu absorber atoms of the pristine $CuFe_2S_3$ and various states of charge.

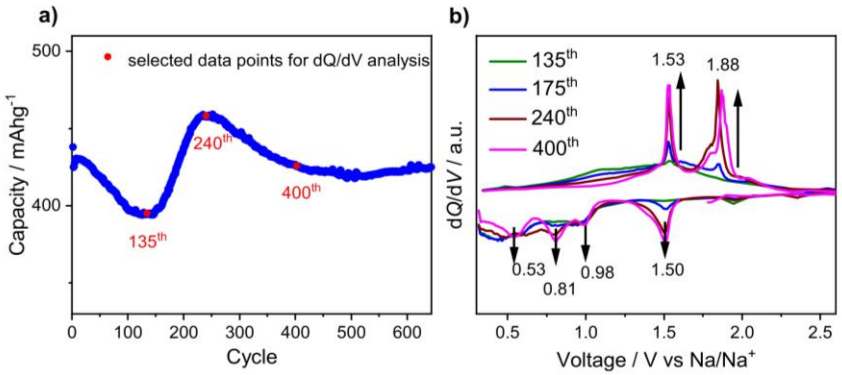

Figure 12. (a) Electrochemical cycling performance in which the selected data points for dQ/dV are highlighted. (b) dQ/dV analysis of selected cycles; the arrows indicate the development of signals during cycling.

The Fe K-edge EXAFS R-plot sequence (Figure 10) shows a clear shift of the first shell peak positions from 2.10 to 1.96 Å and the decrease of the bcc-Fe assigned distance at 4.51 Å for Na removal up to 3 Na/f.u. These findings demonstrate that the amount of elemental Fe decreases and shorter bonds (Fe−S-like) are formed. With further charging, there are only small shifts of the first shell distances to shorter values, which means that there are no significant alterations in the local environment.

For the Cu K-edge, changes are only seen for the release of 4 Na/f.u (Figure 11a). At this stage, the Cu K-edge at 8979 eV decreases abruptly and the main feature shifts to 8982 eV, caused by oxidation of Cu to Cu^+. The pre-edge feature also slowly appears but not as intense as for pristine $CuFe_2S_3$. It can be assumed that after the release of 4 Na/f.u., both Cu^+ and Cu^0 are present, which was not evident from the PXRD data where an intense reflection of Cu is still visible at this stage. The same holds for −5 Na/f.u., but the XANES data show that Cu in large part is already in the oxidized form. The transition at 8986 eV building after the release of 5 Na/f.u. is very evident and is an indication of the tetrahedral environment of Cu. EXAFS supports this conclusion because Cu^0 associated peak positions associated with Cu^0 (at 3.37, 4.17, and 4.85 Å) have almost completely disappeared after the release of 4 Na/f.u. In addition, the position of the first coordination shell shortens from 2.21 to 1.87 Å by Cu−S bond formation (Figure 11b). No other distinct structures are visible, indicating a highly disordered nanoscopic material.

3.5. Investigation of Alterations in the Storage Mechanisms at Later Cycling Stages. The cycle performance curve shows a clear change in capacity during cycling until a nearly constant reversible capacity of 423 mA h g^{-1} is achieved from cycle 400 onward (Figure 12a). Such behavior occurs if the reaction mechanism changes, which can be seen clearly in the dQ/dV curves shown in Figure 12b.

After the first cycle showing reduction signals at 1.50, 0.98, 0.81, and 0.53 V and oxidation events at 1.53 and 1.88 V and the latter exhibiting a shoulder at 1.80 V, the first significant changes occur in cycle 175, which is the beginning of the slope to the maximum in the cycling curve. The intensity of these signals reaches its maximum at cycle 240, which corresponds to the maximum in the cycling performance curve. Reduction signals develop at 1.50, 0.98, 0.81, and 0.53 V, while two very pronounced oxidation signals emerge at 1.53 and 1.88 V. Afterward, only slight alterations could be recognized during the further cycling (small shift of the oxidation signal at 1.88 V to higher potentials).

To gain insights into the reaction mechanisms, the test cells were stopped at the pre-maximum (135th cycle), at the maximum (240th cycle) of the specific capacity curve, and in the constant capacity region (400th cycle) in both discharged

https://doi.org/10.1021/acsami.1c16814
ACS Appl. Mater. Interfaces 2021, 13, 58552−58565

ACS Applied Materials & Interfaces www.acsami.org Research Article

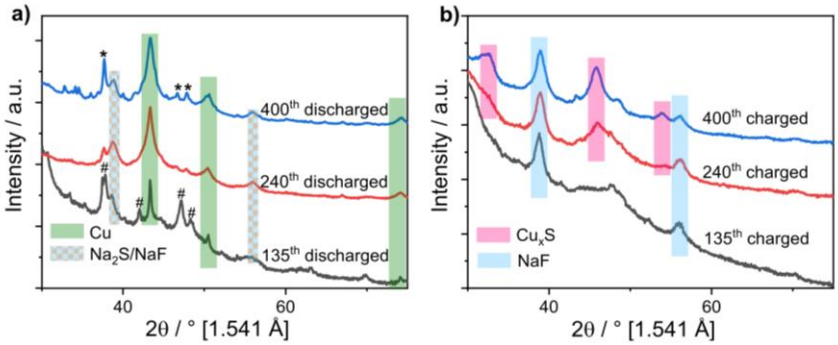

Figure 13. (a) PXRD patterns of the electrode at cycles 135, 240, and 400 in the discharged states [Cu (green square), Na_2S, and NaF (blue/orange square)]. (b) PXRD patterns of the electrode at cycles 135, 240, and 400 in the charged states [Cu_xS (pink square) and NaF (blue square)].

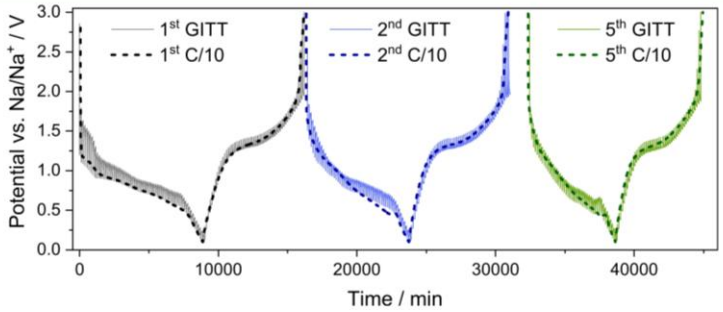

Figure 14. GITT curves of the 1st, 2nd, and 5th cycles of $CuFe_2S_3$ shown with representative C/10 traces. GITT was obtained by applying a current pulse of 10 min and a relaxation time of 120 min.

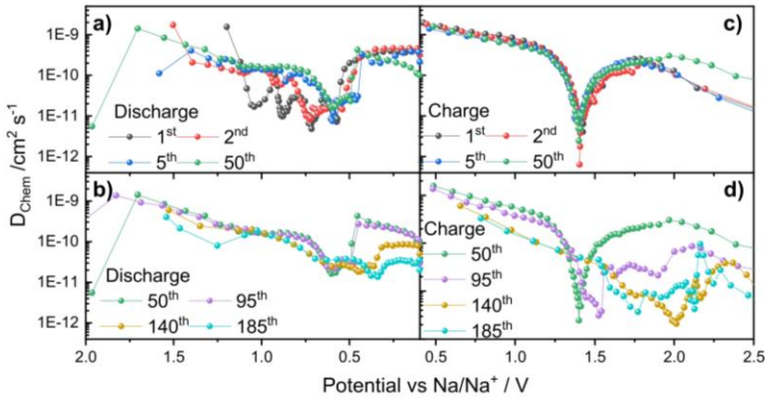

Figure 15. Alteration of chemical diffusion coefficients at different voltages calculated for the 1st, 2nd, 5th, 50th, 95th, 140th, and 185th GITT cycles. (a) Discharge 1st, 2nd, 5th, and 50th, (b) charge 1st, 2nd, 5th, and 50th, (c) discharge 50th, 95th, 140th, and 185th, and (d) charge 50th, 95th, 140th, and 185th.

and charged states, and the products were examined by PXRD (Figure 13).

In the discharged state, reflections of elemental nanocrystalline Cu, Na_2S, and NaF are identified in all three cycles (135, 240, and 400). In the PXRD pattern of the sample recovered in the 135th cycle, an additional crystalline phase appears (*marked with a hash sign*), which is quite similar to the structure of $NaCu_XFe_XS_2$ (space group $P\bar{3}m1$) (see also Figure S6). In the 240th cycle, the intensity of the reflections of this phase decreased strongly and the positions shifted to smaller scattering angles and increased again strongly in the 400th cycle (*marked with asterisks*).

In the charged state (135th cycle), only reflections of NaF are present, which has been formed by a side reaction with the electrolyte and does not take part in the redox reaction. However, in the 400th cycle, new reflections developed, which can be assigned to Cu_xS phases (Cu_2S and/or $Cu_{7.2}S_4$). Neither in the charged nor in the discharged state reflections of Fe related phases can be identified, but the specific capacity requires that Fe participates in the chemical reaction.

https://doi.org/10.1021/acsami.1c16814
ACS Appl. Mater. Interfaces 2021, 13, 58552−58565

3.6. Results of GITT Measurement. GITT was performed to investigate the kinetics during the diffusion of Na^+ in $CuFe_2S_3$. It is especially interesting to observe the change in diffusion depending on the strong decrease in the particle size from a bulk to a nanocrystalline material, which occurs during the first cycle. GITT measurements of cycles 1, 2, 5, 50, 95, 140, and 185 were performed.

The 1st, 2nd, and 5th GITT cycles compared to representative constant current (CC) traces also measured at C/10 are shown in Figure 14. The GITT curves match well with the CC curves, clearly demonstrating that the same chemical processes occur. The diffusion coefficient of Na^+ in $CuFe_2S_3$ as a function of voltage can be determined by solving Fick's second law of diffusion described in eq 2. If very short current pulses are applied, the cell voltage is linearly proportional to the charge/discharge time $\tau^{1/2}$ and eq 2 can be simplified to eq 3.[69−71]

$$D_{\text{chem}} = \frac{4}{\pi}\left(\frac{m_B V_M}{M_B A}\right)^2 \left(\frac{\Delta E_S}{t\left(\frac{dE_\tau}{d\sqrt{t}}\right)}\right)^2 \qquad \text{if } (t) \ll \frac{L^2}{D_{\text{chem}}} \tag{2}$$

$$D_{\text{chem}} = \frac{4}{\pi}\left(\frac{m_B V_M}{M_B A}\right)^2 \left(\frac{\Delta E_S}{t(\Delta E_\tau)}\right)^2 \tag{3}$$

where m_B, M_B, and V_M are the mass loading (g), molecular weight (g mol^{-1}), and molar volume (cm^3 mol^{-1}) of the active material, respectively. A is the contact area between the electrolyte and the active material and was estimated from the electrode geometrical area. ΔE_S and ΔE_τ are the potential changes after subtraction of the IR drop, between two quasi-equilibrium potentials and during the interval of a current pulse as illustrated in ref 70. The D_{chem} values calculated from the GITT potential profiles for every equilibrium step for cycles 1, 2, 5, 50, 95, 140, and 185 for the discharge and charge profiles are displayed in Figure 15. During the first discharge, four significant minima at 1.04, 0.88, 0.71, and 0.57 V of the diffusion coefficient are visible with corresponding values for D_{chem} of $1.67 \times 10^{-}11$, 9.94×10^{-12}, 4.82×10^{-12}, and 7.16×10^{-12} cm^2 s^{-1}, respectively (Figure 15a). These minima correspond to phase transitions, which in turn are associated with a redox process visible in the CV (Figure 2d) or as a voltage plateau in the discharge curve (Figure 2c). The first broad and significant decrease of D_{chem} between 1.10 and 0.95 V, corresponding to the first pseudo plateau in the GITT curve, may be the first Na incorporation into the bulk $CuFe_2S_3$, leading to the phase transition to $CuFeS_2$ and $NaFe_{1.5}S_2$, as this drop does not occur in the subsequent cycles. The other decreases of D_{chem} may also be explained by the electrochemical processes discussed above (Cu^+ reduction to Cu^0 and formation of Na_2S), which leads to classical two-phase mechanisms because the diffusion of metal ions is largely limited by the interfacial resistance between two phases.[72] In the second discharge cycle, the first two intense minima of D_{chem} of the first cycle are not visible but a minimum at 0.93 V, which corresponds to uptake of 1.15 Na/f.u. Based on the ex situ PXRD data, this decrease of the diffusion coefficient D_{chem} = 6.47×10^{-11} cm^2 s^{-1} may be the transition from the unknown crystalline phase to $NaFe_{1.5}S_2$. While in the discharge curves, still small changes from cycles 2−50 occur, and the value for D_{chem} remains very constant in the charge curves and shows a minimum at 1.40 V with $D_{\text{chem}} = 2.43 \times 10^{-12}$ cm^2 s^{-1}, which could be due to the regression of nanocrystalline Na_2S (Figure 15c). The value for D_{chem} in the discharge curve exhibits less fluctuations from cycle 95 onward, and the less pronounced minima occur at different potentials compared to the above-discussed cycles. This may be attributed to the reduced particle sizes and the generation of structural defects, which shorten the solid phase diffusion path length.[73] In the charge curve, significant changes can be observed from cycle 95 onward, which can be deduced from the different minima and confirms the change in the Na storage mechanism. The change leads to smoother curves, with the smallest minimum at 1.35×10^{-11} cm^2 s^{-1} so that these alterations improve the sodium diffusion (Figure 15d).

4. CONCLUSIONS

A multistep, high-temperature synthesis has produced the first reported bulk isocubanite that is close to being phase pure. This material features excellent electrochemical Na storage properties with a high and stable capacity of 422 mA h g^{-1} for over 1000 cycles at a current rate of 0.5 A g^{-1}. Together with the high rate capability, $CuFe_2S_3$ has an exceptionally good potential for application as an anode material in SIBs.

Combining ex situ PXRD and XAS measurements provide useful insights into the Na storage mechanism. The PXRD data demonstrate that up to 2 Na/f.u., the mechanism proceeds via crystalline $CuFeS_2$ and $NaFe_{1.5}S_2$ intermediates until at a capacity of ~300 mA h g^{-1} when almost only elemental Cu is detectable. The remaining capacity must therefore result from the reduction of Fe. While the PXRD data only show that uptake of 5 Na/f.u. leads to the formation of nanocrystalline Na_2S, the XAS studies evidence for >3 Na/.f.u. that the $Fe^{2+/3+}$ cations are successively reduced to Fe^0. Because Na_2S crystallizes only after the uptake of 5 Na/f.u. and during cyclization within the limited potential window no more than 5 Na/f.u. is shuttled, it can be assumed that this limitation leads to improved cyclability. Surprisingly, the charging process again proceeds via $NaFe_{1.5}S_2$ and ends with the formation of a new unknown phase. The conversion process of this phase is reversible as demonstrated by the PXRD data of the second cycle and also proceeds via $NaFe_{1.5}S_2$. Residual fcc-Cu observed in the fully charged state may be beneficial in compensating the poor electrical conductivity of Na_2S.

Due to the unknown phase, it is difficult to predict the mechanism in detail, but it could be expressed like the following eqs 4 and 5

discharge:

$$\begin{aligned} &CuFe_2S_3 \xrightarrow{1 + x(Na + e^-)} 1 - xCuFeS_2 \\ &+ \frac{1 + x}{1.5}NaFe_{1.5}S_2 + xCu \xrightarrow{5 - x(Na + e^-)} 2Fe + Cu \\ &+ 3Na_2S \end{aligned} \tag{4}$$

charge:

$$\begin{aligned} &2Fe + Cu + 3Na_2S \xrightarrow{4Na + 4e^-} Cu + 4/3NaFe_{1.5}S_2 \\ &\xrightarrow{1 + x(Na + e^-)} Cu + Cu_aFe_bS_c \end{aligned} \tag{5}$$

The relatively high crystallinity, which is still obtained even in the second cycle, should be emphasized because the formation of a crystalline phase was not observed in the

https://doi.org/10.1021/acsami.1c16814
ACS Appl. Mater. Interfaces 2021, 13, 58552−58565

overwhelming cases of conversion materials, which were in the fully charged state. Even in the later stages at cycles 135, 240, and even 400, nanocrystalline phases could be identified, showing that a change in the reaction mechanism occurs during cycling in which Cu_xS phases play a dominant role.

Coming back to the question raised in the introduction, the reaction mechanisms show some differences compared to $CuFeS_2$ due to the different Cu/Fe/S ratios. While only one $NaCuFeS_2$ intermediate could be observed in the former, another intermediate forms using isocubanite. Despite the larger iron content, a very good long-term stability is achieved and crystalline products are obtained even at higher cycles, possibly due to the high mobility of Cu. This supports the hypothesis that this phenomenon plays a key role in achieving high cycle stability making these materials promising candidates for anode materials in SIBs.

■ ASSOCIATED CONTENT

Supporting Information

The Supporting Information is available free of charge at https://pubs.acs.org/doi/10.1021/acsami.1c16814.

Rietveld refinement parameters; results of EDX and elemental analyses; discharge and charge profiles at a current rate of 0.5 A g^{-1} in a potential window of 3−0.1 V; comparison of the discharge curves of powder and film cells; crystal structure of $NaFe_{1.5}S_2$; comparison of Rietveld refinements of the discharged sample with and without Fe; determined copper reflection intensities; magnetic hysteresis curve of the fully discharged sample and PXRD pattern of the 400th cycle compared to the calculated pattern of $NaFe_{1.5}S_2$ (PDF)

■ AUTHOR INFORMATION

Corresponding Author

Wolfgang Bensch − *Institute of Inorganic Chemistry, Kiel University, 24118 Kiel, Germany;* orcid.org/0000-0002-3111-580X; Phone: +49 431 880-2091; Email: wbensch@ac.uni-kiel.de; Fax: +49 431 880-1520

Authors

Svenja Senkale − *Institute of Inorganic Chemistry, Kiel University, 24118 Kiel, Germany*

Giannantonio Cibin − *Diamond Light Source (DLS), Didcot, Oxfordshire OX11 0DE, U.K.*

Alan V. Chadwick − *School of Physical Sciences, Ingram Building, University of Kent, Canterbury CT2 7NH, U.K.;* orcid.org/0000-0002-6485-9207

Complete contact information is available at: https://pubs.acs.org/10.1021/acsami.1c16814

Notes

The authors declare no competing financial interest.

■ ACKNOWLEDGMENTS

Financial support by the State of Schleswig-Holstein is gratefully acknowledged. The authors thank the Diamond Light Source (DLS). The authors also thank the DLS for the award of beam time as part of the Energy Materials Block Allocation Group SP14239.

■ REFERENCES

(1) Zubi, G.; Dufo-López, R.; Carvalho, M.; Pasaoglu, G. The Lithium-Ion Battery: State of the Art and Future Perspectives. *Renew. Sustain. Energy Rev.* **2018**, *89*, 292−308.

(2) Armand, M.; Axmann, P.; Bresser, D.; Copley, M.; Edström, K.; Ekberg, C.; Guyomard, D.; Lestriez, B.; Novák, P.; Petranikova, M.; Porcher, W.; Trabesinger, S.; Wohlfahrt-Mehrens, M.; Zhang, H. Lithium-Ion Batteries − Current State of the Art and Anticipated Developments. *J. Power Sources* **2020**, *479*, 228708.

(3) Vikström, H.; Davidsson, S.; Höök, M. Lithium Availability and Future Production Outlooks. *Appl. Energy* **2013**, *110*, 252−266.

(4) Larcher, D.; Tarascon, J.-M. Towards Greener and More Sustainable Batteries for Electrical Energy Storage. *Nat. Chem.* **2015**, *7*, 19−29.

(5) Nayak, P. K.; Yang, L.; Brehm, W.; Adelhelm, P. From Lithium-Ion to Sodium-Ion Batteries: Advantages, Challenges, and Surprises. *Angew. Chem., Int. Ed.* **2018**, *57*, 102−120.

(6) Deng, J.; Luo, W.-B.; Chou, S.-L.; Liu, H.-K.; Dou, S.-X. Sodium-Ion Batteries: From Academic Research to Practical Commercialization. *Adv. Energy Mater.* **2018**, *8*, 1701428.

(7) Li, L.; Zheng, Y.; Zhang, S.; Yang, J.; Shao, Z.; Guo, Z. Recent Progress on Sodium Ion Batteries: Potential High-Performance Anodes. *Energy Environ. Sci.* **2018**, *11*, 2310−2340.

(8) Chen, X.; Zheng, Y.; Liu, W.; Zhang, C.; Li, S.; Li, J. High-Performance Sodium-Ion Batteries with a Hard Carbon Anode: Transition from the Half-Cell to Full-Cell Perspective. *Nanoscale* **2019**, *11*, 22196−22205.

(9) Zheng, Y.; Lu, Y.; Qi, X.; Wang, Y.; Mu, L.; Li, Y.; Ma, Q.; Li, J.; Hu, Y.-S. Superior Electrochemical Performance of Sodium-Ion Full-Cell Using Poplar Wood Derived Hard Carbon Anode. *Energy Storage Mater.* **2019**, *18*, 269−279.

(10) Xie, F.; Xu, Z.; Guo, Z.; Titirici, M.-M. Hard Carbons for Sodium-Ion Batteries and Beyond. *Prog. Energy* **2020**, *2*, 042002.

(11) Klein, F.; Jache, B.; Bhide, A.; Adelhelm, P. Conversion Reactions for Sodium-Ion Batteries. *Phys. Chem. Chem. Phys.* **2013**, *15*, 15876−15887.

(12) Deng, X.; Chen, Z.; Cao, Y. Transition Metal Oxides Based on Conversion Reaction for Sodium-Ion Battery Anodes. *Mater. Today Chem.* **2018**, *9*, 114−132.

(13) Wu, C.; Dou, S. X.; Yu, Y. The State and Challenges of Anode Materials Based on Conversion Reactions for Sodium Storage. *Small* **2018**, *14*, 1703671.

(14) Kim, J. K.; Park, S.-K.; Park, J.-S.; Kang, Y. C. Uniquely Structured Composite Microspheres of Metal Sulfides and Carbon with Cubic Nanorooms for Highly Efficient Anode Materials for Sodium-Ion Batteries. *J. Mater. Chem. A* **2019**, *7*, 2636−2645.

(15) Xiao, Y.; Lee, S. H.; Sun, Y.-K. The Application of Metal Sulfides in Sodium Ion Batteries. *Adv. Energy Mater.* **2017**, *7*, 1601329.

(16) Liu, Y.; Yang, C.; Zhang, Q.; Liu, M. Recent Progress in the Design of Metal Sulfides as Anode Materials for Sodium Ion Batteries. *Energy Storage Mater.* **2019**, *22*, 66−95.

(17) Xu, Q.-T.; Xue, H.-G.; Guo, S.-P. FeS_2 Walnut-like Microspheres Wrapped with RGO as Anode Material for High-Capacity and Long-Cycle Lithium-Ion Batteries. *Electrochim. Acta* **2018**, *292*, 1−9.

(18) Qi, S.; Wu, D.; Dong, Y.; Liao, J.; Foster, C. W.; O'Dwyer, C.; Feng, Y.; Liu, C.; Ma, J. Cobalt-Based Electrode Materials for Sodium-Ion Batteries. *Chem. Eng. J.* **2019**, *370*, 185−207.

(19) Li, S.; He, W.; Liu, B.; Cui, J.; Wang, X.; Peng, D.-L.; Liu, B.; Qu, B. One-Step Construction of Three-Dimensional Nickel Sulfide-Embedded Carbon Matrix for Sodium-Ion Batteries and Hybrid Capacitors. *Energy Storage Mater.* **2020**, *25*, 636−643.

(20) Shan, Y.; Li, Y.; Pang, H. Applications of Tin Sulfide-Based Materials in Lithium-Ion Batteries and Sodium-Ion Batteries. *Adv. Funct. Mater.* **2020**, *30*, 2001298.

(21) Duan, S.-Y.; Piao, J.-Y.; Lin, X.-J.; Sun, Y.-G.; Xu, Y.-S.; Cao, A.-M.; Wan, L.-J. Crystallization-Induced Self-Hollowing of Molybdenum Sulfide Nanoparticles and Their Potential in Sodium Ion Batteries. *Chem. Commun.* **2019**, *55*, 5894−5897.

(22) Kalimuldina, G.; Nurpeissova, A.; Adylkhanova, A.; Adair, D.; Taniguchi, I.; Bakenov, Z. Morphology and Dimension Variations of Copper Sulfide for High-Performance Electrode in Rechargeable Batteries: A Review. *ACS Appl. Energy Mater.* **2020**, *3*, 11480−11499.
(23) Chen, Y.; Hu, X.; Evanko, B.; Sun, X.; Li, X.; Hou, T.; Cai, S.; Zheng, C.; Hu, W.; Stucky, G. D. High-Rate FeS_2/CNT Neural Network Nanostructure Composite Anodes for Stable, High-Capacity Sodium-Ion Batteries. *Nano Energy* **2018**, *46*, 117−127.
(24) Man, Z.; Li, P.; Zhou, D.; Wang, Y.; Liang, X.; Zang, R.; Li, P.; Zuo, Y.; Lam, Y. M.; Wang, G. Two Birds with One Stone: FeS_2@C Yolk−Shell Composite for High-Performance Sodium-Ion Energy Storage and Electromagnetic Wave Absorption. *Nano Lett.* **2020**, *20*, 3769−3777.
(25) Liu, Q.; Gao, J.; Cao, C.; Yin, G.; Jiang, Z.; Ge, M.; Xiao, X.; Lee, W.-K.; Wang, J. Insights into Enhanced Sodium Ion Storage Mechanism in Fe_3S_4: The Coupling of Surface Chemistry, Microstructural Regulation and 3D Electronic Transport. *Nano Energy* **2019**, *62*, 384−392.
(26) Li, Q.; Wei, Q.; Zuo, W.; Huang, L.; Luo, W.; An, Q.; Pelenovich, V. O.; Zhang, Q.; Zhang, Q. Greigite Fe_3S_4 as a New Anode Material for High-Performance Sodium-Ion Batteries. *Chem. Sci.* **2017**, *8*, 160−164.
(27) Qi, S.; Mi, L.; Song, K.; Yang, K.; Ma, J.; Feng, X.; Zhang, J.; Chen, W. Understanding Shuttling Effect in Sodium Ion Batteries for the Solution of Capacity Fading: FeS_2 as an Example. *J. Phys. Chem. C* **2019**, *123*, 2775−2782.
(28) Huang, A.; Wang, Q.; Ma, Z.; Rui, K.; Huang, X.; Zhu, J.; Huang, W. Surface Anionization of Self-Assembled Iron Sulfide Hierarchitectures to Enhance Capacitive Storage for Alkaline-Metal-Ion Batteries. *ACS Appl. Mater. Interfaces* **2019**, *11*, 39991−39997.
(29) Yao, Y.; Zheng, J.; Gong, Z.; Ding, Z.; Zhang, J.; Yu, W.; Bengono, D. A. M.; Li, H.; Zhang, B.; Tong, H. Metal-Organic Framework Derived Flower-like FeS/C Composite as an Anode Material in Lithium-Ion and Sodium-Ion Batteries. *J. Alloys Compd.* **2019**, *790*, 288−295.
(30) Wang, F.; Li, G.; Cui, W. FeS2 Hollow Nanospheres as High-Performance Anode for Sodium Ion Battery and Their Surface Pseudocapacitive Properties. *J. Nanopart. Res.* **2019**, *21*, 121.
(31) Cao, Z.; Song, H.; Cao, B.; Ma, J.; Chen, X.; Zhou, J.; Ma, Z. Sheet-on-Sheet Chrysanthemum-like C/FeS Microspheres Synthesized by One-Step Solvothermal Method for High-Performance Sodium-Ion Batteries. *J. Power Sources* **2017**, *364*, 208−214.
(32) Wang, Q.; Guo, C.; Zhu, Y.; He, J.; Wang, H. Reduced Graphene Oxide-Wrapped FeS_2 Composite as Anode for High-Performance Sodium-Ion Batteries. *Nano-Micro Lett.* **2018**, *10*, 30.
(33) Chen, W.; Qi, S.; Guan, L.; Liu, C.; Cui, S.; Shen, C.; Mi, L. Pyrite FeS_2 Microspheres Anchoring on Reduced Graphene Oxide Aerogel as an Enhanced Electrode Material for Sodium-Ion Batteries. *J. Mater. Chem. A* **2017**, *5*, 5332−5341.
(34) Xiao, Y.; Hwang, J.-Y.; Belharouak, I.; Sun, Y.-K. Na Storage Capability Investigation of a Carbon Nanotube-Encapsulated $Fe_{1-X}S$ Composite. *ACS Energy Lett.* **2017**, *2*, 364−372.
(35) Xiao, Y.; Su, D.; Wang, X.; Wu, S.; Zhou, L.; Shi, Y.; Fang, S.; Cheng, H.-M.; Li, F. CuS Microspheres with Tunable Interlayer Space and Micropore as a High-Rate and Long-Life Anode for Sodium-Ion Batteries. *Adv. Energy Mater.* **2018**, *8*, 1800930.
(36) Chen, Q.; Ren, M.; Xu, H.; Liu, W.; Hei, J.; Su, L.; Wang, L. Dual-Doped Carbon Matrix Hybrid as Superior Anode Materials for Lithium/Sodium Ion Batteries. *ChemElectroChem* **2018**, *5*, 2135−2141.
(37) Shi, B.; Liu, W.; Zhu, K.; Xie, J. Synthesis of Flower-like Copper Sulfides Microspheres as Electrode Materials for Sodium Secondary Batteries. *Chem. Phys. Lett.* **2017**, *677*, 70−74.
(38) Krengel, M.; Hansen, A.-L.; Hartmann, F.; van Dinter, J.; Bensch, W. Elucidation of the Sodium − Copper Extrusion Mechanism in CuCrS2 ‚A High Capacity ‚Long -LifeAnode Material for Sodium -IonBatteries. *Batteries Supercaps* **2018**, *1*, 176−183.
(39) Krengel, M.; Hansen, A.-L.; Kaus, M.; Indris, S.; Wolff, N.; Kienle, L.; Westfal, D.; Bensch, W. CuV_2S_4 : A High Rate Capacity and Stable Anode Material for Sodium Ion Batteries. *ACS Appl. Mater. Interfaces* **2017**, *9*, 21283−21291.
(40) Zhu, L.; Li, Y.; Wang, J.; Zhu, X. Sodium Storage Performance and Mechanism of RGO-Wrapped Nanorod Vanadium Sulfide as an Anode Material for Sodium Ion Batteries. *Solid State Ionics* **2018**, *327*, 129−135.
(41) Senkale, S.; Indris, S.; Etter, M.; Bensch, W. $CuFeS_2$ as a Very Stable High-Capacity Anode Material for Sodium-Ion Batteries: A Multimethod Approach for Elucidation of the Complex Reaction Mechanisms during Discharge and Charge Processes. *ACS Appl. Mater. Interfaces* **2021**, *13*, 26034−26045.
(42) Anger, E.; Maignan, A.; Barbier, T.; Pralong, V. $CuFe_2S_3$ as Electrode Material for Li-Ion Batteries. *RSC Adv.* **2018**, *8*, 26691−26695.
(43) René, C.; Cervelle, B.; Cesbron, F.; Oudin, E.; Picot, P.; Pillard, F. Isocubanite, a New Definition of the Cubic Polymorph of Cubanite $CuFe_2S_3$. *Mineral. Mag.* **1988**, *52*, 509−514.
(44) Barbier, T.; Berthebaud, D.; Frésard, R.; Lebedev, O. I.; Eyert, V.; Maignan, A.; Maignan, A. Structural and Thermoelectric Properties of N-Type Isocubanite $CuFe_2S_3$. *Inorg. Chem. Front.* **2017**, *4*, 424−432.
(45) Nenasheva, S. N.; Kravchenko, T. A. Composition Features of Isocubanite and Polymorphous Modifications of $CuFe_2S_3$ Compound. *Geol. Ore Deposits* **2015**, *57*, 626−633.
(46) Chandra, U.; Parthasarathy, G.; Sharma, P. Synthetic Cubanite $CuFe_2S_3$: Pressure-Induced Transformation to Isocubanite. *Can. Mineral.* **2010**, *48*, 1137−1147.
(47) Pareek, S.; Rais, A.; Tripathi, A.; Chandra, U. Mössbauer Study on Microwave Synthesized (Cu,Fe) Sulfide Composites and Correlation with Natural Mineral—Cubanite. *ICAME 2007*; Springer: Berlin, Heidelberg, 2009; pp 995−1002.
(48) Peled, E.; Menkin, S. Review—SEI: Past, Present and Future. *J. Electrochem. Soc.* **2017**, *164*, A1703.
(49) Hall, S. R.; Stewart, J. M. The Crystal Structure Refinement of Chalcopyrite $CuFeS_2$. *Acta Crystallogr., Sect. B: Struct. Crystallogr. Cryst. Chem.* **1973**, *29*, 579−585.
(50) Xie, Y.-P.; Zhao, S.-J. The Energetic and Structural Properties of Bcc NiCu, FeCu Alloys: A First-Principles Study. *Comput. Mater. Sci.* **2011**, *50*, 2586−2591.
(51) Kitajou, A.; Yamaguchi, J.; Hara, S.; Okada, S. Discharge/Charge Reaction Mechanism of a Pyrite-Type FeS_2 Cathode for Sodium Secondary Batteries. *J. Power Sources* **2014**, *247*, 391−395.
(52) Wang, F.; Robert, R.; Chernova, N. A.; Pereira, N.; Omenya, F.; Badway, F.; Hua, X.; Ruotolo, M.; Zhang, R.; Wu, L.; Volkov, V.; Su, D.; Key, B.; Whittingham, M. S.; Grey, C. P.; Amatucci, G. G.; Zhu, Y.; Graetz, J. Conversion Reaction Mechanisms in Lithium Ion Batteries: Study of the Binary Metal Fluoride Electrodes. *J. Am. Chem. Soc.* **2011**, *133*, 18828−18836.
(53) Li, B.; Huang, L.; Zhong, M.; Wei, Z.; Li, J. Electrical and Magnetic Properties of FeS_2 and $CuFeS_2$ Nanoplates. *RSC Adv.* **2015**, *5*, 91103−91107.
(54) Choi, H.; Seo, J. Y.; Uhm, Y. R.; Sun, G. M.; Kim, C. S. Crystalline Structure and Magnetic Properties of Pyrite FeS_2. *AIP Adv.* **2021**, *11*, 015131.
(55) Xia, J.; Jiao, J.; Dai, B.; Qiu, W.; He, S.; Qiu, W.; Shen, P.; Chen, L. Facile Synthesis of FeS_2 Nanocrystals and Their Magnetic and Electrochemical Properties. *RSC Adv.* **2013**, *3*, 6132−6140.
(56) Kobayashi, K.; Azuma, Y.; Kawashima, K.; Horigane, K.; Akaki, M.; Tokunaga, M.; Akimitsu, J. Magnetic Properties of Chalcopyrite $Cu_{1-x}FeS_2$ at Low Temperatures. *Proceedings of the International Conference on Strongly Correlated Electron Systems (SCES2013)*; Journal of the Physical Society of Japan: Tokyo, Japan, 2014.
(57) Manukyan, A.; Gyulasaryan, H.; Kocharian, A.; Estiphanos, M.; Bernal, O.; Sharoyan, E. Ferromagnetism and Giant Paramagnetism of Copper Nanoparticles in Cum/C Nanocomposites. *J. Magn. Magn. Mater.* **2019**, *488*, 165336.
(58) Raghuvanshi, S.; Satalkar, M.; Tapkir, P.; Ghodke, N.; Kane, S. N. On the Structural and Magnetic Study of $Mg_{1-x}Zn_xFe_2O_4$. *J. Phys.: Conf. Ser.* **2014**, *534*, 012031.

https://doi.org/10.1021/acsami.1c16814
ACS Appl. Mater. Interfaces 2021, 13, 58552−58565

(59) Edmonds, K. W.; Binns, C.; Baker, S. H.; Thornton, S. C.; Norris, C.; Goedkoop, J. B.; Finazzi, M.; Brookes, N. B. Doubling of the Orbital Magnetic Moment in Nanoscale Fe Clusters. *Phys. Rev. B* **1999**, *60*, 472−476.
(60) Zakaria, S. N. A.; Hollingsworth, N.; Islam, H. U.; Roffey, A.; Santos-Carballal, D.; Roldan, A.; Bras, W.; Sankar, G.; Hogarth, G.; Holt, K. B.; de Leeuw, N. H. Insight into the Nature of Iron Sulfide Surfaces During the Electrochemical Hydrogen Evolution and CO_2 Reduction Reactions. *ACS Appl. Mater. Interfaces* **2018**, *10*, 32078−32085.
(61) Womes, M.; Karnatak, R. C.; Esteva, J. M.; Lefebvre, I.; Allan, G.; Olivier-fourcades, J.; Jumas, J. C. Electronic Structures of FeS and FeS_2: X-RAY Absorption Spectroscopy and Band Structure Calculations. *J. Phys. Chem. Solids* **1997**, *58*, 345−352.
(62) Kataby, G.; Koltypin, Y.; Rothe, J.; Hormes, J.; Felner, I.; Cao, X.; Gedanken, A. The Adsorption of Monolayer Coatings on Iron Nanoparticles: Mössbauer Spectroscopy and XANES Results. *Thin Solid Films* **1998**, *333*, 41−49.
(63) Luo, W. K.; Sheng, H. W.; Alamgir, F. M.; Bai, J. M.; He, J. H.; Ma, E. Icosahedral Short-Range Order in Amorphous Alloys. *Phys. Rev. Lett.* **2004**, *92*, 145502.
(64) Gaur, A.; Shrivastava, B. D.; Joshi, S. K. Copper K-Edge XANES of Cu(I) and Cu(II) Oxide Mixtures. *J. Phys.: Conf. Ser.* **2009**, *190*, 012084.
(65) Kau, L. S.; Spira-Solomon, D. J.; Penner-Hahn, J. E.; Hodgson, K. O.; Solomon, E. I. X-Ray Absorption Edge Determination of the Oxidation State and Coordination Number of Copper. Application to the Type 3 Site in Rhus Vernicifera Laccase and Its Reaction with Oxygen. *J. Am. Chem. Soc.* **1987**, *109*, 6433−6442.
(66) Kumar, P.; Nagarajan, R.; Sarangi, R. Quantitative X-Ray Absorption and Emission Spectroscopies: Electronic Structure Elucidation of Cu_2S and CuS. *J. Mater. Chem. C* **2013**, *1*, 2448−2454.
(67) Tagirov, B. R.; Trigub, A. L.; Kvashnina, K. O.; Shiryaev, A. A.; Chareev, D. A.; Nickolsky, M. S.; Abramova, V. D.; Kovalchuk, E. V. Covellite CuS as a Matrix for "Invisible" Gold: X-Ray Spectroscopic Study of the Chemical State of Cu and Au in Synthetic Minerals. *Geochim. Cosmochim. Acta* **2016**, *191*, 58−69.
(68) Mikhlin, Y. L.; Likhatski, M. N.; Bayukov, O. A.; Knyazev, Y.; Velikanov, D. A.; Tomashevich, Y. V.; Romanchenko, A. S.; Vorobyev, S. A.; Volochaev, M. V.; Zharkov, S. M.; Meira, D. M. Valleriite, a Natural Two-Dimensional Composite: X-Ray Absorption, Photoelectron, and Mössbauer Spectroscopy, and Magnetic Characterization. *ACS Omega* **2021**, *6*, 7533−7543.
(69) Weppner, W.; Huggins, R. A. Determination of the Kinetic Parameters of Mixed-Conducting Electrodes and Application to the System Li_3Sb. *J. Electrochem. Soc.* **1977**, *124*, 1569.
(70) Babu, B.; Shaijumon, M. M. Studies on Kinetics and Diffusion Characteristics of Lithium Ions in $TiNb_2O_7$. *Electrochim. Acta* **2020**, *345*, 136208.
(71) Rui, X. H.; Ding, N.; Liu, J.; Li, C.; Chen, C. H. Analysis of the Chemical Diffusion Coefficient of Lithium Ions in $Li_3V_2(PO_4)_3$ Cathode Material. *Electrochim. Acta* **2010**, *55*, 2384−2390.
(72) Wang, J.; Wang, L.; Eng, C.; Wang, J. Elucidating the Irreversible Mechanism and Voltage Hysteresis in Conversion Reaction for High-Energy Sodium−Metal Sulfide Batteries. *Adv. Energy Mater.* **2017**, *7*, 1602706.
(73) Fang, G.; Wu, Z.; Zhou, J.; Zhu, C.; Cao, X.; Lin, T.; Chen, Y.; Wang, C.; Pan, A.; Liang, S. Observation of Pseudocapacitive Effect and Fast Ion Diffusion in Bimetallic Sulfides as an Advanced Sodium-Ion Battery Anode. *Adv. Energy Mater.* **2018**, *8*, 1703155.

https://doi.org/10.1021/acsami.1c16814
ACS Appl. Mater. Interfaces 2021, 13, 58552−58565

4.3 Multi-Method Characterization of the High-Entropy Spinel Oxide $Mn_{0.2}Co_{0.2}Ni_{0.2}Cu_{0.2}Zn_{0.2}Fe_2O_4$: Entropy Evidence, Microstructure, and Magnetic Properties

Ein etwas abweichendes Thema wird in der folgenden Publikation behandelt. Aufgrund des aufkommenden Interesses an entropiestabilisierten Materialien und der Erkenntnis aus den vorherigen Untersuchungen, dass die Synergie von Elementen in einer Verbindung einen durchaus überraschend positiven Effekt haben kann, wurde das Interesse geweckt, sich mit diesen Materialien auseinanderzusetzen. Dabei wurde mit einer Literaturrecherche festgestellt, dass viele Untersuchungen anderer Arbeitsgruppen der Pionierarbeit von Rost et al.[119] nacheiferten und deren Vorgehen auf andere oxidische Systeme wie Spinelle übertragen worden sind. Allerdings wurden diese Materialien in erstaunlich viele Arbeiten nur oberflächlich charakterisiert und postulierten die Entropie-basierte Stabilität nur mittels TEM-Mapping.

In der folgenden Publikation wird über die Synthese eines Spinells berichtet, in dem das Hauptkation Fe^{3+} darstellt und fünf weitere Metallkationen in stöchiometrisch gleichen Äquivalenten für die Entropiestabilisierung sorgen. Ein phasenreiner Spinell mit der Zusammensetzung $Mn_{0.2}Co_{0.2}Ni_{0.2}Cu_{0.2}Zn_{0.2}Fe_2O_4$ wurde mittels Zersetzungsmethode eines Nitratprekursors und anschließender thermischer Behandlung erhalten. Durch Wahl der Sintertemperatur konnte die Partikelgröße vom nanoskaligen Bereich bis hin zu hochkristallinen Material variiert werden. Der Spinell wurde auf seine Entropiestabilisierung mittels *in-situ* XRPD überprüft. Aufnahmen im Transmissionselektronenmikroskop (TEM) zeigten eine homogene Verteilung der Kationen. Um weitere strukturelle Informationen zu erhalten wurden sowohl ^{57}Fe Mößbauer- als auch XAS-Messungen durchgeführt. Die Mößbauer-Studien belegten, dass Fe^{3+} vorliegt und ein Inversionsgrad von ca. 66% vorhanden ist. Die Auswertung der XAS-Messungen erlaubte eine Bestimmung der Valenz der Kationen und deren Verteilung über die Tetraeder- und Oktaederplätze in der Struktur. Untersuchungen des magnetischen Verhaltens ergaben eine außergewöhnlich hohe Sättigungsmagnetisierung des Materials sowie magnetische Austauschwechselwirkungen, welche ferro- oder ferrimagnetisch sind. Während TEM und XRPD bei einer Sintertemperatur von 500 °C auf ein phasenreines Material hindeuten, wurde durch eine Anomalie in der magnetischen Hysteresekurve gezeigt, dass wahrscheinlich zwei magnetische Phasen vorhanden sind. Es stellt sich die Frage, ob magnetische Untersuchungen eine höhere Empfindlichkeit aufweisen und somit in der Lage sind die Feinheiten des Mikrogefüges besser zu erfassen.

Spinelle sind aufgrund ihrer bemerkenswerten physikalischen Eigenschaften seit langem Gegenstand zahlreicher Forschungen und bieten großes Potenzial für Anwendungen wie Energiespeicherung oder in der Katalyse. Die Erforschung dieser neuen Klasse von Spinellen stellt daher eine vielversprechende Möglichkeit dar, gezielter innovative Werkstoffe zu entwickeln.

Veröffentlicht in: *Chemistry—Methods,* **2023**, 3, e202200043.

DOI: doi.org/10.1002/cmtd.202200043

© 2022 The Authors. Published by Wiley-VCH GmbH

Chemistry—Methods

Research Article
doi.org/10.1002/cmtd.202200043

Chemistry Europe
European Chemical Societies Publishing

www.chemistrymethods.org

Multi-Method Characterization of the High-Entropy Spinel Oxide $Mn_{0.2}Co_{0.2}Ni_{0.2}Cu_{0.2}Zn_{0.2}Fe_2O_4$: Entropy Evidence, Microstructure, and Magnetic Properties

Svenja Senkale,[a] Marius Kamp,[b] Stefan Mangold,[c] Sylvio Indris,[d] Lorenz Kienle,[b] Reinhard K. Kremer,[e] and Wolfgang Bensch*[a]

The novel spinel $Cu_{0.2}Co_{0.2}Mn_{0.2}Ni_{0.2}Zn_{0.2}Fe_2O_4$ comprising six transition metal cations was successfully prepared by a solution-combustion method followed by distinct thermal treatments. The entropic stabilization of this hexa-metallic material is demonstrated using in situ high temperature powder X-ray diffraction (PXRD) and directed removal of some of the constituting elements. Thorough evaluation of the PXRD data yields sizes of coherently scattering domains in the nanometre-range. Transmission electron microscopy based methods support this finding and indicate a homogeneous distribution of the elements in the samples. The combination of ^{57}Fe Mössbauer spectroscopy with X-ray absorption near edge spectroscopy allowed determination of the cation occupancy on the tetrahedral and octahedral sites in the cubic spinel structure. Magnetic studies show long-range magnetic exchange interactions which are of ferri- or ferromagnetic nature with an exceptionally high saturation magnetization in the range of 92–108 emu g^{-1} at low temperature, but also an anomaly in the hysteresis of a sample calcined at 500 °C.

Introduction

Entropy stabilized metallic alloys have attracted increasing attention and are widely studied due to their versatile and adjustable properties.[1,2] Yeh et al. define such alloys as solid solutions containing more than five principal elements with equal or near equal atomic percentage.[3] Another definition was given by Mirakel et al. based on the entropy concept. According to this definition the requirement for an entropy stabilized compound is a ΔS_{mix} larger than 1.61 R, where R is the universal gas constant, 8.314 J/mol K.[4] In 2015 Rost et al. extended this concept to high entropy stabilized oxides (HESO's) based on a five component rock salt structure. A configurational entropy value is generated by the random distribution of the constituent metal cations on the cation sublattice, which competes with the formation enthalpies of intermediate compounds.[5] Because the phase stability is dictated by Gibb's energy [Eq. (1)], the single-phase is stabilized with increasing temperatures and increasing number of elements, because the configurational entropy counteracts the enthalpy controlled phase separation.[6]

$$\Delta G_{mix} = \Delta H_{mix} - T\Delta S_{mix} = \Delta H_{mix} + RT\sum_{i=1}^{n} x_i \ln(x_i) \quad (1)$$

With T = temperature, ΔH_{mix} = enthalpy of mixing, ΔG_{mix} = free enthalpy of mixing, R = universal gas constant, x_i = molar concentration of each component

Rost et al. have established some requirements for such entropy controlled systems:[5]

- Low temperature equilibration should transform a single phase back to its multiphase state
- Removing components should result in a non-single phase structure at the same temperature
- The transformation from multiphase to single phase should be endothermic.

So far not only rock salt type structures have been synthesized and investigated, but also spinels,[7–17] fluorite-oxides[18] and perovskites.[19] Through entropy stabilisation, novel element combinations can be obtained in an oxide phase, which may exhibit innovative physical properties. In order to design such systems, however, it is necessary to develop a deeper understanding of these complex multi-element materi-

[a] S. Senkale, Prof. Dr. W. Bensch
Institute for Inorganic Chemistry
Kiel University
Max-Eyth-Str. 2, 4118 Kiel (Germany)
E-mail: wbensch@ac.uni-kiel.de
[b] Dr. M. Kamp, Prof. Dr. L. Kienle
Institute for Materials Science
Kiel University
Kaiserstr. 2, 24143 Kiel (Germany)
[c] Dr. S. Mangold
Institute for Photon Science and Synchrotron Radiation
Karlsruhe Institute of Technology (KIT)
Hermann-von-Helmholtz-Platz 1,
76344 Eggenstein-Leopoldshafen (Germany)
[d] Dr. S. Indris
Institute for Applied Materials
Karlsruhe Institute of Technology
P.O. box 3640, 76021 Karlsruhe (Germany)
[e] Dr. R. K. Kremer
Max Planck Institute for Solid State Research
Heisenbergstrasse 1, 70569 Stuttgart (Germany)

Supporting information for this article is available on the WWW under https://doi.org/10.1002/cmtd.202200043

© 2022 The Authors. Published by Wiley-VCH GmbH. This is an open access article under the terms of the Creative Commons Attribution Non-Commercial License, which permits use, distribution and reproduction in any medium, provided the original work is properly cited and is not used for commercial purposes.

© 2022 The Authors. Published by Wiley-VCH GmbH

Chemistry—Methods | Research Article doi.org/10.1002/cmtd.202200043 | Chemistry Europe European Chemical Societies Publishing

als. Especially, spinels have a very wide range of applications, which makes them of great interest for entropic systems. Adjustable properties for, for example, catalytic oxidation or for use as DNA-based biosensors are conceivable here.[20] Different synthetic approaches have already been successfully applied to obtain entropy stabilized spinels.[7,21] The spinels reported in the literature cited above were all synthesized according to the nominal composition of the following type:

$(A1_{0.2}\ A2_{0.2}\ A3_{0.2}\ A4_{0.2}\ A5_{0.2})_3O_4$ with (A = transition metal).

For expanding the area of spinel-based entropy stabilized solids we developed a new approach according to the following concept:

$(A1_{0.2}\ A2_{0.2}\ A3_{0.2}\ A4_{0.2}\ A5_{0.2})Fe_2O_4$ with (A = 2 + transition metal cations).

This approach has been poorly investigated so far and, in the case of iron as a trivalent cation, to the best of our knowledge just in two similar cases.[22–25] For example, Musicó et al. prepared different high entropy spinels using a high temperature synthesis, which showed varying interesting magnetic properties depending on the elemental composition.[25] Hosseini Mohammadabadi et al. studied among others the magnetic and structural properties of an entropic spinel with increasing Mn content and fascinating results were obtained.[24] Despite various studies, the magnetic interactions are still not fully understood due to the complexity of occupation and oxidation states of the cations.[26–27] The first impressive studies have been performed to unravel the complex spin-electronic models.[28]

Due to the fact that in this system the equal atomic percentages only refer to the used divalent metals, evidences of entropy stabilisation are provided in the present work. Since it is known that manganese-containing ferrites decompose at certain temperatures, this is a useful property to demonstrate whether an entropy stabilized spinel was obtained, since a multiphase state can be obtained that can be used to verify the first two requirements (see below).[29–31] To gain a deeper insight and understanding of the compounds, we investigated the homogeneity at the nanoscale by TEM and determined the oxidation states and the distribution of cations on the octahedral and tetrahedral sites using X-Ray Absorption Spectroscopy (XAS) and Mössbauer spectroscopy. The temperature dependent magnetic properties were also examined.

Results and Discussion

Influence of the amount of glucose on the particle size

A possibility to adjust the crystallite size directly during synthesis is to vary the amount of glucose. Figure 1 shows the different PXRD patterns for different glucose contents and its influence on the products after annealing at 500 °C. The more fuel is used in the combustion reaction, the smaller are the coherently scattering domains of the products. Sizes of the coherently scattering domains vary between 5 and 27 nm (determined by Rietveld refinements) while maintaining the spinel structure (Table 1). The lattice parameter increases with increasing particle sizes which can be explained by, for example, the high surface-to-volume ratio, stress and strain, and disorder of the constituents.

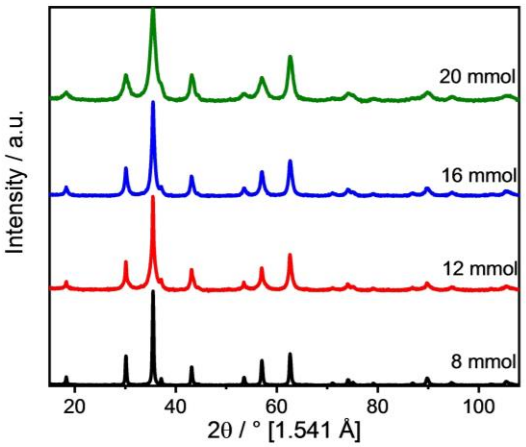

Figure 1. XRD patterns revealing the influence of the amount of glucose on the particle size.

Table 1. Crystallite sizes and lattice parameters of HES1s produced with different amounts of glucose.

Amount of glucose [mmol]	Crystallite size [nm]	Lattice parameter [Å]
8	27.1(3)	8.3867(2)
12	10.0(2)	8.3835(4)
16	9.7(2)	8.3843(4)
20	5.3(1)	8.376(1)

Structural investigation of the synthesized and sintered samples of $Cu_{0.2}Co_{0.2}Mn_{0.2}Ni_{0.2}Zn_{0.2}Fe_2O_4$ (HES1)

Figure 2 shows the PXRD pattern of $Cu_{0.2}Co_{0.2}Mn_{0.2}Ni_{0.2}Zn_{0.2}Fe_2O_4$ (HES1s) in the as synthesized (a.s.) state and the patterns of the sintered samples obtained at $T = 500$, 650, and 1000 °C together with the results of the Rietveld refinements. The lattice parameters and sizes of coherently scattering domains are listed in Table 2. It is unambiguous that the main fraction of the a.s. sample crystallized in the spinel-type structure with space group $Fd\bar{3}m$, whose lattice parameter was determined as $a = 8.4382(2)$ Å (similar to ICSD 184064). In addition to the spinel phase, reflections of another phase are visible and these are assigned to fcc-metals. Due to the calculated amount of 85.1 % for the spinel, at least three metal species are present in this phase mixture. A Rietveld refinement including three metals gives a satisfactory result and the refined lattice parameters of 3.605(1), 3.564(1) and 3.50(1) Å can be assigned to Cu, β-Co and Ni. The electrochemical redox potential, XAS measurements, and magnetic properties (see below) support this assumption. A broadening of the Bragg reflections is observed presumably caused by nanosized coherently scattering domains. The sizes

© 2022 The Authors. Published by Wiley-VCH GmbH

Chemistry—Methods | Research Article doi.org/10.1002/cmtd.202200043 | Chemistry Europe European Chemical Societies Publishing

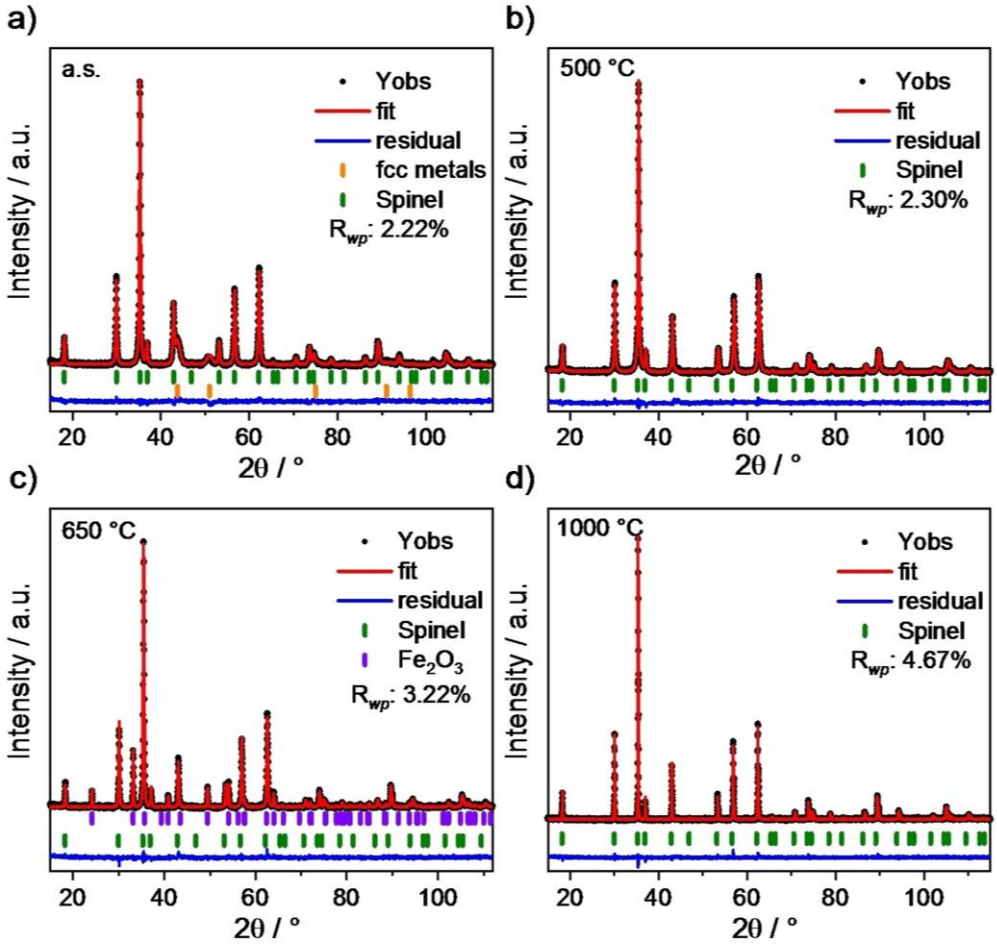

Figure 2. Results of Rietveld refinements against the PXRD patterns of HES1s a.s.; 500 °C, 650 °C and 1000 °C. Observed (black dots), calculated (red) and difference (blue) profiles. Reflection positions are marked as vertical bars.

Table 2. Crystallite size and lattice constant obtained from Rietveld refinements and average crystallite size determined by TEM. Note that an average value of the lattice parameter is given for the metals in HES1 a.s. sample. Estimated standard deviations are given in parentheses.

Samples		Diameter [nm]	Weight percent [%]	Lattice parameter a [Å]	Diameter (TEM) [nm]	Lattice parameter (TEM) a [Å]
HES1s a.s.	Spinel	25.5(6)	86(1)	8.4382(2)	13.9(6)	8.52(6)
	Metals	8–10	14.9(3)	Ø 3.5814(4)		
500 °C	Spinel	27.0(3)	100	8.3867(2)	16.1(6)	8.44(6)
650 °C	Spinel	40.8(5)	79.5(2)	8.3916(1)	28.8(6)	8.52(6)
	Haematite	68(3)	20.5(2)	5.0361(4), 13.7403(6)		
1000 °C	Spinel	cryst.(176)	100	8.40668(5)	cryst.	8.44(6)

of the domains were determined to be 26 nm for the spinel phase and around 8–10 nm for the metals. As illustrated in Figure 2a the experimental pattern matches well with the refined pattern resulting in a very low value for R_{wp} of 2.22%. After heating to 500 °C, the reflections of the metals completely disappeared in the PXRD pattern indicating incorporation into the spinel structure and a phase-pure spinel is obtained with lattice parameter $a = 8.3867(2)$ Å and a crystallite size of 27 nm (Figure 2b), similar to the size determined for the as synthesized sample. The lattice parameter is about 0.05 Å smaller than that of the a.s. sample, which could be explained either by the incorporation of the three metal species as cations and/or by a redistribution of the cations within the different tetrahedral and octahedral positions, due to this incorporation. Further heating

© 2022 The Authors. Published by Wiley-VCH GmbH

Chemistry—Methods | Research Article doi.org/10.1002/cmtd.202200043 | Chemistry Europe European Chemical Societies Publishing

leads to precipitation of haematite (Fe_2O_3, ICSD 161290) at about 600 °C reaching its maximum content of ca. 20.5 wt.% at 650 °C (Figure 2c). This process is accompanied by a slight increase of the unit cell volume of the spinel and a significant growth of the domain sizes to ≈41 nm (Table 2). Another increase of the temperature results in a successive disappearance of reflections of haematite, and at about 1000 °C no reflections of this impurity can be detected (Figure 2d). At this temperature a spinel is formed with a lattice parameter of a = 8.40668(5) Å and high crystallinity. The alterations of the unit cell volume of the spinel during the heating processes are related to various effects like surface distortion of particles induced by the size effects of nanoparticles[32] as well as the distribution of cations between tetrahedral and octahedral positions.[33] The increasing interactions between the various defect-related dipoles will also have an effect[34] as well as stacking faults often observed in *fcc* materials.

Evaluation of the PDF data (see Figure S1 in Supporting Information) confirms the results obtained by the Rietveld refinements regarding domain sizes (determined by spherical damping), lattice parameters, and chemical compositions (Table 3) from samples a.s., 650 °C, and 1000 °C. The volume-averaged mean crystallite morphology could be obtained by evaluating the anisotropic broadening of the Bragg reflections. At lower temperatures the shape is almost spherical, whereas at higher calcination temperatures the shape becomes more edged (Figure S3).

The chemical composition determined by SEM-EDX analysis yields $Mn_{0.21}Co_{0.21}Ni_{0.19}Cu_{0.20}Zn_{0.19}Fe_{2.00}O_4$ after 500 °C treatment which agrees well with the intended atomic ratios. The surface topology was investigated by using SEM images, and they indicate a certain porosity, which decreases with increasing sintering temperature (Figure S4).

Requirements for high entropy stabilization

Rost et al. convincingly demonstrated that the system (Mg; Ni; Co; Cu; Zn)O with rocksalt structure is entropy stabilized and we performed the same experiments to verify the entropy stabilization of the spinel. To demonstrate reversibility, which is a basic requirement for entropy driven systems, the as synthesized sample was heated in an oven between 27 and 900 °C and the changes were monitored with in situ PXRD (Figure 3a). The selected Bragg angles from 29 to 34° 2θ represent a good range to show the structural changes. At the beginning just the reflections of the spinel and the reference material ZrO_2 are visible. Further heating to T = 650 °C led to the development of reflections of Fe_2O_3 like observed during the ex situ experiments. With increasing temperature, the intensity of the reflections of Fe_2O_3 is significantly reduced until they are hardly detectable at 900 °C. When the sample is cooled down, the

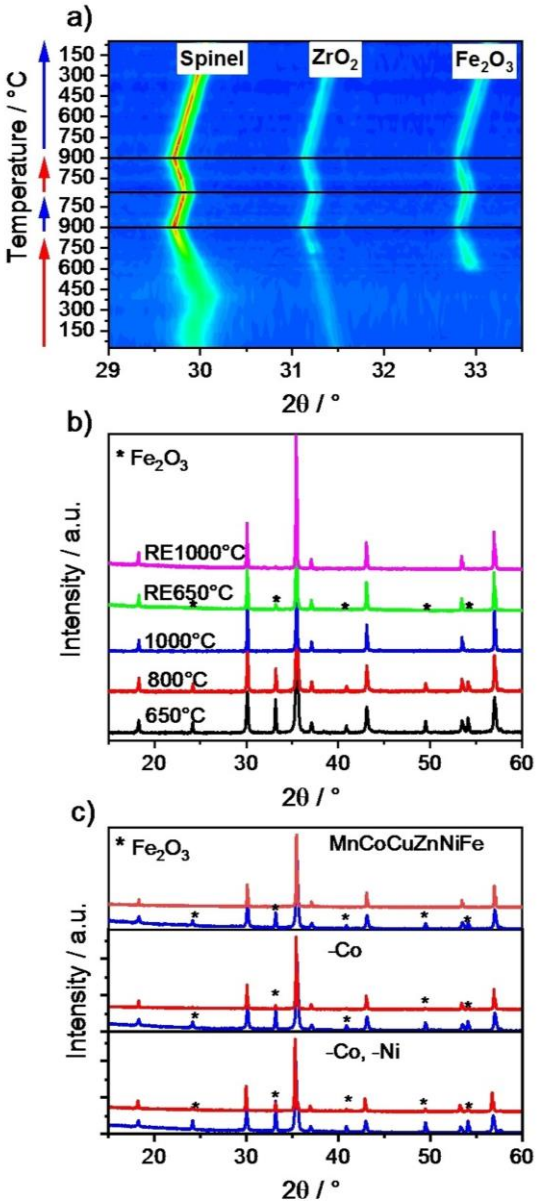

Figure 3. a) In situ XRD intensity map as a function of 2θ and temperature; note that ZrO_2 is used as reference material b) Ex situ XRD analysis of samples heat-treated at different temperatures (RE for returned to). c) removal of components from the initial material and heat treatments at 650 °C (blue) and 1000 °C (red).

Table 3. Crystallite size and lattice parameters obtained from PDF refinements. Estimated standard deviations are given in parentheses.

Samples		Diameter [nm]	Lattice parameters [Å]
HES1s a.s.	Spinel	30	8.4509(1)
	Metals	5	3.5832(4)
HES1s 650 °C	Spinel	49	8.4030(1)
	Haematite	63	5.0458(8), 13.763(4)
HES1s 1000 °C	Spinel	Cryst.	8.4098(1)

© 2022 The Authors. Published by Wiley-VCH GmbH

Chemistry—Methods | Research Article doi.org/10.1002/cmtd.202200043 | Chemistry Europe European Chemical Societies Publishing

intensity of reflections of Fe_2O_3 significantly increases again. Hence, the reversibility of this reaction is impressively demonstrated. Due to the temperature limitation of our in situ stage we were not able to heat to temperatures higher than 900 °C, and therefore an additional ex situ experiment was performed (Figure 3b). It is obvious that heating to 1000 °C leads to formation of a phase pure spinel phase. Low temperature equilibration at 650 °C (Figure 3b, RE650 °C, green pattern) transforms the spinel back into the multiphase state and annealing of this phase mixture at 1000 °C again (Figure 3b, RE1000C, pink pattern) results in crystallization of a single-phase spinel.

Another requirement for entropy-stabilized samples is that removing single components from the mixture results in an increase of the transition temperature for the transformation into the phase-pure product due to the lowered entropy. Removing either Co or Co/Ni it can be undoubtedly demonstrated that at 1000 °C no single-phase product is obtained due to the increased transition temperature, which additionally proves the entropy stabilization of our system (Figure 3c).

TEM investigations

The combination of different TEM methods (HRTEM, SAED and STEM-EDX) was mainly used to study the homogeneity of HES1 samples at 500 °C and 1000 °C. An overview TEM image in Figure 4a displays the crystallite sizes of the HES1 500 °C

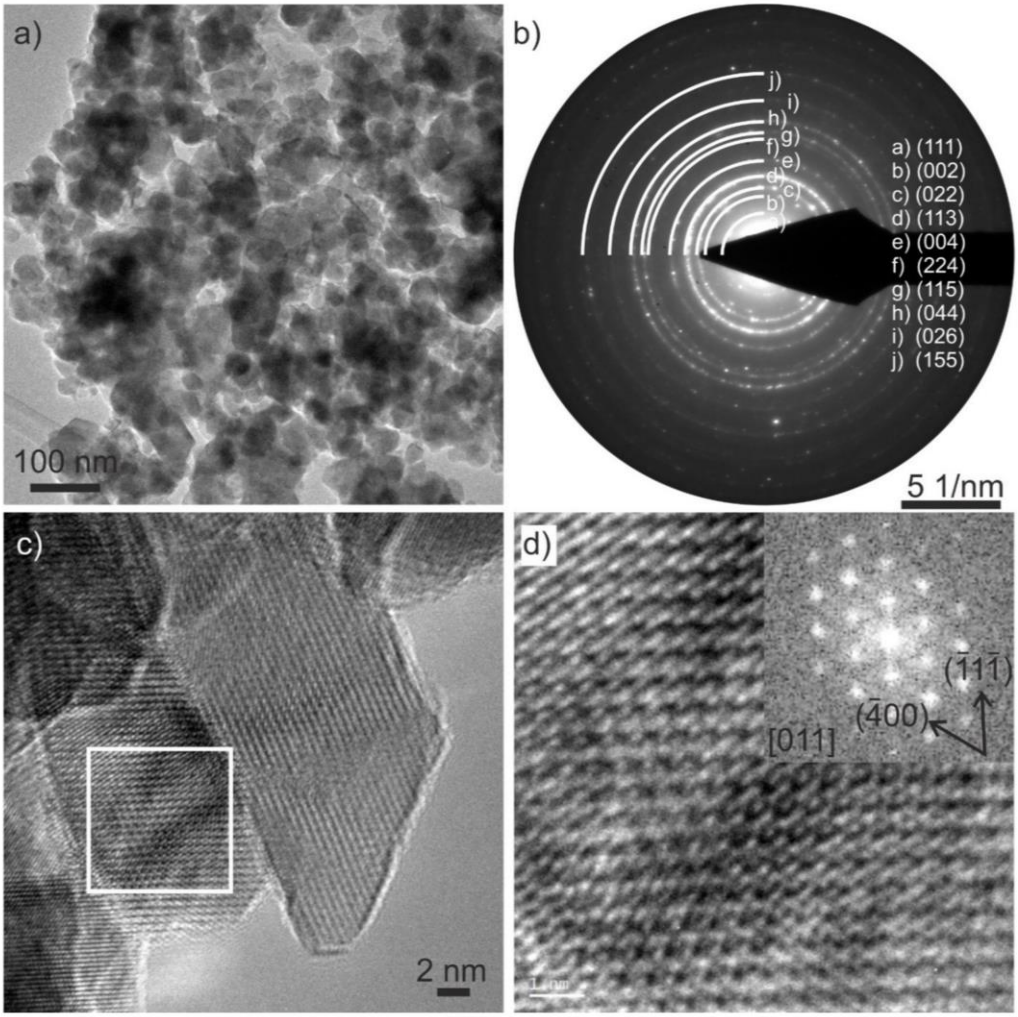

Figure 4. TEM analysis of HES 500 °C sample, a) TEM image shows agglomeration of the powder. b) Reflection intensity on concentric rings in the SAED pattern can be assigned to a spinel phase (described before), the respective crystallographic planes are marked. The crystal structure was verified by c) an HRTEM micrograph showing different crystallites (the marked area is magnified in d)) and d) a magnified HRTEM micrograph with a fast Fourier transform indicating the spinel phase in a [1 1 0] zone axis orientation.

© 2022 The Authors. Published by Wiley-VCH GmbH

Chemistry—Methods | Research Article doi.org/10.1002/cmtd.202200043 | Chemistry Europe European Chemical Societies Publishing

sample. The respective SAED pattern (Figure 4b) from the same sample position shows reflection intensity on concentric rings that can be assigned to a single-phase spinel structure. In particular, no reflection intensities of additional phases such as copper, cobalt, or nickel were observed. The spinel phase formation was verified by HRTEM and respective fast Fourier transforms (Figure 4c and d), showing a pattern that indicates the spinel phase crystallites in the [0 1 1] zone axis. However, the STEM-EDX elemental mapping (Figure S5 and S6) evidences an inhomogeneous distribution of the Cu signal, while the Zn, Mn, Co, Fe, and O signals are homogeneously distributed. This observation indicates partial segregation of Cu, however, the absence of reflection intensities of elemental Cu suggests the formation of an amorphous phase (e.g., CuO_x or CuO_xH_y). It is possible that the segregation of a Cu phase might be induced by the electron beam during STEM-EDX elemental mapping. Figures S6b and S6c show the sample after electron beam irradiation with obvious contrast variations in HAADF-STEM and TEM imaging, respectively. The absence of reflection intensities of a Cu phase before (Figure S6d) and after (Figure S6e) beam irradiation suggests the formation of an amorphous Cu-rich phase. These Cu-rich precipitates can be intrinsic to the sample or formed by the electron beam. In both cases, their amorphous structure would explain why they are not evident in XRD.

The TEM investigation of the HES1 1000 °C sample demonstrates the presence of the spinel phase with a large crystallite size, which is verified by SAED and HRTEM micrographs. A SAED pattern in the [−1 4 −1] zone axis and a HRTEM micrograph with a Fourier transform in the [1 3 0] zone axis is depicted in Figure 5a) and b), respectively. STEM-EDX elemental mapping (c) indicates a homogeneous distribution of all elements on the given scale, without the partial segregation of Cu, which was observed for the HES1 500 °C sample. This observation might be attributed to the large crystallite size of the HES1 1000 °C sample.

Furthermore, dark-field TEM imaging can be used to obtain crystallite size distributions of all four HES1s samples. In dark-field TEM the randomly distributed crystallites partially fulfill the Bragg condition resulting in bright contrast of the crystallites in the images. The increase of average crystallite size with the increasing sintering temperature verifies the results from the Rietveld refinements (Table 2). The histograms (Figure S7) are fitted with a Lognormal distribution function which gives an average crystallite size of 13.9 ± 0.2 nm, 16.1 ± 0.6 nm, and 28.8 ± 1.4 nm for the HES1 a.s., 500 °C, and 650 °C samples, respectively. In accordance to the results of the Rietveld refinement, the HES1 1000 °C sample shows an almost single crystalline structure (crystallite size > 150 nm).

Determination of $Fe^{2+/3+}$ distribution with Mössbauer spectroscopy

Figure 6 shows the room-temperature ^{57}Fe Mössbauer spectra of the high-entropy spinel oxides. The sample heated to 1000 °C clearly shows a sextet pattern revealing magnetic ordering in the spinel structure, even at room temperature. The broad lines in this sextet show an asymmetry that can be described either by superposition of multiple sextets or by a distribution of hyperfine fields. A reasonable fit can be achieved with two sextets with isomer shifts (IS) of 0.29 mm/s and 0.36 mm/s, respectively (Table 4). These values evidence that exclusively trivalent Fe^{3+} is present in the sample. The values of the quadrupole splitting (QS) for the two spectra (Table 4) undoubtedly support the assignment of Fe^{3+}. The hyperfine field of the major sextet (68 %) amounts to 47.8 T, while that of the minor sextet (32 %) is 44.0 T. Similar values have been reported for $MgFe_2O_4$[35] while for $MnFe_2O_4$ slightly larger hyperfine fields have been observed.[36] This is reasonable since $MnFe_2O_4$ contains a larger concentration of paramagnetic cations in comparison to the high-entropy spinels. The broad lines (see Γ values in Table 4) in these sextets and the asymmetry of the single lines are caused by the mixing of the multiple metal ions on the different cation sites in the spinel structure resulting in many different next-nearest neighbor environments around the Fe^{3+} cations. The intensity ratio of 2:1 suggests a random distribution of Fe^{3+} ions on the octahedral and tetrahedral sites of the spinel structure.

The sample heated to 650 °C also shows these two contributions, with similar values for IS, Γ, QS, and a similar intensity ratio of about 2:1 (Table 4). In addition, a third sextet contribution is clearly visible (blue sextet in Figure 6) with IS = 0.37 mm/s, QS = −0.23 mm/s, and a hyperfine field B_{hf} of 51.4 T. These values are consistent with the presence of α-Fe_2O_3 (hematite),[37] in accordance with the PXRD results discussed above. Again, only trivalent Fe^{3+} is present in this sample. It is interesting to note that the splitting of the main sextets is reduced in the sample heated to 650 °C (B_{hf} = 46.4 and 42.2 T,

Table 4. Fit parameters used to describe the Mössbauer spectra of the high-entropy spinel oxides: isomer shift (IS), quadrupole splitting (QS), hyperfine field (B_{hf}), line width (Γ), and area fraction. IS, QS, and Γ are given in mm/s. B_{hf} is given in T. Note that the second fitted contribution of the spectrum of the a.s. sample represents the modelling of the background.

sample	IS	QS	B_{hf}	Γ	area frac.
500 °C	0.289(1)	−0.007(2)	47.2(1)	0.608(5)	67.8 %
	0.333(5)	−0.055(9)	43.2 (1)	1.01(2)	32.2 %
650 °C	0.281(2)	−0.010(4)	46.4(1)	0.62(1)	50.0 %
	0.341(8)	−0.08(2)	42.2(1)	1.02(3)	25.6 %
	0.371(1)	−0.231(3)	51.4(1)	0.324(5)	24.4 %
1000 °C	0.287(1)	−0.006(1)	47.8(1)	0.568(3)	68.2 %
	0.355(3)	−0.046(7)	44.0(1)	0.95(1)	31.8 %
a.s.	0.336(2)	0.771(3)	–	0.904(8)	45.8 %
	0.250(2)	7.094 ± 0.135	–	8.0(4)	54.2 %

© 2022 The Authors. Published by Wiley-VCH GmbH

Chemistry—Methods | Research Article doi.org/10.1002/cmtd.202200043 | Chemistry Europe European Chemical Societies Publishing

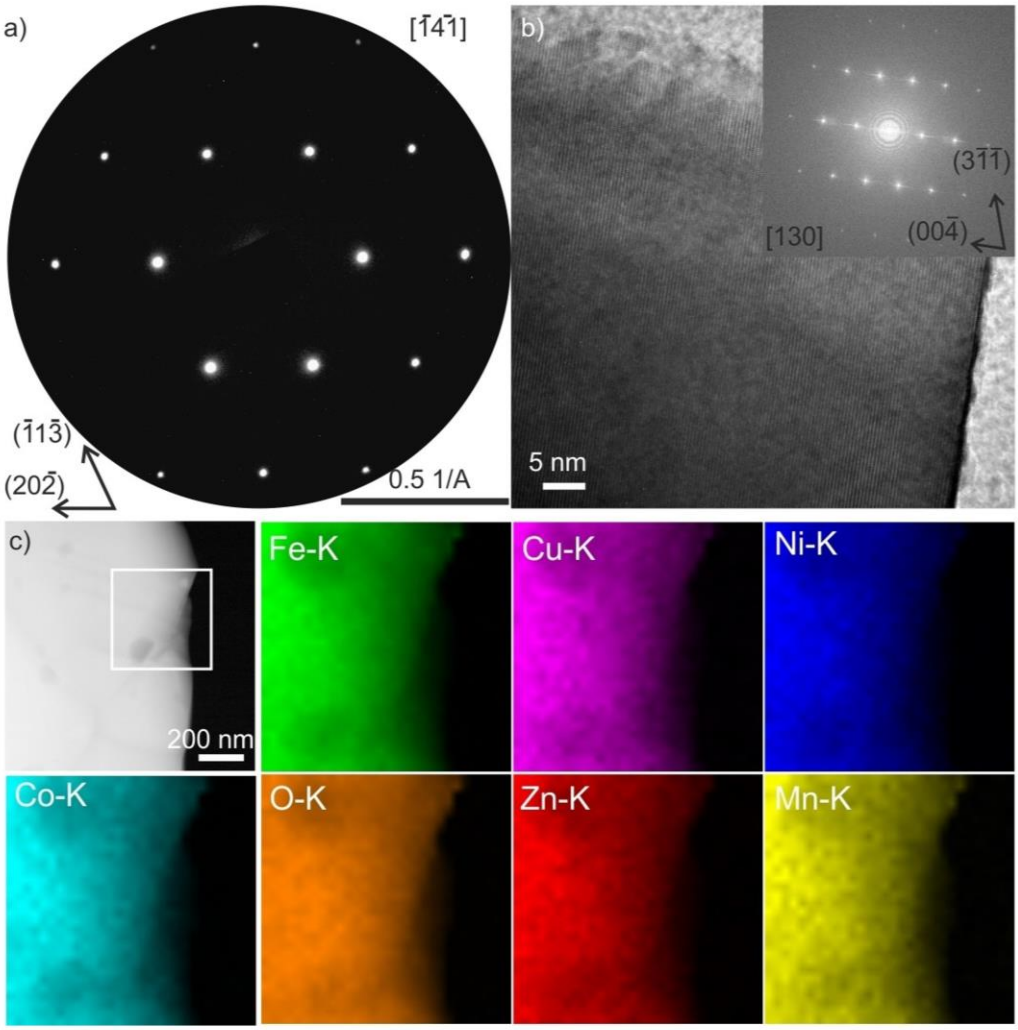

Figure 5. TEM analysis of the HES 1000 °C sample: a) SAED pattern in [−1 4 −1] zone axis verifies the one-phase spinel formation with large (> 150 nm in diameter) crystallite sizes, underlined by a HRTEM micrograph and a fast Fourier transform from a single crystallite with [1 3 0] zone axis orientation. c) STEM-EDX elemental mapping shows a homogeneous distribution of the elements, darker contrast in the HAADF-STEM-image seems to be based on thickness variation.

cf. Table 1) compared to the phase obtained at 1000 °C (47.8 and 44.0 T), probably due to the loss of some Fe in the spinel phase caused by the formation of α-Fe_2O_3.

The spectrum of the material heated to 500 °C is very similar to that of the sample annealed at 1000 °C and gives almost identical fit parameters (Table 4). The fact that the intensity ratio of the two sextets of the main phase (dark red and light red sextets in Figure 6) is always 2:1 for all sintering temperatures (500 °C, 650 °C, and 1000 °C) reveals that Fe cations forming hematite are removed from both crystallographic sites at 650 °C and they are also reinserted on both sites at 1000 °C.

The spectrum of the as-prepared sample shows a doublet with isomer shift IS = 0.34 mm/s and quadrupole splitting QS = 0.77 mm/s. The IS value reveals Fe^{3+} ions on the octahedral sites in the spinel structure. The large line width of this doublet (Γ = 0.90 mm/s) again shows the good mixing of the multiple metal ions around the Fe^{3+} ions. The fact that only a doublet can be observed in this case shows that a magnetic ordering does not occur in the nanocrystalline sample at room temperature. This might be caused by a broad distribution of crystallite sizes, and at least for some fraction of the sample the small crystallite sizes seem to lower the Curie temperature, as it was observed earlier for other nanocrystalline materials.[38,39] A broader background contribution in this spectrum is described with a second doublet with large splitting and large line width of the single lines. This broad component reveals the poor

© 2022 The Authors. Published by Wiley-VCH GmbH

Chemistry—Methods
Research Article
doi.org/10.1002/cmtd.202200043
Chemistry Europe
European Chemical Societies Publishing

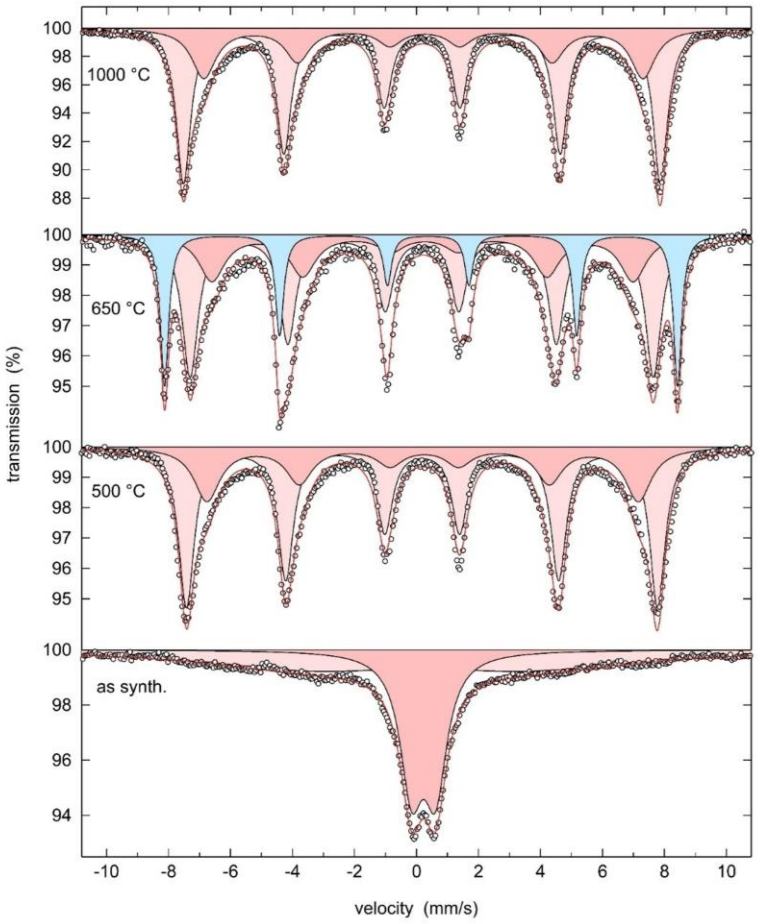

Figure 6. ^{57}Fe Mössbauer spectra of the as-synthesized high-entropy spinel oxide and the samples heated to 500 °C, 650 °C, and 1000 °C. The experimental data points are shown as white spheres, the overall fit as red line, and the subspectra are shown as blue and red doublets/sextets.

crystallinity of this sample and the high degree of disorder. Furthermore, the presence of metallic Ni and Co particles might result in a large variation of local magnetic fields.

Since the crystallite size of the 500 °C sample differs only slightly from that of the a. s. sample, these results confirm that the incorporation of the metals -still present in elemental form in the a. s. sample- drastically changes the magnetic properties (see section 2.7).

The random distribution of Fe^{3+} also supports the assumption of an entropy stabilized spinel.

Investigation of the local environments via X-ray absorption spectroscopy

The XAS results will be discussed in more detail per element in the XANES and EXAFS region. While the XANES region will be used to extract the oxidation state, the structural information will be extracted by using the EXAFS part. The edge position in comparison to reference spectra with well-known oxidation state can be used to get information about average oxidation state in the respective sample. As expected the lower R-region in the Fourier transform (FT) is for most of the samples with oxidation state larger than zero and a nearest neighbor oxygen pretty similar. The region from 2.2–3.5 Å gives valuable information about the environment of the metals in the spinel. An octahedral coordination will show two peaks, the tetrahedral coordination only one significant peak at a higher R-value (Figure 7).

The Mn K-edge region

The edge position of the XANES spectra (Figure 8a) indicates an average oxidation state of three for HES1s a. s. and HES1s 1000, while it is slightly larger for HES1s 500 and 650 (3.5 ± 0.2).

© 2022 The Authors. Published by Wiley-VCH GmbH

Chemistry—Methods
Research Article
doi.org/10.1002/cmtd.202200043
Chemistry Europe
European Chemical Societies Publishing

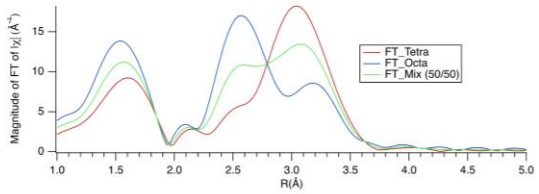

Figure 7. Simulated Fourier Transform (FT) spectra for a backscatter atom in tetrahedral or octahedral crystallographic site in the spinel structure and the spectrum for the mixed case.

The EXAFS spectra show a more complex picture (Figure 8a). In the HES1s 500 and 650 samples Mn cations are mainly octahedrally coordinated, while in HES1s 1000 may be a half-half mix of octahedral and tetrahedral coordinated Mn atoms are present (Figure 8b, compare also Figure 7).

Fe K-edge region

The edge position of the XANES spectra indicates an average oxidation state of three for all samples, and only the Fe cations in HES1s 500 may have a slightly lower oxidation state (Figure 8c).

For HES1s 650 most of the Fe cations seem to be located on octahedral sites (more than 80%) and for the remaining samples a distribution of ≈2/3 on octahedral and ≈1/3 on tetrahedral sites is observed, that is, a random distribution of Fe

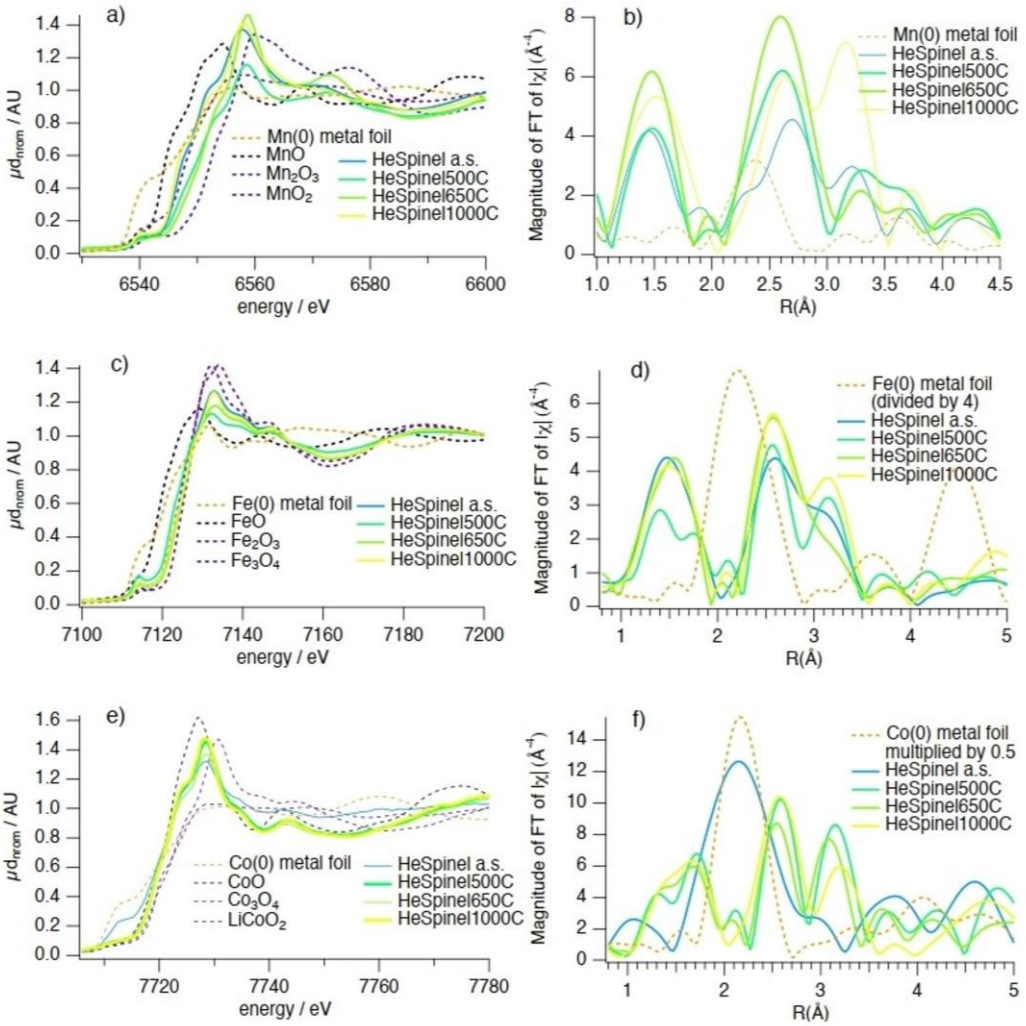

Figure 8. The XANES region of the a) Mn K-edge c) Fe K-edge and e) Co K-edge of the spin samples and of selected reference compounds for comparison; b), d) and f) R-region of the corresponding samples and metal foils (b) Mn, d) Fe, f) Co).

© 2022 The Authors. Published by Wiley-VCH GmbH

Chemistry—Methods | Research Article doi.org/10.1002/cmtd.202200043 | Chemistry Europe European Chemical Societies Publishing

on the available sites. The limited possible measurement range and a Si111 crystal glitch do not allow a more detailed analysis. The oxidation state of 3+ and the random distribution of Fe on tetrahedral/octahedral sites are in good agreement with the Mössbauer results described above.

Co K-edge region

Figure 8e demonstrates that the Co K-edge position of the XANES spectra indicates an average oxidation state of two or slightly higher for samples HES1s 500, HES1s 650, and HES1s 1000. The sample HES1s a.s. contains 2/3 Co in oxidation state zero and 1/3 in oxidation state 2+. The FT of the HES1s a.s. is in good agreement with the XANES results. The blue curve in Figure 8f shows a broad peak together with three additional peaks: one at low R value and two at high R values. The centre of the broad peaks matches with that of the metallic Co foil, that is, it represents the typical Co–Co distance. While the HES1s 1000 sample has a slightly lower amount of occupied tetrahedral sites, the Co atoms in HES1s 500 and 650 show 2/3 octahedral and 1/3 tetrahedral coordination.

Ni K-edge region

The extractable information for the XANES at the Ni K-edge is very similar to that for the Co K-edge. The Ni K-edge position of the XANES spectra indicates an average oxidation state of +2 or slightly higher for samples HES1s 500, HES1s 650, and HES1s 1000. The sample HES1s a.s. consists of 2/3 Ni in oxidation state zero and 1/3 oxidation state 2+ (Figure 9a).

Due to the longer measureble k-range the extractable information of the FT shows much more details compared to the Mn and Fe K-edges. For HES1s 500, HES1s 650, and HES1s 1000 Ni is mainly in an octahedral coordination in the FT. The FT of the HES1s a.s. is in perfect agreement with the XANES results. The violet curve in Figure 9b shows a broad peak with a shoulder at low and high R values, and the centre of the main and broad peak matches with that of metallic Ni evidencing the presence Ni(0) particles.

Cu K-edge region

The XANES spectra at the Cu K-edge can be interpreted similar to those of Ni and Co. A mixture of ≈2/3 Cu^0 and ≈1/3 Cu^{2+} is present in HES1s a.s., while for the remaining samples the average oxidation state is +2 (Figure 9c). The octahedral coordination of Cu^{2+} is evidenced by the two signals located at ≈1.4 and ≈2.6 Å in the FT (Figure 9d) for HES1s 500, HES1s 650, and HES1s 1000. The presence of ≈2/3 metal environment is clearly detected in the FT of HES1s a.s. as the intense signal at ≈2.2 Å matches with that of the Cu foil. The remaining ≈1/3 Cu^{2+} cations are most probably in an octahedral coordination environment.

Zn K-edge region

The XANES spectra of all samples agree well with the presence of most Zn atoms in the oxidation state 2+ (Figure 9e). In contrast to the other elements, the Zn^{2+} cations are solely in a tetrahedral coordination as can be extracted from the FT curves shown Figure 9f. The HES1s a.s. shows a much lower peak intensity, which may indicate very small particles.

Magnetic properties

Magnetic hysteresis loops were measured at room temperature and at 5 K up to 90 kOe, which are displayed in Figure 10. In addition, zfc/fc curves were collected at H = 250 and 1000 Oe from 293 to 2 K (Figure 11). The relevant parameters extracted from the hysteresis loops such as maximal magnetization (M_M), remanent magnetization (M_R) and coercivity (H_C) are listed in Table 5.

The magnetization curves collected at 5 K of the as synthesized sample already exhibits hysteresis. The coercive fields markedly increase for the 500 °C and the 650 °C annealed sample indicative of substantial ferri- or ferromagnetic anisotropy, whereas magnetic hysteresis for the sample annealed at 1000 °C decreases and almost vanishes, resembling a soft ferromagnetic behaviour (Figure 10a–d). The coercive fields correlate with the crystallinity of the sample. For the 500 °C, 650 °C, and 1000 °C samples Figure 11 reveals a linear increase of the coercive fields as a function of the inverse average crystallite size (see Table 2), that is, the smaller the average crystallite size the larger is the coercive field (see Equation (4)).

For all samples hysteresis disappears at room temperature (Figure 10a–d). For the a.s. and the 500 °C sample full saturation cannot be reached even at the largest external magnetic field which is a hint to magnetic frustration and/or a very large crystalline anisotropy, which may be associated with substantial

Table 5. Magnetic properties of the as synthesized sample and samples sintered at 500 °C and 1000 °C.

sample	T [K]	M_M [emu/g]	Magnetic moments [μ_B]	H_C [Oe]	M_R [emu/g]	K 10^3 [erg/g]
a.s.	5	60.9	2.6	824.3	16.8	52.3
	300	46.5	2.0	29.2	1.2	1.4
500 °C	5	92.6	3.9	2414.4	56.9	232.9
	300	71.2	3.0	50.1	5.5	3.7
1000 °C	5	107.7	4.6	101.8	12.2	11.42
	300	81.2	3.4	6.4	0.9	0.5

© 2022 The Authors. Published by Wiley-VCH GmbH

Chemistry—Methods | Research Article doi.org/10.1002/cmtd.202200043 | Chemistry Europe European Chemical Societies Publishing

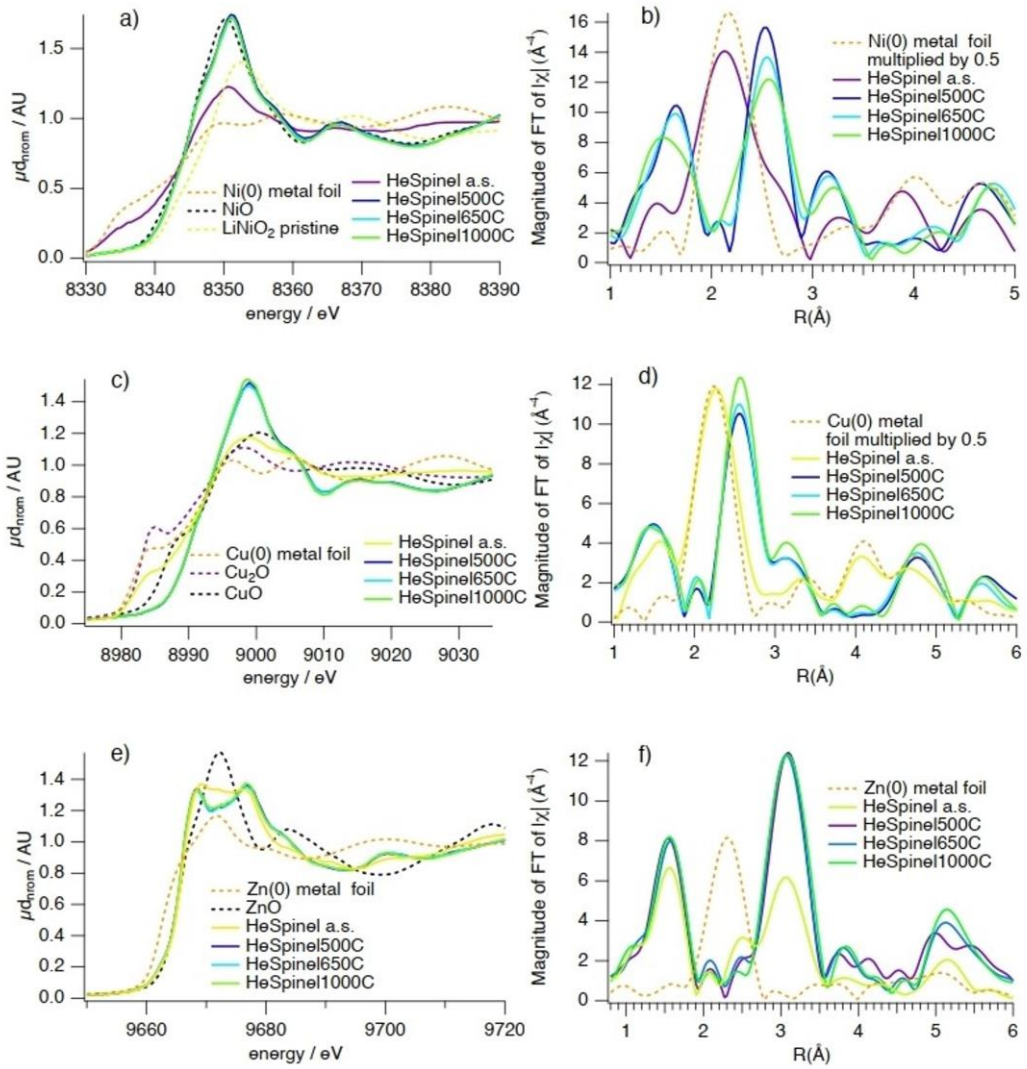

Figure 9. The XANES region of the a) Ni K-edge c) Cu K-edge and e) Zn K-edge of the spinel samples and of selected reference compounds for comparison; b), d) and f) R region of the corresponding samples and metal foils (b) Ni, d) Cu, f) Zn).

surface disorder of the crystallites.[40–42]. The shape of the hysteresis curves of the a.s. samples can possibly be attributed to the presence of two different magnetic contributions, one of the spinel and a softer contribution which we tentatively assign to a minor phase or to intrinsic structural inhomogeneity. For the a.s. sample it is highly likely that the cation distribution is inhomogeneous at the atomic level and one may assume that different small magnetic regions coexist. In addition, nanoparticles are prone to structural defects which also affect the magnetic properties. Impact of Co and Ni metallic nanoparticles to the observed behaviour may also be considered. The value of M_M (Figure 10a) at H = 90 kOe is estimated to be 60.1 emu g^{-1} at 5 K. But taking into account that ≈15% of the phase mixture consists of the metals Co, Ni, and Cu of where only Cu is non-magnetic, the real value for M_M of the spinel phase cannot be seriously estimated. The values for H_C and M_R indicate that the ferri-/ferromagnetic components are soft magnets. After heating the sample to 500 °C (Figure 10b) slight changes of the shape of the hysteresis loop are seen and like for the as synthesized sample two magnetic components seem to contribute to the hysteresis. Initial considerations suggested that an impurity of hematite, not visible in the XRD data, is responsible for this anomaly. However, the hysteresis loop of the 650 °C sample demonstrates that this is not the case and the origin

© 2022 The Authors. Published by Wiley-VCH GmbH

Chemistry—Methods
Research Article
doi.org/10.1002/cmtd.202200043
Chemistry Europe
European Chemical Societies Publishing

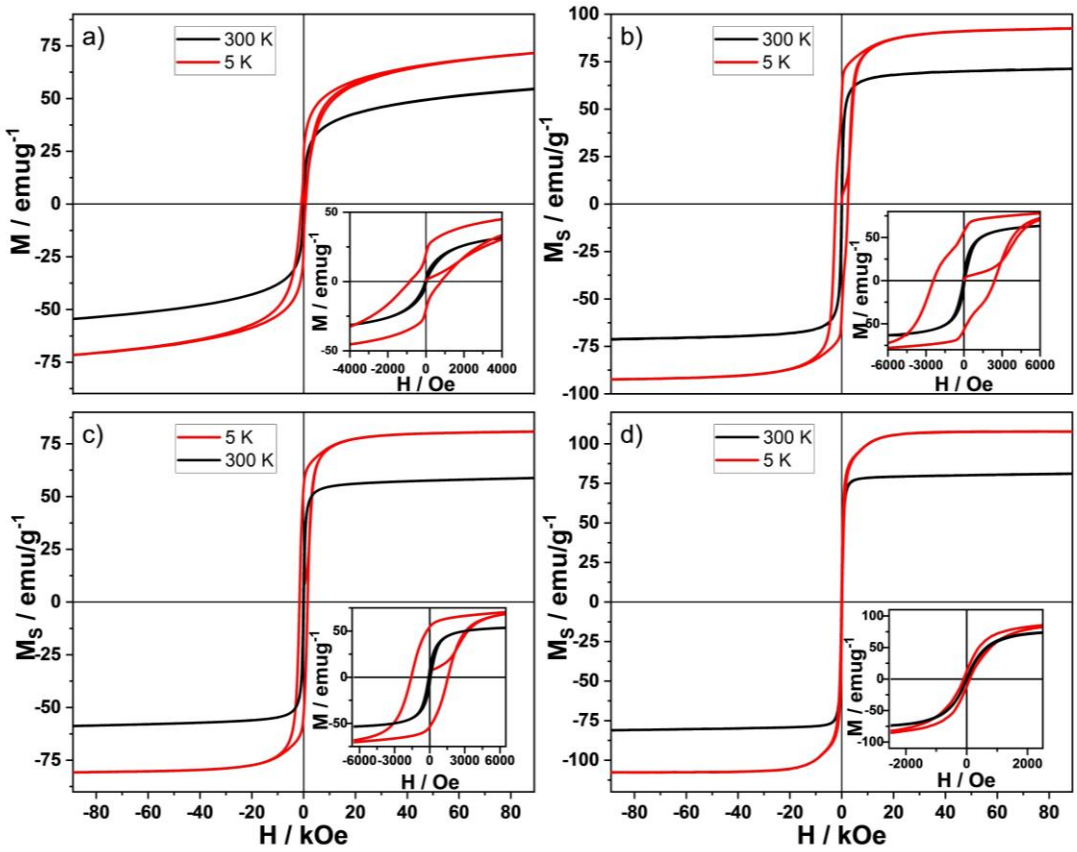

Figure 10. Magnetic hysteresis loops of a) HES1 a.s., b) HES1 500 °C, c) HES1 650 °C and d) HES1 1000 °C at 300 K (black) and 5 K (red), the inset shows the coercivity region.

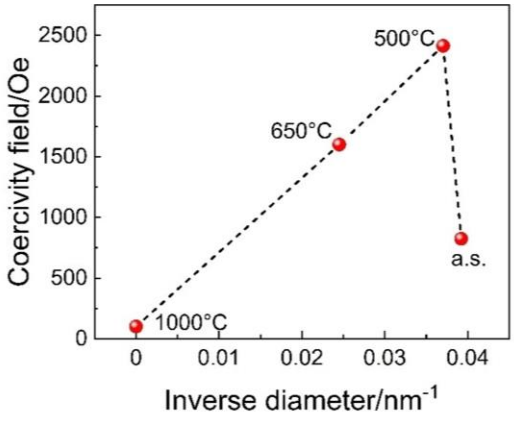

Figure 11. Diagram of linear dependence of the coercivity field versus inverse average crystallite size.

must be different (Figure 10c). Since the crystallite size of the a.s. and 500 °C samples is still on the nanoscale with 25 and 27 nm, respectively, and the crystalline order is still not well developed, magnetic domain effects could also be responsible for the shape of the hysteresis curve (also for the a.s. sample). The splitting of the zfc-fc curve of the 500 °C sample occurs at much higher temperature than for the 1000 °C sample indicating a pronounced domain pinning, and taking into account domain rotations the shape of the hysteresis curve is caused by these effects. Like for the a.s. sample the M(H) cycle is not closed at low magnetic fields up to ≈11 kOe, that is, the magnetic irreversibility is still present but clearly reduced compared to the a.s. sample. In the highest field the hysteresis curve of the 500 °C sample is almost indicating reduction of the surface spin disordered layer and/or of the magnetic frustration. These effects as well as the incorporation of Co, Ni, and Cu into the spinel, which may result in a redistribution of the cations to the tetrahedral/octahedral sites, contribute to the increase in M_M to 92.6 emu g^{-1}. We note that this is an exceptionally high saturation magnetization for 27 nm particles. The strong increase in coercivity from 1648 to 4827 Oe may also be explained by incorporation of Co and Ni into the spinel structure because especially cobalt ferrites possess a high

© 2022 The Authors. Published by Wiley-VCH GmbH

Chemistry—Methods | Research Article doi.org/10.1002/cmtd.202200043 | Chemistry Europe European Chemical Societies Publishing

magnetic anisotropy.[43,44] The precipitation of hematite leads to a slight decrease of the saturation magnetization, which is more pronounced at 5 K, which is quite conclusive due to the magnetic behaviour of hematite (Figure 10c).[45]

Sintering at 1000 °C leads to much larger particles and a larger M_M of 107.7 emu/g (Figure 10c). In contrast to the other samples the M(H) curve is now closed suggesting the removal of magnetic irreversibility. Possible explanations for the enhanced M_M are the reduction of surface effects such as spin canting as evidenced by saturation of the magnetization at relatively low magnetic fields and/or the higher crystallinity, better cation ordering and lower amounts of structural defects.[42] For spinels with general formula AB_2O_4 three different superexchange interactions mainly contribute to the net magnetization: A–A, B–B and A–B with the latter being the strongest one. The B–B interaction is antiferromagnetic but less strong than the ferromagnetic A–B exchange. Hence, the increased value for M_M indicates a redistribution of the cations over the tetrahedral and octahedral sites strengthening the magnetic exchange interactions.

The calculated magnetic moments using Equation (2) increase from 2.6 to 3.9 μ_B (Table 5).[46]

$$\mu_S[\mu_B] = M_M[\frac{\text{emu}}{\text{g}}] \times M_{\text{mol}}[\frac{\text{g}}{\text{mol}}]/5585.8[\frac{\text{emu}}{\text{mol}}] \quad (2)$$

where μ_S = magnetic moments, M_M = maximal magnetization and M = molecular weight

These M_M values are significantly higher than those reported for ferrites containing divalent transition metal cations (Table 6) indicating a better exchange interaction.

The coercivity is strongly dependent on the particle size and in the single domain region it decreases with increasing particle size according to Equation (3),[55]

$$H_C = a + \frac{b}{D} \quad (3)$$

where a and b = constants and D = diameter of the particle, while in the multi-domain region it decreases with increasing particle size according to Equation (4):

$$H_{Ci} = g - \frac{h}{D^{3/2}} \quad (4)$$

where g and h = constants and D = diameter of the particle

This explains the decrease in coercivity with increasing crystallite size and proves that the multi domain state dominates (see also Figure 11).[43]

The total magnetic anisotropy constant K (see Table 5) was calculated via Equation (5):[56]

$$K = \frac{M_S \times H_C}{0.96} \quad (5)$$

But the values for K should be considered as a first estimate because the Stoner–Wohlfahrt model is only applicable if the magnetic nanoparticles do not interact.

For the as synthesized sample the zfc-fc curves show a clear splitting for both applied magnetic fields (Figure 12a). Next to nanosized metal particles, the spinel type material is the main fraction and one can assume that the crystallites of the spinel phase dominate the magnetic anisotropy behaviour. For the 500 °C sample the magnetic anisotropy is even larger than for the as synthesized sample, which is reflected in the zfc-fc curves where the magnetic anisotropy field significantly influences the shape of the curves. A small magnetic field is applied after zfc and due to the large magnetic anisotropy, the magnetisation is low until there is enough thermal energy to overcome the energy barrier for alignment of the spins (Figure 12b). Hence, a large splitting of the zfc and fc curves occurs for the 500 °C sample. The blocking temperature T_B and the curve splitting at irreversible temperature T_{irr} (the largest size of unblocked particles) were determined to be 273 and 297 K, respectively. In contrast to many superparamagnetic materials the zfc curve does not pass a well pronounced cusp and the broad maximum indicates a wide energy barrier distribution. The high thermomagnetic irreversibility (TMI) evidenced by the strong divergence between the zfc and fc curves in the 500 °C sample is significantly reduced for the compound obtained at 1000 °C which contains large multidomain crystallites and less disorder (Figure 12c) leading also to a shift of the splitting of the zfc-fc curves to lower temperatures.

Conclusions

We demonstrated that solution combustion is a powerful method to prepare a starting material for high-entropy spinels consisting of six transition metal cations. Due to the reductive atmosphere during the combustion reaction, metallic nanoparticles precipitated which was evidenced by PXRD and XANES

Table 6. Comparison of the saturation magnetization of the divalent ferrites in comparison to HES1s.

composition	M_M Bulk [emu/g]	M_M Nano (~15 nm) [emu/g]	Reference
$MnFe_2O_4$	98 (5 K)	54 (RT)	[47]
Fe_3O_4	92 (5 K)	56 (RT)	[48,49]
$CoFe_2O_4$	94 (5 K)	30 (RT)	[50,51]
$NiFe_2O_4$	53 (4.2 K)	23 (RT)	[48],[52]
$CuFe_2O_4$	33 (4.2 K)	27–51 (RT)	[53]
$ZnFe_2O_4$	0	65 (RT)	[54]
HEO 500 °C	–	71 (RT)	actual work
HEO 1000 °C	108 (5 K)	–	actual work

© 2022 The Authors. Published by Wiley-VCH GmbH

Chemistry—Methods
Research Article
doi.org/10.1002/cmtd.202200043
Chemistry Europe
European Chemical Societies Publishing

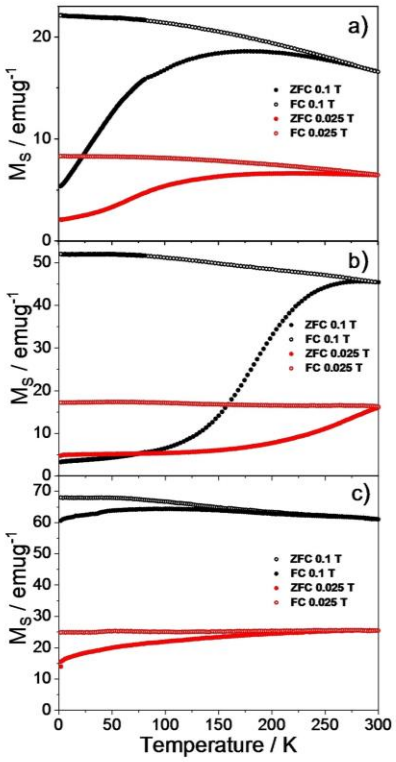

Figure 12. ZFC-FC curves of a) HES1 a.s., b) HES1 500 °C and c) HES1 1000 °C with an applied magnetic field of 1000 Oe and 250 Oe.

investigations. These nanoparticles, however, were completely integrated into the spinel structure by moderate thermal treatment without changing the sizes of coherently scattering domains in the nano-regime. Only at the highest temperature (1000 °C), a well crystalline sample was formed. Thus, we were able to synthesize and study a new class of high-entropy spinels, both as nanoscopic and as highly crystalline materials to get a deeper insight into the nature of such materials. The entropic stabilization of the spinel with general composition $(A1_{0.2}A2_{0.2}A3_{0.2}A4_{0.2}A5_{0.2})Fe_2O_4$ (A1-A5 represent transition metal cations) was evidenced by in situ PXRD and by removal of single constituents of the spinel. The excellent microscopic homogeneity is demonstrated by the PXRD data, SAED and HRTEM micrographs as well as STEM elemental mapping (for the 1000 °C sample). The results of Mössbauer measurements and the information extracted from XANES spectra indicate that ≈2/3 of the Fe^{3+} occupies the octahedral sites and ≈1/3 occupies the tetrahedral sites in the spinel structure, resulting in a degree of inversion of about 66%. The XANES data collected on the K-edges of the other elements suggest that a majority of the cations are randomly distributed between the octahedral and tetrahedral sites, except for Zn^{2+} which is solely in a tetrahedral coordination geometry and Cu^{2+} and eventually Ni^{2+} in an octahedral coordination. Ignoring the measurement uncertainties and assuming full occupancy of the oxygen positions, the following spinel results from these data: $(Co_{0.07}Mn_{0.1}Zn_{0.2}Fe_{0.67})_T(Co_{0.13}Ni_{0.2}Cu_{0.2}Mn_{0.1}Fe_{1.33})_OO_4$.

Magnetic studies show a remarkable high saturation magnetization, where the non-magnetic zinc on the tetrahedral sites is beneficial by inducing an imbalance of the magnetic moments in this antiferromagnetic system. In the present sample the random distribution of the magnetic cations over the crystallographic sites has a positive impact. While TEM and PXRD studies of the 500 °C sample indicate a single phase, the magnetic data show that there may be two magnetic components contributing to the hysteresis, raising the question of whether the magnetic studies are more sensitive and therefore reveal more subtleties of the microstructure. Spinels exhibit a number of outstanding physical properties that have long made them the target of numerous research efforts for a wide range of applications, such as energy storage or catalytic applications.[57–59] Therefore, research into this new class of spinels is an ideal prerequisite for the development of new innovative materials.

Experimental

Chemicals

Metal nitrates and glucose were purchased from Merck and Grüssing. All chemicals used in this study were used as received without further purification.

Synthesis of $Cu_{0.2}Co_{0.2}Mn_{0.2}Ni_{0.2}Zn_{0.2}Fe_2O_4$ (HES1s)

0.47 g (1.6 mmol) $Co(NO_3)_2 \cdot 6H_2O$, 0.39 g (1.6 mmol) $Cu(NO_3)_2 \cdot 3H_2O$, 0.40 g (1.6 mmol) $Mn(NO_3)_2 \cdot 4H_2O$, 0.47 g (1.6 mmol) $Ni(NO_3)_2 \cdot 6H_2O$, 0.48 g (1.6 mmol) $Zn(NO_3)_2 \cdot 6H_2O$, 6.45 g (16.0 mmol) $Fe(NO_3)_3 \cdot 9H_2O$ and 1.6 g (8.0 mmol) glucose were placed in a mortar and 2 drops of water were added until a homogenous viscous material was formed. The sample was transferred to a pre-heated (T = 400 °C, 30 min) round bottom flask with a heating coat and maintained at this temperature for 20 min. During the synthesis, gases evolved which were passed into a washing flask. The formed black powder was naturally cooled to room temperature through a drying column. Afterwards, the samples were subsequently sintered at different temperatures. Accordingly, the samples are labeled as HES1s a.s. (as synthesized) and HES1s T (T = 500, 650 and 1000 °C).

Materials characterization

Powder X-ray diffraction (PXRD) investigations were carried out in transmission and reflexion geometry on a Panalytical Empyrean with $Cu_{K\alpha}$ radiation (λ = 1.54058 Å), a focusing mirror and a PIXcel1D detector. Rietveld refinements[60] against the powder patterns were performed with the program Topas Academic 6.0.[61]

For the in situ temperature resolved XRPD experiments, an X'Pert Pro MPD diffractometer from PANalytical (Ni-filtered $Cu_{K\alpha}$ radiation) with a PIXcel detector equipped with an Anton Paar HTK 1200 N high temperature chamber was used. The detector settings were adjusted to reduce the effect of sample fluorescence. Heating steps of 100 °C were applied in the temperature range 100–500 °C, above this range the increment was 25 °C until a temperature of 900 °C

© 2022 The Authors. Published by Wiley-VCH GmbH

Chemistry—Methods | Research Article doi.org/10.1002/cmtd.202200043 | Chemistry Europe European Chemical Societies Publishing

was reached. All patterns were measured for ~20 min at constant temperature covering a 2θ range of 22–45°.

Total scattering X-ray experiments were performed in Debye–Scherrer geometry using high-energy synchrotron radiation (60 keV, λ = 0.20708 Å) at beamline P02.1 at Petra III (DESY, Hamburg). The total scattering patterns, collected with a XRD1621 Perkin Elmer amorphous silicon image plate detector at a distance of 354 mm, were transformed into atomic pair distribution functions (PDF), G(r), using xPDFsuite.[62] An empty capillary was measured under identical conditions in order to subtract glass contributions to the PDF of the sample. LaB_6 (NIST 660b) was used as standard material to calibrate the instrumental contribution. Theoretical models were fit to the PDF data in the range of 1.7 to 50.0 Å with PDFgui (details in the Supporting Information).[63]

SEM images and EDX data were recorded with a Gemini Ultra55Plus from Zeiss with a SD-Detector from Oxford. Acceleration voltage of 20 kV was applied to detect the K-lines of the elements.

Transmission electron microscopy (TEM): The crystallite size and the morphology were investigated by dark-field and bright-field TEM imaging, while the crystal structure analysis was performed by high-resolution TEM (HRTEM) and selected area electron diffraction (SAED) using a FEI Tecnai F30 STwin G^2 microscope with 300 kV acceleration voltage. For the chemical analysis scanning TEM (STEM), a high-angle annular dark-field detector, and energy dispersive X-ray spectroscopy (Si(Li) detector with EDAX system) was used. The TEM samples were prepared on Al grids with a thin carbon carrier film, therefore the sample powder was dispersed in butanol and drop-casted on the grid.

Analyses of the magnetic properties were done with a Quantum Design PPMS Model 600 in the ACMS setup applying magnetic fields between 1 and 9 Tesla at temperatures of 2–300 K. The samples were prepared from finely ground powder that was encapsulated into a gelatine capsule. The magnetization of the as synthesized sample (a.s.) sample was corrected for the amount of spinel obtained from the Rietveld refinement. A diamagnetic correction was not applied because the standard deviation of the measuring instrument is higher than the diamagnetic value of the samples.

^{57}Fe Mössbauer spectroscopy was performed at room temperature in transmission mode with a constant acceleration spectrometer and a ^{57}Co(Rh) source. All isomer shifts are given relative to that of α-Fe at room temperature.

X-Ray absorption spectroscopy: All samples were measured synchronously in fluorescence and transmission mode at the XAS beamline at the synchrotron at the KIT. Measurements were done with a Si<111>-crystal pair of the double crystal fixed exit monochromator (DCM). Oxford X-Spec ionizations chambers (filling adjusted to 15% in the first chamber, 30% in the second chamber, 60% signal absorption in the third chamber, calculated at 7.5 keV) were used as transmission detectors and an one-element Vortex®-90EX Silicon Drift Detector with XIA xMap detector-electronic for the fluorescence detection. Depending on the resulting signal-to-noise ratio either the transmission or the fluorescence signal was used for the XANES and EXAFS data evaluation. The measurements were undertaken inside a vacuum chamber to maximize the signal-to-noise ratio and reduce the possibility of beam-based sample damage. The samples were transferred with a sample transfer system. Data acquisition was done in step-by-step mode using constant steps of 5, 2 before and 0.5 eV before and in the edge region. After the edge region passed through, constant k-increments of 0.05 were used until the next absorption edge (12–13 *k*, Mn, Fe, Co, Ni) or until 16 *k*. Except for Zn K-edge scans the length of the spectra were limited by the start of the next absorption edge. The *k*-range and thus the spatial resolution of EXAFS measurements were not limited by the noise but due to the limited *k*-range (especially Mn and Fe). These multiple absorption edges lead to a complex background, which is why software based on EXAFS123 in IgorPro (wavemetrics) was used for data analysis.(https://web.archive.org/web/20051031210215/http://www.haverford.edu/chem/Scarrow/EXAFS123/). The core functions of EXAFS123 allow one to analyze the data more accurately than many other EXAFS data analysis programs. In addition to the XANES and EXAFS background subtraction, PCA component analyses were applied based on the existing functions implemented in IgorPro. The XANES and EXAFS curves were extracted for all spectra and were added up as μd data.

Supporting Information Summary

Supporting Information contains graphics of PDF analysis and crystallite morphology, SEM and TEM images and histograms of the crystallite sizes.

Acknowledgments

Financial support by the State of Schleswig-Holstein is acknowledged. The authors thank the German Electron Synchrotron (DESY) and Huayna Terraschke for beamtime allocation. Furthermore, we would like to thank Dr.-Ing. Torben Dankwort for TEM investigations.

Conflict of Interest

The authors declare no conflict of interest.

Data Availability Statement

The data that support the findings of this study are available from the corresponding author upon reasonable request.

Keywords: High-entropy spinel oxides · Magnetic properties · Microstructure · Mössbauer spectroscopy · XANES

[1] Y. Zhang, T. T. Zuo, Z. Tang, M. C. Gao, K. A. Dahmen, P. K. Liaw, Z. P. Lu, *Prog. Mater. Sci.* **2014**, *61*, 1.
[2] S. Wei, F. He, C. C. Tasan, *J. Mater. Res.* **2018**, *33*, 2924.
[3] J.-W. Yeh, *JOM* **2013**, *65*, 1759.
[4] D. B. Miracle, J. D. Miller, O. N. Senkov, C. Woodward, M. D. Uchic, J. Tiley, *Entropy* **2014**, *16*, 494.
[5] C. M. Rost, E. Sachet, T. Borman, A. Moballegh, E. C. Dickey, D. Hou, J. L. Jones, S. Curtarolo, J.-P. Maria, *Nat. Commun.* **2015**, *6*, 8485.
[6] R. Witte, A. Sarkar, R. Kruk, B. Eggert, R. A. Brand, H. Wende, H. Hahn, *Phys. Rev. Mater.* **2019**, *3*, 034406.
[7] A. Mao, F. Quan, H.-Z. Xiang, Z.-G. Zhang, K. Kuramoto, A.-L. Xia, *J. Mol. Struct.* **2019**, *1194*, 11.
[8] J. Dąbrowa, M. Stygar, A. Mikuła, A. Knapik, K. Mroczka, W. Tejchman, M. Danielewski, M. Martin, *Mater. Lett.* **2018**, *216*, 32.
[9] A. Mao, H.-Z. Xiang, Z.-G. Zhang, K. Kuramoto, H. Zhang, Y. Jia, *J. Magn. Magn. Mater.* **2020**, *497*, 165884.

© 2022 The Authors. Published by Wiley-VCH GmbH

Chemistry—Methods | Research Article doi.org/10.1002/cmtd.202200043 | Chemistry Europe European Chemical Societies Publishing

[10] Z. Grzesik, G. Smoła, M. Miszczak, M. Stygar, J. Dąbrowa, M. Zajusz, K. Świerczek, M. Danielewski, *J. Eur. Ceram. Soc.* **2020**, *40*, 835.
[11] M. Stygar, J. Dąbrowa, M. Moździerz, M. Zajusz, W. Skubida, K. Mroczka, K. Berent, K. Świerczek, M. Danielewski, *J. Eur. Ceram. Soc.* **2020**, *40*, 1644.
[12] M. Fracchia, M. Manzoli, U. Anselmi-Tamburini, P. Ghigna, *Scr. Mater.* **2020**, *188*, 26.
[13] D. Wang, Z. Liu, S. Du, Y. Zhang, H. Li, Z. Xiao, W. Chen, R. Chen, Y. Wang, Y. Zou, S. Wang, *J. Mater. Chem. A* **2019**, *7*, 24211.
[14] H. Chen, N. Qiu, B. Wu, Z. Yang, S. Sun, Y. Wang, *RSC Adv.* **2020**, *10*, 9736.
[15] K.-H. Tian, C.-Q. Duan, Q. Ma, X.-L. Li, Z.-Y. Wang, H.-Y. Sun, S.-H. Luo, D. Wang, Y.-G. Liu, *Rare Met.* **2022**, *41*, 1265.
[16] Z. Sun, Y. Zhao, C. Sun, Q. Ni, C. Wang, H. Jin, *Chem. Eng. J.* **2022**, *431*, 133448.
[17] B. Wang, J. Yao, J. Wang, A. Chang, *J. Alloys Compd.* **2022**, *897*, 163188.
[18] K. Chen, X. Pei, L. Tang, H. Cheng, Z. Li, C. Li, X. Zhang, L. An, *J. Eur. Ceram. Soc.* **2018**, *38*, 4161.
[19] S. Jiang, T. Hu, J. Gild, N. Zhou, J. Nie, M. Qin, T. Harrington, K. Vecchio, J. Luo, *Scr. Mater.* **2018**, *142*, 116.
[20] G. Wang, J. Qin, Y. Feng, B. Feng, S. Yang, Z. Wang, Y. Zhao, J. Wei, *ACS Appl. Mater. Interfaces* **2020**, *12*, 45155.
[21] S. K. Shaw, A. Gangwar, A. Sharma, S. K. Alla, S. Kavita, M. Vasundhara, S. S. Meena, P. Maiti, N. K. Prasad, *J. Alloys Compd.* **2021**, *878*, 160269.
[22] S. Marik, D. Singh, B. Gonano, F. Veillon, D. Pelloquin, Y. Bréard, *Scr. Mater.* **2020**, *186*, 366.
[23] S. Marik, D. Singh, B. Gonano, F. Veillon, D. Pelloquin, Y. Bréard, *Scr. Mater.* **2020**, *183*, 107.
[24] F. Hosseini Mohammadabadi, S. M. Masoudpanah, S. Alamolhoda, H. R. Koohdar, *J. Alloys Compd.* **2022**, *909*, 164637.
[25] B. Musicó, Q. Wright, T. Z. Ward, A. Grutter, E. Arenholz, D. Gilbert, D. Mandrus, V. Keppens, *Phys. Rev. Mater.* **2019**, *3*, 104416.
[26] A. Sarkar, R. Kruk, H. Hahn, *Dalton Trans.* **2021**, *50*, 1973.
[27] J. Cieslak, M. Reissner, K. Berent, J. Dabrowa, M. Stygar, M. Mozdzierz, M. Zajusz, *Acta Mater.* **2021**, *206*, 116600.
[28] A. Sarkar, B. Eggert, R. Witte, J. Lill, L. Velasco, Q. Wang, J. Sonar, K. Ollefs, S. S. Bhattacharya, R. A. Brand, H. Wende, F. M. F. de Groot, O. Clemens, H. Hahn, R. Kruk, *Acta Mater.* **2022**, *226*, 117581.
[29] J. Z. Msomi, T. Moyo, J. J. Dolo, *Hyperfine Interact.* **2010**, *197*, 59.
[30] M. Stoia, C. Păcurariu, E.-C. Muntean, *J. Therm. Anal. Calorim.* **2017**, *127*, 155.
[31] E. Ranjith Kumar, T. Arunkumar, T. Prakash, *Superlattices Microstruct.* **2015**, *85*, 530.
[32] K. Heinemann, H. Poppa, *Surf. Sci.* **1985**, *156*, 265.
[33] S. Bid, S. K. Pradhan, *Mater. Chem. Phys.* **2003**, *82*, 27.
[34] Z. Tian, C. Zhu, J. Wang, Z. Xia, Y. Liu, S. Yuan, *J. Magn. Magn. Mater.* **2015**, *377*, 176.
[35] S. Permien, S. Indris, M. Scheuermann, U. Schürmann, V. Mereacre, A. K. Powell, L. Kienle, W. Bensch, *J. Mater. Chem. A* **2015**, *3*, 1549.
[36] S. Permien, H. Hain, M. Scheuermann, S. Mangold, V. Mereacre, A. K. Powell, S. Indris, U. Schürmann, L. Kienle, V. Duppel, S. Harm, W. Bensch, *RSC Adv.* **2013**, *3*, 23001.
[37] S. J. Oh, D. C. Cook, H. E. Townsend, *Hyperfine Interact.* **1998**, *112*, 59.
[38] V. Šepelák, A. Feldhoff, P. Heitjans, F. Krumeich, D. Menzel, F. J. Litterst, I. Bergmann, K. D. Becker, *Chem. Mater.* **2006**, *18*, 3057.
[39] V. Šepelák, I. Bergmann, A. Feldhoff, P. Heitjans, F. Krumeich, D. Menzel, F. J. Litterst, S. J. Campbell, K. D. Becker, *J. Phys. Chem. C* **2007**, *111*, 5026.
[40] R. Topkaya, Ö. Akman, S. Kazan, B. Aktaş, Z. Durmus, A. Baykal, *J. Nanopart. Res.* **2012**, *14*, 1156.
[41] Ò. Iglesias, A. Labarta, *Phys. Condens. Matter* **2004**, *343*, 286.
[42] M. Rahimi, P. Kameli, M. Ranjbar, H. Salamati, *J. Nanopart. Res.* **2013**, *15*, 1865.
[43] Y. Kumar, P. M. Shirage, *J. Mater. Sci.* **2017**, *52*, 4840.
[44] Q. Song, Z. J. Zhang, *J. Phys. Chem. B* **2006**, *110*, 11205.
[45] Ö. Özdemir, D. J. Dunlop, T. S. Berquó, *Geochem. Geophys. Geosyst.* **2008**, *9*.
[46] A. B. Gadkari, T. J. Shinde, P. N. Vasambekar, *J. Mater. Sci. Mater. Electron.* **2009**, *21*, 96.
[47] B. Aslibeiki, P. Kameli, M. H. Ehsani, *Ceram. Int.* **2016**, *42*, 12789.
[48] A. Berkowitz, J. Lahut, C. VanBuren, *IEEE Trans. Magn.* **1980**, *16*, 184.
[49] Y. Wei, B. Han, X. Hu, Y. Lin, X. Wang, X. Deng, *Procedia Eng.* **2012**, *27*, 632.
[50] Z. Chen, L. Gao, *Mater. Sci. Eng. B* **2007**, *141*, 82.
[51] J. L. López, H.-D. Pfannes, R. Paniago, J. P. Sinnecker, M. A. Novak, *J. Magn. Magn. Mater.* **2008**, *320*, e327.
[52] M. Salavati-Niasari, F. Davar, T. Mahmoudi, *Polyhedron* **2009**, *28*, 1455.
[53] G. F. Goya, H. R. Rechenberg, J. Z. Jiang, *J. Appl. Phys.* **1998**, *84*, 1101.
[54] Z.Ž. Lazarević, Č. Jovalekić, V. N. Ivanovski, A. Rečnik, A. Milutinović, B. Cekić, N.Ž. Romčević, *J. Phys. Chem. Solids* **2014**, *75*, 869.
[55] M. George, S. S. Nair, A. M. John, P. A. Joy, M. R. Anantharaman, *J. Phys. Appl. Phys.* **2006**, *39*, 900.
[56] H. Yang, Z. Wang, L. Song, M. Zhao, J. Wang, H. Luo, *J. Phys. Appl. Phys.* **1996**, *29*, 2574.
[57] T. Tatarchuk, M. Bououdina, J. Judith Vijaya, L. John Kennedy, in *Nanophysics Nanomater. Interface Stud. Appl.* (Eds: O. Fesenko, L. Yatsenko), Springer International Publishing, Cham **2017**, 305.
[58] K. K. Kefeni, B. B. Mamba, *Sustain. Mater. Technol.* **2020**, *23*, e00140.
[59] O. Vozniuk, N. Tanchoux, J.-M. Millet, S. Albonetti, F. Di Renzo, F. Cavani, in *Stud. Surf. Sci. Catal.* (Eds: S. Albonetti, S. Perathoner, E. A. Quadrelli), Elsevier **2019**, 281.
[60] H. M. Rietveld, *J. Appl. Crystallogr.* **1969**, *2*, 65.
[61] A. Coelho, **2016**. ■■Dear Author, please complete this reference■■
[62] X. Yang, P. Juhas, C. L. Farrow, S. J. L. Billinge, **2015**, arXiv Preprint arXiv:1402.3163 [Cond-Mat]. DOI: https://doi.org/10.48550/arXiv.1402.3163.
[63] C. L. Farrow, P. Juhas, J. W. Liu, D. Bryndin, E. S. Božin, J. Bloch, T. Proffen, S. J. L. Billinge, *J. Phys. Condens. Matter* **2007**, *19*, 335219.

Manuscript received: July 5, 2022

© 2022 The Authors. Published by Wiley-VCH GmbH

5. Weitere nicht publizierte Ergebnisse

In einem weiteren Projekt, welches noch nicht publiziert wurde, wurde ein drittes Kupfer-Eisen-Sulfid synthetisiert. Es handelt sich um die kupferreiche Verbindung Cu_5FeS_4, dem Bornit, oder auch Buntkupferkies genannt. Die Synthese wurde, ähnlich zu den anderen Sulfiden, mittels Hochtemperatursynthese als Bulkmaterial hergestellt. Bornit wird aufgrund seines hohen Kupferanteils gerne als Kupfer-Erz verwendet.

In dieser Studie wurden die elektrochemischen Eigenschaften von Bornit untersucht und mit den vorher untersuchten Materialien $CuFeS_2$ und $CuFe_2S_3$ verglichen. Dabei lag ein Fokus darauf herauszufinden, ob es eine Korrelation zwischen dem Kupfer/Eisen-Verhältnis und der elektrochemischen Performance gibt. Ein weiteres Hauptaugenmerk war auch bei diesem Material, den zugrundeliegenden Mechanismus aufzuklären, um ein besseres Verständnis für diese Art von Anodenmaterialien zu erhalten.

Bornit zeigte bei den elektrochemischen Untersuchungen ebenfalls eine sehr gute Langzeitstabilität von über 700 Zyklen bei einer Kapazität von 372 mAh g^{-1}. Hierbei erzielte Bornit, berechnet auf die theoretische Kapazität, die beste Leistung, indem konstant 87% der theoretischen Kapazität erreicht wurde, gefolgt von $CuFeS_2$ mit 76 % und $CuFe_2S_3$ mit 71 %. Dies ist ein Hinweis auf den positiven Einfluss des höheren Kupferanteils.

Auch bei Bornit entsteht während des ersten Entladezyklus ein Chvilevaite-Intermediat, $NaCu_2S_2$. Während dieses Intermediat bei den anderen Sulfiden nur kurzfristig auftritt, bleibt es bei Cu_5FeS_4 bis zur Aufnahme von etwa 5 Na konstant vorhanden, bevor es durch weitere Natrium-Aufnahme in Na_2S und FeS_x umgewandelt wird. Die Reflexe des Bornits selbst sind schon nach der Aufnahme von einem Natrium pro Formeleinheit fast vollständig verschwunden.

Zusammenfassend belegen die Untersuchungen, dass die Synergie aus Kupfer und Eisen in einem sulfidischen System zu außerordentlich guten elektrochemischen Eigenschaften führt, die mit den binären Sulfiden ohne Additive oder aufwendigem nanoskopischen Design so noch nicht erhalten wurden. Dabei hat ein höherer Anteil an Kupfer in manchen Bereichen einen positiven Einfluss, jedoch zeigt sich auch, dass dies nicht immer der Fall ist und der Kosten-Nutzen-Faktor abgewogen werden muss.

High temperature syntheses of different copper iron sulfides: a comparative study of their application as anode materials in sodium batteries

Svenja Senkale[a], Wolfgang Bensch[a*]

[a] *Institute of Inorganic Chemistry, Kiel University, Max-Eyth-Str.2, 24118 Kiel, Germany*

Keywords: sodium ion battery, anode material, ternary sulfides, $CuFeS_2$, Cu_5FeS_4, $CuFe_2S_3$, X-Ray scattering, pair distribution function,

1. Introduction

Energy demand has increased by over 160% percent in the last 50 years and the curve is still rising.[1] Due to the rising cost of fossil fuels and the impact of gas emissions like CO_2 on the environment, the urge to find alternatives is increasing.[120] This leads to a great demand for renewable energies like wind and solar energy. However, this call for renewable energy also entails some challenges. Due to the natural strong fluctuations that renewable energies are undergoing, a balance must be created between electricity generation and demand. This is important to ensure a smooth supply of electricity to the grid, which has a constant frequency and strong fluctuations can lead to severe consequences. [121] The storage of energy by the use of pumped storage plants is a common method, but in some regions, it is difficult to be realized due to the flat relief, water deficiency in some areas or the electricity must be transported over long distances which is sometimes accompanied by high efficiency losses.[122] An alternative provides large-scale energy storage systems (LSESS), in which excess energy can be stored and quickly released when needed.

Nowadays, lithium-ion batteries (LIB's) are the most widely used rechargeable batteries in portable applications. The demand for LIB's is increasing, especially in the field of electric mobility.[123] If LSESS with sizes in the range of 10 KWh up to 1 GWh were integrated, the enormous demand for lithium would cause the price to rise alarmingly, considering the easily accessible Li reserves stored in politically sensitive regions. In addition, despite innovative recycling strategies, Li resources could reach their limits. Not to mention the negative impact on the environment caused by the mining of Li and the production of batteries.[123]

On the basis of these facts, there is an urgent need to find a low-cost and abundant alternative. Sodium seems to be a promising candidate. It is the fourth most abundant element in the Earth's crust and possess similar chemical and physical properties like Lithium. The higher redox potential of -2.71 eV and weight 22.99 g/mol, which induce a lower energy density, play no significant role in the field of LSESS.

Nevertheless, the larger radius of Na^+ and the different bonding characteristics leads to different thermodynamic and kinetic properties in sodium-ion batteries (SIB's).[53] This is particularly evident with respect to the choice of the anode material. Graphite, which is the most common anode material for LIBs, cannot be used as an anode for Na without special modifications, although even larger cations such as potassium intercalate in graphite.[124] The use of hard carbons has already achieved great success, but it is associated with high costs and efforts to synthesize these materials, and carbonizing at low temperatures leads to a greater irreversible capacity during cycling. These are causes why a commercialization is not reached yet.[23] To achieve higher capacities, conversion materials are a promising alternative, because due to the usually complete reduction of the metal cations, a larger amount of alkali metal ions can be shuttled per formula unit. However, even these types of anode materials exhibit hurdles that must be overcome, such as limited cyclability due to contact loss caused by high volume work.[71,125] Many conversion materials have already been studied, such as alloys, polyanionic compounds or metal chalcogenides. In the case of SIBs, sulfides are advantageous over oxides because the M-S bond is weaker, which leads to kinetic advantages, and less polar, which results in a decrease of the overpotential.[71] The challenges of contact loss are often overcome by modifications such as the addition of conductive materials like graphene or carbon nanotubes or by designing nanoscopic materials like nanoflowers or tubes. However, this requires considerable efforts and is often accompanied by high costs.

In our recent studies, we have succeeded in designing materials that neither contain additives nor are available as nanostructured materials. They are incorporated into the electrochemical cell as bulk material, which could be shown for ternary copper iron sulfides. While the binary sulfides show poor cyclability,[53,89,90] the ternary compounds such as $CuFeS_2$ and $CuFe_2S_3$ exhibit stability to over 1000 cycles at capacities above 400 mAh g^{-1}.[126,127]

Based on this background, we have synthesized the Cu-rich sulfide Cu_5FeS_4. We extensively studied the electrochemical properties and compared them with the performance of the other two compounds $CuFeS_2$ and $CuFe_2S_3$. The focus of the investigations was on both the

electrochemical properties and the underlying reaction mechanisms in relation to the different Cu:Fe ratios of the three materials. The results may give hints on the influence of the metal ratio so that more targeted anode materials can be designed in the future.

2. Experimental section

2.1 Synthesis of copper iron sulfides

Cu_5FeS_4 was prepared following the procedure reported for $CuFeS_2$ and $CuFe_2S_3$ [126,127]. Stoichiometric amounts of copper (99.9% purity, sourced from Alfa Aesar), iron (99.99% purity, also from Alfa Aesar), and sulfur (99.999% purity, also from Alfa Aesar) were combined and pulverized in a mortar. This mixture was then placed in a vacuum-sealed quartz tube (pressure maintained below 10^{-4} mbar) and gradually heated to 550 °C at a rate of 25 °C per hour. The temperature was maintained at 550 °C for one day, followed by a similar gradual heating process to 950 °C, which was sustained for 5 days. Subsequently, the sample was allowed to naturally cool to room temperature over a 24-hour period.

Following this cooling process, the sample was retrieved from the quartz tube and further ground in an agate mortar within an argon-filled glovebox.

2.2 Electrochemical tests

Each electrode was prepared by combining 70% by weight of $CuFeS_2$, $CuFe_2S_3$, or Cu_5FeS_4, 20% by weight of SUPER C65 Carbon (sourced from Timcal, Switzerland), and 10% by weight of polyvinylidene difluoride (PVdF, obtained from Solvay, Germany), all suspended in NMP (N-methyl-2-pyrrolidone). These mixtures were evenly spread onto either Cu or Al foil using a doctor-blade casting method. The electrode foils were then dried in a vacuum oven at 60 °C for a duration of 24 hours. Subsequently, 10 mm discs were punched out, each containing approximately 1.1 to 1.7 mg of active material.

The assembly of Swagelok® type cells was conducted within an argon-filled glovebox, ensuring that water and oxygen content remained below 1 ppm. Sodium metal was used as the anode, and glass fiber filter disks (from Whatman, United Kingdom) and Celgard® membrane were employed as separators. The electrolyte consisted of a solution containing 1 M sodium trifluoromethanesulfonate ($NaCF_3SO_3$, sourced from Sigma-Aldrich, 98%) in bis(2-methoxyethyl) ether (diglyme, 99+% anhydrous, from Acros).

Galvanostatic measurements were performed using a BST8-WA (MTI Corporation) and BTS 3000 (Neware) battery analyzer. For ex situ measurements, approximately 20 mg of a mixture containing 70% of the sulfide and 30% Super C65 carbon were pressed into pellets at 5 t/50 mm^2, prepared in Swagelok type cells as described earlier, and discharged/charged against Na in Swagelok® cells with a C/20 rate (MTI BST8-WA). After a defined Na uptake/release, the electrochemical reaction was interrupted, and the cells were disassembled within an argon-filled glovebox. The pellets were then retrieved, washed with anhydrous bis(2-methoxyethyl) ether (diglyme), and dried for 24 hours.

Cyclic voltammetric measurements were conducted using a Zahner XPot at a scan rate of 0.1 mVs^{-1}, ranging between 0.01 and 3.00 V. For the galvanostatic intermittent titration technique (GITT) experiment, a current pulse with a duration of 10 minutes at a current rate of 0.11 A (equivalent to C/10) was applied. After each pulse, a relaxation time of 120 minutes was allowed to reach quasi-equilibrium potentials. This procedure was executed within the potential range of 0.1−3.0 V.

2.3 Material characterizations

Powder X-ray diffraction (XRD) investigations were carried out in transmission geometry on a Panalytical Empyrean with Cu Kα radiation, a focusing mirror and PIXcel1D detector. For *ex-situ* synchrotron XRD and pair distribution function analyses measurements the powders were placed in borosilicate capillaries with a diameter of 0.7 mm.

SEM images and EDX data were obtained with a Gemini Ultra55Plus from Zeiss with a SD Detector from Oxford. Acceleration voltage of 20 kV was applied to detect the K-Lines of the elements.

3. Results and Discussion

3.1 Characterization of pristine Cu_5FeS_4

Above 530 K, bornite takes on an antifluorite-type structure within a cubic unit cell (space group: $Fm\bar{3}m$), wherein two cation vacancies are present.[98] These vacancies, along with copper and iron cations, are randomly distributed among the eight available cation sites. Upon cooling below 540 K, the vacancies start to organize, forming a supercell with lattice parameters related to the cubic high-temperature phase through 2a × 2a × 2a known as the 2a structure. As the temperature decreases further, below 460 K, bornite undergoes a transformation into an orthorhombic unit cell (space group *Pbca*) with dimensions of 4a × 2a × 2a, designated as 4a. This 4a structure features alternating zinc blende and antifluorite subcells. Though the specific arrangement of copper and iron cations in the 4a and 2a structures remains uncertain.[128]

Comparing the experimental and calculated XRD patterns it is obvious that Cu_5FeS_4 crystallizing in the $Fm\bar{3}m$ was obtained. The slight differences in the intensities of some Bragg reflections are probably the result of twinning or else of phenomena such as stacking faults and rotational disorder (Figure 1).

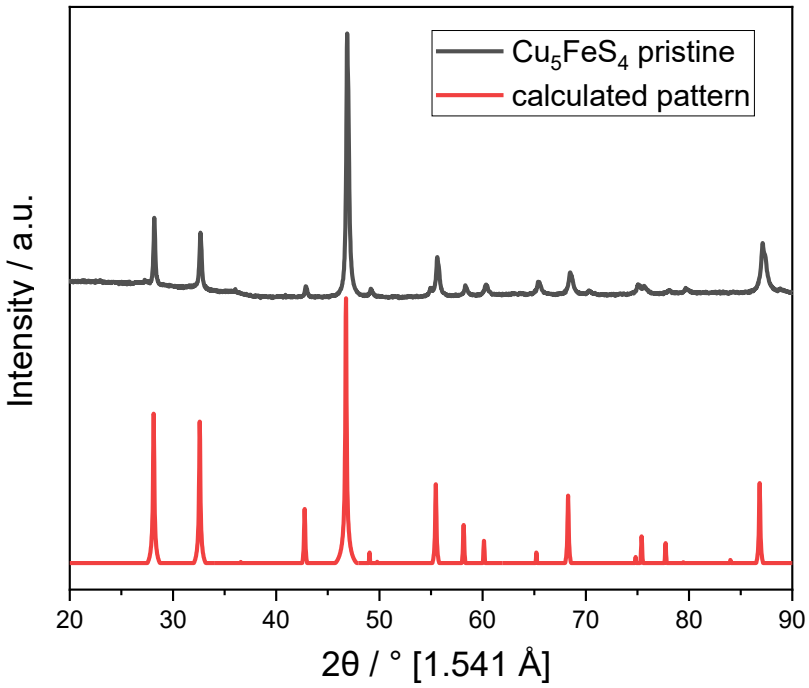

Figure 1: XRD patterns of Cu_5FeS_4 compared to calculated data from the literature. [129]

EDX measurements were performed to verify the stoichiometric composition (Table 1). From the results, a composition of $Cu_{4.8}Fe_{0.9}S_{4.2}$ is be obtained. Since the S Kα emission is easily absorbed by the matrix thus not giving a precise concentration, an additional elemental analysis was performed to determine the sulfur amount (Table 2). To calculate the composition the results for S of the EA were compared to the theoretical value of 25.56 wt. % S in Cu_5FeS_4. To get the full composition the Cu/Cr ratio from the EDX measurements were taken into account and a composition of $Cu_5Fe_{1.1}S_4$ is estimated.

Table 1: Results of EDX measurements of Cu_5FeS_4 powder in the as pristine material.

Sample	**Cu / at%**	**Fe / at%**	**S / at%**
Cu_5FeS_4	48.44	9.31	42.25
Composition	$Cu_{4.8}Fe_{0.9}S_{4.2}$		

Table 2: Results of the elemental analysis of Cu_5FeS_4 powder in the as pristine material.

Sample	**N /wt%**	**C /wt%**	**H /wt%**	**S /wt%**
Cu_5FeS_4	0	0	0	25.40

3.2 Electrochemical characterisation

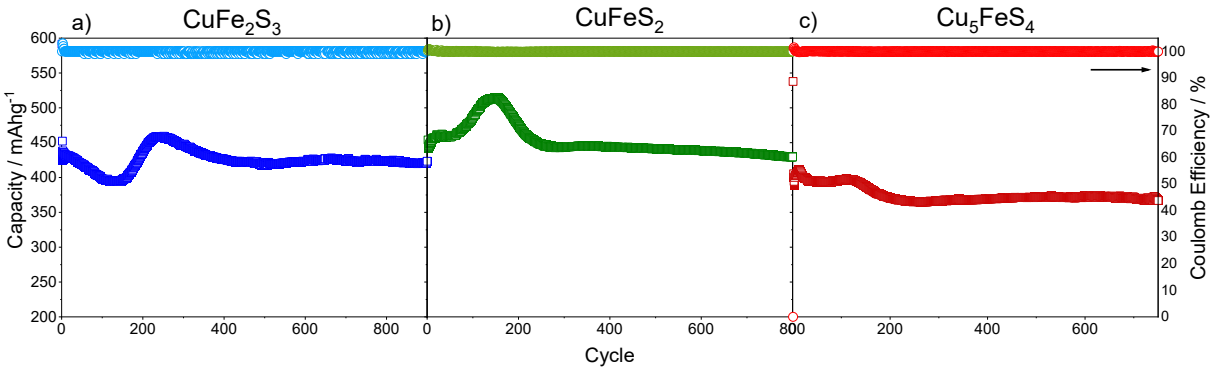

Figure 2: Electrochemical cycling performance of Na/$CuFe_2S_3$ (blue), Na/$CuFeS_2$ (green) and Na/Cu_5FeS_4 (red) at a current rate of 0.5 A g^{-1} in the potential windows of 3.0−0.3 V and the corresponding Coulombic Efficiencies (lighter colour) on the right scale.

The cycling performances of all three copper iron sulphides at 0.5 Ag^{-1} are shown in Figure 2. In all three curves, a maximum is passed before a constant capacitance is reached, indicating a change in the reaction mechanism. A closer look on the curves reveals some clear differences of the cycling behaviour between the three samples. For $CuFe_2S_3$ the capacity first decreases reaching a minimum (395 mAh g^{-1}) at cycle number 136 and afterwards increases reaching the

maximum capacity of 458 mAh g^{-1} (cycle 242). In the next cycles the capacity decreases until a nearly stable value of 422 mAh g^{-1} is achieved for the remaining 600 cycles (Figure 2a). The second compound $CuFeS_2$ shows a clearly different behaviour visible in Figure 2b. In the first few cycles the capacity slightly increases and exhibits a plateau between the 10 and 60 cycles before a further capacity gain is observed. The maximum (513 mAh·g^{-1}) is reached at the 135th cycle and on further cycling continuously decreases to 444 mAh·g^{-1} which is nearly stable up to the final cycle. For Cu_5FeS_4 the capacity is first slightly enhanced and passes a not well-pronounced maximum in the 116th cycle (397 mAh·g^{-1}) before it declines to 365 mAh·g^{-1} and a final capacity of approx. 372 mAh·g^{-1} from the 300th cycle onwards (Figure 2c). Further observations are that for $CuFe_2S_3$ the constant capacity after the maximum is higher than reached before the maximum, while for $CuFeS_2$ it is approximately identical and Cu_5FeS_4 shows a significantly lower capacity compared to the early stages of cycling. Therefore, the electrochemical performance after the maximum seems to be positively influenced by a higher iron content. The temporal occurrence of the maximum also seems to be dependent on the Cu:Fe ratio, since for the Fe-rich $CuFe_2S_3$ the maximum occurs significantly later (start from cycle 145) than for the Cu-rich Cu_5FeS_4 (start from cycle 85).

The theoretical capacities for $CuFe_2S_3$, $CuFeS_2$, and Cu_5FeS_4 are 592, 584 and 427 mAh g^{-1}. It has been established in previous studies that limiting the potential window significantly increases the cycling stability, hence a potential window of 3.0 - 0.3 V was applied. All three materials show exceptionally high cycle stability with more than 700 cycles. $CuFeS_2$ achieves the highest constant capacity of 444 $mAhg^{-1}$, followed by $CuFe_2S_3$ with 422 and Cu_5FeS_4 with 372 $mAhg^{-1}$. The Coulombic efficiencies are higher than 99.9% after the first three cycles (Figure 2). In relation to the theoretical capacity, the materials achieve 71% ($CuFe_2S_3$), 76% ($CuFeS_2$) and 87% (Cu_5FeS_4) in the limited potential window. Here, a higher copper content seems to have a positive effect on the capacity gained.

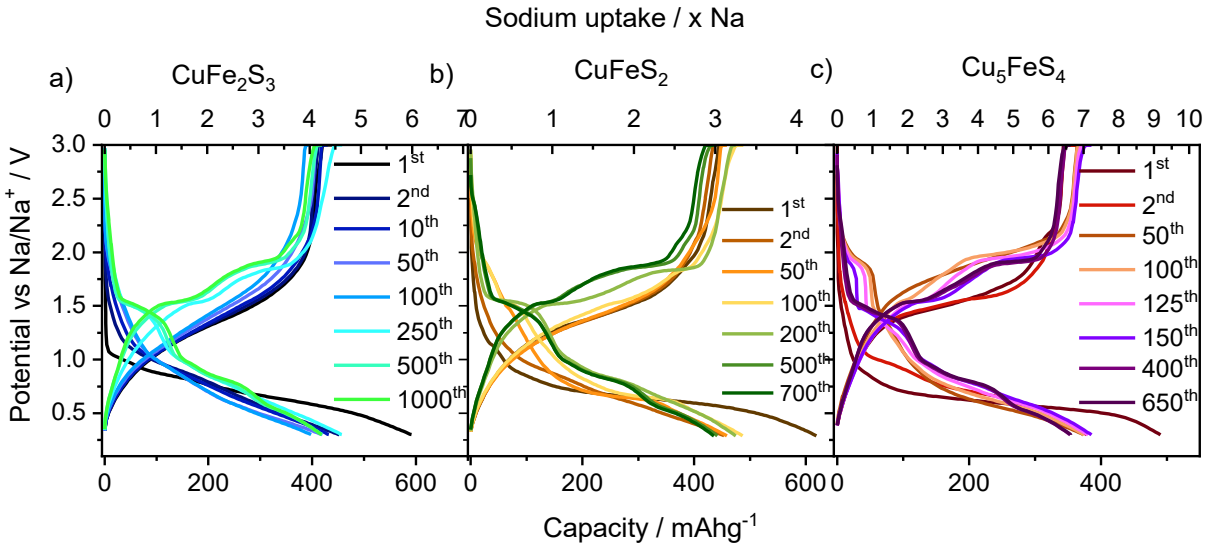

Figure 3: Discharge and charge profiles at a current rate of 0.5 A g^{-1} of various cycles. a) $CuFeS_2$, b) $CuFe_2S_3$ and c) Cu_5FeS_4.

Galvanostatic cycling curves are shown in Figure 3. The first charging and discharging cycle shows no pronounced plateaus for all anodes, and only long pseudo-plateaus are observed in the discharge curve for $CuFe_2S_3$ and $CuFeS_2$ at 0.7 and at 0.6 V for Cu_5FeS_4. In the charge curve, the pseudo-plateau of the former two materials is at 1 – 1.5 V. This is slightly more pronounced for Cu_5FeS_4 from 1.4 to 1.6 V. After passing through the maximum of the cycle stability curve (Figure 2), the galvanostatic curves of all three materials look almost identical. Three plateaus develop in the discharge curve at 1.5, 0.9 and 0.5 V and plateaus are observed in the charge curve at 1.5 and 1.9 V. The most important difference can be seen for Cu_5FeS_4, where a further discharge plateau forms at 1.9 V from cycle 5 onwards, which recedes from cycle 50 to ~200. This difference is also evident in the CV measurements (Figure 4). Whereas the curves for $CuFe_2S_3$ and $CuFeS_2$ barely differ in the first 5 cycles (with the exception of the first cycle), there are already significant changes for Cu_5FeS_4. It can be recognised that the ratios of the two superimposed oxidation processes at 1.46 and 1.56 V change significantly. While the peak at 1.46 V decreases, the signal at 1.56 V increases significantly in the second cycle before it decreases as well until a broad wide signal occurs. Additional oxidation signal forms at 2.15 V. These oxidation signals at 1.56 V and 2.15 V seem to correspond to the Cu_2S vs. Na.[130]

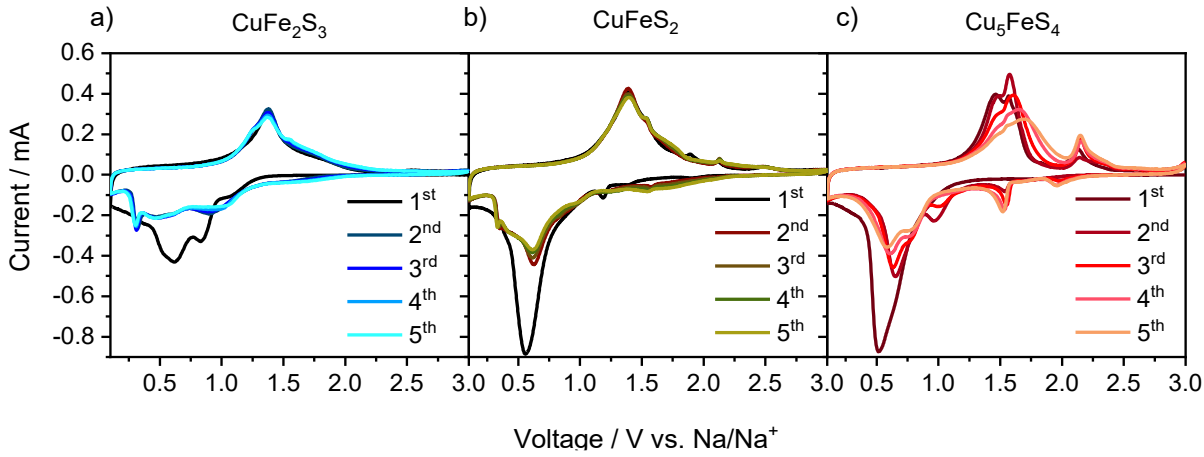

Figure 4: CV analysis in the potential window 3.0−0.1 V for cycles 1 to 5 collected for a) Na/$CuFe_2S_3$, b) $CuFeS_2$ and c) Cu_5FeS_4.

The rate capability investigations with current rates of 0.1, 0.5, 1.0, 2.0, 5.0 and again 0.2 A g^{-1} applied for 12 cycles are shown in Figure 5. The associated values of the specific capacity and the percentage capacity retention related to the specific capacity of the first current rate are listed in Table 3. All three materials show very good rate capability. However, $CuFeS_2$ exhibits a better rate capability compared to $CuFe_2S_3$, especially at current rates up to 2 Ag^{-1}. The higher Cu content seems to have a positive effect here. Since no further improvement can be observed for Cu_5FeS_4, it can be assumed that a distinct minimum of Cu is required to achieve an improved rate capability.

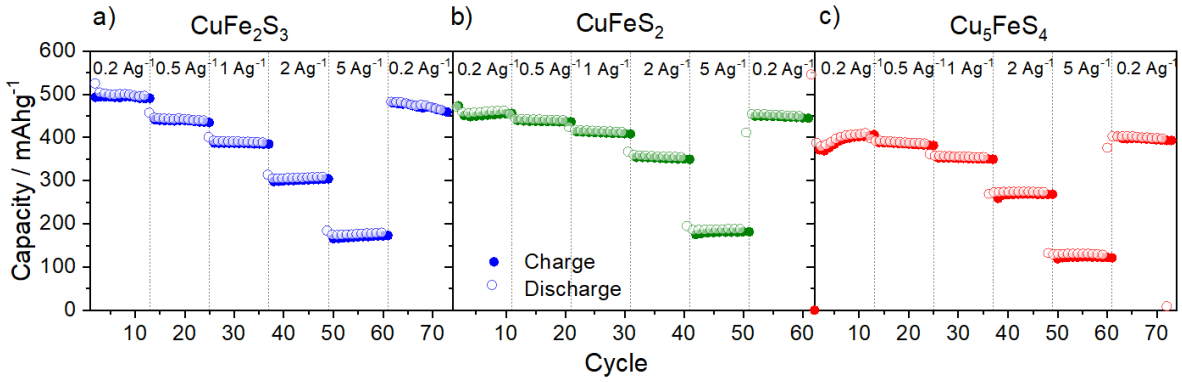

Figure 5: Rate capability at several current rates from 0.2 to 5 A g^{-1} for a) $CuFe_2S_3$, b) $CuFeS_2$ and c) Cu_5FeS_4.

Table 3: Gained capacities and related percentage at different current rates for $CuFe_2S_3$, $CuFe_2S_3$ and Cu_5FeS_4.

Rate [Ag^{-1}]	$CuFe_2S_3$		$CuFeS_2$		Cu_5FeS_4	
	Capacity [$mAhg^{-1}$]	%	Capacity [$mAhg^{-1}$]	%	Capacity [$mAhg^{-1}$]	%
0.2	497.8	100	456.8	100	402.9	100
0.5	440.4	88.5	137.5	95.8	385.1	95.6
1.0	386.2	77.6	411.1	90.0	351.5	87.1
2.0	301.1	60.5	351.3	76.9	268.8	66.7
5.0	169.8	34.1	180.6	39.5	123.7	30.7
0.2	470.2	94.5	449.2	98.3	396.5	98.4

During cycling, all three materials undergo a change in the reaction mechanism before they show a constant retention of capacity. These changes become more apparent in the dQ/dV curves (Figure 6). New oxidation signals appear at about 1.5 and 1.9 V and reduction signals at 1.5, 1.0, 0.75 and 0.6 V. If the curves of the constant capacity retention are compared, it is striking that the oxidation signal at 1.53 V is almost the same, while the peak at 1.86-1.91 V behaves differently, both in position and in shape. While for Cu_5FeS_4 the signal appears as one event and is shifted to higher potentials, the curves of $CuFeS_2$ and $CuFe_2S_3$ show both a shoulder on the left flank at 1.81 V and also on the right side, whereas latter being most pronounced for $CuFe_2S_3$.

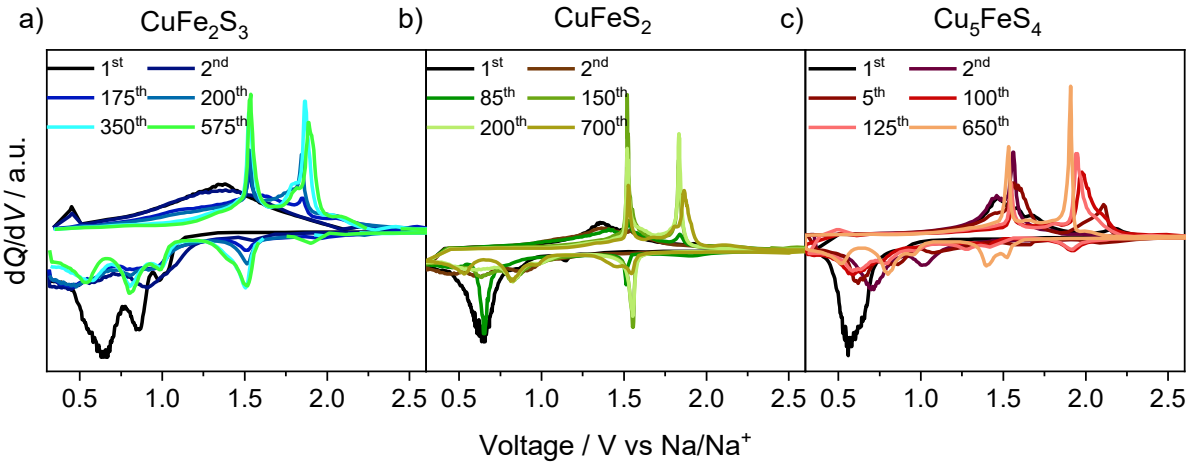

Figure 6: dQ/dV analysis of selected cycles from a) $CuFe_2S_3$, b) $CuFeS_2$ and c) Cu_5FeS_4.

An ex situ investigation of the electrode material at 1.9 V of $CuFe_2S_3$ in the 135th cycle could show that this signal represents the formation of the intermediate $NaCu_xFe_yS_2$.[127] Since the structural position of Fe and Cu is identical and the ratio of Cu:Fe in this intermediate can vary (from $NaCu_2S_2$ to $NaFe_{1.5}S_2$), this could be the explanation for the differences in this oxidation event.

3.3 Ex-situ X-ray diffraction investigations

To gain a better understanding for these materials working as anode materials, ex situ XRD investigations were performed after specific uptake and release of sodium amounts of the first cycle. The XRD patterns with increasing (discharge process) and decreasing (charge process) Na content are displayed in Figure 8 to Figure 10.

It should be mentioned at the outset that the intermediate $NaCu_xFe_yS_2$ (Chvilevaite), which crystallizes in the space group $P\bar{3}m1$ seems to play a fundamental role in all these copper-iron-sulfide materials. Cu and Fe occupy the same structural position and their composition can vary from $NaCu_2S_2$ to $NaFe_{1.5}S_2$, so that it is difficult to determine exactly via XRD which composition is present in these nanostructured samples. The crystal structure of $NaCuFeS_2$ is shown in Figure 7. The structure is related to the $CaAl_2Si_2$ structure type and can be described as a hcp packing of sulfur atoms with Na occupying the octahedral sites in the van der Waals gap whereas Cu and Fe are randomly distributed in the edge sharing sulfur tetrahedra. Along the *c*- axis (Figure 7b), channels are formed between the tetrahedral units in which the sodium atoms are located. The presence of channels and van der Waals gaps supports the diffusion of Na^+ ions.

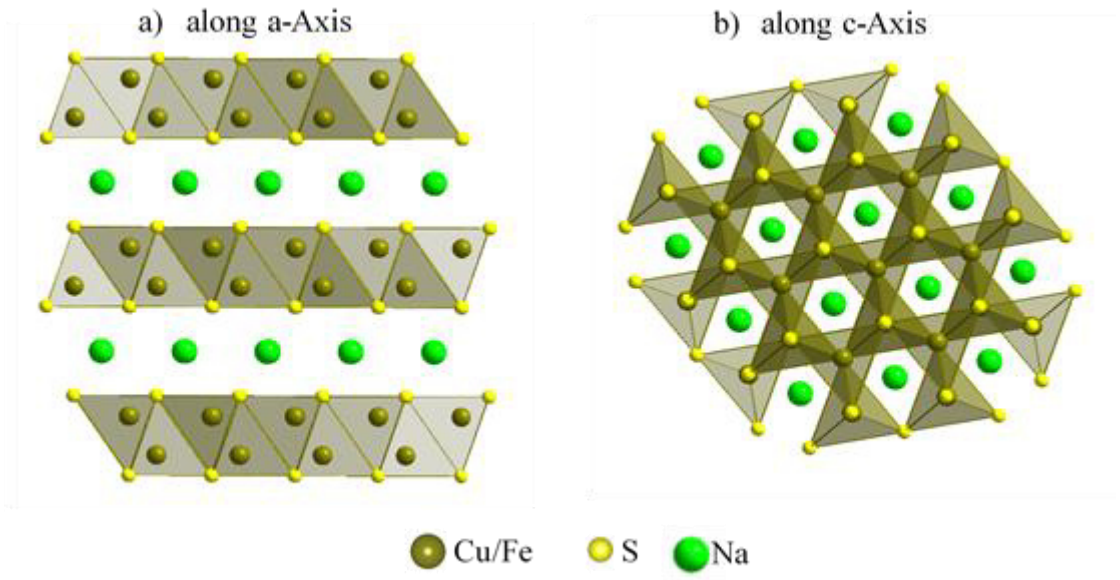

Figure 7: Chrystal structure of Chvilevaite; a) along *a*-axis; b) along *c*-Axis (created with the software VESTA 3.5.8).

In investigations of the binary metal sulfides Cu_xS and FeS_x as anode materials against lithium and sodium, the mechanism is usually postulated via a M_2FeS_2 or via a M_yCu_xS intermediate (M=Li, Na).[78,131–133] In most cases, however, the argument is based on XPS or CV measurements. Structural evidence via XRD was only rarely provided; in most cases, the postulated intermediate could not be detected via XRD. In the case of the ternary sulfides, this evidence was obtained for all three materials.

The occurring mechanisms have all in common that they show Cu, Na_2S and a strongly modulated background in the discharged state, due to amorphous α-Fe. The pathway proceeds always via a Chvilevaite structured intermediate, but with varying reflection intensities and sometimes occurring in parallel with other intermediates. While the mechanism of discharge in $CuFeS_2$ only involves formation of $NaCuFeS_2$ (in this case is most pronounced, as the stoichiometry fits exactly, see Figure 8, for $CuFe_2S_3$ crystalline $CuFeS_2$ is formed simultaneously with $NaCuFeS_2$, which disappears up to a sodium uptake of 3/f.u. Between 1 and 3 Na/f.u. Cu^+ is reduced to elemental copper. Further sodium uptake is leads to the reduction of Fe^{3+} to elemental iron (Figure 8a). Detailed description of the mechanism can be found in publications of Senkale et al.

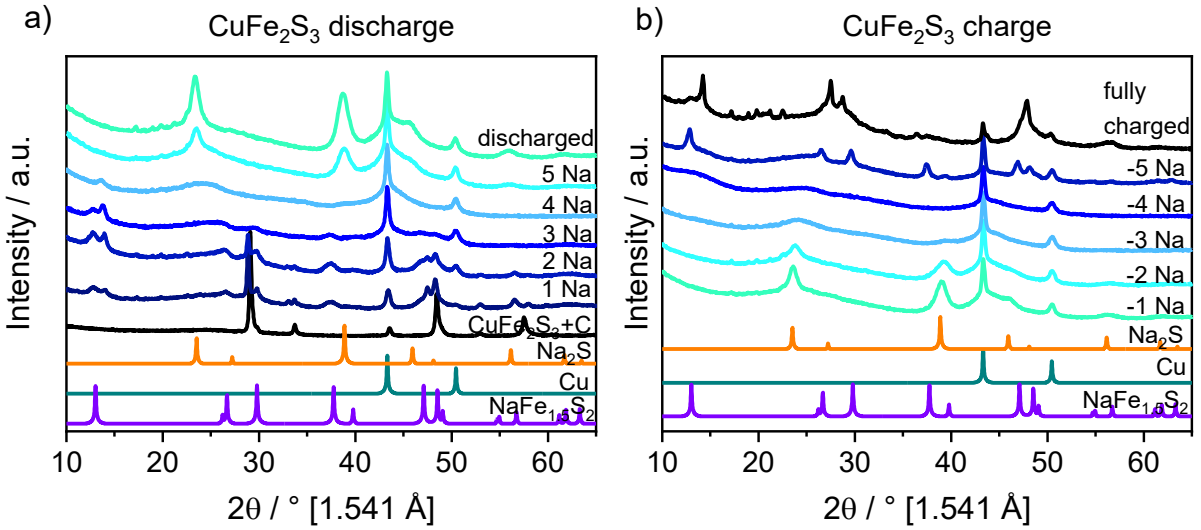

Figure 8: Ex situ X-ray diffraction patterns of the Na/$CuFe_2S_3$ electrode collected at several states of discharge/charge compared to simulated patterns of Na_2S, $NaFe_{1.5}S_2$, and Cu.

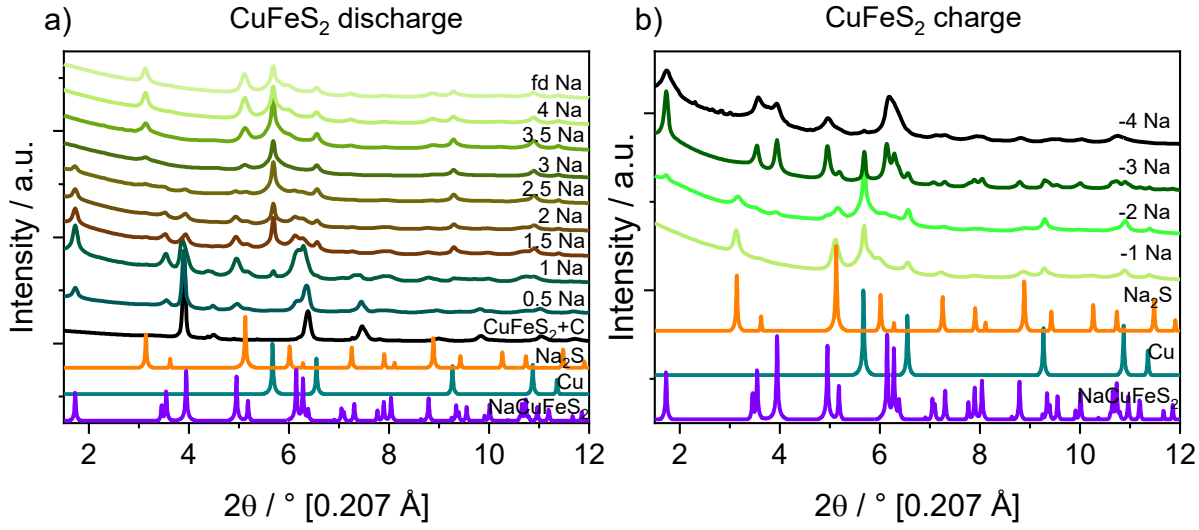

Figure 9: Ex situ X-ray diffraction patterns of the Na/$CuFeS_2$ electrode collected at several states of discharge/charge compared to simulated patterns of Na_2S, $NaCuFeS_2$, and Cu.

The discharge mechanism in Cu_5FeS_4 proceeds in slightly different way. At an uptake of 1 Na/f.u. the intensity of the reflections of Cu_5FeS_4 strongly decrease, but are still visible, while new reflection at 12.8 and 29.7 °2θ can be assigned to the Chvilevaite $NaCu_xFe_yS_2$ phase and to Cu_2S marked with an asterisk (chalcocite $P4_32_12$) (Figure 10a). In addition, a small part of Cu^+ was reduced to elementary copper. During uptake of further sodium, the intensity of reflections related to Cu^0 increases markedly, while the intensity of reflections of initially observed phases decreases. The amount of $NaCu_xFe_yS_2$ and Cu_2S show only a minimal increase. Up to 4 Na/f.u. reflections of Cu_5FeS_4 are completely disappeared and the reflections of Chalcocite Cu_2S are also drastically reduced, whereas the content of Chvilevaite remains quite constant. The amount of Cu^0 is increasing until an uptake of 6 Na/f.u. From this point

onwards reflections assigned to Na_2S developed and all other reflections disappeared. Therefore, we assume that a mechanism will take place in approximately the following way:

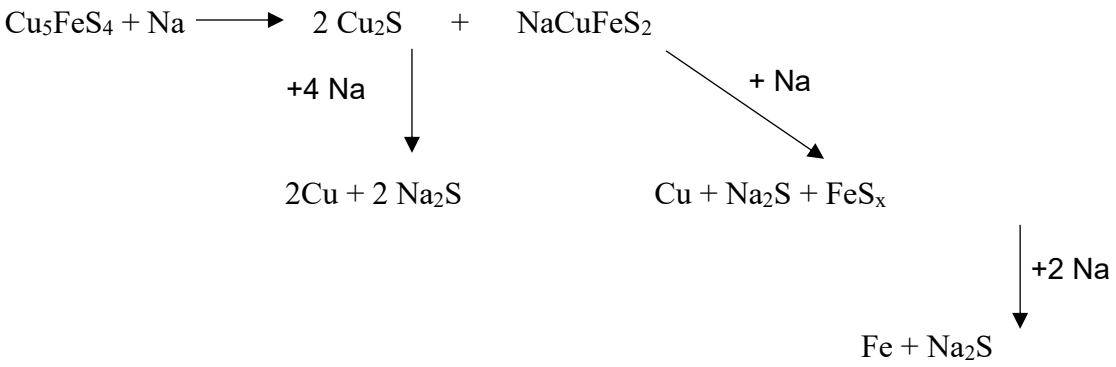

During charging, all materials show the same starting steps. At first reflections of Na_2S disappear, whereas the reflections of Cu are still evident, indicating that Fe is oxidized at first. The $NaCu_xFe_yS_2$ intermediate appears in Cu_5FeS_4 after a release of 7 Na/f.u., for $CuFeS_2$ the appearance of this phase is observed after 3 Na/f.u. and for $CuFe_2S_3$ reflections of $NaCu_xFe_yS_2$ are seen after 5 Na/f.u. For $CuFe_2S_3$ an unknown new phase occurs in the fully charged state, whereas for $CuFeS_2$ the intermediate structure is still visible with a strong broadening of the reflections. For Cu_5FeS_4 most probably the two phases Cu_5FeS_4 and Cu_2S occur in the fully charged state (Figure 10b).

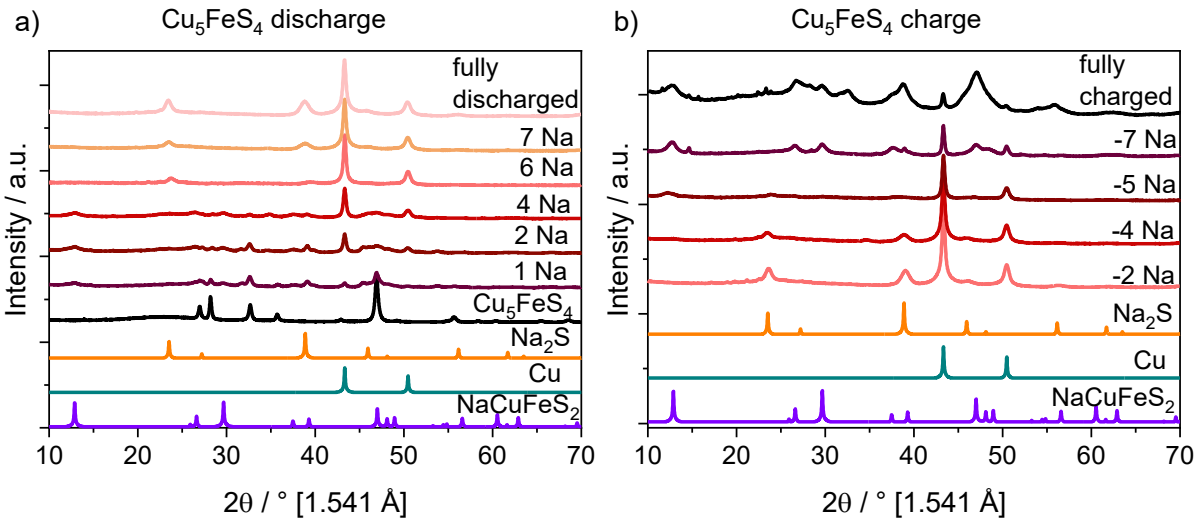

Figure 10: Ex situ X-ray diffraction patterns of the Na/Cu_5FeS_4 electrode collected at several states of discharge/charge compared to simulated patterns of Na_2S, $NaCuFeS_2$, and Cu.

3.5 GITT measurements

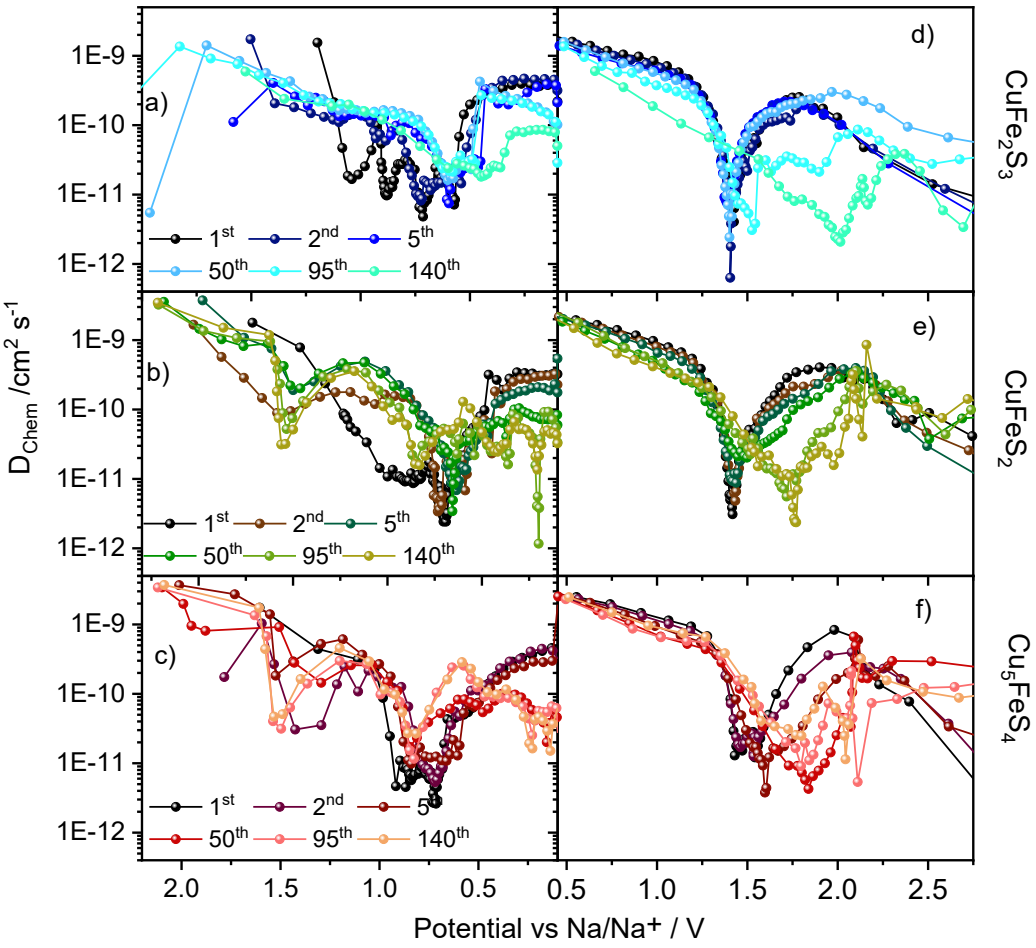

Figure 11: Alteration of chemical diffusion coefficients at different voltages calculated for the 1st, 2nd, 5th, 50th, 95th and 140th GITT cycles. (a) Discharge $CuFe_2S_3$, (b) Discharge $CuFeS_2$, (c) Discharge Cu_5FeS_4. (d) Charge $CuFe_2S_3$, (e) Charge $CuFeS_2$, (f) Charge Cu_5FeS_4.

GITT tests were conducted for cycles 1, 2, 5, 50, 95, and 140 (Figure 11). Of particular interest was the observation of diffusion variation linked to a significant reduction in particle size, transitioning from bulk to nanocrystalline form, which takes place during the initial cycle. The diffusion coefficient of Na^+ (D_{Chem}) as a function of voltage can be determined by solving Fick's second law of diffusion.[41,134] D_{Chem} values calculated from the GITT potential profiles are displayed in Figure 11. In the first discharge cycle, four significant minima at 1.0, 0.9, 0.71, and 0.57 V can be seen for $CuFe_2S_3$, while there is a very pronounced minimum at 0.9 V for

$CuFeS_2$ which is also present for Cu_5FeS_4 but it is somewhat narrower. For both $CuFeS_2$ and Cu_5FeS_4 a significant minimum is visible at 0.7 V. The broader minimum matches with the pseudo-plateau in the discharge curve. The 0.8 V corresponds approximately to the uptake of the first Na/f.u., so that this is the first Na incorporation including the formation of $NaCuFeS_2$. The behaviour is comparable for Cu_5FeS_4, but this phenomenon is much weaker, which could be caused by the formation of a less crystalline Chvilevaite intermediate. The sharper minimum at 0.7 V corresponds to the uptake of 2 Na/f.u. for $CuFeS_2$ as well as for Cu_5FeS_4. So these decreases may be explained by the following electrochemical processes taking place at this point like the decomposition of the intermediate and the formation of Na_2S and Cu. From cycle 2 to 50, almost only the intense minimum at 0.7 V remains for all samples except for Cu_5FeS_4. Here, in the second cycle, a further decrease of D_{Chem} at 1.4 V can be observed, which quickly recedes and reappears from cycle 50 onwards, becoming much more intense with subsequent cycles and having its minimum at 1.5 V. This minimum also develops for $CuFeS_2$ from cycle 50 onwards. It has to be noted that for $CuFe_2S_3$ this minimum cannot be identified in contrast to the other two materials. While the value for D_{Chem} is subject to significant fluctuations in the discharge cycles, it remains fairly constant in the charge curves of $CuFe_2S_3$ and $CuFeS_2$ up to cycle 50 with a pronounced minimum at 1.4 V. Only in the subsequent cycles the minimum shifts to higher voltages. This lowering of D_{Chem} could be due to the regression of the nanocrystalline intermediate. Cu_5FeS_4 undergoes large changes from the first cycle onwards, clearly indicating that the sodium storage mechanism is undergoing continuous changes. From cycle 95 for $CuFe_2S_3$ and from cycle 50 for $CuFeS_2$, major changes in the curve of D_{Chem} begin as well, so that the previously constant mechanism is exposed to alterations. Consequently, $CuFe_2S_3$ shows the most stable mechanism before changes occur, followed by $CuFeS_2$ and Cu_5FeS_4. This is consistent with the cycling stability curves. The cycled maximum of each sample occurs earlier or later in the identical order. Overall, the minima become wider with increasing cycle number. However, only for $CuFe_2S_3$ does this smoothing of the curves also lead to a decrease in the diffusion coefficient for both discharge and charge processes. This can be attributed to the reduced particle sizes and the formation of structural defects, which shorten the diffusion path lengths for Na^+ in the solid phase. For the other two samples, improved diffusion occurs only in the discharge curves, while the diffusion coefficient for the charge process remains similar.

4. Conclusions

In this comparative study, three different copper iron sulfides were investigated and compared with respect to their suitability as anode materials in sodium ion batteries. In addition to the electrochemical properties, the reaction mechanisms were also compared. All three materials exhibited outstanding electrochemical properties which could not be achieved by their binary counterparts without additives or complex modifications. All materials were used as bulk materials and showed very good cycling stability, despite the initial pulverization that always occurs during conversion reactions. $CuFeS_2$ achieved the highest constant capacity of 444 mAh g^{-1}, followed by $CuFe_2S_3$ with 422 and Cu_5FeS_4 with 372 mAh g^{-1}. If this is calculated to the theoretical values, the materials mentioned reach 71 % ($CuFe_2S_3$), 76 % ($CuFeS_2$) and 87 % (Cu_5FeS_4) in the restricted potential window. This finding indicate that a higher Cu content has a positive effect on the capacity gained.

The materials demonstrate impressive ability for higher current rates. Even after subjecting them to current densities as high as 5 Ag^{-1}, all three sulfides return to their original capacity, which was observed at a current density of 0.2 Ag^{-1}. $CuFeS_2$ appears to have a slight advantage over the other materials, as it achieved capacity percentage (relative to the initial rate) remaining consistently 10-15% better compared to the other two samples, especially at higher current densities like e.g. 2 Ag^{-1}. This indicates that a certain level of copper seems to be advantageous, while an increased amount does not lead to further improvement.

The reaction mechanisms of the first cycle were investigated and elucidated. All mechanisms proceed via a Chvivelaite intermediate. While this can be seen as clearly visible reflections in the XRD patterns for $CuFe_2S_3$ and $CuFeS_2$ and plays a strong role, it seems to be minor important for Cu_5FeS_4. The intermediate shows only a low crystallinity and appears in parallel with a copper sulfide phase, Cu_xS. One assumption is that the Fe^{3+} cation with its high mobility contributes significantly to the formation of the intermediate. In the case of $CuFe_2S_3$, it was observed in a previous study that in the second cycle this Chvivelaite intermediate acts as the initial substance, is degraded upon sodium uptake and is recovered with the following charge cycle.

In this research, some new insights into this type of anode materials have been obtained. The synergistic effect of copper and iron could be clearly demonstrated with outstanding cycling and rate stability. Interesting insights into the influence of the copper-iron ratio were achieved, which may be of great benefit for future targeted designs of anode materials.

Author Information

Corresponding Author

*E-mail: wbensch@ac.uni-kiel.de, phone: +49 431 880-2091, fax: +49 431 880-1520

Notes

The authors declare no competing financial interest.

Acknowledgments

Financial support by the State of Schleswig-Holstein is gratefully acknowledged. The authors thank the German Electron Synchrotron (DESY). Parts of this research were carried out at PETRA III. We kindly thank Huayna Terraschke for beamtime allocation.

6. Zusammenfassung und Ausblick

Im Rahmen dieser Arbeit wurde der Fokus auf die Untersuchung von Kupfer-Eisen-Sulfiden als potentielle Anodenmaterialien in NIB gelegt. Diese Elemente wurden bewusst gewählt, da sie umweltfreundlich und abundant sind und zudem verhältnismäßig kostengünstig sind im Vergleich zu anderen Übergangsmetallen. Ein wichtiger Aspekt während der Synthese war die Herstellung eines Volumenmaterials ohne Additive wie u.a. Kohlenstoffderivate oder andere Trägermaterialien, z.B. CNTs oder Graphen, um eine teure und aufwendige Synthese zu vermeiden.

Bei den Untersuchungen war das finale Ziel, die zugrundeliegenden Reaktionsmechanismen der Natriumaufnahme und -abgabe der Anodenmaterialien aufzuklären und deren Performance besser zu verstehen. Dabei zeigte sich, dass die Materialien zwar einige Ähnlichkeiten bei den Reaktionswegen aufwiesen, aber der Einfluss der Kristallstruktur und die unterschiedlichen Kupfer-/Eisen-Verhältnisse doch zu einigen Unterschieden führten.

Es folgt eine kurze Zusammenfassung der wichtigsten Ergebnisse und welche Aspekte zukünftig noch untersucht werden müssen, um mit diesen Ergebnissen einen weiteren Meilenstein in der Batterieforschung zu erreichen.

Um die elektrochemische Leistung der verschiedenen Materialien zu bewerten, wurde der Fokus zunächst auf Langzeit-Zyklen- und Ratenstabilitätsmessungen gelegt. Bei allen Materialien konnte im ersten Zyklus eine Überschreitung der theoretischen Kapazität beobachtet werden, die durch die Bildung der SEI begründet ist. Alle drei Materialien weisen eine hohe Zyklenstabilität von über 700 Zyklen auf. $CuFeS_2$ erreicht die höchste konstante Kapazität von 444 mAh g^{-1}, gefolgt von $CuFe_2S_3$ mit 422 und Cu_5FeS_4 mit 372 mAh g^{-1}. Bezogen auf die theoretische Kapazität erreichen die genannten Materialien 71 % ($CuFe_2S_3$), 76 % ($CuFeS_2$) und 87 % (Cu_5FeS_4) im eingeschränkten Potenzialfenster von 3.0-0.3 V. Diese Beobachtung deutet darauf hin, dass sich ein höherer Kupfergehalt positiv für die maximale Kapazität auswirkt.

Die Materialien weisen eine sehr gute Strombelastbarkeit auf. Selbst nach Anwendung von Stromdichten von 5 Ag^{-1} erreichen alle 3 Sulfide ihre anfängliche Kapazität, die sie bei 0.2 Ag^{-1} erreicht haben, wieder. Hierbei scheint $CuFeS_2$ etwas besser zu sein als die anderen Materialien, da die prozentual erreichte Kapazität (im Vergleich zur Startrate) gerade bei den höheren Stromraten, als Beispiel bei 2 Ag^{-1}, noch um 10-15% besser ist. Dieser Befund deutet

darauf hin, dass ein gewisses Minimum an Kupfer förderlich ist und durch einen größeren Gehalt jedoch keine weitere Verbesserung erreicht wird.

Um den Reaktionsmechanismus zu entschlüsseln, wurde eine Vielzahl an weiteren ergänzenden Charakterisierungstechniken eingesetzt, die unter anderem den elektronischen Zustand und die strukturelle Ordnung erfassen. Die drei Verbindungen weisen bei der Na-Aufnahme einen gemeinsamen Reaktionsschritt, nämlich die Bildung des Intermediats $NaCu_xFe_yS_2$, welche eine Chvilevaite verwandte Struktur aufweist. Dieses Intermediat scheint eine Schlüsselrolle zu spielen und nanokristalline Strukturen dieses Intermediats können selbst nach mehreren hundert Zyklen bei $CuFe_2S_3$ und Cu_5FeS_4 nachgewiesen werden zusammen mit Cu_xS, Cu und Na_2S. Dies ist ein erstaunliches Ergebnis, da bei den meisten Konversionsreaktionen nach wenigen Zyklen nur noch amorphe Phasen vorliegen. Der Erhalt einer gewissen Kristallinität scheint die Langzeitstabilität deutlich zu verbessern, da der Kontaktverlust aufgrund der verringerten Volumenarbeit und der guten elektrischen Leitfähigkeit einzelner identifizierter Phasen minimiert wird.

Perspektivisch sollte strategisch untersucht werden ob die elektrochemischen Eigenschaften noch weiter optimiert werden können, zum Beispiel durch die Wahl des Leitsalzes, des Binders und deren Menge. Die hier untersuchten Übergangsmetallsulfide werden als Anode genutzt, während metallisches Natrium als Gegenelektrode verwendet wurde. Für anwendungsnahe Zwecke sind jedoch Vollzellen erforderlich. Dies wirft folgende Fragen auf: Gibt es passende Kathodenmaterialien und welche Elektrolyte sollen in einer Vollzelle verwendet werden? Wie gut ist deren elektrochemische Leistung? Ebenso sollte die Beladung auf dem Elektrodenfilm variiert werden, um den Einfluss der Schichtdicke und des aktiven Materials pro cm^2 zu untersuchen. Die elektrochemische Dilatometrie (ECD) in situ (operando) wäre in der Lage, Informationen über die Ausdehnung/Schrumpfung einer Elektrode während des Zellzyklus zu liefern.

Da weder Kupfersulfide noch Eisensulfide als Bulkmaterial solche außergewöhnlich guten elektrochemischen Eigenschaften wie die ternären Verbindungen zeigen, scheinen synergistische Effekte eine wichtige Rolle zu spielen. Daraus entstand die Idee sich mit Mehr-Element-Systemen wie den entropie-stabilisierten Materialien zu befassen, deren Eigenschaften in der dritten Publikation diskutiert wurden. Es wurde gezeigt, dass eine oberflächliche Untersuchung dieser Materialien nicht ausreicht, um sowohl die Phasenreinheit als auch die Entropiestabilisierung zu beweisen. Durch die Untersuchung der magnetischen

Eigenschaften konnte nachgewiesen werden, dass durchaus interessante neue Eigenschaften generiert werden können. Um diese innovativen Materialien in die Thematik des Einsatzes von Übergangsmetallsulfiden in NIB einzubinden, wäre perspektivisch höchst interessant sulfidische entropiestabilisierte Verbindungen zu synthetisieren und in NIB zu untersuchen.

7. Literaturverzeichnis

[1] T. Kober, H.-W. Schiffer, M. Densing, E. Panos, *Energy Strategy Reviews* **2020**, *31*, 100523.
[2] U.S. Energy Information Administration, **2019**.
[3] O. US EPA, "Inventory of U.S. Greenhouse Gas Emissions and Sinks," https://www.epa.gov/ghgemissions/inventory-us-greenhouse-gas-emissions-and-sinks, **2017**.
[4] "Climate Data for Action | Climate Watch | Emissions and Policies https://www.climatewatchdata.org/?source=cait,**2023**
[5] H. Ritchie, M. Roser, P. Rosado, *Our World in Data* **2022**.
[6] "IEA – International Energy Agency," https://www.iea.org/data-and-statistics/data-products, **2023**
[7] M. Schumann, D. Schulz, *Hamburger Beiträge zum technischen Klimaschutz* **2021**.
[8] Ł. Sobol, A. Dyjakon, *Energies* **2020**, *13*, 4267.
[9] C. Kurien, A. K. Srivastava, *Integr. Environ. Assess*. Manag. **2020**, *16*, 234–244.
[10] P. Wolfram, T. Wiedmann, *Appl. Energy* **2017**, *206*, 531–540.
[11] V. Smil, *Energy Transitions: Glob. j. manag. persp , 2nd Edition*, Praeger, **2016**.
[12] C. Buchal, H.-D. Karl, H.-W. Sinn, **n.d.**, 16.
[13] H.-W. Sinn, *Eur. Econ. Rev.* **2017**, *99*, 130–150.
[14] "Unlocking the Green Hydrogen Revolution," https://www.siemensgamesa.com/en-int/products-and-services/hybrid-and-storage/green-hydrogen/unlocking-the-green-hydrogen-revolution, **2021.**
[15] "World Energy Outlook 2020 – Analysis," https://www.iea.org/reports/world-energy-outlook-**2020.**
[16] H. Ambrose, A. Kendall, *J. Ind. Ecol.* **2020**, *24*, 80–89.
[17] F. Meng, J. McNeice, S. S. Zadeh, A. Ghahreman, *Miner. Process. Extr. Metall. Rev.* **2021**, *42*, 123–141.
[18] X. He, S. Kaur, R. Kostecki, *Joule* **2020**, *4*, 1357–1358.
[19] X. Zhao, H. Yang, Y. Wang, Z. Sha, *J. Electroanal. Chem. Interfacial Electrochem.* **2019**, *850*, 113389.
[20] J. Xiao, X. Li, K. Tang, D. Wang, M. Long, H. Gao, W. Chen, C. Liu, H. Liu, G. Wang*, Mater. Chem. Front.* **2021**, *5*, 3735–3764.
[21] M. Chen, Q. Liu, S.-W. Wang, E. Wang, X. Guo, S.-L. Chou, *Adv. Energy Mater*. **2019**, *9*, 1803609.
[22] C. Hakim, N. Sabi, I. Saadoune, *J. Energy Chem.* **2021**, *61*, 47–60.
[23] F. Xie, Z. Xu, Z. Guo, M.-M. Titirici, *Prog. Energy* **2020**, *2*, 042002.
[24] H. Hou, X. Qiu, W. Wei, Y. Zhang, X. Ji, *Adv. Energy Mater.* **2017**, *7*, 1602898.
[25] M. Krengel, A.-L. Hansen, F. Hartmann, J. van Dinter, W. Bensch, *Batteries Supercaps* **2018**, *1*, 176–183.
[26] M. Krengel, A.-L. Hansen, M. Kaus, S. Indris, N. Wolff, L. Kienle, D. Westfal, W. Bensch, *ACS Appl. Mater. Interfaces* **2017**, *9*, 21283–21291.
[27] J. O. Besenhard, G. Eichinger, *J. Electroanal. Chem. Interfacial Electrochem*. **1976**, *68*, 1–18.
[28] G. Eichinger, J. O. Besenhard, *J. Electroanal. Chem. Interfacial Electrochem* **1976**, *72*, 1–31.
[29] M. B. Armand, M. Duclot, *Electrochemical Generators for Producing Current and New Materials for Their Manufacture*, **1981**, US4303748A.
[30] M. S. Whittingham, *Science* **1976**, *192*, 1126–1127.
[31] K. Mizushima, P. C. Jones, P. J. Wiseman, J. B. Goodenough, *Mater. Res. Bull.* **1980**, *15*, 783–789.
[32] A. Yoshino, *Nat Energy* **2021**, *6*, 449–449.
[33] Y. Nishi, *Electrochem. Soc. Interface* **2016**, *25*, 71.

[34] W. He, W. Guo, H. Wu, L. Lin, Q. Liu, X. Han, Q. Xie, P. Liu, H. Zheng, L. Wang, X. Yu, D.-L. Peng, *Adv. Mater.* **2021**, *33*, 2005937.

[35] Q. Wang, L. Jiang, Y. Yu, J. Sun, *Nano Energy* **2019**, *55*, 93–114.

[36] Y. Wang, N. An, L. Wen, L. Wang, X. Jiang, F. Hou, Y. Yin, J. Liang, *J. Energy Chem*. **2021**, *55*, 391–419.

[37] X. Ji, Q. Xia, Y. Xu, H. Feng, P. Wang, Q. Tan, *J. Power Sources* **2021**, *487*, 229362.

[38] "Global EV Outlook 2022 – Analysis," https://www.iea.org/reports/global-ev-outlook-**2022**.

[39] G. Zubi, R. Dufo-López, M. Carvalho, G. Pasaoglu, *Renewable and Sustainable Energy Rev.* **2018**, *89*, 292–308.

[40] N. Nitta, F. Wu, J. T. Lee, G. Yushin, *Mater. Today* **2015**, *18*, 252–264.

[41] B. Babu, M. M. Shaijumon, *Electrochim. Acta* **2020**, *345*, 136208.

[42] D. Sauer, G. Fuchs, B. Lunz, M. Leuthold, *Technology Overview on Electricity Storage - Overview on the Potential and on the Deployment Perspectives of Electricity Storage Technologies*, **2012**.

[43] V. A. Agubra, J. W. Fergus, *J.Power Sources* **2014**, *268*, 153–162.

[44] S. J. An, J. Li, C. Daniel, D. Mohanty, S. Nagpure, D. L. Wood, *Carbon* **2016**, *105*, 52–76.

[45] A. Wang, S. Kadam, H. Li, S. Shi, Y. Qi, *Comput. Mater.* **2018**, *4*, 1–26.

[46] J. Janek, W. G. Zeier, *Nat. Energy* **2016**, *1*, 1–4.

[47] I. Alerts, "Sodium Carbonate Prices - Historical & Forecast Data in Several Countries," https://www.intratec.us/chemical-markets/sodium-carbonate-price, **2023.**

[48] K. Vignarooban, R. Kushagra, A. Elango, P. Badami, B.-E. Mellander, X. Xu, T. G. Tucker, C. Nam, A. M. Kannan, *Int. J. Hydrogen Energy* **2016**, *41*, 2829–2846.

[49] R. D. Shannon, *Acta Cryst A* **1976**, *32*, 751–767.

[50] C. Vaalma, D. Buchholz, M. Weil, S. Passerini, *Nat. Rev. Mater.* **2018**, *3*, 1–11.

[51] N. Yabuuchi, K. Kubota, M. Dahbi, S. Komaba, *Chem. Rev.* **2014**, *114*, 11636–11682.

[52] H. Pan, Y.-S. Hu, L. Chen, *Energy Environ.Sci.* **2013**, *6*, 2338–2360.

[53] P. K. Nayak, L. Yang, W. Brehm, P. Adelhelm, *Angew. Chem. Int. Ed* **2018**, *57*, 102–120.

[54] Q. Liu, S. Li, S. Wang, X. Zhang, S. Zhou, Y. Bai, J. Zheng, X. Lu, *J. Phys. Chem. Lett.* **2018**, *9*, 5567–5573.

[55] D. Aurbach, Y. Ein-Eli, *J. Electrochem. Soc.* **1995**, *142*, 1746.

[56] D. A. Stevens, J. R. Dahn, *J. Electrochem. Soc.* **2001**, *148*, A803.

[57] R. C. Asher, S. A. Wilson, *Nature* **1958**, *181*, 409–410.

[58] B. Jache, P. Adelhelm, *Angew. Chem.* **2014**, *126*, 10333–10337.

[59] H. Kim, J. Hong, Y.-U. Park, J. Kim, I. Hwang, K. Kang, *Adv. Funct. Mater.* **2015**, *25*, 534–541.

[60] Q. Liu, R. Xu, D. Mu, G. Tan, H. Gao, N. Li, R. Chen, F. Wu, *Carbon Energy* **2022**, *4*, 458–479.

[61] X. Chen, C. Liu, Y. Fang, X. Ai, F. Zhong, H. Yang, Y. Cao, *Carbon Energy* **2022**, *4*, 1133–1150.

[62] Y. Sun, J. Tang, K. Zhang, J. Yuan, J. Li, D.-M. Zhu, K. Ozawa, L.-C. Qin, *Nanoscale* **2017**, *9*, 2585–2595.

[63] Y.-X. Wang, S.-L. Chou, H.-K. Liu, S.-X. Dou, *Carbon* **2013**, *57*, 202–208.

[64] R. M. N. M. Rathnayake, T. T. Duignan, D. J. Searles, X. S. Zhao, *Phys. Chem. Chem. Phys*. **2021**, *23*, 3063–3070.

[65] W. Luo, Z. Jian, Z. Xing, W. Wang, C. Bommier, M. M. Lerner, X. Ji, *ACS Cent. Sci.* **2015**, *1*, 516–522.

[66] L. Wang, Z. Wei, M. Mao, H. Wang, Y. Li, J. Ma, *Energy Storage Mater.* **2019**, *16*, 434–454.

[67] X. Xie, Z. Ao, D. Su, J. Zhang, G. Wang, *Adv. Funct.Mater.* **2015**, *25*, 1393–1403.

[68] M. M. Doeff, J. Cabana, M. Shirpour, *J. Inorg. Organomet. Polym.* **2014**, *24*, 5–14.

[69] N. Wang, C. Chu, X. Xu, Y. Du, J. Yang, Z. Bai, S. Dou, *Adv. Energy Mater.* **2018**, *8*, 1801888.

[70] Z.-G. Liu, R. Du, X.-X. He, J.-C. Wang, Y. Qiao, L. Li, S.-L. Chou, *Chem. Sus. Chem.* **2021**, *14*, 3724–3743.

[71] F. Klein, B. Jache, A. Bhide, P. Adelhelm, *Phys.Chem. Chem. Phys.***2013**, *15*, 15876–15887.

[72] C. Wu, S.-X. Dou, Y. Yu, *Small* **2018**, *14*, 1703671.

[73] L. Fang, N. Bahlawane, W. Sun, H. Pan, B. B. Xu, M. Yan, Y. Jiang, *Small* **2021**, *17*, 2101137.
[74] L. Li, R. Jacobs, P. Gao, L. Gan, F. Wang, D. Morgan, S. Jin, *J. Am. Chem. Soc.* **2016**, *138*, 2838–2848.
[75] B. Chen, X. Zhong, G. Zhou, N. Zhao, H.-M. Cheng, *Adv. Mater.* **2022**, *34*, 2105812.
[76] B. Shi, W. Liu, K. Zhu, J. Xie, *Chem. Phys.Letters* **2017**, *677*, 70–74.
[77] Y. Yao, J. Zheng, Z. Gong, Z. Ding, J. Zhang, W. Yu, D. A. M. Bengono, H. Li, B. Zhang, H. Tong, *J. Alloys Compd.* **2019**, *790*, 288–295.
[78] C. Feng, L. Zhang, M. Yang, X. Song, H. Zhao, Z. Jia, K. Sun, G. Liu, *ACS Appl. Mater. Interfaces* **2015**, *7*, 15726–15734.
[79] L. Cao, X. Gao, B. Zhang, X. Ou, J. Zhang, W.-B. Luo, *ACS Nano* **2020**, *14*, 3610–3620.
[80] Z. Lu, N. Wang, Y. Zhang, P. Xue, M. Guo, B. Tang, Z. Bai, S. Dou, *Electrochim. Acta* **2018**, *260*, 755–761.
[81] Z. Cao, H. Song, B. Cao, J. Ma, X. Chen, J. Zhou, Z. Ma, *J.Power Sources* **2017**, *364*, 208–214.
[82] J. Koo Kim, S.-K. Park, J.-S. Park, Y. Chan Kang, *J.Mater. Chem. A* **2019**, *7*, 2636–2645.
[83] W. Chen, S. Qi, L. Guan, C. Liu, S. Cui, C. Shen, L. Mi, *J.Mater. Chem. A* **2017**, *5*, 5332–5341.
[84] Q. Wang, C. Guo, Y. Zhu, J. He, H. Wang, *Nano-Micro Lett.* **2018**, *10*, 30.
[85] H. Qi, L. Wang, T. Zuo, S. Deng, Q. Li, Z. Liu, P. Hu, X. He, *Chem. Electro Chem.* **2020**, *7*, 78–85.
[86] Y. Xiao, J.-Y. Hwang, I. Belharouak, Y.-K. Sun, *ACS Energy Lett.* **2017**, *2*, 364–372.
[87] L. David, R. Bhandavat, G. Singh, *ACS Nano* **2014**, *8*, 1759–1770.
[88] D. Xu, W. Chen, M. Zheng, X. Huang, Y. Fang, X. Yu, *Electrochim. Acta* **2018**, *265*, 419–429.
[89] Y. Xiao, D. Su, X. Wang, S. Wu, L. Zhou, Y. Shi, S. Fang, H.-M. Cheng, F. Li, *Adv. Energy Mater.***2018**, *8*, 1800930.
[90] Q. Chen, M. Ren, H. Xu, W. Liu, J. Hei, L. Su, L. Wang, *Chem. Electro Chem.* **2018**, *5*, 2135–2141.
[91] Y. Chen, X. Hu, B. Evanko, X. Sun, X. Li, T. Hou, S. Cai, C. Zheng, W. Hu, G. D. Stucky, *Nano Energy* **2018**, *46*, 117–127.
[92] Z. Man, P. Li, D. Zhou, Y. Wang, X. Liang, R. Zang, P. Li, Y. Zuo, Y. M. Lam, G. Wang, *Nano Lett.* **2020**, *20*, 3769–3777.
[93] Q. Liu, J. Gao, C. Cao, G. Yin, Z. Jiang, M. Ge, X. Xiao, W.-K. Lee, J. Wang, *Nano Energy* **2019**, *62*, 384–392.
[94] Q. Li, Q. Wei, W. Zuo, L. Huang, W. Luo, Q. An, V. O. Pelenovich, L. Mai, Q. Zhang, *Chem. Sci.* **2017**, *8*, 160–164.
[95] S. R. Hall, J. M. Stewart, *Acta Cryst. B* **1973**, *29*, 579–585.
[96] B. S. Shah, J. B. Raval, D. Kumar, S. H. Chaki, M. P. Deshpande, *J.Alloys Compd.* **2023**, *938*, 168566.
[97] R. R. Gainov, F. G. Vagizov, V. A. Golovanevskiy, V. A. Ksenofontov, G. Klingelhöfer, V. V. Klekovkina, T. G. Shumilova, I. N. Pen'kov, *Hyperfine Interact.* **2014**, *226*, 51–55.
[98] N. Morimoto, *Acta Cryst.* **1964**, *17*, 351–360.
[99] U. Chandra, G. Parthasarathy, P. Sharma, *Can. Mineral.* **2010**, *48*, 1137–1147.
[100] S. Pareek, A. Rais, A. Tripathi, U. Chandra, in *ICAME 2007* (Eds.: N.S. Gajbhiye, S.K. Date), Springer, Berlin, Heidelberg, **2009**, pp. 995–1002.
[101] P. Eisenberger, R. G. Shulman, B. M. Kincaid, G. S. Brown, S. Ogawa, *Nature* **1978**, *274*, 30–34.
[102] L. B. McCusker, R. B. Von Dreele, D. E. Cox, D. Louër, P. Scardi, *J. Appl. Cryst.* **1999**, *32*, 36–50.
[103] A. A. Coelho, *J. Appl. Cryst.* **2018**, *51*, 210–218.
[104] C. A. Young, A. L. Goodwin, *J.Mater. Chem.* **2011**, *21*, 6464–6476.
[105] T. Proffen, S. J. L. Billinge, T. Egami, D. Louca, *Z. Kristallogr. - Cryst. Mater.* **2003**, *218*, 132–143.
[106] T. Egami, S. J. L. Billinge, *Underneath the Bragg Peaks: Structural Analysis of Complex Materials*, Elsevier, **2003**.
[107] S. E. Ashbrook, S. Sneddon, *J. Am. Chem. Soc.* **2014**, *136*, 15440–15456.
[108] D. D. Laws, H.-M. L. Bitter, A. Jerschow, *Angew. Chem. Int. Ed.* **2002**, *41*, 3096–3129.

[109] I. J. Lowe, *Phys. Rev. Lett.* **1959**, *2*, 285–287.
[110] E. R. Andrew, A. Bradbury, R. G. Eades, *Nature* **1959**, *183*, 1802–1803.
[111] B. Gee, H. Eckert, *Solid State Nucl. Magn. Reson*. **1995**, *5*, 113–122.
[112] A. Seidel, B. Schimiczek, U. Tracht, B. Boddenberg, *Solid State Nucl. Magn. Reson.* **1997**, *9*, 129–141.
[113] K. Paradowska, I. Wawer, *J. Pharm. Biomed. Anal.* **2014**, *93*, 27–42.
[114] R. L. Mößbauer, *Nobel Lect.* **1961**.
[115] T. Glaser, *Angew. Chem.* **2011**, *123*, 10195–10196.
[116] S. DeBenedetti, G. Lang, R. Ingalls, *Phys. Rev. Lett.* **1961**, *6*, 60–62.
[117] E. Murad, in *Iron in Soils and Clay Minerals* (Eds.: J.W. Stucki, B.A. Goodman, U. Schwertmann), Springer Netherlands, Dordrecht, **1988**, pp. 309–350.
[118] W. D. Lehmann, H.-R. Schulten, *Chem. unserer Zeit* **1976**, *10*, 163–174.
[119] C. M. Rost, E. Sachet, T. Borman, A. Moballegh, E. C. Dickey, D. Hou, J. L. Jones, S. Curtarolo, J.-P. Maria, *Nat. Commun.* **2015**, *6*, 8485.
[120] B. H. Kreps, *Am. J. Econ. Sociol.* **2020**, *79*, 695–717.
[121] A. Orlov, J. Sillmann, I. Vigo, *Nat Energy* **2020**, *5*, 108–110.
[122] J. Menéndez, J. M. Fernández-Oro, M. Galdo, J. Loredo, *J. of Energy Storage* **2020**, *28*, 101234.
[123] R. B. Kaunda, *J. Energy Nat. Resour. Law* **2020**, *38*, 237–244.
[124] Z. Wang, S. M. Selbach, T. Grande, *RSC Adv.* **2014**, *4*, 4069–4079.
[125] Z. Hu, Q. Liu, S.-L. Chou, S.-X. Dou, *Adv. Mater.* **2017**, *29*, 1700606.
[126] S. Senkale, S. Indris, M. Etter, W. Bensch, *ACS Appl. Mater. Interfaces* **2021**, *13*, 26034–26045.
[127] S. Senkale, G. Cibin, A. V. Chadwick, W. Bensch, *ACS Appl. Mater. Interfaces* **2021**, DOI 10.1021/acsami.1c16814.
[128] S. O. J. Long, A. V. Powell, P. Vaqueiro, S. Hull, *Chem. Mater.* **2018**, *30*, 456–464.
[129] Y. Kanazawa, N. Morimoto, *Canad. Mineral.* ***1978****, 16, 397-407.*
[130] J. Cai, Z. Chen, X. Meng, *J. Compos. Sci.* **2020**, *4*, 184.
[131] H. Li, K. Wang, S. Cheng, K. Jiang, *ACS Appl. Mater. Interfaces* **2018**, *10*, 8016–8025.
[132] Z. Shadike, Y.-N. Zhou, F. Ding, L. Sang, K.-W. Nam, X.-Q. Yang, Z.-W. Fu, *J.Power Sources* **2014**, *260*, 72–76.
[133] A. Nasu, A. Sakuda, T. Kimura, M. Deguchi, A. Tsuchimoto, M. Okubo, A. Yamada, M. Tatsumisago, A. Hayashi, *Small* **2022**, *18*, 2203383.
[134] W. Weppner, R. A. Huggins, *J. Electrochem. Soc.* **1977**, *124*, 1569.

8. Anhang

8.1 Electronic Supporting Information

8.1.1 $CuFeS_2$ as a Very Stable High-Capacity Anode Material for Sodium-Ion Batteries: A Multimethod Approach for Elucidation of the Complex Reaction Mechanisms during Discharge and Charge Processes

Supplementary Information

$CuFeS_2$ as a very stable high-capacity anode material for sodium-ion batteries: a multi-method approach for elucidation of the complex reaction mechanisms during discharge and charge processes

*Svenja Senkale[a], Sylvio Indris[b], Martin Etter[c], Wolfgang Bensch[a]**

[a] Institute of Inorganic Chemistry, Kiel University, Max-Eyth-Str.2, 24118 Kiel, Germany; wbensch@ac.uni-kiel.de

[b] Institute for Applied Materials, Karlsruhe Institute of Technology, P.O. box 3640, 76021 Karlsruhe, Germany

[c] Deutsches Elektronen-Synchrotron (DESY), Notkestr. 85, 22607 Hamburg, Germany

Table S1: Refined unit cell parameters and reliability values derived from the XRD and PDF data for pristine $CuFeS_2$.

	XRD	**PDF**
	value	value
Crystal system	Tetragonal	Tetragonal
Space group	*I-42d*	*I-42d*

***a*=*b* (Å)**	5.28830(9)	5.2851(2)
***c* (Å)**	10.4181(2)	10.4028(7)
cell volume (Å^3)	291.36(1)	290.58(3)
R_{wp}	4.49	14.62
R_p	3.19	

Table S2: Results of EDX measurements of $CuFeS_2$ powder in the as-synthesized state.

Sample	Cu / at%	Fe / at%	S / at%
$CuFeS_2$	29.28	27.75	42.92
Composition	$Cu_{1.17}Fe_{1.11}S_{1.72}$		

Table S3: Results of the elemental analysis of the $CuFeS_2$ sample. Sulphanilamide was used as reference. To calculate the composition the results for S of the EA were compared to the theoretical value of 34.94 wt. % S in $CuFeS_2$ leading to a composition $Cu_xFe_xS_{2.02}$). To get the full composition the Cu/Cr ratio from the EDX measurements were taken into account.

Sample	N / wt%	C / wt%	H / wt%	S / wt%
$CuFeS_2$	0	0	0	35.24

2

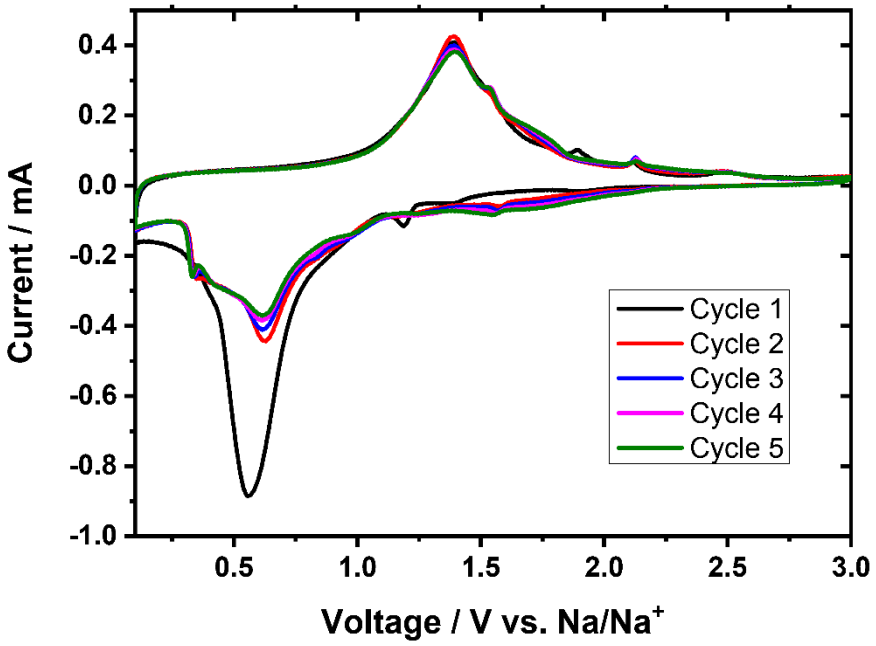

Figure S1: Cyclic voltammogram of the first five cycles of $CuFeS_2$.

Figure 1 shows the first four cyclic voltammograms of $CuFeS_2$ electrode between 0.1 and 3.0 V measured at a scan rate of 0.1 mVs^{-1}. For the first cycle two significant reduction peaks are observed at 1.18 V and 0.55 V and a weak shoulder at 0.38 V while a broad oxidation peak at 1.38 V including a shoulder at 1.55 V and two small signals at 1.89 V and 2.11 V occur. A much more widespread peak at 2.48 V is also visible. The reduction peak at 1.13 V disappears after the first cycle and is associated with the reduction of the impurity from FeS_2.[1,2] The strong reduction peak is due to the conversion reaction. The small shoulder might be caused by a formation of the SEI formation. The following cycles differ from the first one showing a broad reduction peak at 0.61 V with a broad shoulder at 0.44 V and a more pronounced signal at 0.33 V. Also a weak broad signal from 0.84 to 1.09 V is occurred as well as a weak signal at 1.56 V which slowly shifts to

3

lower voltages. The oxidation peak is still equal but a new broad shoulder at 1.71 V is formed. The small signal at 1.89 V disappears whereas the signal at 2.11 shifts to 2.13 V. The Voltage of the other peaks are still the same but the intensity of the peaks decreases slowly from the second cycle on, which shows that the reaction is certain reversible but still changes slightly. Further researches on reversibility of this system will be reported later.

Table S4: Reflection intensities determined via a single reflection fits using the program FULLPROF.

Sample / reference	Cu (111)	Cu(200)	(111)/(200)
1.5 Na	6504	1305	5.0
2 Na	4783	957	5.0
2.5 Na	9664	1884	5.1
3 Na	9645	2118	4.6
3.5 Na	15006	3331	4.5
4 Na	9063	2301	3.9
fully discharged	8035	1847	4.3
-1 Na	9725	2332	4.2
-2 Na	8601	1990	4.3
-3 Na	2658	822	3.2
Xia et al.[3]	22	14	1.6
Rao et al.[4]	5	3	1.5
Swanson et al.[5]	100	46	2.2

4

Table S5: Rietveld refinement parameters obtained from the ex-situ XRD data of samples containing different amounts of Na/formula unit.

sample		$CuFeS_2$	$NaCuFeS_2$	Cu	Na_2S	Fe
0.5 Na	Space group	*I-42d*	*P-3m1*			
	a (Å)	5.3048(8)	3.8567(4)			
	b (Å)	5.3048(8)	3.8567(4)			
	c (Å)	10.458(3)	6.865(3)			
	Cryst. Size (nm)	>200	8.1(3)			
	Strain (%)	0.34(2)	0.48(3)			
1 Na	Space group	*I-42d*	*P-3m1*	*Fm-3m*		
	a (Å)	5.358(3)	3.8650(9)	3.613(1)		
	b (Å)	5.358(3)	3.8650(9)	3.613(1)		
	c (Å)	10.53(1)	6.871(3)	3.613(1)		
	Cryst. Size (nm)	>200	8.6(3)	18(1)*		
	Strain e_0 (%)	0.51(7)	0.51(3)	n.i.*		
1.5 Na	Space group	*I-42d*	*P-3m1*	*Fm-3m*		
	a (Å)	5.359(2)	3.864(1)			
	b (Å)	5.359(2)	3.864(1)			
	c (Å)	10.515(5)	6.868(3)			

5

	Cryst. Size (nm)	12(1)*	8.3(3)	18(1)*	
	Strain (%)	n.i.*	0.5(3)	n.i.*	
2 Na	Space group		*P-3m1*	*Fm-3m*	
	a (Å)		3.877(1)	3.6079(4)	
	b (Å)		3.877(1)	3.6079(4)	
	c (Å)		6.860(3)	3.6079(4)	
	Cryst. Size (nm)		10(1)	18(3)	
	Strain (%)		0.47(5)	0.21(2)	
2.5 Na	Space group		*P-3m1*	*Fm-3m*	
	a (Å)		3.916(6)	3.615(2)	
	b (Å)		3.916(6)	3.615(2)	
	c (Å)		6.90(2)	3.615(2)	
	Cryst. Size (nm)		5.3(7)	14(2)	
	Strain (%)		1(3)	0.26(3)	
3 Na	Space group			*Fm-3m*	*Fm-3m*	*Im-3m*
	a (Å)			3.619(2)	6.553(6)	2.885(4)
	b (Å)			3.619(2)	6.553(6)	2.885(4)
	c (Å)			3.619(2)	6.553(6)	2.885(4)

6

	Cryst. Size (nm)	12(1)	8(2)	2(1)
	Strain (%)	0.32(2)	0.6(1)	2(1)
3.5 Na	Space group	*Fm-3m*	*Fm-3m*	*Im-3m*
	a (Å)	3.619(2)	6.554(4)	2.888(3)
	b (Å)	3.619(2)	6.554(4)	2.888(3)
	c (Å)	3.619(2)	6.554(4)	2.888(3)
	Cryst. Size (nm)	12(1)	22(7)	1.2(2)
	Strain (%)	0.29(2)	0.7(1)	1.8(6)*
4 Na	Space group	*Fm-3m*	*Fm-3m*	*Im-3m*
	a (Å)	3.6175(9)	6.556(3)	2.893(3)
	b (Å)	3.6175(9)	6.556(3)	2.893(3)
	c (Å)	3.6175(9)	6.556(3)	2.893(3)
	Cryst. Size (nm)	13(1)	52(28)	3(1)
	Strain (%)	0.28(2)	0.71(4)	1.8(6)*
Fully discharged	Space group	*Fm-3m*	*Fm-3m*	*Im-3m*
	a (Å)	3.6161(8)	6.558(2)	2.897(2)
	b (Å)	3.6161(8)	6.558(2)	2.897(2)
	c (Å)	3.6161(8)	6.558(2)	2.897(2)

7

	Cryst. Size (nm)		n.i.*	32(5)	4(1)
	Strain (%)		n.i.*	0.67(3)	1.8(3)*
-1 Na	Space group		*Fm-3m*	*Fm-3m*	*Im-3m*
	a (Å)		3.6192(7)	6.519(3)	2.888(3)
	b (Å)		3.6192(7)	6.519(3)	2.888(3)
	c (Å)		3.6192(7)	6.519(3)	2.888(3)
	Cryst. Size (nm)		12(1)	16(2)	2(1)*
	Strain (%)		0.28(2)	0.76(3)	1.8*
-2 Na	Space group	*P-3m1*	*Fm-3m*	*Fm-3m*	*Im-3m*
	a (Å)	3.877(5)	3.616(1)	6.502(3)	2.916(3)
	b (Å)	6.850(8)	3.616(1)	6.502(3)	2.916(3)
	c (Å)	6.850(8)	3.616(1)	6.502(3)	2.916(3)
	Cryst. Size (nm)	6(1)	21(2)	24(8)	4(1)*
	Strain (%)	0.3(1)	0.22(1)	0.85(6)	1.8*
-3 Na	Space group	*P-3m1*	*Fm-3m*		
	a (Å)	3.8656(4)	3.6137(3)		
	b (Å)	3.8656(4)	3.6137(3)		
	c (Å)	6.850(1)	3.6137(3)		

8

	Cryst. Size (nm)	18.5(7)	n.i.*
	Strain (%)	0.131(4)	n.i.*
-4 Na	Space group	*P-3m1*	
	a (Å)	3.846(2)	
	b (Å)	6.881(7)	
	c (Å)	6.881(7)	
	Cryst. Size (nm)	6.2(6)	
	Strain (%)	0.49(5)	

* Note that the particle size has a strong correlation to the microscopic anisotropic strain. (n.i. not indicated)

9

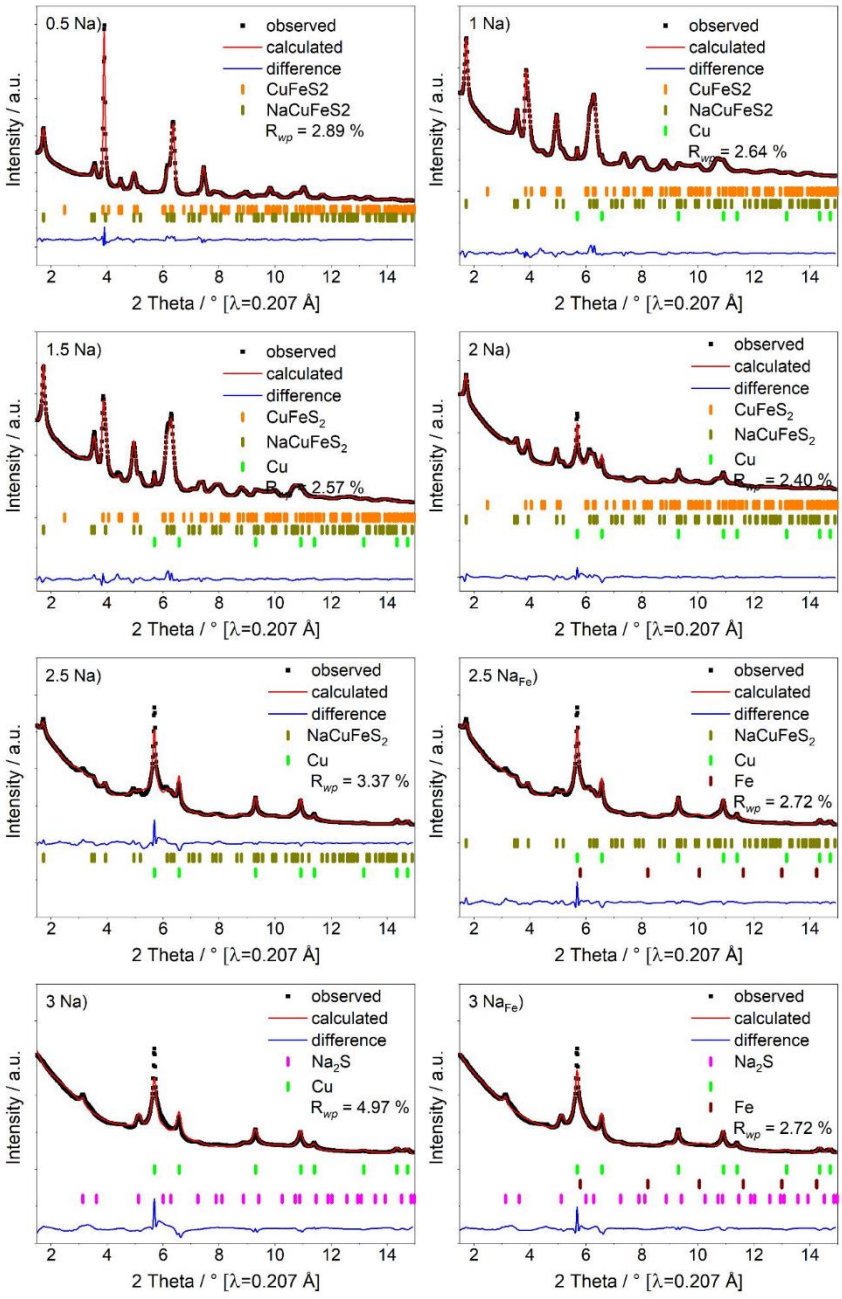
0.5 Na)
observed
calculated
difference
CuFeS2
NaCuFeS2
R_{wp} = 2.89 %
1 Na)
observed
calculated
difference
CuFeS2
NaCuFeS2
Cu
R_{wp} = 2.64 %
1.5 Na)
observed
calculated
difference
$CuFeS_2$
$NaCuFeS_2$
Cu
R_{wp} = 2.57 %
2 Na)
observed
calculated
difference
$CuFeS_2$
$NaCuFeS_2$
Cu
R_{wp} = 2.40 %
2.5 Na)
observed
calculated
difference
$NaCuFeS_2$
Cu
R_{wp} = 3.37 %
2.5 Na_{Fe})
observed
calculated
difference
$NaCuFeS_2$
Cu
Fe
R_{wp} = 2.72 %
3 Na)
observed
calculated
difference
Na_2S
Cu
R_{wp} = 4.97 %
3 Na_{Fe})
observed
calculated
difference
Na_2S
Fe
R_{wp} = 2.72 %
Intensity / a.u.
2 Theta / ° [λ=0.207 Å]
2
4
6
8
10
12
14

10

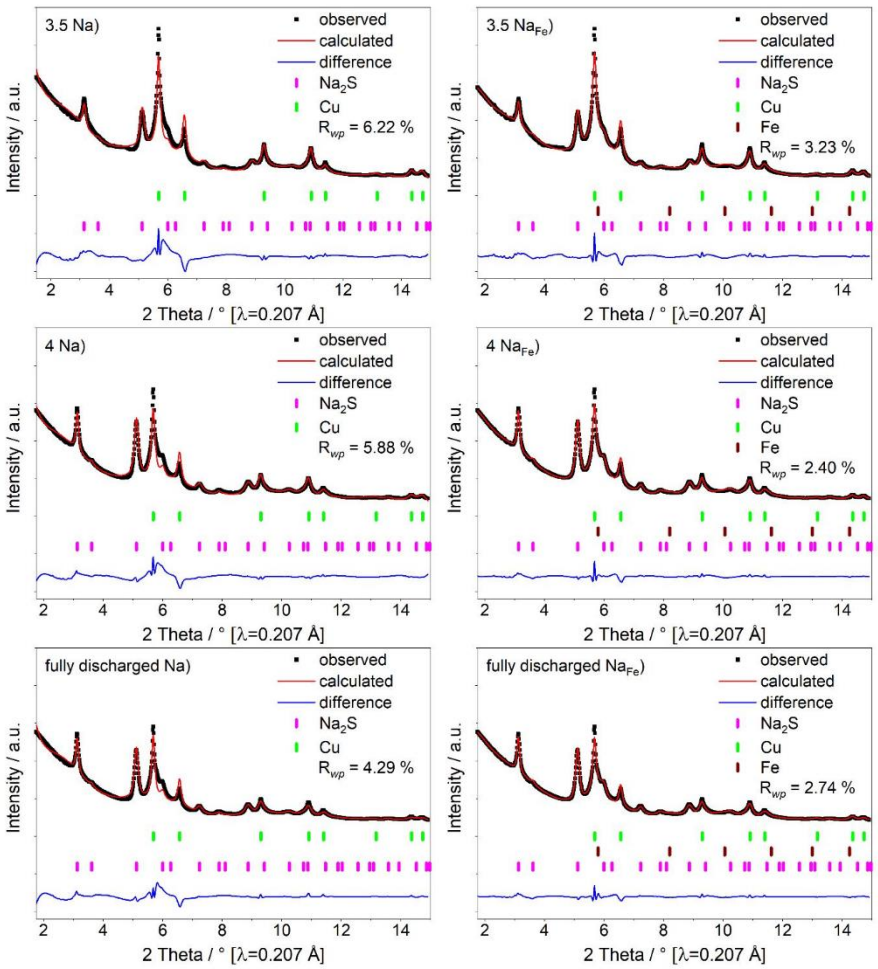
3.5 Na)
observed
calculated
difference
Na2S
Cu
Rwp = 6.22 %
3.5 NaFe)
Fe
Rwp = 3.23 %
4 Na)
Rwp = 5.88 %
4 NaFe)
Rwp = 2.40 %
fully discharged Na)
Rwp = 4.29 %
fully discharged NaFe)
Rwp = 2.74 %
Intensity / a.u.
2 Theta / ° [λ=0.207 Å]

11

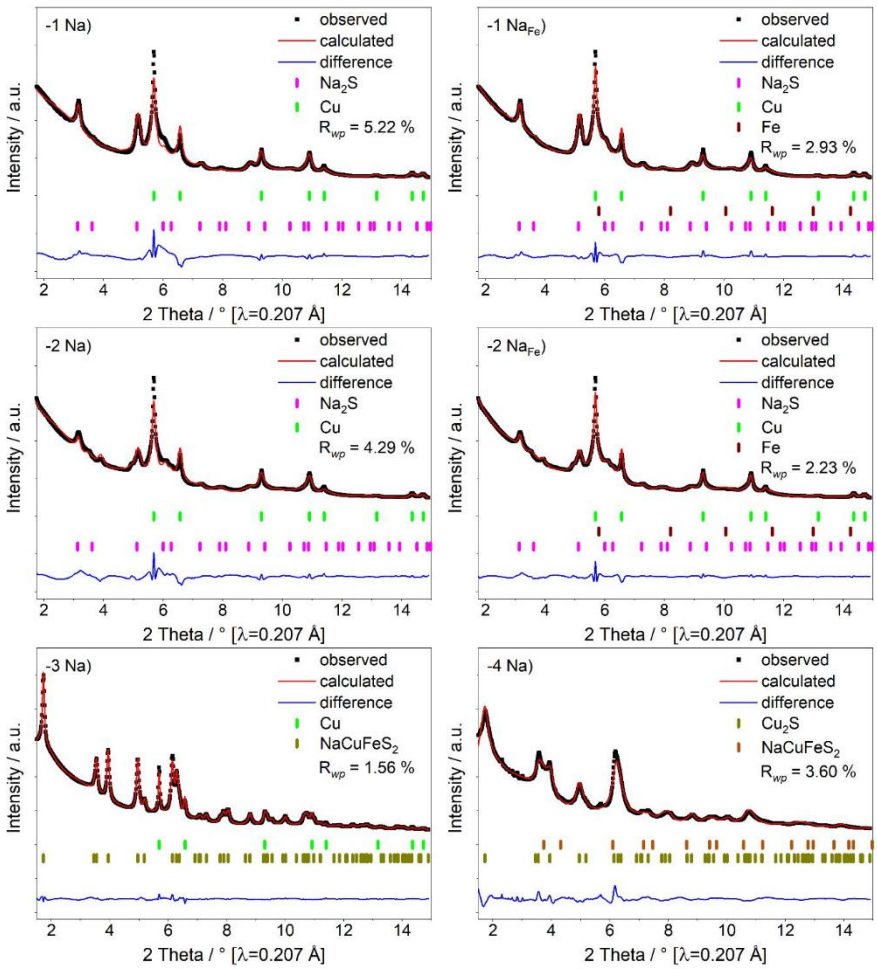

Figure S2: Results of the Rietveld refinements of the XRD pattern of $CuFeS_2$ at different stages of discharge and charge. Observed (black line), calculated (red line) and difference (blue line) profiles. Vertical bars indicate the positions of Bragg reflections.

Table S6: Comparison of the R_{wp} values for the Rietveld refinements without nanocrystalline Fe and considering nanosized Fe in the model.

Sample	**XRD**			**PDF**		
	R_{wp}	R_{wp} (Fe)	R_{wp} (Fe) - R_{wp}	R_{wp}	R_{wp} with Fe	R_{wp} (Fe) - R_{wp}
1.5 Na	2.57	2.53	0.04	20.47	20.32	0.15
2 Na	2.40	2.20	0.20	21.92	17.31	4.61
2.5 Na	3.37	2.72	0.65	23.01	16.29	6.72
3 Na	4.97	3.16	1.81	27.70	19.45	8.25
3.5 Na	6.22	3.23	2.99	29.23	17.60	11.63
4 Na	5.88	2.40	3.48	30.04	17.39	12.65
Fully discharged	4.29	2.74	1.55	29.57	19.21	10.36
-1 Na	5.22	2.93	2.29	28.41	19.16	9.25
-2 Na	4.22	2.23	1.99	26.60	21.30	5.30
-3 Na	1.56	1.49	0.07	18.14	16.33	1.81

13

Table S7: Results of the refinements of the PDF data for the samples investigated at different stages of discharge and charge.

Sample		**$CuFeS_2$**	**$NaCuFeS_2$**	**Cu**	**Na_2S**	**Fe**
0.5 Na	Space group	*I-42d*	*P-3m1*			
	a (Å)	5.2966(4)	3.8520(3)			
	b (Å)	5.2966(4)	3.8520(3)			
	c (Å)	10.466(1)	6.832(1)			
	Domain radius (nm)	>200	3.28(2)			
1 Na	Space group	*I-42d*	*P-3m1*	*Fm-3m*		
	a (Å)	5.367(1)	3.8605(3)	3.6064(6)		
	b (Å)	5.367(1)	3.8605(3)	3.6064(6)		
	c (Å)	10.497(4)	6.8514(9)	3.6064(6)		
	Domain radius (nm)	16(5)	4.04(2)	3.8(1)		
1.5 Na	Space group	*I-42d*	*P-3m1*	*Fm-3m*		
	a (Å)		3.8804(7)	3.6130(2)		
	b (Å)		3.8804(7)	3.6130(2)		
	c (Å)		6.844(2)	3.6130(2)		

14

	Domain radius (nm)	3.1(1)	3.22(1)		
2 Na	Space group	*P-3m1*	*Fm-3m*		
	a (Å)	3.8811(9)	3.6138(2)		
	b (Å)	3.8811(9)	3.6138(2		
	c (Å)	6.867(3)	3.6138(2		
	Domain radius (nm)	3.04(4)	3.19(2)		
2.5 Na	Space group	*P-3m1*	*Fm-3m*	*Fm-3m*	*Im-3m*
	a (Å)	3.8809(4)	3.6149(1)	6.547(6)	2.926(2)
	b (Å)	3.8809(4)	3.6149(1)	6.547(6)	2.926(2)
	c (Å)	6.852(6)	3.6149(1)	6.547(6)	2.926(2)
	Domain radius (nm)	2.51(7)	3.00(1)	2.1(1)	0.84(2)
3 Na	Space group		*Fm-3m*	*Fm-3m*	*Im-3m*
	a (Å)		3.6160(2)	6.538(3)	2.886(2)
	b (Å)		3.6160(2)	6.538(3)	2.886(2)
	c (Å)		3.6160(2)	6.538(3)	2.886(2)

15

	Domain radius (nm)	2.16(8)	2.26(6)	0.9(2)
3.5 Na	Space group	*Fm-3m*	*Fm-3m*	*Im-3m*
	a (Å)	3.6161(1)	6.533(1)	2.888(2)
	b (Å)	3.6161(1)	6.533(1)	2.888(2)
	c (Å)	3.6161(1)	6.533(1)	2.888(2)
	Domain radius (nm)	2.79(1)	3.05(5)	0.79(1)
4 Na	Space group	*Fm-3m*	*Fm-3m*	*Im-3m*
	a (Å)	3.6156(1)	6.5411(8)	2.868(1)
	b (Å)	3.6156(1)	6.5411(8)	2.868(1)
	c (Å)	3.6156(1)	6.5411(8)	2.868(1)
	Domain radius (nm)	2.41(1)	2.87(3)	0.89(1)
Fully discharged	Space group	*Fm-3m*	*Fm-3m*	*Im-3m*
	a (Å)	3.6148(2)	6.5400(9)	2.871(2)
	b (Å)	3.6148(2)	6.5400(9)	2.871(2)
	c (Å)	3.6148(2)	6.5400(9)	2.871(2)

16

	Domain radius (nm)		2.56(1)	3.27(4)	0.88(2)
-1 Na	Space group		*Fm-3m*	*Fm-3m*	*Im-3m*
	a (Å)		3.6153(3)	6.514(1)	2.879(2)
	b (Å)		3.6153(3)	6.514(1)	2.879(2)
	c (Å)		3.6153(3)	6.514(1)	2.879(2)
	Domain radius (nm)		2.40(1)	2.48(3)	0.74(2)
-2 Na	Space group	*P-3m1*	*Fm-3m*	*Fm-3m*	*Im-3m*
	a (Å)	3.774(6)	3.6155(1)	6.515(2)	2.912(2)
	b (Å)	3.774(6)	3.6155(1)	6.515(2)	2.912(2)
	c (Å)	6.88(2)	3.6155(1)	6.515(2)	2.912(2)
	Domain radius (nm)	8.1(7)	3.12(9)	2.24(4)	0.86(2)
-3 Na	Space group	*P-3m1*	*Fm-3m*		
	a (Å)	3.8614(2)	3.6128(2)		
	b (Å)	3.8614(2)	3.6128(2)		
	c (Å)	6.8337(7)	3.6128(2)		

17

	Domain radius (nm)	5.54(2)	6.43(5)
-4 Na	Space group	*P-3m1*	Cu_2S *Fm-3m*
	a (Å)	3.8390(6)	6.150(6)
	b (Å)	3.8390(6)	6.150(6)
	c (Å)	6.827(2)	6.150(6)
	Domain radius (nm)	2.04(1)	0.41(1)

18

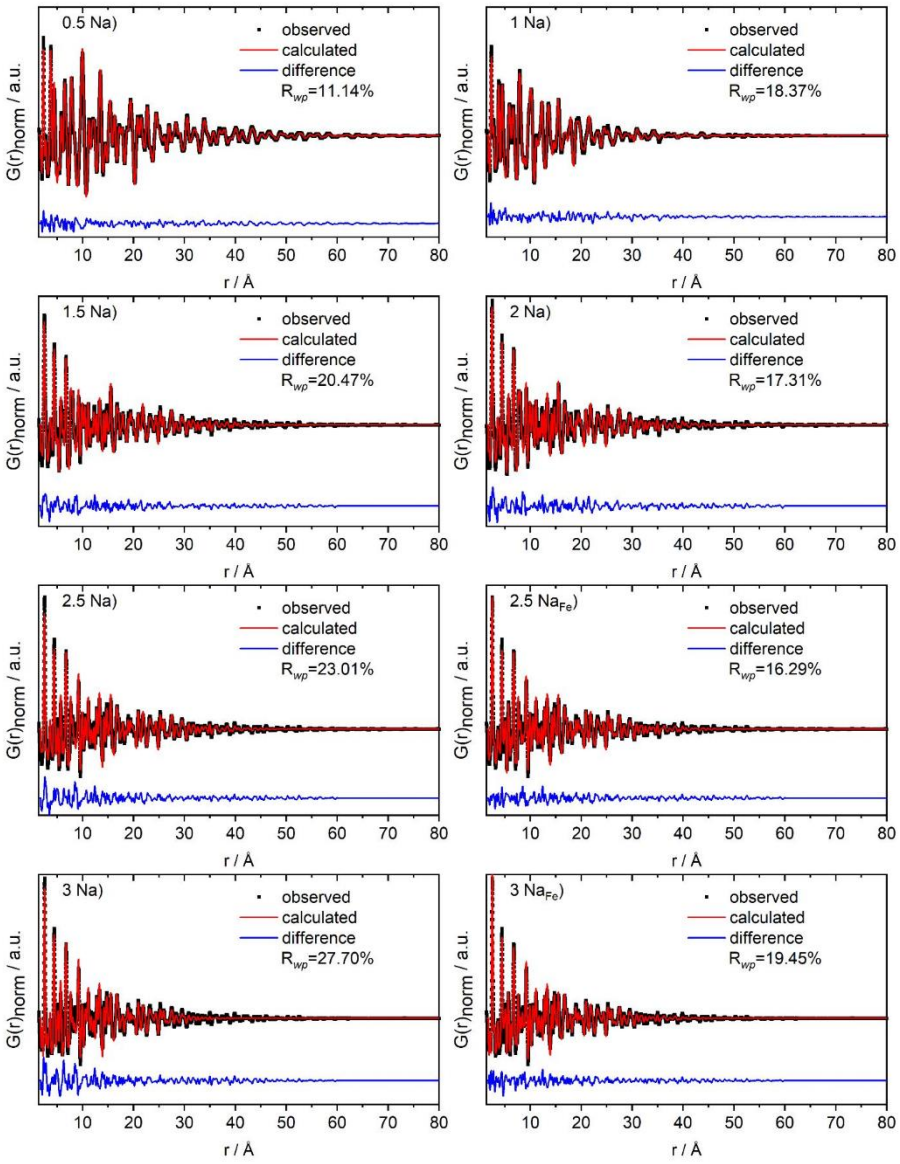
0.5 Na)
observed
calculated
difference
R_{wp}=11.14%
1 Na)
R_{wp}=18.37%
1.5 Na)
R_{wp}=20.47%
2 Na)
R_{wp}=17.31%
2.5 Na)
R_{wp}=23.01%
2.5 Na_{Fe})
R_{wp}=16.29%
3 Na)
R_{wp}=27.70%
3 Na_{Fe})
R_{wp}=19.45%
G(r)norm / a.u.
r / Å
10 20 30 40 50 60 70 80

19

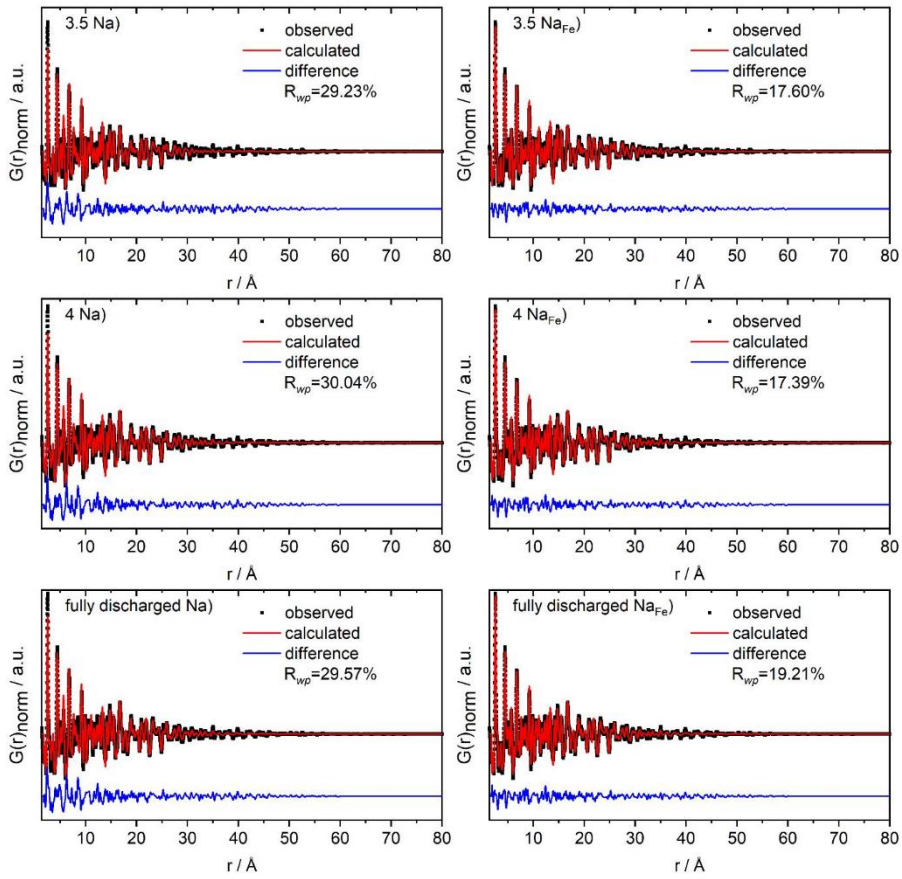
3.5 Na)
observed
calculated
difference
R_{wp}=29.23%
3.5 Na_{Fe})
R_{wp}=17.60%
4 Na)
R_{wp}=30.04%
4 Na_{Fe})
R_{wp}=17.39%
fully discharged Na)
R_{wp}=29.57%
fully discharged Na_{Fe})
R_{wp}=19.21%
G(r)norm / a.u.
r / Å
10 20 30 40 50 60 70 80

20

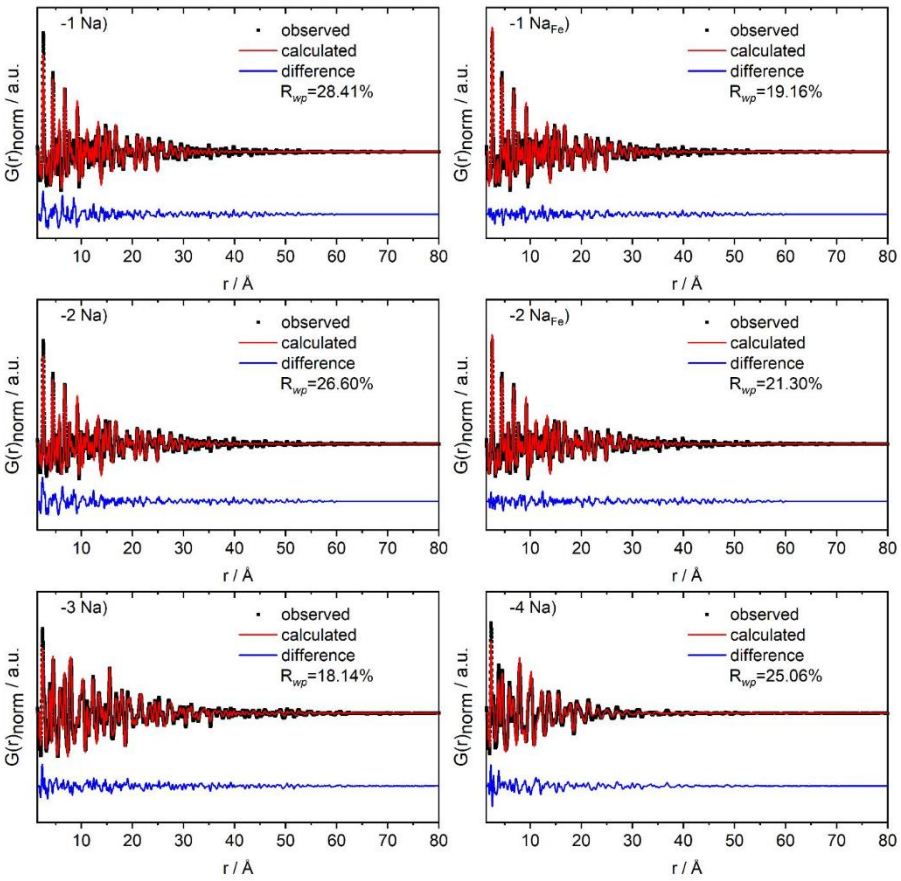

Figure S3: Results of the refinements of the PDF data of the samples at different stages of Na uptake and Na release. Observed (black line), calculated (red line) and Difference (blue line) profiles.

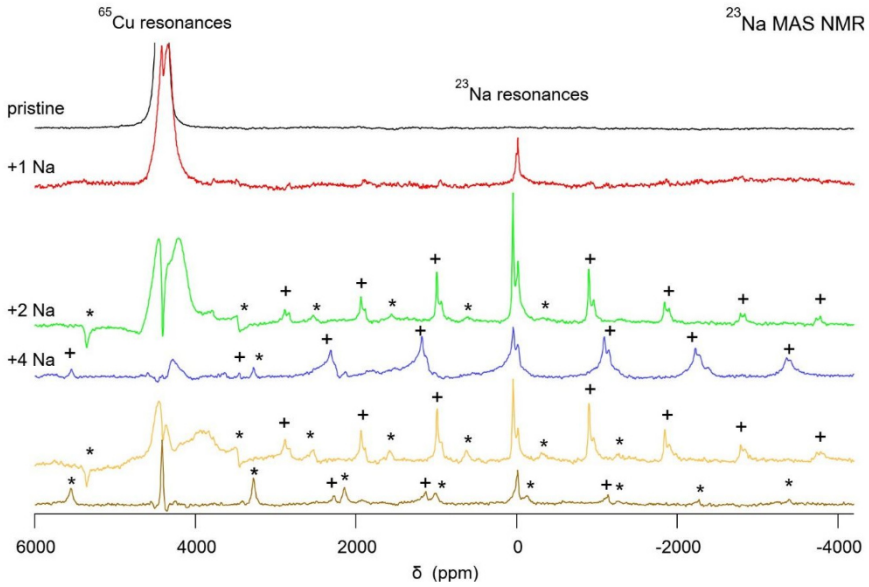

Figure S4: Full view of the ^{23}Na MAS NMR spectra of CuFeS2 for different discharge/charge states. The spinning speed was 50-60 kHz. The strong signal at about 4400 ppm is a ^{63}Cu resonance and belongs mainly to the RF coil made of metallic Cu and located around the rotor/sample. The fact that for some spectra this resonance shows some spinning sidebands reveals that part of this signal stems from metallic Cu inside the spinning sample.

Table S8: Comparison of unit cell parameters and molar volumes for different compounds observed during cycling of Na/$CuFeS_2$ cells.

	V_{cell} / [Å^3]	Z	V_m / [cm^3 mol^{-1}]
$CuFeS_2$	290.92	4	43.80
$NaCuFeS_2$	88.82	1	53.49
Cu	47.23	4	7.11

22

Fe	24.06	2	7.24
Na_2S	279.21	4	42.04
FeS_x	245.18	8	18.45
Cu_2S / $Cu_{1.8}S$	191.3 /180.25	4	27.97
$Cu_{7.2}S_4$	173.46	1	104.46
Cu_5FeS_4	166.37	1	100.19

Table S9: Calculation of the expected volume changes.

	Charged state	Discharges state	Volume change [%]
1st cycle complete discharge	$CuFeS_2$	Fe + Cu + $2Na_2S$	225 %
1st cycle until 3 Na	$CuFeS_2$	Cu + 0.5 Fe + 0.5 FeS_x + 1.5 Na_2S	189 %
Further cycles	$NaCuFeS_2$	Cu + 0.5 Fe + 0.5 FeS_x + 1.5 Na_2S	155%
Steady state	Cu_5FeS_4 + 4 FeS_x	5 Fe + 2.5 Na_2S + 0.69 $Cu_{7.2}S_4$	121%

The molar volumes V_m for the compounds in Table S8 were calculated from their unit cell volumes V_{cell} and number of formula units in the cell Z. To calculate the volume changes in Table S9, the sums of the molar volumina of the compounds in the discharged state were related to the sums of the molar volumina of the compounds in the charged state.

(1) Lu, Z.; Wang, N.; Zhang, Y.; Xue, P.; Guo, M.; Tang, B.; Bai, Z.; Dou, S. Pyrite FeS_2@C Nanorods as Smart Cathode for Sodium Ion Battery with Ultra-Long Lifespan and Notable Rate Performance from Tunable Pseudocapacitance. *Electrochim. Acta* **2018**, *260*, 755–761. https://doi.org/10.1016/j.electacta.2017.12.031.

(2) Shadike, Z.; Zhou, Y.-N.; Ding, F.; Sang, L.; Nam, K.-W.; Yang, X.-Q.; Fu, Z.-W. The New Electrochemical Reaction Mechanism of Na/FeS_2 Cell at Ambient Temperature. *J. Power Sources* **2014**, *260*, 72–76. https://doi.org/10.1016/j.jpowsour.2014.03.011.

(3) Xie, Y.-P.; Zhao, S.-J. The Energetic and Structural Properties of Bcc NiCu, FeCu Alloys: A First-Principles Study. *Comput. Mater. Sci.* **2011**, *50* (9), 2586–2591. https://doi.org/10.1016/j.commatsci.2011.03.046.

(4) Srinivasa-Rao, S.; Anantharaman, T. R.; Accurate Evaluation of Lattice Parameters of Alpha Brasses *Curr. Sci.* 1963, **32**, 262.

(5) Swanson, H. E.; Tatge, E.; *Standard X-Ray Diffraction Powder Patterns, Natl. Bur. Stand. Circ.* **539** (U.S. GPO, Washington, D.C., 1953), Vol. 1, p. 15.

24

8.1.2 Synthetically Produced Isocubanite as an Anode Material for Sodium-Ion Batteries: Understanding the Reaction Mechanism during Sodium Uptake and Release

Supplementary Information

Synthetic produced Isocubanite as anode material for sodium-ion batteries: understanding the reaction mechanism during sodium uptake and release

Svenja Senkale[a], Giannantonio Cibin[b], Alan V. Chadwick[c], Wolfgang Bensch[a*]

[a] *Institute of Inorganic Chemistry, Kiel University, Max-Eyth-Str.2, 24118 Kiel, Germany, wbensch@ac.uni-kiel.de*

[b] *Diamond Light Source (DLS), Harwell Science and Innovation Campus, Didcot, Oxfordshire OX11 0DE, United Kingdom*

[c] *School of Physical Sciences, Ingram Building, University of Kent, Canterbury, CT2 7NH, United Kingdom*

Table S1: Refined unit cell parameters and reliability values derived from the PXRD data for pristine $CuFe_2S_3$.

	XRD
	value
Crystal system	Cubic
Space group	*F-43m*
***a=b=c* (Å)**	5.3045(9)
cell volume (Å³)	149.26(8)
R_{wp}	3.26
R_p	2.16
gof	1.58

Table S2: Results of EDX measurements of $CuFe_2S_3$ powder in the as-synthesized state.

Sample	**Cu / at%**	**Fe / at%**	**S / at%**
$CuFe_2S_3$	18.39	35.495	46.115
Composition	$Cu_1Fe_{1.93}S_{2.51}$		

Table S3: Results of the elemental analysis of the $CuFe_2S_3$ sample. Sulphanilamide was used as reference. To calculate the composition the results for S of the EA were compared to the theoretical value of 35.44 wt. % S in $CuFe_2S_3$ leading to a composition $Cu_xFe_xS_{2.96}$). To get the full composition the Cu/Fe ratio from the EDX measurements were taken into account.

Sample	N / wt%	C / wt%	H / wt%	S / wt%
$CuFe_2S_3$	0	0	0	35.025

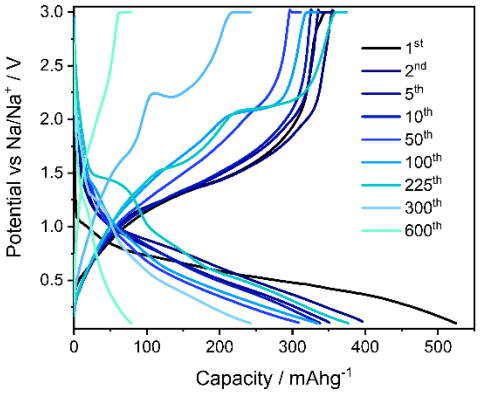

Figure S1: Discharge and charge profiles at a current rate of 0.5 Ag^{-1} in a potential window of 3 – 0.1 V of various cycles.

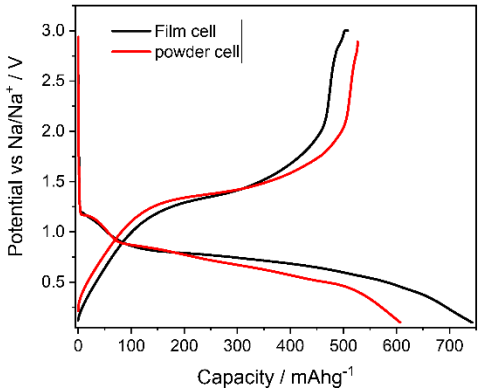

Figure S2: Discharge and charge profiles of the first cycle for a film cell (black) and a powder cell (red).

2

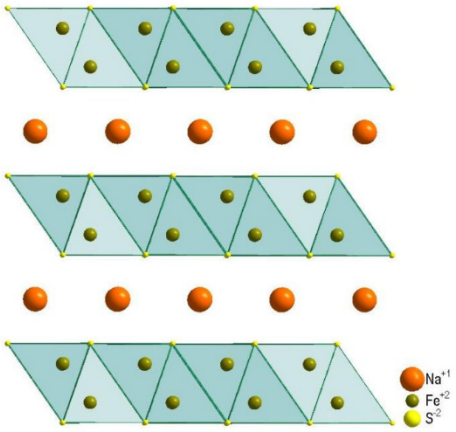

Figure S3: Crystal structure of $NaFe_{1.5}S_2$.

The proportions of the peak profile from the device for the Riedvelt refinements were determined using a fundamental approach.

```
LP_Factor(0) 'Monochromator


  Lam_recs
  {
    0.0159  1.534753  3.6854
    0.5691  1.540596  0.4370
    0.0762  1.541058  0.6000
    0.2517  1.544410  0.5200
    0.0871  1.544721  0.6200
  }


     Rp 240
     Rs 240
Full_Axial_Model(20,  22, 14, 3.05 , 6.1) '3.05
Slit_Width(!swdth, 0.5)
Divergence(, 0.03125)
```

The volume-averaged particle sizes were extracted from the following macro:

```
LVol_FWHM_CS_G_L(1, value[LVol], 0.89, value[FWHM],@ , value[CS_G],@ , value[CS_L])
```

Table S4: Rietveld refinement parameters obtained from the ex-situ XRD data of samples containing different amounts of Na/formula unit.

sample	$CuFeS_2$	$NaFe_{1.5}S_2$	Cu	Na_2S	Fe

1 Na	Space group	*I-42d*	*P-3m1*	*Fm-3m*	
	a (Å)	5.415(1)	3.853(6)	3.6101(7)	
	b (Å)	5.415(1)	3.8567(4)	3.6101(7)	
	c (Å)	10.499(2)	6.877(5)	3.6101(7)	
	Cryst. Size (nm)	35(3)	6(1)	23(2)	
	Strain (%)	0.075(3)	0.48(3)	n.i.*	
Fully discharged	Space group			*Fm-3m*	*Fm-3m*	*Im-3m*
	a (Å)			3.616(1)	6.585(1)	2.887(2)
	b (Å)			3.616(1)	6.585(1)	2.887(2)
	c (Å)			3.616(1)	6.585(1)	2.887(2)
	Cryst. Size (nm)			15.6(6)*	5.3(2)	1.2(4)
	Strain c_0 (%)			n.i.*	n.i.*	n.i.*
-2 Na	Space group			*Fm-3m*	*Fm-3m*	*Im-3m*
	a (Å)			3.617(1)	6.507(3)	2.904(2)
	b (Å)			3.617(1)	6.507(3)	2.904(2)
	c (Å)			3.617(1)	6.507(3)	2.904(2)
	Cryst. Size (nm)			17.0(4)*	3.8(3)	1.5(1)
	Strain (%)			n.i.*	n.i.*	n.i.*
-5 Na	Space group		*P-3m1*	*Fm-3m*		
	a (Å)		3.8720(9)	3.6132 (7)		

b (Å)	3.8720(9)	3.6132 (7)
c (Å)	6.864(2)	3.6132 (7)
Cryst. Size (nm)	12.8(9)	19.8(5)
Strain (%)	0.47(5)	n.i.*

Table S5: Reflection intensities determined via a single reflection fits using the program FULLPROF.

Sample / reference	Cu (111)	Cu(200)	(111)/(200)
5 Na	11310	2977	3.8
fully discharged	10150	2843	3.6
Xia et al.[1]	22	14	1.6
Rao et al.[2]	5	3	1.5
Swanson et al.[3]	100	46	2.2

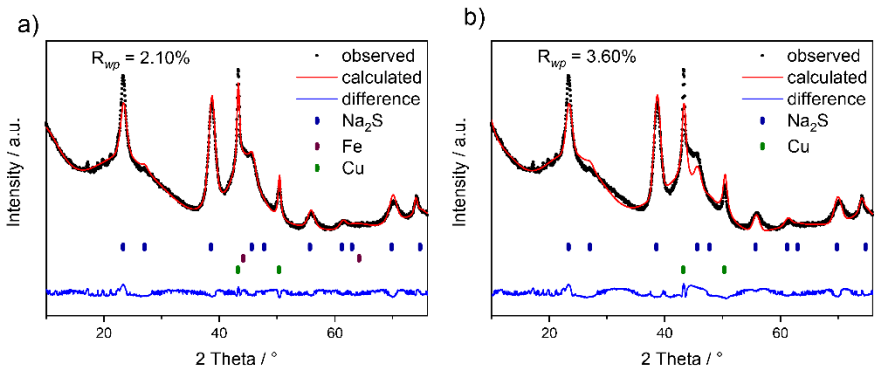

Figure S4: Results of the Rietveld refinements of the XRD pattern of $CuFe_2S_3$ at fully discharged stage. a) Including nanosized iron b) just calculated with Na_2S and Cu. Observed (black line), calculated (red line) and difference (blue line) profiles. Vertical bars indicate the positions of Bragg reflections.

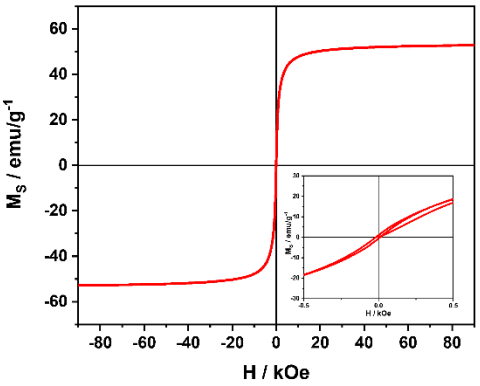

Figure S5: Magnetic Hysteresis curve of the fully discharged sample measured at 5K. The inset shows a magnification of the splitting.

Table S6: Magnetic Parameters extracted from the magnetic hysteresis curve.

	M_s [emu g^{-1}]	H_c [Oe]	n_B[μ_B]
Fully discharged sample ($Na_6CuFe_2S_3C_9$)	52.9	29	
Calculated to Fe			2.4

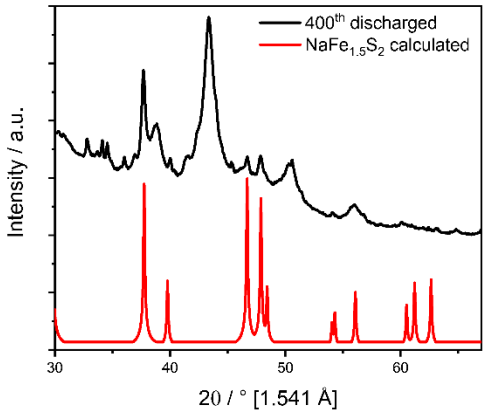

Figure S5: XRD pattern of the 400th cycle compared to the calculated pattern of $NaFe_{1.5}S_2$.

(1) Xie, Y.-P.; Zhao, S.-J. The Energetic and Structural Properties of Bcc NiCu, FeCu Alloys: A First-Principles Study. *Comput.l Mater. Sci.* **2011**, *50* (9), 2586–2591. https://doi.org/10.1016/j.commatsci.2011.03.046.
(2) Srinivasa-Rao, S.; Anantharaman, T. R.; Accurate Evaluation of Lattice Parameters of Alpha Brasses *Curr. Sci.* 1963, **32**, 262.
(3) Swanson, H. E.; Tatge, E.; *Standard X-Ray Diffraction Powder Patterns, Natl. Bur. Stand. Circ.* **539** (U.S. GPO, Washington, D.C., 1953), Vol. 1, p. 15.

8.1.3 Multi-Method Characterization of the High-Entropy Spinel Oxide $Mn_{0.2}Co_{0.2}Ni_{0.2}Cu_{0.2}Zn_{0.2}Fe_2O_4$: Entropy Evidence, Microstructure, and Magnetic Properties

Chemistry—Methods

Supporting Information

Multi-Method Characterization of the High-Entropy Spinel Oxide $Mn_{0.2}Co_{0.2}Ni_{0.2}Cu_{0.2}Zn_{0.2}Fe_2O_4$: Entropy Evidence, Microstructure, and Magnetic Properties

Svenja Senkale, Marius Kamp, Stefan Mangold, Sylvio Indris, Lorenz Kienle, Reinhard K. Kremer, and Wolfgang Bensch*

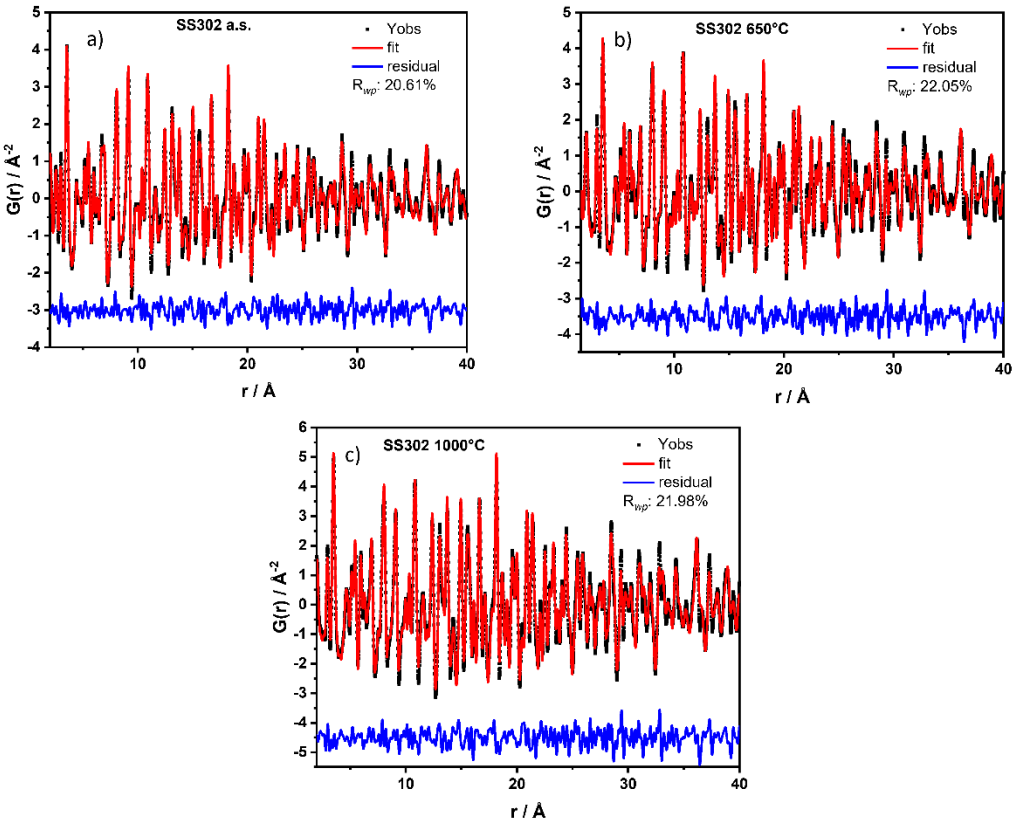

Figure S1. PDF analysis of a) a.s. b) 650°C and c) 1000°C. Observed (black line), calculated (red line) and Difference (blue line) profiles.

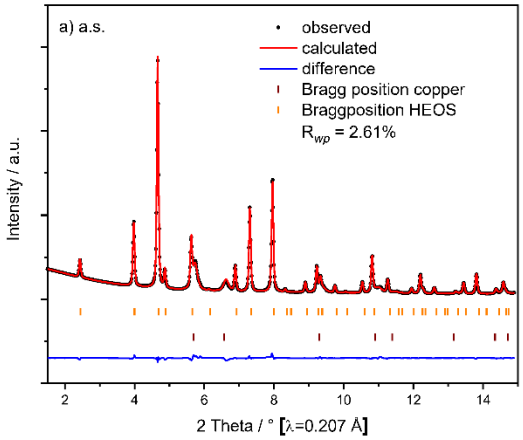

a) a.s.

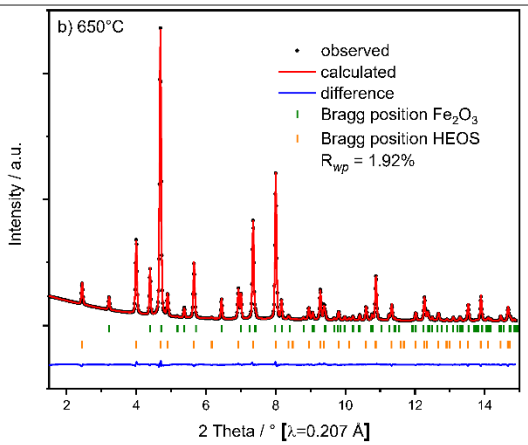

b) 650°C

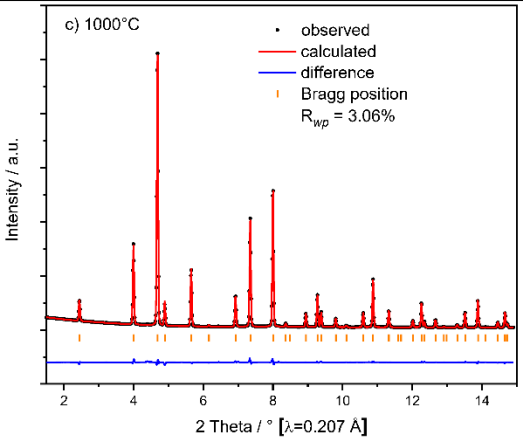

c) 1000°C

Figure S2. Rietveld refinement XRD patterns of HES1s a.s.; 500 °C, 650 °C and 1000 °C. Observed (dots), calculated (red) and difference (blue) profiles. Reflection positions are marked as vertical bars

Table S1. Diameter and lattice constant obtained from Rietveld refinements of the Synchrotron XRD Data.

samples		Crystalline size [nm]	Lattice constant [Å]
SS302 a.s.	spinel	31	8.436
	copper	13	3.581
SS302 650°C	spinel	48	8.387
	Haematite	110	5.035, 13.739
SS302 1000°C	spinel	Cryst.	8.393

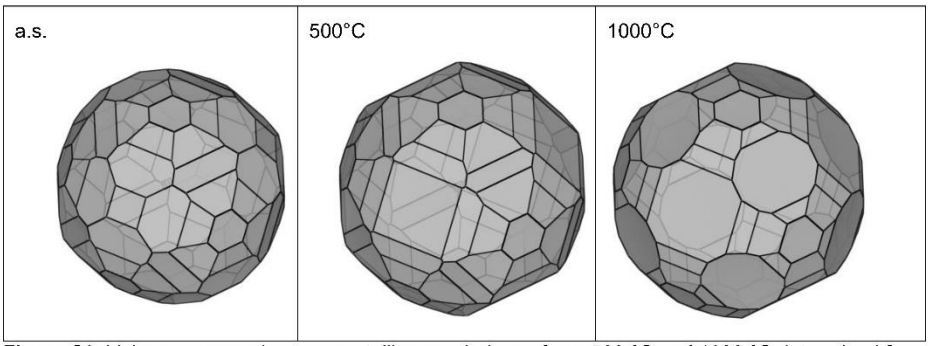

Figure S3. Volume averaged mean crystallite morphology of a.s. 500 °C and 1000 °C determined from anisotropic broadening with *Topas Academic*[1]. Visualization of crystallite morphologies using Vesta.[2]

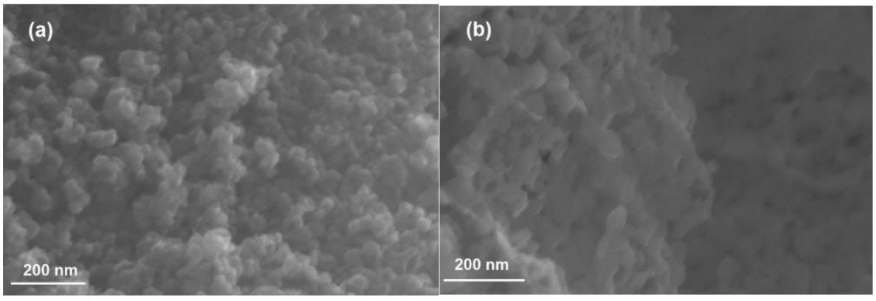

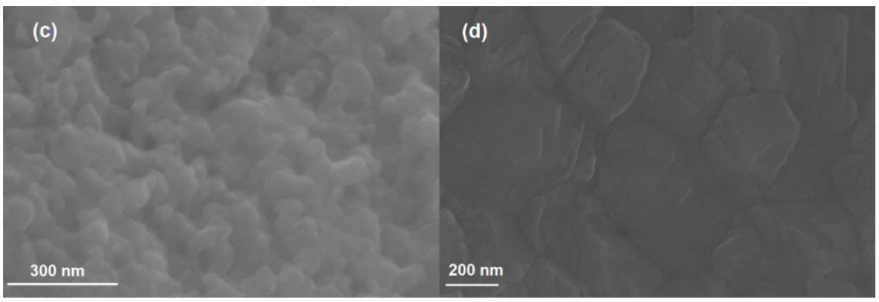

Figure S4. SEM images of the samples a) a.s., b) 500 °C,c) 650 °C and d)1000 °C.

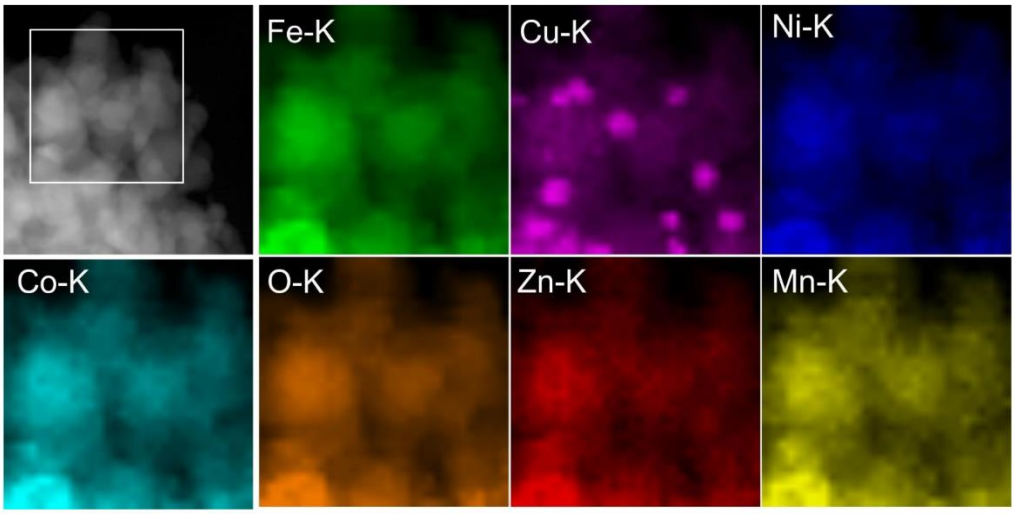

Figure S5. STEM EDX elemental mapping of the 500 °C tempered sample at the position marked by a white square. Cu elemental maps show Cu-rich precipitates. Such segregation might be caused by electron beam heating during elemental mapping. The absence of Cu and CuO reflection intensities in SAED patterns (cf. Figure xyz) indicate the formation of amorphous Cu-rich segregations possibly caused by electron beam damage.

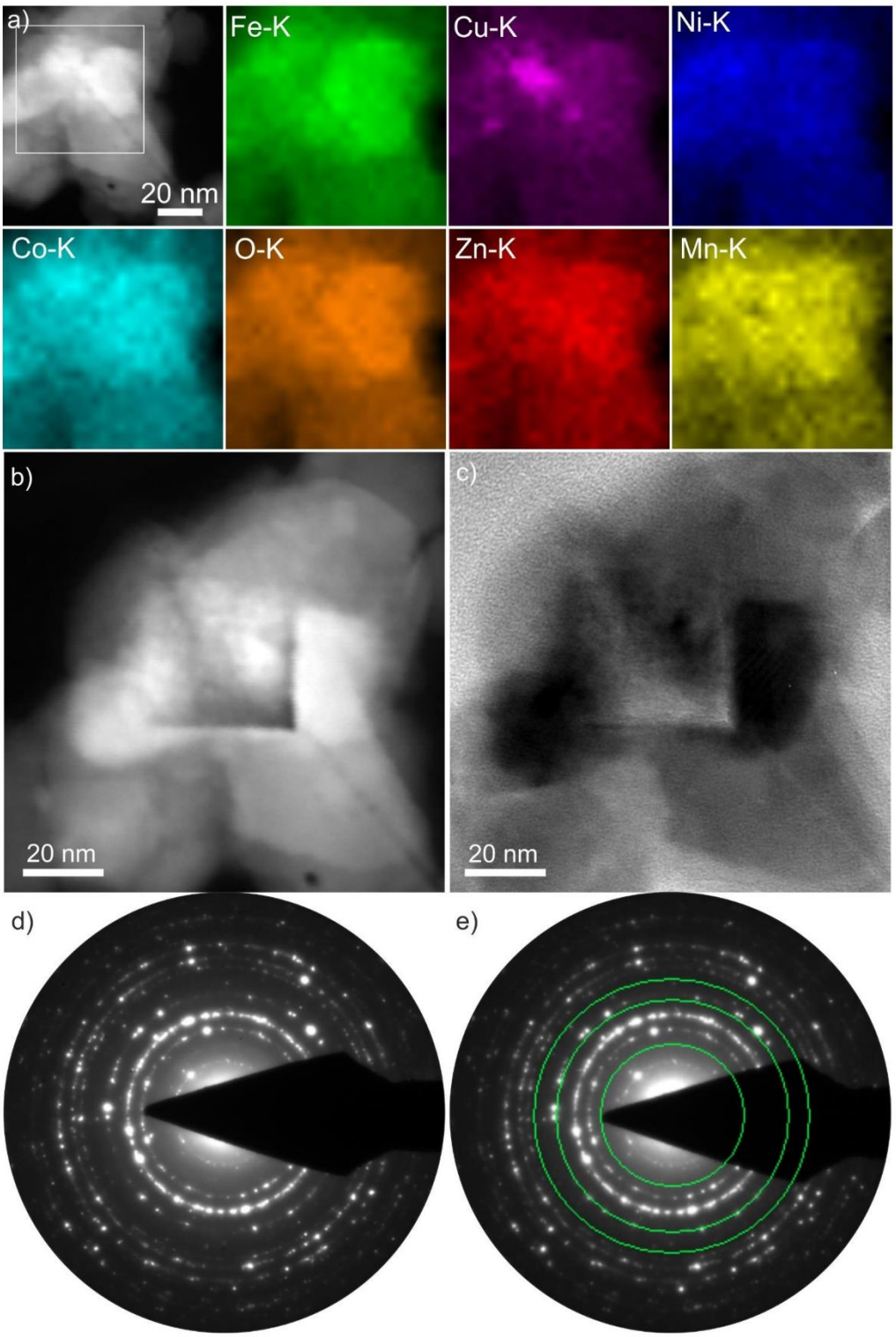
a)
20 nm
Fe-K
Cu-K
Ni-K
Co-K
O-K
Zn-K
Mn-K
b)
20 nm
c)
20 nm
d)
e)

Figure **S6**: a) STEM EDX elemental mapping of the 500 °C tempered sample at the position marked by a white square. A homogeneous distribution of the Ni, Zn, Mn, Fe, and Co is shown on this scale. However, the Cu map (purple) shows the partially high signal of Cu that might show the segregation of Cu, but the homogeneous distribution of the O signal (orange) indicates the formation of CuO. The STEM EDX elemental mapping was performed for circa 30 minutes and the electron beam, scanning over the sample, caused sample damage shown in b) a HAADF-STEM and c) a TEM image. In accordance to the XRD results no reflection intensity of Cu was measured in SAED patterns taken of the sample d) prior electron beam irradiation and e) after electron irradiation, the green circles indicate the expected position of reflection intensity from a Cu phase.

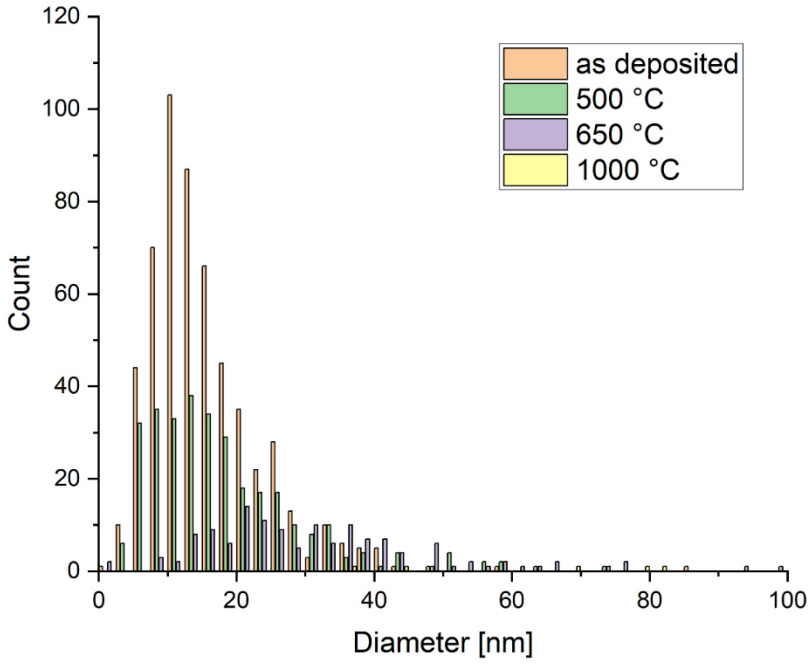

Figure S7. Histograms showing the size distribution of the crystallite sizes in the HES1 samples. The crystallite sizes were determined from dark field images.

References

(1) Coelho, A. Topas Academic 6.0. Coleho Software: Brisbane, Queensland, Australia 2016.
(2) Momma, K.; Izumi, F. VESTA 3 for Three-Dimensional Visualization of Crystal, Volumetric and Morphology Data. *J Appl Cryst* **2011**, *44* (6), 1272–1276. https://doi.org/10.1107/S0021889811038970.

8.2 Publikationsliste

1. CuFeS2 as a Very Stable High-Capacity Anode Material for Sodium-Ion Batteries: A Multimethod Approach for Elucidation of the Complex Reaction Mechanisms during Discharge and Charge Processes

   S. Senkale, S. Indris, M. Etter, W. Bensch, ACS Appl. Mater. Interfaces **2021**, 13 (22), 26034–26045.

2. Synthetically Produced Isocubanite as an Anode Material for Sodium-Ion Batteries: Understanding the Reaction Mechanism during Sodium Uptake and Release.

   S. **Senkale,** G. Cibin, A.V. Chadwick, W. Bensch, ACS Appl. Mater. Interfaces **2021**.

3. Multi-Method Characterization of the High-Entropy Spinel Oxide $Mn_{0.2}Co_{0.2}Ni_{0.2}Cu_{0.2}Zn_{0.2}Fe_2O_4$: Entropy Evidence, Microstructure, and Magnetic Properties

   S. Senkale, M. Kamp, S. Mangold, S. Indris, L. Kienle, R. K. Kremer, W. Bensch, Chem.-Methods, **2023**, 3, e202200043

Co-Autorenschaft:

4. Degradation of Sesame Oil Phenolics Using Magnetic Immobilized Laccase

   R. Amin, A. Khorshidi, W.Bensch, **S. Senkale**, M.A. Faramarzi, Catalysis Letters, **2020,** 150:3086–3095.

5. Electrochemical insertion of Li into nanocrystalline $MnFe_2O_4$: a study of the reaction mechanism

   S. Permien, H. Hain, M. Scheuermann, S. Mangold, V. Mereacre, A. K. Powell, S. Indris, U. Schürmann, L. Kienle, V. Duppel, **S. Harm**, W. Bensch, RSC Adv., **2013**, 3, 23001-23014.

8.3 Danksagung und Widmung

An dieser Stelle möchte ich mich bei allen bedanken, die mich während der Anfertigung meiner Doktorarbeit mit ihrem Fachwissen und ihrer Geduld unterstützt und motiviert haben. Besonders möchte ich dem Arbeitskreis Bensch für die tolle Arbeitsatmosphäre danken.

Ein spezieller Dank gebührt meinem Doktorvater Prof. Dr. Wolfgang Bensch, der mir dieses interessante Thema zur Verfügung stellte und mich während der gesamten Zeit fachlich betreut und begleitet hat.

Ein großes Dankeschön auch an meine Kooperationspartner Sylvio Indris, Martin Etter, Giannantonio Cibin, Alan Chadwick, Marius Kamp. Lorenz Kienle, Stefan Mangold und Reinhard Kremer, ohne die ist es nicht möglich gewesen wäre, derart qualitativ hochwertige Studien zu publizieren.

Ebenfalls möchte ich meiner Familie danken, insbesondere meinem Ehemann, die mir mit viel Geduld und Motivationshilfe zur Seite gestanden hat.

Ihnen gilt mein herzlichster Dank!

Ich widme diese Arbeit meiner verstorbenen Mutter, die leider viel zu früh von uns ging und somit den Abschluss meiner Doktorarbeit nicht miterleben kann.

Ich danke ihr für all die Jahre, die sie an meine Seite war, immer ein offenes Ohr für mich hatte und mich in all meinem Tun unterstützt hat.

Du hast immer an mich geglaubt!

Ich vermisse Dich!